



HAL
open science

Modeling of austenite to ferrite transformation in steels

Nataliya Perevoshchikova

► **To cite this version:**

Nataliya Perevoshchikova. Modeling of austenite to ferrite transformation in steels. Other. Université de Lorraine, 2012. English. NNT : 2012LORR0342 . tel-01749481

HAL Id: tel-01749481

<https://hal.univ-lorraine.fr/tel-01749481>

Submitted on 29 Mar 2018

HAL is a multi-disciplinary open access archive for the deposit and dissemination of scientific research documents, whether they are published or not. The documents may come from teaching and research institutions in France or abroad, or from public or private research centers.

L'archive ouverte pluridisciplinaire **HAL**, est destinée au dépôt et à la diffusion de documents scientifiques de niveau recherche, publiés ou non, émanant des établissements d'enseignement et de recherche français ou étrangers, des laboratoires publics ou privés.



AVERTISSEMENT

Ce document est le fruit d'un long travail approuvé par le jury de soutenance et mis à disposition de l'ensemble de la communauté universitaire élargie.

Il est soumis à la propriété intellectuelle de l'auteur. Ceci implique une obligation de citation et de référencement lors de l'utilisation de ce document.

D'autre part, toute contrefaçon, plagiat, reproduction illicite encourt une poursuite pénale.

Contact : ddoc-theses-contact@univ-lorraine.fr

LIENS

Code de la Propriété Intellectuelle. articles L 122. 4

Code de la Propriété Intellectuelle. articles L 335.2- L 335.10

http://www.cfcopies.com/V2/leg/leg_droi.php

<http://www.culture.gouv.fr/culture/infos-pratiques/droits/protection.htm>

THÈSE

Pour l'obtention du titre de

Docteur de l' Université de Lorraine

Spécialité : Science et Ingénierie des Matériaux et Métallurgie

Présentée par

Nataliya PEREVOSHCHIKOVA

Modeling of austenite to ferrite transformation in steels

Thèse soutenue publiquement le 13 novembre 2012 à Nancy devant le jury composé de:

Mme S. Fries	Ruhr-Universität Bochum	Examineur
Mr M. Gouné,	ICMMB Bordeaux	Examineur, Rapporteur
Mr Y. Le Bouar,	LEM ONERA-CNRS	Examineur
Mr S. van der Zwaag,	TU Delft	Examineur, Rapporteur
Mme S. Denis,	IJL SI2M	Encadrant
Mr B. Appolaire,	LEM ONERA	Encadrant
Mr J. Teixeira,	IJL SI2M	Encadrant

Institut Jean Lamour - Département SI2M

Université de Lorraine – Pôle M4: matière, matériaux, métallurgie, mécanique

Je voudrais dédier cette thèse à Guillaume LaBelle

Acknowledgements

Cette thèse a été effectuée au sein de l'équipe « Microstructures et contraintes » de l'Institut Jean Lamour à Nancy. Le travail n'aurait pas abouti sans le soutien précieux et permanent de plusieurs personnes que je tiens à remercier dans ces quelques lignes.

Je tiens tout d'abord à remercier Benoît Appolaire pour m'avoir guidée, encouragée, conseillée. Merci Benoît pour tes explications, ta confiance et les conseils pour la programmation, la rédaction d'article et ce manuscrit.

Mes remerciements vont également à Julien Texeira, pour la gentillesse et la patience qu'il a manifestées à mon égard durant cette thèse, pour tous les conseils pour la programmation et la rédaction de ce manuscrit.

Je remercie Sabine Denis ainsi qu'Elisabeth Aeby-Gautier, directrice de l'équipe, pour m'avoir accueillie au sein de leurs institutions, et pour les conseils stimulants.

Je remercie vivement Benoît Denand, ingénieur d'études à l'IJL, pour son aide indispensable à la mise en œuvre et au traitement des expériences, sa bonne humeur et sa gentillesse qui ont rendu la réalisation des essais de cinétique très agréable.

Je tiens à remercier sincèrement l'ensemble du personnel du Laboratoire, chercheurs, techniciens, et secrétaires.

Mr Sybrand Van der Zwaag et Mr Mohamed Gouné ont accepté d'être les rapporteurs de cette thèse et je les en remercie. Merci également à Mme Suzanna Fries et Mr Yann Le Bouar pour leur participation au jury. Je les remercie tous pour leurs remarques enrichissantes dont j'ai essayé de tenir compte dans la version finale du manuscrit.

Je remercie mon père, ma mère, ma soeur, mon amour Anton, et mon cher coloc et ami Valerio pour leur affection et soutien constants.

Contents

Contents	v
Résumé étendu	1
Introduction	13
1 Computation of α/γ thermodynamic equilibrium	17
1.1 Thermodynamic description	20
1.1.1 CalPhaD Formalism	20
1.1.2 Multiple Sublattices model	25
1.1.3 Equilibrium conditions in a closed system	28
1.1.3.1 Binary alloys	28
1.1.3.2 Multicomponent alloys	30
1.1.4 Convex hull construction	32
1.1.4.1 Discretization	33
1.1.4.2 Quick hull algorithm	35
1.1.4.3 Determination of the phase fields	37
1.1.4.4 Search for a single tie-line	40
1.2 Results	41
1.2.1 Fe-C system	41
1.2.2 Fe-C-Cr system	44
1.2.3 Fe-C-Cr-Mo system	55
1.3 Conclusion	59

2	Thick interface model for the $\gamma \rightarrow \alpha$ transformation	61
2.1	The model description	64
2.1.1	α/γ interface	64
2.1.2	Coupling with the bulks	71
2.1.3	Governing equations	73
2.1.3.1	Limit cases	73
2.1.3.2	Data	76
2.2	Massive transformation in Fe-Ni alloys	77
2.3	Fe-C-X alloys	83
2.3.1	Limit cases	84
2.3.2	Deviations from the limit cases	90
2.3.3	Choice of a relevant ternary system	92
2.3.4	Specific algorithms	95
2.3.5	Growth regimes	104
2.3.6	Isothermal growth of α	107
2.3.6.1	Below the zero-partition line	109
2.3.6.2	Above the zero-partition line	112
2.3.7	Discussion	119
2.4	Conclusion	122
 3	 Diffuse interface model for the $\gamma \rightarrow \alpha$ transformation	 125
3.1	Phase field model	127
3.1.1	Model of Kim, Kim, Suzuki	127
3.1.2	Phase field parameters	132
3.2	Phase field Mobility	134
3.2.1	Interface dissipation	135
3.2.2	2 nd order matched asymptotic analysis	138
3.2.2.1	Outer expansion	140
3.2.2.2	Inner expansion	142
3.2.2.3	Particular cases	156
3.3	Interface mobility in Fe-C alloys	161
3.3.1	Local equilibrium at the interface	163
3.3.2	Mixed-mode growth	169

CONTENTS

3.4	Interface mobility in Fe-C-X alloys	172
3.4.1	Kinetic pathways in isothermal condition	174
3.5	Conclusion	181
A	CalPhaD thermodynamic database for Fe-C-Cr	183
B	Main function of convex hull building in numerical language	189
C	The hybrid algorithm applied to Fe-C-Ni	193
D	Data for the kinetic calculations	197
E	Interface mobility in Fe-C	199
	References	205

CONTENTS

Résumé étendu

Introduction

Les aciers sont utilisés dans presque toutes les industries en tant que matériaux de structure essentiels. Ceci est en partie dû à la grande quantité de minerai de fer disponible et à l'efficacité des procédés d'extraction mais aussi au large spectre de propriétés mécaniques que l'on peut atteindre grâce aux éléments d'alliage et aux traitements thermomécaniques appropriés qui autorisent une grande richesse de microstructures. En effet, les transformations allotropiques du fer à pression atmosphérique avec la possibilité de formation de carbures, donnent une richesse inégalée de microstructures résultant de différentes transformations de phases.

Parmi toutes les transformations à l'état solide dans les aciers, la transformation allotropique de l'austénite γ (phase cubique à faces centrées) en ferrite α (phase cubique centrée) est très importante car elle conduit à la formation de nombreuses microstructures, telles que la ferrite allotriomorphe, la ferrite de Widmanstätten, la bainite, la perlite et même la martensite quand cette phase métastable est considérée comme une phase cubique centrée déformée sursaturée en carbone. De plus, dans les aciers dual phase la transformation $\gamma \rightarrow \alpha$ transformation contrôle les transformations ultérieures, par exemple bainitique ou martensitique.

Il est bien connu que cette transformation est contrôlée par la diffusion, au moins aux températures les plus élevées, où la morphologie allotriomorphe est observée. Elle a ainsi été étudiée depuis longtemps, tant d'un point de vue expérimental que d'un point de vue de la modélisation. Au premier ordre, les caractéristiques cristallographiques ne semblaient pas cruciales pour la morphologie de la ferrite à haute température, comme en témoigne l'utilisation du terme allotriomorphe pour désigner la ferrite aux joints de grains. Par conséquent, des concepts com-

muns à la solidification s'appuyant sur la description des diagrammes de phases et des phénomènes de transport dans les phases en volume ont été employés très tôt pour prédire la cinétique de transformation. Si des prédictions satisfaisantes par rapport aux mesures ont pu être obtenues rapidement dans le système binaire Fe-C, la cinétique reste « énigmatique » dans les aciers alliés même dans les systèmes ternaires simples comme Fe-C-X. Différents facteurs contribuent à la grande complexité de la cinétique dans les alliages ternaires. D'une part, les diagrammes ternaires impliquent plus de degrés de liberté pour choisir la conode qui représente les concentrations aux interfaces, même si l'on suppose l'équilibre local. D'autre part, la particularité de la cinétique dans les systèmes Fe-C-X est en partie due à la très grande différence de diffusivités chimiques entre le carbone interstitiel et l'élément substitutionnel X. Finalement, il existe de plus en plus de preuves que les phénomènes d'interface prennent une part importante dans l'ensemble du processus et seraient déterminants pour expliquer la cinétique inattendue.

Dans l'énorme quantité d'études sur la transformation $\gamma \rightarrow \alpha$, une étude supplémentaire pourrait apparaître absolument inutile. En effet, la plupart des modèles présentés dans les chapitres suivants sont déjà connus. Néanmoins, il est rapidement apparu au cours de ce travail que ces modèles contiennent implicitement des difficultés cachées, qui nécessitent des analyses approfondies et des solutions pratiques (du point de vue des méthodes numériques et des algorithmes). Si les résultats peuvent paraître modestes par rapport à la pleine compréhension de la transformation $\gamma \rightarrow \alpha$ dans les aciers ternaires, nous espérons que la présente étude sera utile, tout d'abord en mettant en évidence les difficultés et les limites des différents modèles malgré les affirmations optimistes de la littérature puis en proposant quelques solutions alternatives et extensions et finalement en montrant clairement ce que l'on peut réellement attendre des différents modèles.

La présente thèse contient trois parties, tout à fait indépendantes, ce qui reflète la manière dont elle a été conduite. Chaque partie est autocohérente, et contient en particulier une conclusion indépendante qui élimine la nécessité d'une conclusion générale qui serait redondante.

La première étape nécessaire pour décrire la transformation de phases est une bonne prédiction thermodynamique. En ce qui concerne les aciers multiconstitués, l'approche Calphad semble être le seul moyen pratique et cohérent pour avancer. Cependant, trouver l'équilibre à partir des énergies de Gibbs qui entrent dans cette description n'est pas aussi simple qu'il y paraît lors de l'utilisation aveugle de logiciels dédiés. Dans le chapitre 1, nous allons donc proposer un nouvel algorithme hybride combinant la construction d'une enveloppe convexe avec la méthode classique de Newton-Raphson. Nous montrerons ses possibilités pour des aciers ternaires Fe-C-Cr et quaternaires Fe-C-Cr-Mo dans des cas particulièrement difficiles.

Dans le chapitre 2, nous allons étudier un modèle d'interface épaisse visant à prédire l'ensemble du spectre des conditions à l'interface α/γ au cours de la croissance de la ferrite, de l'équilibre complet au paraéquilibre avec des cas intermédiaires qui seront les plus intéressants. En effet, nous allons montrer que certaines cinétiques particulières peuvent être prévues avec un minimum de paramètres d'ajustement, en prenant en compte principalement la diffusion dans l'interface épaisse. Nous allons aussi donner un regard critique sur les capacités réelles de ce type de modèle.

Finalement, dans le chapitre 3, nous allons étudier le modèle de champ de phase développé pendant la thèse précédente sur ces sujets [155] à Nancy. Tout d'abord, une analyse approfondie des conditions à l'interface données par le modèle sera réalisée en utilisant la technique des développements asymptotiques. En utilisant les connaissances fournies par cette analyse, nous allons nous concentrer sur le rôle de la mobilité intrinsèque d'interface sur la cinétique, à la fois dans le cas simple d'alliages binaires Fe-C et dans le cas plus complexe d'alliages Fe-C-Mn.

Chapitre 1

Calcul de l'équilibre thermodynamique α/γ

Des logiciels pour calculer les équilibres thermodynamiques dans matériaux multiphasés et multiconstitués sont aujourd'hui couramment utilisés pour l'analyse d'expériences, la conception d'alliages ou la maîtrise de paramètres procédé. Il est très souvent mentionné que la pertinence des prévisions repose fortement sur la qualité des bases de données construites à partir d'expériences et de calculs ab-initio. C'est évidemment vrai et des efforts importants sont faits pour obtenir des données expérimentales fiables et construire des bases de données. Mais il est moins souvent souligné que les calculs d'équilibres thermodynamiques dans les alliages multiphasés et multiconstitués à partir de modèles analytiques de l'énergie de Gibbs (par exemple CalPhaD) exigent aussi des algorithmes efficaces et fiables. La plupart des logiciels commerciaux utilisés pour le traitement des systèmes multiphasés et multiconstitués en science et ingénierie des matériaux s'appuient sur des algorithmes de résolution d'équations non linéaires. La méthode bien connue de Newton-Raphson (NR) est la plus fréquemment utilisée. En effet, elle permet de faire des calculs rapides grâce à ses propriétés de convergence quadratique, mais malheureusement au détriment de la fiabilité en raison de son caractère local. L'algorithme NR peut effectivement être pris au piège par des minima locaux métastables, et même diverger si l'estimation initiale est loin du vrai minimum. Il convient de noter que de mauvaises estimations, soit métastables soit même instables dans le pire des cas, peuvent être beaucoup plus difficiles à détecter durant les calculs cinétiques qui utilisent des conditions d'équilibre local à l'interface et de ce fait, peuvent conduire à des situations instables. Nous avons été confrontés à une telle situation lors de notre travail sur la transformation de l'austénite en ferrite dans les aciers Fe-C-Cr ce qui nous a obligé à trouver un algorithme plus robuste, combinant une première étape globale suivie d'une étape de raffinement rapide par la méthode NR.

Ces dernières années ont vu un regain d'approches globales, en particulier dans le domaine des modélisations CalPhaD afin d'éviter les inconvénients mentionnés ci-dessus de la méthode NR. Différentes solutions pour déterminer le minimum global ont été proposées à ce jour en science des matériaux : elles reposent toutes

plus ou moins sur la recherche de l'enveloppe convexe approximative de l'hypersurface de l'énergie de Gibbs discrétisée à la suite de travaux antérieurs en pétrologie [49] ou en ingénierie chimique [94]. La première solution, proposée par Chen et coll. [39] et implémentée dans le logiciel Pandat [41] utilise un type de méthode « brute force » avec une simplicité conceptuelle comme principal avantage : les calculs sont réduits à des tests simples de coplanarité parmi les ensembles possibles de pseudo-composés stoechiométriques qui résultent de la discrétisation de l'espace des concentrations. Si dans le principe cette méthode peut être appliquée à n'importe quel système, elle est susceptible de conduire à des temps de calculs importants lorsque le nombre d'espèces ou de composés augmente : en effet le temps de calcul est en N^3 , N étant le nombre de noeuds du maillage. En vue de concevoir un algorithme plus performant en terme de temps de calcul, Emelianenko et coll. [55] ont tiré avantage de certaines caractéristiques géométriques de l'hypersurface de l'énergie de Gibbs donnée par les dérivées premières et les dérivées secondes par rapport aux concentrations. Leur algorithme a été appliqué à des alliages binaire et ternaire seulement et peut devenir impraticable pour de plus grandes dimensions. Pour les alliages binaires, ce qu'on appelle le Graham scan algorithme a également été modifié par [40] : le temps de calcul est en N et l'algorithme est beaucoup plus rapide que l'algorithme original de [41] mais il ne peut malheureusement pas être étendue aux alliages multiconstitués. Plus récemment enfin, Belov et coll. [23] ont montré des résultats en utilisant un algorithme d'enveloppe convexe mis en oeuvre dans leur logiciel « PhDi package » consacré aux alliages binaires et ternaires ; malheureusement, ils n'ont pas fourni de détails sur l'algorithme d'enveloppe convexe mis en oeuvre, ni discuté de leur solution en termes d'efficacité de calcul.

Nous introduisons un nouvel algorithme hybride pour améliorer la fiabilité des calculs d'équilibre. L'objectif n'est pas de calculer de façon générale les diagrammes de phases dans tous les systèmes multiphasés multiconstitués. Mais, l'algorithme a été conçu pour traiter correctement l'équilibre entre deux phases dans les calculs cinétiques. A notre avis, l'algorithme est particulièrement fiable et efficace pour être adopté comme stratégie générale dans des logiciels de constructions de diagrammes de phases. Dans notre algorithme hybride, l'équilibre est toujours calculé en utilisant NR dans l'étape finale. Cependant, les erreurs po-

tentielles de NR sont évitées en trouvant d'abord une bonne estimation initiale de la solution. Cette première étape est basée sur la détermination de l'enveloppe convexe pour les deux hypersurfaces des énergies de Gibbs des deux phases. Pour construire cette enveloppe convexe de manière efficace, nous avons utilisé l'algorithme répandue QuickHull [20] adapté à nos calculs spécifiques pour réduire le temps de calcul. Il est appliqué à l'équilibre ferrite-austénite α/γ dans les aciers ternaires et quaternaires. Dans un premier temps, nous rappelons brièvement les ingrédients du « Compound Energy model » (par ex. [74]) adopté pour les énergies de Gibbs de α et γ en tenant compte du carbone comme espèce interstitielle. Ensuite, l'algorithme est détaillé, en utilisant les systèmes ternaires particuliers Fe-C-X ($X = \text{Ni}, \text{Cr}, \text{Mn}$) pour illustrer les différentes étapes. Le bilan en termes de temps de calcul entre la construction de l'enveloppe convexe et l'étape suivante de NR est examiné pour obtenir le meilleur compromis. Enfin, des séquences de calculs dans le système quaternaire Fe-C-Cr-Mo pour des plages de température démontrent le gain apporté par l'algorithme hybride pour les calculs automatiques de diagramme de phase.

Chapitre 2

Modèle à interface épaisse pour la transformation

$\gamma \rightarrow \alpha$

La transformation $\gamma \rightarrow \alpha$ dans les aciers est la transformation contrôlée par la diffusion la plus étudiée. Outre les travaux concernant les mécanismes à l'échelle atomique (par exemple [4]), l'approche la plus courante pour prédire les cinétiques de transformation de phases contrôlées par la diffusion repose sur le concept que l'on appelle interface abrupte : les interfaces sont réduites à des surfaces mathématiques avec des propriétés thermodynamiques et cinétiques intrinsèques comme dans le travail fondateur de Gibbs [63]. Même si ce n'est pas le seul moyen de traiter des interfaces comme on le verra dans le chapitre suivant, il s'est avéré comme le moyen le plus pratique pour développer des modèles de microstructures à l'échelle du millimètre, c'est-à-dire dans un Volume Élémentaire Représentatif (VER) pour la mécanique des structures (par exemple [17, 95]).

Deux étapes sont intrinsèquement impliquées dans cette approche. Tout d'abord, le problème de transport dans le volume des phases doit être résolu en prenant en compte l'interface mobile par les bilans locaux de soluté reliant les sauts de concentration de soluté, la vitesse et les sauts de flux [142]. Puis, certaines conditions doivent être imposées à l'interface (parfois appelées fonctions réponse [18]) qui sont les conditions aux limites nécessaires pour la diffusion dans le volume. Les premiers travaux considéraient généralement l'équilibre local à l'interface, car c'est le cas le plus simple. De plus, le problème de la frontière mobile peut être traité analytiquement, car pour certaines géométries simples (plan, cylindre, sphère ...), l'interface est une iso-concentration. Par conséquent, des solutions similaires à celles des problèmes de diffusion peuvent être utilisées comme dans les travaux précurseurs de Stefan [145], Zener [163], Frank [60], Ivantsov [91] et Horvay et Cahn [83]. Si cela est généralement une bonne hypothèse lorsqu'il s'agit de la solidification des métaux et alliages dans des conditions normales (celles qui prévalent dans la plupart des procédés de coulée industriels), c'est moins évident à l'état solide. En effet, (i) il existe très souvent des contraintes cristallographiques entre les phases solides qui coexistent [43, 44]. Des marches ont été

observées, même à haute température, aux interfaces généralement considérées implicitement comme incohérentes [5]. De plus, (ii) les diffusivités à l'état solide sont généralement beaucoup plus faibles que dans un liquide. En outre, lorsque la température diminue dans des domaines où les phases solides prévalent, les mobilités atomiques diminuent également et l'équilibre est moins susceptible d'être atteint.

Cependant, dans de nombreux cas, l'hypothèse de l'équilibre local donne des résultats satisfaisants, en particulier dans les alliages métalliques binaires dilués donnant lieu à des précipitations [157]. C'est également le cas pour les transformations dans les alliages multiconstitués à hautes températures, c'est-à-dire pas trop loin de l'équilibre, et quand toutes les diffusivités sont du même ordre de grandeur, par exemple [66, 120]. Dans d'autres cas, cette hypothèse ne peut prédire la cinétique correctement. Aussi, différentes améliorations ont été proposées pour la description des processus de diffusion dans le volume : diffusion dans des systèmes finis avec soft impingement [57], court-circuit de diffusion (par exemple par « collector plate mechanism » [2]) ou prise en compte de complexités géométriques (dans ce cas, en s'appuyant sur des modèles numériques) [154]. Mais toutes ces améliorations ne sont pas suffisantes pour expliquer de nombreux phénomènes observés, en particulier les cinétiques lentes et stases à des fractions inférieures à l'équilibre [6]. La voie la plus prometteuse pour tenir compte de toutes ces caractéristiques surprenantes repose sur la description des phénomènes interfaciaux. Ce n'est pas une nouvelle tendance, puisque les transformations contrôlées par l'interface ont été considérées très tôt comme le cas opposé aux transformations contrôlées par la diffusion [44]. Dans le contexte des aciers multiconstitués, des conditions hors équilibre ont été suggérées par Hultgren pour les éléments substitutionnels seulement, situation appelée paraéquilibre [86]. Cependant, du fait que le paraéquilibre constitue un cas limite sans partition pour les espèces substitutionnelles, la condition à l'interface peut être exprimée sans aucune connaissance des processus interfaciaux impliqués. En parallèle, les travaux sur le « solute drag » par des joints de grains ont mis en évidence le rôle de la diffusion aux interfaces/joints de grains pour expliquer des variations importantes mais en même temps curieuses de la cinétique des frontières mobiles [32, 81]. Des concepts similaires appliqués à la solidification rapide [82] ainsi qu'aux transfor-

mations massives [79, 81] ont bénéficié du cadre cohérent élaboré progressivement par Hillert pour le traitement des interfaces hors équilibre [71, 76]. Appliquant la thermodynamique des processus irréversibles classique (par ex. [68]), Hillert a proposé de diviser l'énergie de Gibbs dissipée en différentes contributions identifiées dans les différents problèmes mentionnés ci-dessus : la dissipation par la friction de l'interface (transformation contrôlée par l'interface) et la dissipation par la diffusion dans l'interface dite « trans-interface diffusion » (solidification rapide et traînage de soluté). Des avancées récentes ont été réalisées par Odqvist dans une série d'études [124, 125, 127] qui représentent de grandes améliorations par rapport aux approches précédentes (par ex. [56, 136]).

Le premier objectif de ce chapitre est d'enrichir les modèles d'interface abrupt utilisés couramment pour gérer les évolutions de microstructure dans des problèmes à grande échelle [120, 121]. Par conséquent, nous avons conservé la structure de ce type de modèle en nous appuyant sur la résolution de l'équilibre local couplée à la diffusion en volume à l'aide de modèles analytiques simples. Toutefois, l'hypothèse de l'équilibre local a été relaxée grâce à la description des processus irréversibles à l'intérieur de l'interface dans le cadre proposé par Hillert [73] et inspiré par le modèle d'Odqvist [127]. En second lieu, ce modèle est destiné à être utilisé pour étudier les cinétiques particulièrement curieuses dans des aciers ternaires Fe-C-X qui n'ont pas été complètement expliquées ni prédites jusqu'à présent.

Par conséquent, le chapitre est structuré comme suit. Tout d'abord, le cadre général du modèle est détaillé (§2.1). Ensuite, il est appliqué au cas le plus simple présentant une dissipation à l'interface significative, c'est-à-dire la transformation massive $\gamma \rightarrow \alpha$ dans les alliages binaires Fe-Ni, pour illustrer certaines caractéristiques spécifiques du modèle (§2.2). Enfin, la dernière partie est consacrée à des alliages ternaires Fe-C-X visant à étudier les capacités du modèle à interface épaisse pour traiter des cinétiques « énigmatiques » (§2.3).

Chapter 3

Interface diffuse pour la transformation $\gamma \rightarrow \alpha$

Comme montré dans le chapitre précédent, faire une séparation nette entre l'interface et le volume des phases peut causer de sérieux problèmes en terme de robustesse dans des systèmes montrant des régimes cinétique très différents comme les alliages Fe-C-X. Le développement d'algorithmes spéciaux s'est donc avéré obligatoire pour surmonter ces problèmes et obtenir des conditions initiales satisfaisantes pour poursuivre. De plus, il a été conclu que les phénomènes les plus intéressants sont susceptibles de se produire dans l'interface. C'est pourquoi, nous avons opté pour un modèle de champ de phases qui a donné des résultats intéressants pour la transformation $\gamma \rightarrow \alpha$ dans des alliages Fe-C-X dans un travail antérieur [155]. En effet, bien que les modèles à champ de phases sont de plus en plus « gourmands » en ressources calcul (car ce sont des modèles à champs complets), ils ne peuvent pas être affectés par les problèmes rencontrés avec les modèles à interface épaisse. Le couplage avec le volume est en effet transparent et ne demande pas d'effort particulier. De plus, ils permettent d'obtenir des profils de concentration plus réalistes car (i) ils tiennent compte naturellement du « soft impingement » qui est très important dans les modifications des régimes de croissance comme le montre [155, 156]. (ii) Ils tiennent naturellement compte de la diffusion dans la phase α qui peut jouer un rôle non négligeable pendant les traitements anisothermes (voir par exemple [35, 36, 37]). Néanmoins la flexibilité offerte par l'interface diffuse doit être analysée en détail. Ainsi, même si la cohérence thermodynamique est retenue, les résultats du modèle en termes de concentrations interfaciales nécessitent une attention particulière. En effet, l'inconvénient de l'interface diffuse est que les différents processus dissipatifs sont plus difficiles à identifier que dans le modèle à interface épaisse du chapitre §2.

Aussi la motivation de ce chapitre est double.

- (i) D'abord donner une analyse détaillée de la mobilité du champ de phase. D'une part, ceci permettra de faire des comparaisons avec le modèle à interface épaisse dans le futur. D'autre part, cela confirmera les expressions proposées précédemment dans [155] pour obtenir des résultats pertinents dans le système Fe-C-X.

(ii) Puis, analyser un aspect qui a été négligé dans le chapitre précédent comme dans [155] : l'effet d'une mobilité finie de l'interface. En effet, il y a débat pour savoir si la mobilité de l'interface est essentielle ou non pour prédire la cinétique de la transformation $\gamma \rightarrow \alpha$ dans des aciers Fe-C-X [1, 35, 61, 115, 139, 144]. Même si la modélisation est très avancée dans les alliages binaires ou dans des alliages multiconstitués avec des diffusivités des éléments comparables, le challenge concerne les aciers Fe-C-X.

Ce chapitre est organisé de la manière suivante :

D'abord, nous décrivons brièvement le modèle champ de phases proposé dans [155] et utilisé dans ce travail. Puis, nous consacrons une partie à l'analyse des conditions à l'interface avec pour objectif une meilleure compréhension des résultats du modèle champ de phases en particulier pour ce qui concerne la mobilité du champ de phase. Finalement, nous étudierons l'influence de la mobilité de l'interface sur les régimes de croissance dans les alliages Fe-C et finalement dans les alliages Fe-C-X.

Introduction

Steels are used in almost all industries as an essential structural materials. This is partly due to the large amount of iron ores and efficient processes to extract the metal, but also because a large spectrum of mechanical properties can now be achieved by suitable alloying and thermo-mechanical treatments. This large spectrum is permitted by the rich microstructures that steels can feature. Indeed, the allotropic transformations that Fe exhibits at normal pressure together with the capabilities of forming carbides, give an unrivaled richness of microstructures, ensuing from different combined phase transformations.

Among all the transformations at the solid state in steels, the allotropic transformation of austenite γ (fcc phase) into ferrite α (bcc phase) is very important because it takes part into many microstructures, such as allotriomorphic ferrite, Widmanstätten ferrite, bainite, pearlite, and even martensite when this metastable phase is considered as a deformed bcc phase supersaturated in carbon. Moreover, in dual phase steels, the $\gamma \rightarrow \alpha$ transformation controls the subsequent transformations, e.g. bainite or martensite.

It is well known that this transformation is diffusion-controlled, at least at the highest temperatures where allotriomorphic morphology is observed. It has thus been investigated for a long time, both from an experimental point of view and from a modeling point of view. At first order, the crystallographic features did not appear crucial for the high temperature ferrite morphology, as testified by the use of “allotriomorphic” to denote ferrite at grain boundaries. Consequently, concepts common with solidification relying on the description of phase diagrams and of transport processes in bulk phases have been employed early to predict transformation kinetics. If good predictions with respect to measurements have rapidly been obtained in the binary Fe-C system, the kinetics remain puzzling in

alloyed steels, even in simple ternary systems, i.e. Fe-C-X. Different factors contribute to the much higher complexity of kinetics in ternary alloys. First, ternary diagrams involve more degrees of freedom for selecting the tie-line representing interfacial concentrations, even if local equilibrium is assumed. Second, much of the peculiarity of the kinetics in Fe-C-X systems is partly due to the very large difference in chemical diffusivities between interstitial carbon and substitutional X. Finally, there are more and more evidences that interface phenomena take an important part in the whole process, and would be decisive to explain unexpected kinetics.

In the huge amount of studies about the $\gamma \rightarrow \alpha$ transformation, an additional investigation could appear quite unnecessary. Indeed, most of the models presented in the subsequent chapters are already known. However, it has rapidly appeared during the course of the present work that those models involve implicit hidden difficulties, which necessitate deep analyses and practical solutions (from the point of view of numerical methods and algorithms). If the results may appear very modest with respect to the full understanding of the $\gamma \rightarrow \alpha$ transformation in ternary steels, we hope that the present study will be useful, first by rendering clear the difficulties and limitations of the different models despite the optimistic claims of the literature; second by proposing a few alternative solutions and extensions; and third by clearly showing what can really be expected from the different models.

The present thesis contains three parts, quite independent, reflecting the way that has been followed. Each part is self-consistent, in particular containing independent conclusions which will remove the need for a redundant general conclusion.

The first necessary step to describe phase transformation is a good thermodynamic prediction. Concerning multicomponent steels, the CalPhaD approach seems to be the only practical and consistent way to proceed. However, finding equilibrium from the Gibbs energies entering this description is not as straightforward as it may seem when using blindly devoted softwares. In chapter §1, we will thus propose a new hybrid algorithm combining the construction of a convex hull to the more classical Newton-Raphson method. We will demonstrate its ca-

pabilities on ternary Fe-C-Cr and quaternary Fe-C-Cr-Mo steels, with particular stiff features.

In chapter §2, we will investigate a thick interface model aiming at predicting the whole spectrum of conditions at an α/γ interface during ferrite growth, from full equilibrium to paraequilibrium, with intermediate cases as the most interesting feature. Indeed, we will show that some peculiar kinetics can be predicted with a minimum of fitting parameters, accounting mainly for diffusion inside the thick interface. We will also give a critical view of the real capabilities of this kind of model.

Finally, in chapter §3, we will investigate the phase field model developed during the previous thesis on this topics [155] in Nancy. First, a thorough analysis on the conditions at the interface delivered by the model will be carried out using the technique of matched asymptotic expansions. Using the insights provided by this analysis, we will focus on the role of the intrinsic interface mobility on the kinetics, both in simple binary Fe-C alloys and in the more complex case of Fe-C-Mn alloys.

Chapter 1

Computation of α/γ thermodynamic equilibrium

Softwares calculating thermodynamic equilibria in multiphase and multicomponent materials are now commonly used for analyzing experiments, designing alloys or refining process parameters. It is very often mentioned that the relevance of the predictions heavily relies on the quality of the databases built upon experiments and ab-initio calculations. This is obviously true, and tremendous efforts are pursued for getting reliable data and for building databases. But it is less often emphasized that computations of thermodynamic equilibria in multiphase and multicomponent alloys from analytical Gibbs energy models (e.g. *CalPhaD*) also require efficient and reliable algorithms. Most of the commercial softwares used for handling multicomponent and multiphase systems in materials science and engineering rely on some nonlinear equations solving algorithms. The well-known *NR* (Newton-Raphson) method is the most frequently used. Indeed, it allows for fast computations with quadratic convergence, but unfortunately to the detriment of reliability due to its local nature. *NR* algorithm can indeed be trapped by local metastable minima, or can even diverge, if the initial estimate is far from the true minimum. It is worth mentioning that wrong estimates, i.e. metastable, or even unstable in the worst cases, may be much more difficult to detect during kinetic calculations which uses local equilibrium conditions at the interface, and by the way, may lead to unstable situations. This is such a situation

that we have been facing when working on the austenite to ferrite transformation in Fe-C-Cr steels, and which has urged us to find a more robust algorithm, combining a first global step and a fast refining *NR* step.

These last years have seen a resurgence of global approaches, in particular in the field of *CalPhaD* modeling, for avoiding the above mentioned drawbacks of *NR*. Different solutions to assess the global minimum have been proposed so far in materials science: they more or less all rely on finding the approximate convex hull of the discretized Gibbs hypersurface, closely following earlier works in petrology [49] and chemical engineering [94]. The first solution, proposed by Chen et al. [39] and implemented in Pandat software [41], uses some kind of brute force method with conceptual simplicity as the main advantage: computations are reduced to simple coplanarity checks between all possible sets of stoichiometric pseudo-compounds which result from the discretization of the concentration spaces. In principle this method can be applied to any system, it is very likely to become very time consuming when increasing the number of species or components: indeed, its computational cost scales as N^3 where N is the number of nodes in the discretization grid. Aiming at designing an algorithm with better performances in terms of computational costs, Emelianenko et al. [55] have taken advantage of some relevant geometric features of the Gibbs energy hypersurface given by derivatives and second derivatives with respect to concentrations: the grid of pseudo-compounds used for the coplanarity checks is adaptatively refined only in relevant regions. Their algorithm has been illustrated for binary and ternary alloys only, but may become unpractical for higher dimensions. For binary alloys, the so-called Graham scan algorithm has also been modified by [40]: scaling as N , and so much faster than the brute force original algorithm of [41], it unfortunately cannot be extended to multicomponent alloys. Finally, more recently, Belov et al. [23] have shown results using some convex hull algorithm implemented in their PhDi package, devoted to binary and ternary alloys: unfortunately, they have not provided any detail on the particular convex hull algorithm implemented, neither have they discussed their solution in terms of computational efficiency.

We introduce a new hybrid algorithm for improving the reliability of equilibrium calculations. As such, it is not intended for the general purpose of computing

phase diagrams in any multiphase and multicomponent systems. Instead, it has been designed for handling correctly single two-phase equilibria, in kinetic calculations. But, in our view, it has revealed to be particularly reliable and efficient for being adopted as a general strategy in softwares devoted to phase diagrams constructions. In our hybrid algorithm, equilibrium is still computed using *NR* as the final step. But potential failures of *NR* are avoided by first finding a good initial guess for the solution. This first step is based on the determination of the convex hull for the two phases Gibbs energy hypersurfaces. To build this convex hull efficiently, we have used the popular QuickHull algorithm of [20], adapted to our specific calculations for further reduction of computational cost. It will be illustrated on ferrite-austenite α/γ equilibria in ternary and quaternary steels. At first, we will briefly recall the basic ingredients of the Compound Energy model (e.g. [74]) adopted for the Gibbs energies of α and γ , accounting for the presence of C as an interstitial species. Then, the algorithm will be detailed, using the particular ternary systems Fe-C-X ($X = \text{Ni, Cr, Mn}$) for illustrating the different steps. The balance in terms of computational cost between the convex hull construction and the *NR* successive step will be investigated for achieving the best compromise. Finally, sequences of calculations in the quaternary system Fe-C-Cr-Mo over temperature ranges will show the benefit of the proposed hybrid algorithm for automatic phase diagram calculations.

1.1 Thermodynamic description

1.1.1 CalPhaD Formalism

Due to the increasing industrial interest in alloy design and materials optimization, comprehensive thermodynamic database are being developed in the framework of the *CalPhaD* method, which in combination with commercial software for Gibbs energy minimization can be used to predict phase stabilities in almost all alloy systems of technical relevance. In the *CalPhaD* method one collects all experimental information on phase equilibria in a system and all thermodynamic information obtained from thermochemical and thermophysical studies (heat capacities, temperature, pressure, volume, concentration ...). The thermodynamic properties of each phase are then obtained from a mathematical model for the Gibbs each phase in a studied system.

For a given atomic structure (e.g. liquid, crystalline phase), the Gibbs energy of one mole of atoms in phase φ is arbitrarily decomposed as:

$$G_m^\varphi = G_m^{\text{ref}} + G_m^{\text{id}} + G_m^{\text{ex}} + G_m^p + G_m^{\text{mag}} \quad (1.1)$$

where G_m^{ref} and G_m^{id} are, respectively, the Gibbs energy contributions of the pure components, and of the ideal entropy mixing. The excess Gibbs energy contribution which is also called the chemical interaction term, G_m^{ex} , is necessary to account for immiscibility or chemical ordering. The Gibbs energy contributions accounting for changes in molar volumes, G_m^p , and magnetic ordering, G_m^{mag} , are of a non-chemical nature. In the present study, G_m^p is neglected.

G_m^{ref} depends linearly on the concentrations of the alloying elements. This term can thus be written as:

$$G_m^{\text{ref}} = \sum_{i=1}^e x_i {}^0G_i \quad (1.2)$$

where x_i is the mole fraction of species i , 0G_i is the molar Gibbs energy of pure i , and e is the total number of chemical species. 0G_i is evaluated from an arbitrary reference state. As usually done in *CalPhaD* databases, the *HSER* (Standard Element Reference) convention is adopted.

In an ideal solution, the Gibbs energy of mixing is equal to G_m^{id} , which is always negative:

$$G_m^{\text{id}} = RT \sum_{i=1}^e x_i \ln x_i \leq 0 \quad (1.3)$$

which means that complete mixing of the pure substances is energetically favorable at positive temperatures.

The *CalPhaD* models take the ideal solution model as a reference and the behavior of the real mixture is approximated using corrections within G_m^{ex} .

In a binary alloy containing two components A and B , this excess term can be written as:

$$G_m^{\text{ex}} = x_A x_B \sum_k {}^k L_{AB} (x_A - x_B)^k \quad (1.4)$$

where k is called the order of interaction and the interaction parameters ${}^k L_{AB}$ describe the intensity of the interaction between components A and B , depending on the phase and on temperature. When $k = 0$, Eq. (1.4) involves only the zeroth-order interaction, and the solution behaves like a regular solution [30].

For higher-order interactions empirical Redlich-Kister polynomials are usually used [30].

In a ternary alloy containing three components A , B and C , the excess molar Gibbs energy can be written as:

$$\begin{aligned} G_m^{\text{ex}} = & x_A x_B \sum_k {}^k L_{AB} (x_A - x_B)^k + x_A x_C \sum_k {}^k L_{AC} (x_A - x_C)^k \\ & + x_B x_C \sum_k {}^k L_{BC} (x_B - x_C)^k + x_A x_B x_C {}^0 L_{AB:C} \end{aligned} \quad (1.5)$$

where ${}^k L_{AB}$, ${}^k L_{AC}$ and ${}^k L_{BC}$ are the binary interaction parameters and ${}^0 L_{AB:C}$ is the ternary interaction parameter. These parameters depend only on temperature.

The magnetic contribution is very important in ferromagnetic substances such as Fe, Cr, Co or Ni. The model proposed by Inden [90] for pure metals and sub-

sequently extended to alloys by Hillert and Jarl [78] is widely used in *CalPhaD* models. It describes the transition from the disordered state to the magnetically ordered state by a series based on the normalized temperature $\tau = T/T_c$ and the magnetic moment β_m . T_c is the Curie (ferromagnetic alloy) or Néel temperature (antiferromagnetic alloy).

Above the Curie temperature, $\tau > 1$:

$$G_m^{\text{mag}} = -RT \ln(\beta_m + 1) \left(\frac{\tau^{-5}}{10} + \frac{\tau^{-15}}{315} + \frac{\tau^{-25}}{1500} \right) / \left(\frac{518}{1125} + \frac{11692}{15975} \left(\frac{1}{p} - 1 \right) \right) \quad (1.6)$$

For $\tau < 1$

$$G_m^{\text{mag}} = RT \ln(\beta_m + 1) \left\{ 1 - \left[\frac{79\tau^{-1}}{140p} + \frac{474}{497} \left(\frac{1}{p} - 1 \right) \left(\frac{\tau^3}{6} + \frac{\tau^9}{135} + \frac{\tau^{15}}{600} \right) \right] \right\} / \left(\frac{518}{1125} + \frac{11692}{15975} \left(\frac{1}{p} - 1 \right) \right) \quad (1.7)$$

Parameter p depends only on the structure. For fcc(γ) and bcc(α) phases, $p=0.28$ and $p=0.4$, respectively (Appendix A). For a ternary alloy containing three components A , B and C , T_c and β_m in Eqs. (1.6) and (1.7) can be expressed as:

$$\begin{aligned} \beta = & x_A \beta_A + x_B \beta_B + x_C \beta_C + x_A x_B^k \beta_{AB} (x_A - x_B)^k \\ & + x_A x_C^k \beta_{AC} (x_A - x_C)^k + x_B x_C^k \beta_{BC} (x_B - x_C)^k \\ & + x_A x_B x_C^k \beta_{AB:C} \end{aligned} \quad (1.8)$$

$$\begin{aligned} T_c = & x_A T_{cA} + x_B T_{cB} + x_C T_{cC} + x_A x_B^k T_{cAB} (x_A - x_B)^k \\ & + x_A x_C^k T_{cAC} (x_A - x_C)^k + x_B x_C^k T_{cBC} (x_B - x_C)^k \\ & + x_A x_B x_C^k T_{cAB:C} \end{aligned} \quad (1.9)$$

It is worth mentioning that when the alloy is antiferromagnetic, T_c and β have negative values in the databases of the commercial thermodynamic software ThermoCalc [147]. The real T_c and β are then obtained by dividing Eqs. (1.8) and Eqs. (1.9) by a negative n which depends on the phase. This parameter should simply be regarded as a mean for obtaining a smooth variation of T_c and β across the composition range where the magnetic character changes [85].

Recent ab-initio calculation by Korzhaviy [103] for alloys between ferromagnetic Fe and antiferromagnetic Cr indicate that the magnetic moments in the ferromagnetic as well as paramagnetic states vary very smoothly with composition and do not approach zero or very close to the Cr side. If this would be the general case, it would have been possible to start the magnetic description at low temperature. The drawback of starting from high temperatures is that some magnetic contributions at high temperatures must be included into the description of chemical effects on the excess Gibbs energy. However, that has not caused any practical problems so far and should be negligible if the magnetic entropy varies linearly across the system. Korzhaviy's results for the Fe-Cr system indicate that this may almost be the case in that system.

Subsequently 1.1.3, the chemical potentials μ_i in each phase, will be used to compute equilibrium. The chemical potential are the partial derivative at constant temperature and pressure of the Gibbs energy with respect to the number of moles n_i of element i :

$$\mu_i = \left. \frac{\partial G}{\partial n_i} \right|_{T,p,n_{j \neq i}} \quad (1.10)$$

where G is the total Gibbs energy.

For using the available expressions such as Eq. (1.10), we need the chemical potentials as a function of the molar Gibbs energy, G_m , and of the molar fractions, x_i .

By definition:

$$G = n G_m \quad (1.11)$$

with n the total number of moles of elements.

Then,

$$\mu_i = \left. \frac{\partial(n G_m)}{\partial n_i} \right|_{T,p,n_{j \neq i}} \quad (1.12)$$

using $n = n_1 + \dots + n_{\tilde{n}}$

$$\mu_i = G_m + n \left. \frac{\partial G_m}{\partial n_i} \right|_{T,p,n_{j \neq i}} \quad (1.13)$$

When G_m is a function of x_i , partial derivatives with respect to molar concentrations are introduced instead.

$$\left. \frac{\partial}{\partial n_i} \right|_{n_{j \neq i}} = \sum_{j=1}^{\tilde{n}} \left. \frac{\partial x_j}{\partial n_i} \right|_{n_{k \neq i}} \left. \frac{\partial}{\partial x_j} \right|_{x_{k \neq j}} \quad (1.14)$$

with \tilde{n} the total number of species.

Using the definitions of the molar fractions:

$$\left. \frac{\partial x_j}{\partial n_i} \right|_{n_{k \neq i}} = \begin{cases} \frac{1-x_j}{n} & i = j \\ -\frac{x_j}{n} & i \neq j \end{cases} \quad (1.15)$$

finally

$$\mu_i = G_m + \left. \frac{\partial G_m}{\partial x_i} \right|_{n_{k \neq i}} - \sum x_j \left. \frac{\partial G_m}{\partial x_j} \right|_{n_{k \neq j}} \quad (1.16)$$

Equation (1.16) will be used to define the equilibrium. Between two phases it will also be shown that the chemical potentials can conveniently be used to define the driving force for internal reactions, such as phase transformation or diffusion.

1.1.2 Multiple Sublattices model

In the previous section we have introduced a thermodynamic model for solutions described by molar fractions. However, in crystalline solids different types of atoms can be located on separate sublattices. The Compound Energy Formalism (*CEF*) has been introduced by Hillert and Staffansson [80] (see also [74]) to deal with such systems. In the case of steels, substitutional (X= Cr, Ni, Mo . . .) and interstitial (C or Va, for vacancies) constituents are distributed into two separate sublattices s .

The amount of one element in a given phase φ is described by the site fraction ${}^l y_i$, defined as ${}^l n_i/n^l$ where ${}^l n_i$ is the mole number of i in sublattice l and n^l is the total mole number of sites in l . The site fractions verify:

$$\sum_i {}^l y_i^\varphi = 1 \quad \forall \varphi, \forall l \quad (1.17)$$

and

$$0 \leq {}^l y_i^\varphi \leq 1 \quad (1.18)$$

Equations (1.17) and (1.18) can be viewed as constraints of the thermodynamic model. They have to be taken into account when manipulating thermodynamic quantities or when evaluating phase equilibria.

When calculating the Gibbs energy for a multi-sublattice phase the Gibbs energy is built upon the Gibbs energies of the so-called pure compounds rather than pure components as in one-sublattice solution models. For an illustrative purpose, consider the usual sublattice model for $(\text{Fe})_1(\text{C}, \text{Va})_3$ for the bcc phase in the Fe-C system. The substitutional sublattice is entirely occupied by Fe atoms, whereas the interstitial sublattice contains C atoms and/or vacancies. If Cr is added to the substitutional sublattice, the bcc phase must be described by the following compound $(\text{Fe}, \text{Cr})_1(\text{C}, \text{Va})_3$.

In that case, the Gibbs energy per mole of compound reads:

$$\begin{aligned}
\tilde{G}^{\text{bcc}} &= {}^0y_{\text{Fe}} {}^1y_{\text{Va}} G_{\text{Fe:Va}}^{\text{bcc}} + {}^0y_{\text{Fe}} {}^1y_{\text{C}} G_{\text{Fe:C}}^{\text{bcc}} \\
&\quad + {}^0y_{\text{Cr}} {}^1y_{\text{Va}} G_{\text{Cr:Va}}^{\text{bcc}} + {}^0y_{\text{Cr}} {}^1y_{\text{C}} G_{\text{Cr:C}}^{\text{bcc}} \\
&\quad + RT ({}^1y_{\text{C}} \ln {}^1y_{\text{C}} + {}^1y_{\text{Va}} \ln {}^1y_{\text{Va}}) + 3 RT ({}^0y_{\text{Fe}} \ln {}^0y_{\text{Fe}} + {}^0y_{\text{Cr}} \ln {}^0y_{\text{Cr}}) \\
&\quad + \tilde{G}^{\text{ex}} + \tilde{G}^{\text{mag}} \tag{1.19}
\end{aligned}$$

where ”:” in the subscript is used to distinguish sublattices. In the more general case of multicomponent alloys with two sublattices, the Gibbs energy of phase φ per mole of compound reads:

$$\tilde{G}^\varphi = \sum_i^{\in s} \sum_j^{\in t} {}^s y_i {}^t y_j {}^0 G_{i:j} + RT \sum_l^{\in \{s,t\}} a_l \sum_i^{\in l} {}^l y_i \ln {}^l y_i + \tilde{G}^{\text{ex}} + \tilde{G}^{\text{mag}} \tag{1.20}$$

where ${}^0 G_{i:j}$ is the Gibbs energy of a compound with constituent i in the substitutional lattice s and constituent j in the interstitial lattice t , including vacancies. The parameters a_l in equation (1.20) are the number of sites in sublattice l per mole of compound ($a_s = 1$ and $a_t = 3$ for bcc; $a_s = 1$ and $a_t = 1$ for fcc).

The excess Gibbs energy is expressed in terms of Redlich-Kister polynomials ${}^p L$ of degree p accounting phenomenologically for the interactions between the different species. Binary interactions concern both sublattices between i and j in sublattice s for ${}^p L_{ij:k}$, and between j and k in sublattice t for ${}^p L_{i:jk}$. Then:

$$\begin{aligned}
\tilde{G}^{\text{ex}} &= \sum_i^{\in s} \sum_{j \neq i}^{\in s} \sum_k^{\in t} {}^s y_i {}^s y_j {}^t y_k {}^p L_{ij:k} ({}^s y_i - {}^s y_j)^p \\
&\quad + \sum_i^{\in s} \sum_j^{\in t} \sum_{k \neq j}^{\in t} {}^s y_i {}^t y_j {}^t y_k {}^p L_{i:jk} ({}^t y_j - {}^t y_k)^p + \dots \tag{1.21}
\end{aligned}$$

where the dots stand for higher order interaction terms (e.g. ${}^p L_{i:ijkl}$ for interactions between the pair i, j in the first sublattice and the pair l, k in the second sublattice).

The parameters entering the magnetic contribution \tilde{G}^{mag} (Eqs.(1.6) and (1.7)),

T_c and β are also expanded as Redlich-Kister polynomials:

$$\beta^\varphi = \sum_i^{\in t} \sum_j^{\in t} {}^s y_i {}^t y_j {}^0 \beta_{i:j} + \beta^{\text{ex}} \quad (1.22)$$

$$T_c^\varphi = \sum_i^{\in t} \sum_j^{\in t} {}^s y_i {}^t y_j {}^0 T_{c:i:j} + T_c^{\text{ex}} \quad (1.23)$$

where

$$\beta^{\text{ex}} = \sum_i^{\in s} \sum_{j \neq i}^{\in s} \sum_k^{\in t} {}^s y_i {}^s y_j {}^t y_k {}^p \beta_{i,j::k} ({}^s y_i - {}^s y_j)^p \quad (1.24)$$

$$T_c^{\text{ex}} = \sum_i^{\in s} \sum_{j \neq i}^{\in s} \sum_k^{\in t} {}^s y_i {}^s y_j {}^t y_k {}^p T_{c:ij:k} ({}^s y_i - {}^s y_j)^p \quad (1.25)$$

In the case of phases with species associated with only one sublattice, it is possible to relate one-to-one the mole fractions x_i and the site fractions ${}^l y_i$:

$$x_i = \frac{a_l {}^l y_i}{a_s + a_t (1 - {}^t y_{\text{Va}})} \quad (1.26)$$

where $(1 - {}^t y_{\text{Va}})$ discards the interstitial vacancies from the total number of atoms. When site fractions are introduced for describing the composition of the phases, the chemical potential must be expressed with partial derivatives with respect to site fractions:

$${}^l \mu_i = \tilde{G} + \frac{1}{a_l} \left(\frac{\partial \tilde{G}}{\partial {}^l y_i} - \sum {}^l y_i \frac{\partial \tilde{G}}{\partial {}^l y_i} \right) \quad (1.27)$$

1.1.3 Equilibrium conditions in a closed system

Looking for thermodynamic equilibrium in a closed system containing one mole of atoms at given temperature T and pressure p requires the minimization of the total Gibbs energy:

$$G_m = \sum_{\varphi} f^{\varphi} G_m^{\varphi}(T, p, x_i^{\varphi}) \quad (1.28)$$

with some constraints:

$$\sum_{\varphi} f^{\varphi} x_i^{\varphi} - x_i^0 = 0 \quad \forall i \quad (1.29)$$

$$\sum_i x_i^{\varphi} - 1 = 0 \quad \forall \varphi \quad (1.30)$$

$$\sum_{\varphi} f^{\varphi} - 1 = 0 \quad (1.31)$$

where f^{φ} is the mole fraction of phase φ , x_i^{φ} the mole fraction of species i in φ , and x_i^0 the overall mole fraction of species i .

1.1.3.1 Binary alloys

To illustrate the conditions of thermodynamic equilibrium ensuing from the minimization of Eq. (1.28) with the constraints Eqs. (1.29)-(1.31), we start with a simple binary alloy A-B composed of two phases α and γ (Fig. 1.1). Consider the particular alloy with the average composition x_B^0 at given temperature and pressure. Suppose that it is first composed of phases $\alpha 1$ and $\gamma 1$. Its molar Gibbs energy, ${}^0\tilde{G}_m$ is given by the intersection between the segment $[\alpha 1; \gamma 1]$ and the vertical line at x_B^0 (thin dashed line). Then, the compositions of α and γ are varied in such a way that ${}^0\tilde{G}_m$ decreases gradually along the vertical line at x_B^0 , e.g. α goes to $\alpha 2$ and γ to $\gamma 2$ respectively. This process is repeated until ${}^0\tilde{G}_m$ can no longer decrease. As illustrated in Fig. 1.1, the minimum of ${}^0\tilde{G}_m$ will finally be reached when α and γ are situated on the tangent common to both Gibbs energy curves, at x_B^{α} and x_B^{γ} . Hence, the practical graphical construction to find equilibrium between two phases in a binary alloy is called the common tangent

construction. The equivalent algebraic conditions reads (e.g. [109]):

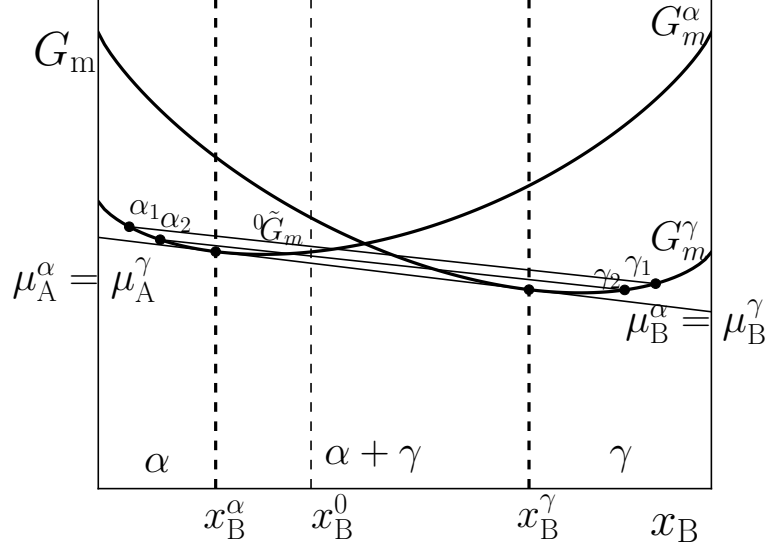


Figure 1.1: Common tangent construction.

$$\begin{cases} \mu_A^\alpha = \mu_A^\gamma \\ \mu_B^\alpha = \mu_B^\gamma \end{cases} \quad (1.32)$$

where the conditions $T^\alpha = T^\gamma = T$ and $p^\alpha = p^\gamma = p$ have been omitted and will be implicitly considered to hold at equilibrium, except when explicitly stated. Hence, the common tangent construction amounts to the equality of chemical potentials of all species in both phases. It is worth noting that the equilibrium concentrations x_B^α and x_B^γ are independent of the nominal concentration x_B^0 . In other words, in binary alloys, solving Eqs. (1.32) without the constraint of solute balance Eq. (1.29)₁ is sufficient to determine thermodynamic equilibrium.

It may be convenient to write Eqs. (1.32) in terms of diffusion potentials (§2) $\Phi_i^\varphi = \mu_i^\phi - \mu_{\text{ref}}^\phi$, where ref denotes a one element taken as a reference. Eqs. (1.32)

then becomes:

$$\begin{cases} \Phi_B^\alpha = \Phi_B^\gamma \\ \mu_A^\alpha = \mu_A^\gamma \end{cases} \quad (1.33)$$

Graphically (Fig. 1.1), the first condition states that both tangents to G_m^α and G_m^γ are parallel. The second one states that both tangent intersect the axis of pure A at the same point.

1.1.3.2 Multicomponent alloys

In the case of ternary or more alloy, the condition of thermodynamic equilibrium between two-phases at given temperature and pressure is still given by the equality of chemical potentials of all components in both phases, generalizing the system of equations (1.32). Geometrically, the rule of common tangents is transposed into a common tangent hyperplanes in a space of n -dimension, where n is the number of chemical species.

In the case of equilibrium between two-phases with the same substitutional and interstitial atoms between two lattices, the equilibrium conditions are formally identical to the system (1.33), with the difference that Eqs. (1.33)₃, (1.33)₄ involve the substitutional and interstitial sublattices:

$$\begin{cases} {}^s\Phi_i^\alpha = {}^s\Phi_i^\gamma & \forall i \neq \text{ref} \in s \\ {}^s\mu_{\text{ref}}^\alpha = {}^s\mu_{\text{ref}}^\gamma \\ {}^t\Phi_i^\alpha = {}^t\Phi_i^\gamma & \forall i \neq \text{Va} \in t \\ {}^t\mu_{\text{Va}}^\alpha = {}^t\mu_{\text{Va}}^\gamma \end{cases} \quad (1.34)$$

where ref is taken as the reference element in the substitutional lattice s and Va identifies vacancies taking as the reference element in the interstitial lattice t .

The diffusion potential in lattice l reads:

$${}^l\Phi_i = {}^l\mu_i - {}^l\mu_{\text{ref}} = {}^l\mu_i - {}^l\mu_{\text{ref}} = \frac{1}{a_l} \left[\frac{\partial G_m}{\partial y_i} - \frac{\partial G_m}{\partial y_{\text{ref}}} \right] \quad (1.35)$$

Assuming that ${}^t\mu_{\text{Va}} = 0$ at thermal equilibrium, system (1.34) reduces to:

$$\begin{cases} {}^s\Phi_i^\alpha &= {}^s\Phi_i^\gamma & \forall i \neq \text{ref} \in s \\ {}^s\mu_{\text{ref}}^\alpha &= {}^s\mu_{\text{ref}}^\gamma \\ {}^t\mu_i^\alpha &= {}^t\mu_i^\gamma \end{cases} \quad (1.36)$$

The following constraints ensuing from the conservation of sites in a sublattice Eq. (1.17) must be appended to Eqs. (1.36):

$$\sum_i y_i^\varphi = 1 \quad \forall i \in l, \quad \forall l, \quad \forall \varphi \quad (1.37)$$

In contrast with binary alloys, in ternary or higher alloys, equality of chemical potentials defines a set of pairs of composition defining tie-lines, with the extremities delimiting the two-phase region. Hence, to solve Eqs. (1.36) it is necessary to specify the nominal composition x_i^0 of a given alloy in the case of a closed system, and append the following solute balances:

$$\begin{cases} x_i^\alpha f^\alpha + x_i^\gamma (1 - f^\alpha) = x_i^0 & \forall i \neq \text{ref} \\ \sum_i x_i^\varphi = 1 & \forall \varphi \end{cases} \quad (1.38)$$

where we have substituted f^γ by $1 - f^\alpha$. It is worth noting that the mole fractions x_i^φ are functions of the site fractions in the same phase. In the particular case where species can be differentiated between substitutional and interstitial atoms Eq. (1.26) can be used.

Finally, Finding the constrained minimum of \tilde{G}_m from Eq. (1.28) amounts to

solve the following nonlinear system (e.g. [74, 109]):

$$\left\{ \begin{array}{ll} {}^s\Phi_i^\alpha(\mathbf{y}^\alpha) = {}^s\Phi_i^\gamma(\mathbf{y}^\gamma) & \forall i \neq \text{ref} \in s \\ {}^s\mu_{\text{ref}}^\alpha(\mathbf{y}^\alpha) = {}^s\mu_{\text{ref}}^\gamma(\mathbf{y}^\gamma) & \\ {}^t\mu_i^\alpha(\mathbf{y}^\alpha) = {}^t\mu_i^\gamma(\mathbf{y}^\gamma) & \forall i \neq \forall a \in t \\ \sum_{i \in l} {}^l y_i^\varphi = 1 & \forall \varphi, \quad \forall l \\ x_i^\alpha(\mathbf{y}^\alpha) f^\alpha + x_i^\gamma(\mathbf{y}^\gamma) (1 - f^\alpha) = x_i^0 & \forall i \neq \text{ref} \end{array} \right. \quad (1.39)$$

where all the dependence on the site fractions are explicitly stated, and where \mathbf{y}^φ denotes the vector containing all site fractions in all sublattices in phase φ ($\mathbf{y}^\varphi = (y_i^\varphi)$).

Solving Eqs. (1.39), using the CEM (Eqs. (1.20)-(1.25)) to express the chemical potentials provides the site fractions ${}^l y_i^\varphi$ of all the constituents (chemical species and vacancies) in both phases, as well as the phase fractions f^φ which minimize the total Gibbs energy of the closed system.

1.1.4 Convex hull construction

Eqs. (1.33) constitute a system of nonlinear equations which must be solved together with constraints Eqs.(1.29)-(1.31) to determine thermodynamic equilibrium. For this purpose, the well-known Newton-Raphson (*NR*) [134] method is the most frequently used. The advantage of the method is that it converges quadratically, i.e. the method is one of the fastest when it converges. Unfortunately, it has a severe drawback: it is expected to converge only near the solution. When starting far from the real solution, *NR* can either diverge or converge to some local minimum. This is such a situation that we have been facing when working on the austenite to ferrite transformation especially in some Fe-X-C and Fe-X-Y-C systems (e.g. X = Cr, Ni, Mn and Y = Mo), and which has urged us to find a more robust algorithm, combining a first global step and a fast refining *NR* step. For the first step, we have adapted the Quickhull algorithm with the

general dimension Beneath-Beyond algorithm [20] for computing the convex hull of the Gibbs energy surfaces. The obtained convex hull can be used to find an initial guess close to equilibrium.

As started above, Newton-Raphson (*NR*) algorithm (e.g. [134]), usually used to solve system (1.39), can fail to converge to the real solution. To avoid such failures, it is necessary to make it starting from an initial guess not too far from the solution, especially when the Gibbs energies contain non-convex regions and multiple local minima. This situation is likely to occur quite often during kinetic calculations because the operative tie-line can span large regions of concentrations during a growth or a dissolution process. Hence, instead of following a blind trial and error procedure, we have chosen to compute an approximate convex hull of the Gibbs hypersurfaces, and to locate the nominal composition in this hull for assessing a good initial tie-line. We detail algorithm using the particular ternary system Fe-C-Cr for illustrating the different steps.

1.1.4.1 Discretization

First, the Gibbs energies are discretized on a grid with N^d nodes, where N is the number of nodes along one whole species axis and $d = n - 1$ is the number of independent species Fig. 1.2a. It is worth noting that the grid is directly built in the x_i space, despite the use of site fractions for computing the Gibbs energies Eqs. (1.6), (1.7), (1.20), (1.21). Site fractions y_i can be seen as internal variables rather than primary variables, obtained unambiguously in our particular α/γ using Eqs. (1.26). For simplifying the analyses, only the range $0 < x_C \leq 0.5$ common to both fcc and bcc structures has been considered for building the convex hull (Fig. 1.2b): indeed equilibria involving bcc with $x_C \in [0.5, 0.75]$ are unlikely to be observed between ferrite and austenite in real systems.

Moreover, an irregular grid has been used with refinement in the Fe-rich region to be particularly investigated:

$$N_{\text{total}} = \begin{cases} x_C = \left(\frac{i}{N-1}\right)^2 & i \in [0; \text{int}((N-1)/\sqrt{2})] \\ x_{\text{Cr}} = \frac{i}{N-1} & i \in [0; N-1] \end{cases} \quad (1.40)$$

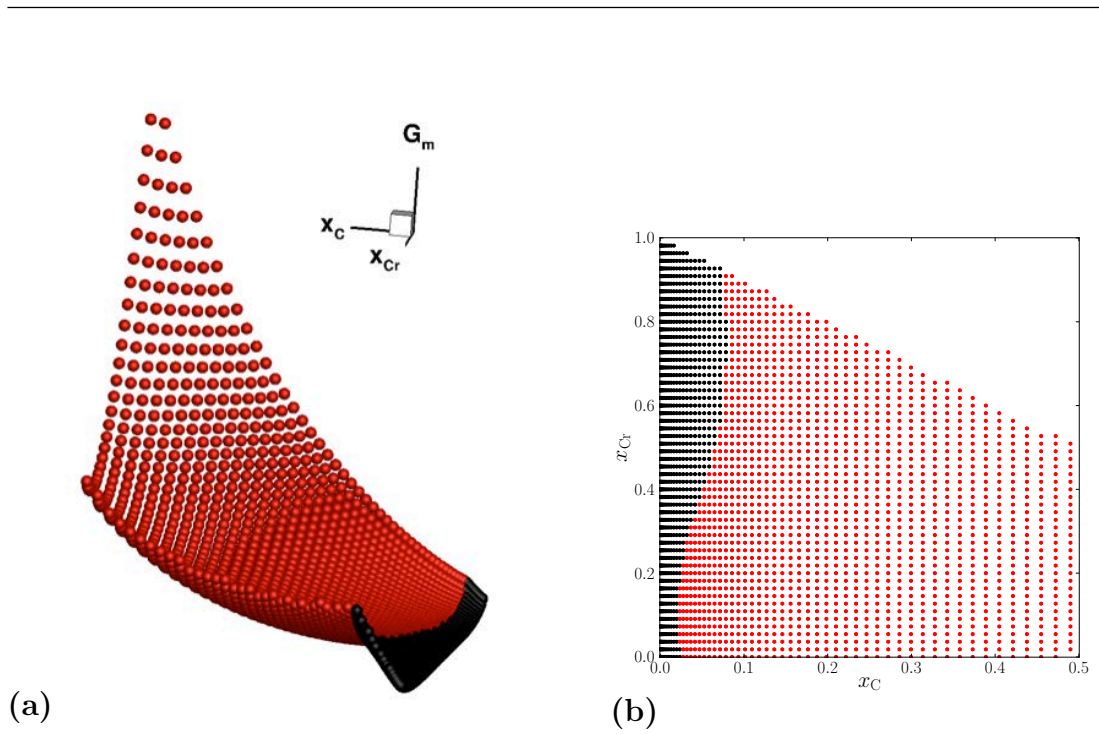


Figure 1.2: Discretized Calphad Gibbs energies of α and γ in Fe-C-Cr using *FEDAT* database, at 600 °C (concentration axes are x_C and x_{Cr}). Red dots are for γ and black ones for α . Only lower dots have been plotted for clarity.

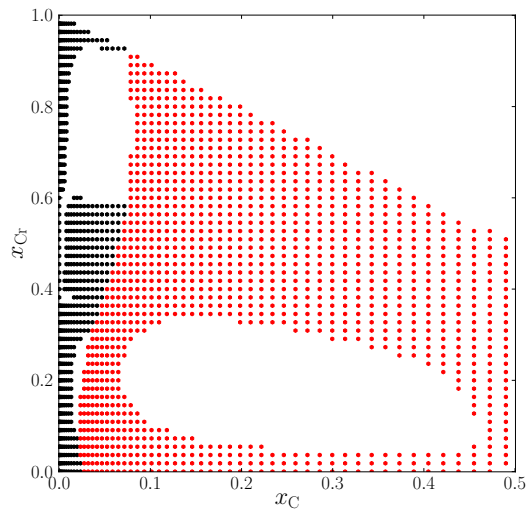


Figure 1.3: Remaining labelled nodes (black= α , red= γ) of the initial grids when non-convex parts are discarded.

where int denotes the integer part of a real number. For that case the total number of nodes is $[1 + \text{int}(N/\sqrt{2})]N$. Nodes are then attributed the lowest Gibbs energies and labelled with respect to the corresponding phases (e.g. black nodes and red nodes correspond to α and γ phases respectively in Figs. 1.2-1.3). Moreover, nodes belonging to non-convex regions are detected by computing the stability function Ψ [109]:

$$\Psi = \prod_{i>1} x_i \det \left(\frac{\partial^2}{\partial x_j \partial x_k} (\tilde{G}_m/RT) \right) \quad (1.41)$$

where \det stands for the determinant of a matrix. Nodes with $\Psi < 0$ can be discarded if they do not belong to the binary axes (Fig. 1.3).

1.1.4.2 Quick hull algorithm

The next step is the computation set of the convex hull of the finite set of remaining nodes. The convex hull is a convex polytope composed of a finite set of convex polyhedra called facets (of dimension d) delimited by edges (of dimension $d - 1$) forming ridges, built upon $n = d + 1$ vertices at some given nodes of the initial set. For a ternary system with $d = 2$ independent concentrations, facets are simply triangles and their sides define the ridges.

Because optimizing the computation time is mandatory for such a process in a multidimensional space, the Quick-Hull algorithm of [20] has been chosen. Indeed, it is (i) one of the few algorithms able to handle multidimensional problems, and (ii) one of the fastest. Relying on the d -dimension Beneath-Beyond strategy, it scales as $N_{\text{total}} \log r$ where r is the number of processed nodes among the initial N_{total} nodes. Moreover, further reduction in computation time was achieved by modifying the original algorithm, exploiting the unidirectionality of the Gibbs convex hull downward the G_m axis.

The d -dimension Beneath-Beyond algorithm is incremental: nodes are added one by one to the convex hull of the previously processed nodes. It relies on simple geometric calculations: signed distances to hyperplanes. Indeed, the basic operation consists in determining whether nodes are above or below facets defining hyperplanes: when above, a node is discarded; when below, it may be

temporarily included into the convex hull. Given n vertices of coordinates \mathbf{x}^j with $\mathbf{x}^j = (x_1^j, \dots, x_n^j)$, the cartesian equation of the hyperplane defined by these vertices reads:

$$\sum_{j=1}^n D_j x_j = D_0 \quad (1.42)$$

where the D_j are the following determinants:

$$D_0 = \begin{vmatrix} x_1^1 & \dots & x_n^1 \\ \vdots & \vdots & \vdots \\ x_1^n & \dots & x_n^n \end{vmatrix} \quad D_j = \begin{vmatrix} \dots & x_{j-1}^1 & 1 & x_{j+1}^1 & \dots \\ \vdots & \vdots & \vdots & \vdots & \vdots \\ \dots & x_{j-1}^n & 1 & x_{j+1}^n & \dots \end{vmatrix} \quad \text{for } j > 0 \quad (1.43)$$

The distance Δ from a point of coordinates \mathbf{x} to this hyperplane reads:

$$\Delta = \frac{\sum_{j=1}^n D_j x_j - D_0}{\pm \sqrt{\sum_{j=1}^n D_j^2}} \quad (1.44)$$

For completeness, a detailed description of the algorithm is given now. At the beginning, all nodes are assigned an active status, i.e. they will be accounted for in the process. An initial facet f_0 is built with the nodes corresponding to the d corners of the Gibbs simplex delimiting the concentrations hyperplane. The furthest node below the hyperplane defined by f_0 is picked up to build d new facets f_i with the d corners. The facets f_i together with the corresponding nodes enter into the temporary convex hull. It can be noted that the nodes defining f_0 always belong to the convex hull but not f_0 .

Each facet f_i included into the temporary convex hull is then processed recursively.

- (i) All active nodes are checked whether they are outside or inside the temporary convex hull, for ensuring that the convex hull is built in the right direction. For that purpose, the sign of the distances from f_i are compared to the sign of the distance between nodes of f_i and f_0 : if the signs are opposite (equal), nodes are outside (inside) and are considered as visible (invisible) from f_i .
- (ii) The furthest node j outside the convex hull is found thanks to its signed distance to f_i .

(iii) The so-called horizon of node j with respect to facet f_i is then determined as follows: facets f_k neighboring f_i are successively investigated to check whether node j is visible from f_k . It is worth noting that the efficiency of the process strongly relies on the tree data structure relating the facets. The ridges of the visible facets f_k which are the furthest from node j define the horizon of node j .

(iv) The facets delimited by the horizon are excluded from the temporary convex hull. Moreover, the nodes of facets f_i and f_k not belonging to the horizon are assigned inactive states, and definitely discarded from the search process. Finally, a cone of new facets, built with node j and the horizon ridges, is included into the temporary convex hull.

This process is repeated until all active nodes are included into the convex hull. Fig. 1.4 shows projections on the composition Gibbs simplex of the convex hull during the construction in the case of α/γ equilibrium in Fe-C-Cr at 600 °C.

This algorithm has been implemented using the C++ language, benefiting from its object-oriented features for building and spanning the tree structures describing the hulls. The main functions used in the code are described in Appendix B.

1.1.4.3 Determination of the phase fields

In order to check the reliability of our algorithm by comparing our results with those of Thermo-Calc, the phase fields have to be determined from the approximate convex hull. The analysis is again restricted to the case of ternary alloys for visualization, but its extension to higher order systems is straightforward as it relies on simple geometric operations. First, the irregular grid is converted back to a regular grid (x'_C, x'_{Cr}) with $x'_C = \sqrt{x_C}$ and $x'_{Cr} = x_{Cr}$ such that $\Delta x'_C = \Delta x'_{Cr} = \Delta x' = 1/(N - 1)$. Second, the distances $d''_{i=1,3}$ in this regular grid between nodes belonging to a given facet are computed. Third, these distances are compared to the nearest neighbour distance defined as $\sqrt{2}\Delta x'$.

In Fig. 1.5, different facets are illustrated which are typically found in approximate convex hulls. When two distances d'_i among three are equal or shorter than $\Delta x'$, the facet belongs to a one-phase field (Fig. 1.5a). When only one distance d'_i is equal or shorter than $\Delta x'$, the facet belongs to a two-phase field (Fig. 1.5b). Finally, when $d'_i > \Delta x' \forall i$, the facet is a three-phase field (Fig. 1.5c).

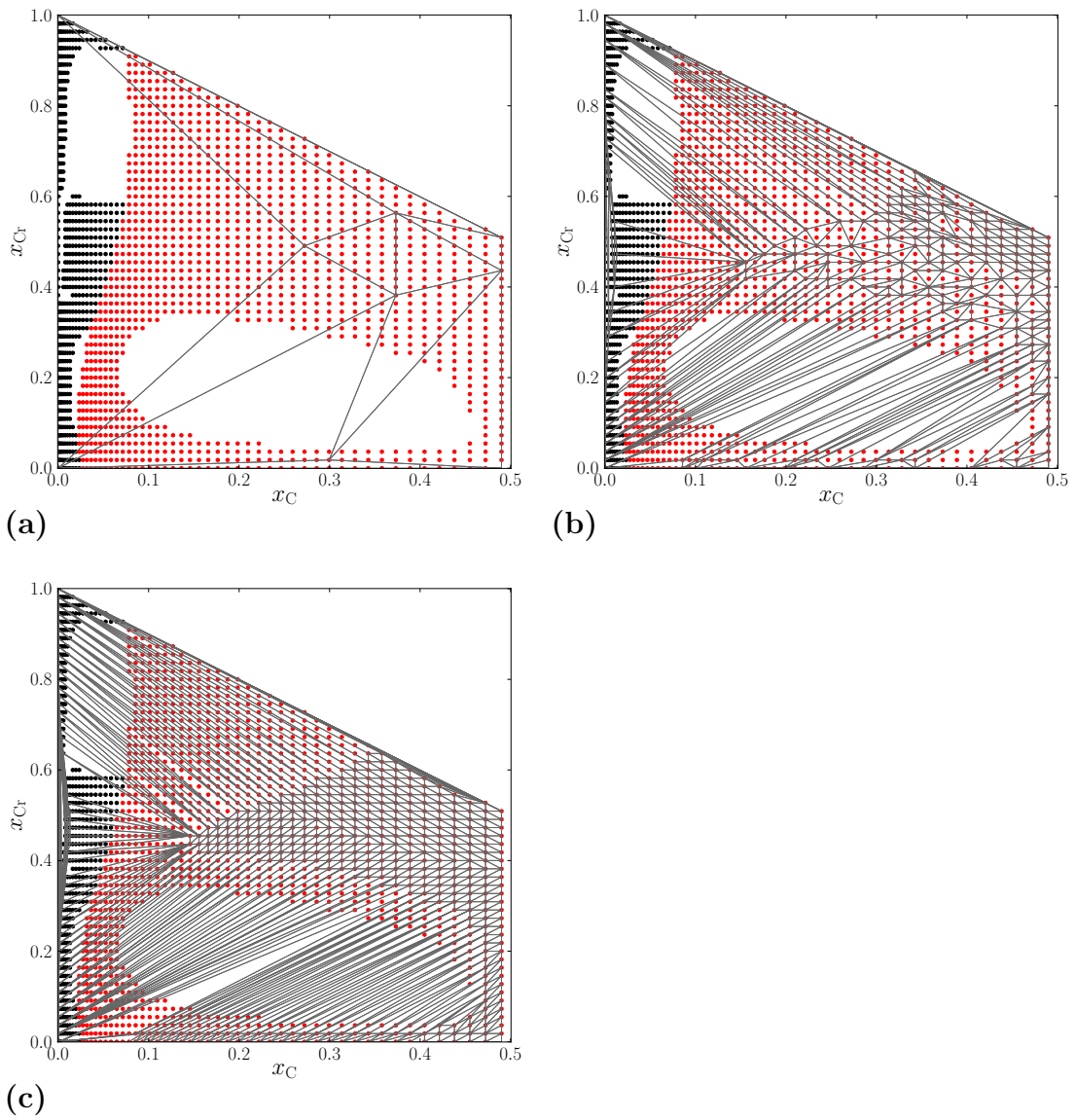


Figure 1.4: Construction of the convex hull: (a) step 10; (b) step 200; (c) final step. Triangles are the projections of the facets.

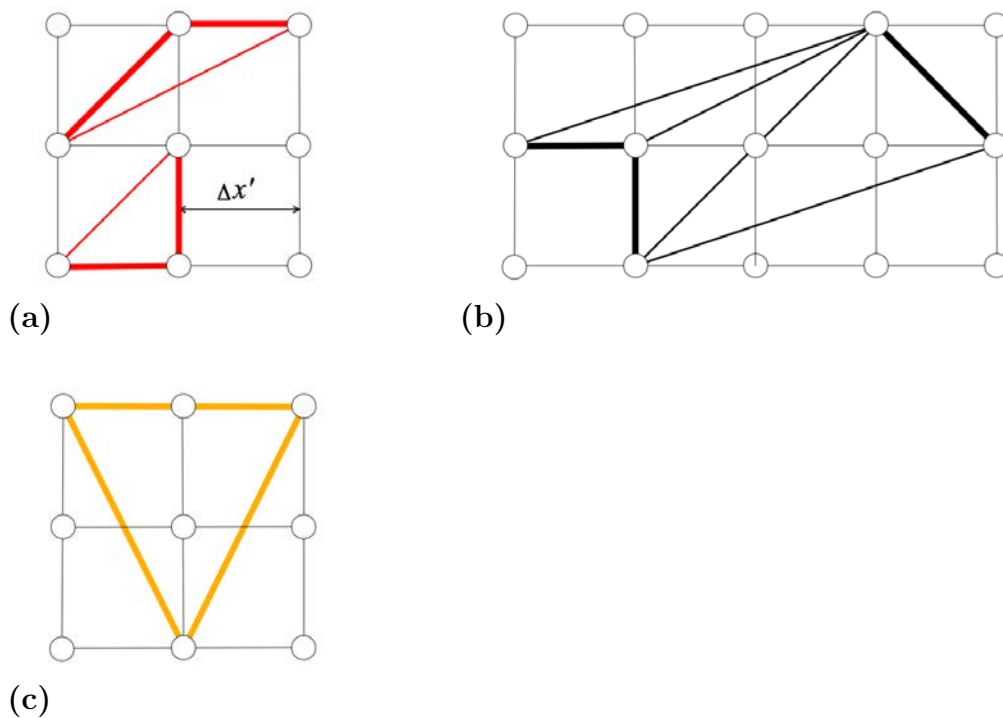


Figure 1.5: Possible facets in the convex hull projected on a regular grid (bold lines correspond to $d_i \leq \sqrt{2} \Delta x'$). (a) facets in a one-phase field; (b) facets in a two-phase field; (c) three-phase field facet.

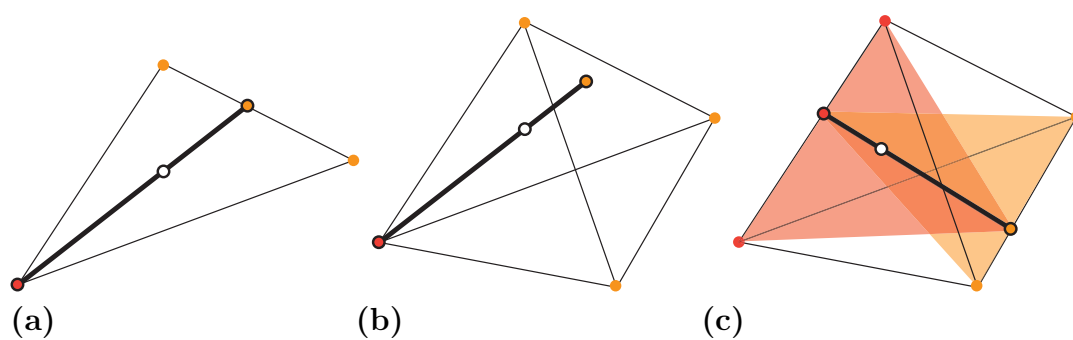


Figure 1.6: Geometrical construction for determining the approximate tie-line corresponding to the white dot: (a) ternary alloy; (b-c) quaternary alloy.

1.1.4.4 Search for a single tie-line

In ternary or higher alloys, the equilibrium concentrations between two phases correspond to a tie-line. In order to obtain the equilibrium concentrations, in alloy of any dimension it is necessary to solve the system (1.39), using the Newton-Raphson (*NR*) algorithm. As an initial estimate for *NR* method one approximate equilibrium tie-line is obtained from convex hull. Once the convex hull is built, a particular tie-line corresponding to a given nominal composition c^0 can be approximately found by elementary geometric calculations. The first step is to look for the facet F which contains c^0 when projected on the Gibbs simplex hyperplane. The whole set of facets is thus spanned until the distance between c^0 and the facet center of mass is smaller than the distances between the facet vertices and the center of mass.

The last step consists in finding an approximate tie-line if c^0 is in a d -phase field for an alloy with $n = d + 1$ species. For a ternary alloys, this step is trivial because facet F is a triangle (Fig. 1.6a). Indeed, the approximate tie-line passes through c^0 (white dot) and ends up at the vertex (red dot) with the phase label which is different from the phase label of the two other vertices (orange dots).

For quaternary alloys, two cases can be distinguished when c^0 is in a two-phase field. (i) When three vertices over the four belong to the same phase (Fig. 1.6b), the tie-line starts from the single vertex (red dot), passes through c^0 (white dot) and ends up on the opposite face (delimited by the three orange dots). (ii) When two vertices belong to the one of two phases and other two vertices belong to the second phase the tie-line is given by the intersection between the two planes build with the two vertices and c^0 (Fig. 1.6c). Generalization of the previous operations is straightforward for higher order alloys, involving mainly intersections between hyperplanes in n -dimension spaces. Finally, the approximate tie-line is used as an initial guess for the standard Newton-Raphson algorithm [134] solving the nonlinear system (1.39).

1.2 Results

In this section we present the results of our hybrid algorithm and discuss its efficiency in terms of CPU time for Fe-C, Fe-C-X (where X = Cr, Ni or Mn elements), Fe-C-Cr-Mo alloys.

For illustrating the influence of the initial discretization on the approximate equilibrium obtained from the convex hull, we have considered different number of nodes N along one concentration axis ranging from 2 to 175. We have tested our algorithm at different temperatures and different nominal concentration to span large domains of the different two-phase diagrams.

In order to illustrate the failures of the NR method we have used two different schemes of calculation for the stepping process over large temperature ranges $[T_1; T_2]$. In the first scheme, referred to as *partial scheme*, the convex hull is built at T_1 and used for initializing the NR calculation at this temperature. Then, for the subsequent temperatures, the equilibrium tie-line at the previous temperature is used as an initial guess for NR. In the second scheme, referred to as *full scheme*, the convex hull is built at each temperature, and used for initializing the NR calculations.

Moreover, the balance in terms of computational cost between the convex hull construction and the NR successive step will be investigated for achieving the best compromise.

Finally, to ensure the validity of our results we have compared them with results from the *tcs* version of Thermo-Calc with the global minimization option using the same *FEDAT* database [15].

1.2.1 Fe-C system

In Figure 1.7, the equilibrium mole fraction of carbon in austenite obtained from the quickhull (*QH*) algorithm is plotted as a function of temperature for different discretizations (N ranging from 2 to 175), along with results from Thermo-Calc. As expected, increasing N improves the agreement between quickhull and Thermo-Calc *tcs*. The agreement can be considered as very satisfactory for $N \geq 175$.

Next, for illustrating the benefit to choose the approximate equilibrium deduced

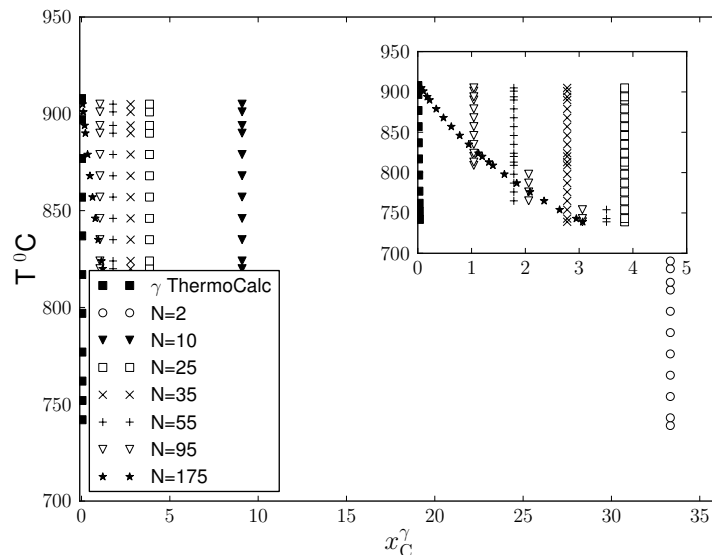


Figure 1.7: Approximate equilibrium x_C^γ vs. temperature in Fe-C obtained with Quickhull with different discretizations N .

from the convex hull (Fig. 1.7) as the initial guess for NR , we have reproduced the Fe-C phase diagram, focusing on the $\alpha + \gamma$ phase field, above the eutectoid temperature (Fig. 1.8). For determining the full phase diagrams, successive calculations must be performed at different temperatures and at different overall concentrations, following a prescribed mapping pattern. Usually, the equilibrium values at the previous step is chosen as the initial guess for the current NR . Because the topology of the phase boundaries in Fe-C alloys does not change drastically, NR quickly converges to the correct equilibrium values. In the next section for higher order alloys, it will be shown that the calculation scheme has to be controlled more carefully.

Fig. 1.8 shows the two-phase field $\alpha + \gamma$ in the temperature range $[738^\circ\text{C}; 912^\circ\text{C}]$ predicted with our hybrid scheme $QH + NR$. It is clear that the agreement with Thermo-Calc is perfect. Our hybrid scheme $QH + NR$ has been examined in terms of computational cost, comparing the CPU times of both steps, QH and NR , for the particular nominal composition Fe-0.5mol.%C. In Fig. 1.9, the CPU times have been plotted vs. N for the successive steps, QH (white) and NR (black), at 600°C (triangles) and 800°C (dots). For QH , the CPU times are greater at 800°C

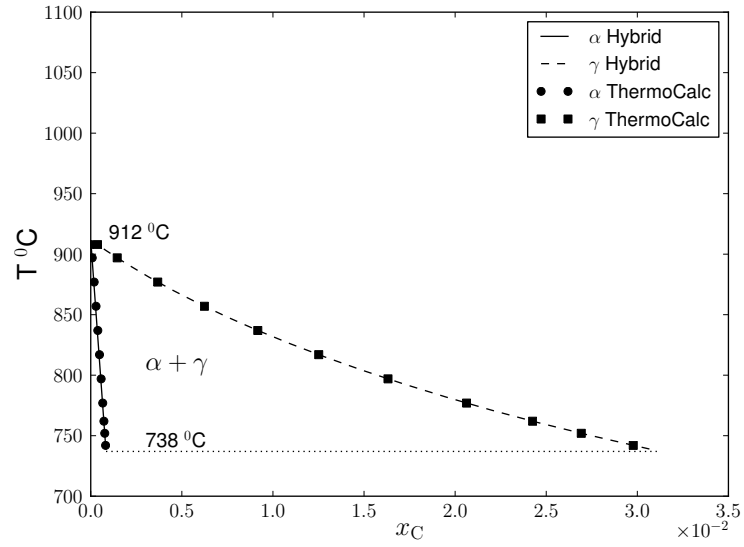


Figure 1.8: Fe-C phase diagrams calculated by the new hybrid (solid and dotted lines) and ThermoCalc (black dots) methods.

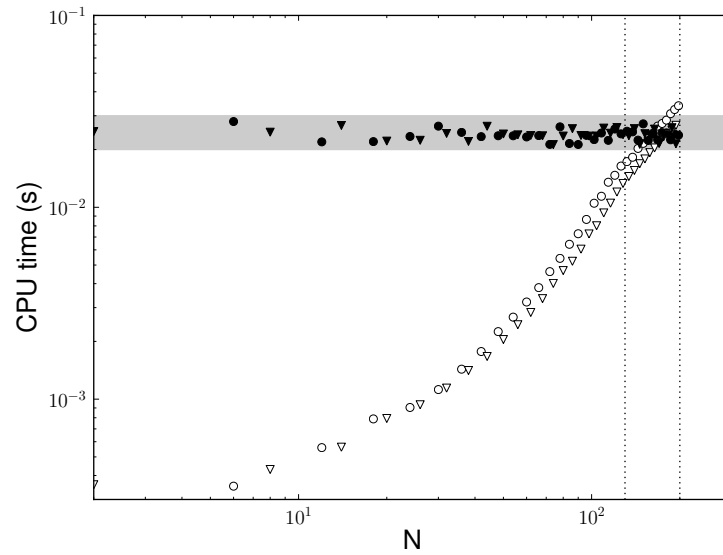


Figure 1.9: CPU times vs. N of QH (white) and subsequent NR (black) for Fe-0.5mol.%C at 600 $^{\circ}\text{C}$ (triangles) and 800 $^{\circ}\text{C}$ (dots).

than at 600°C and this difference increases with N . For NR , the difference is almost not visible. The trends are similar for both temperatures. The CPU time for QH increases with N because the γ phase field becomes larger and contains a large number of segments as T increases. On the contrary, the CPU time for NR exhibits a slight decrease. The best compromise seems to be around $N = 175$. Similar trends have been observed for other nominal compositions in Fe-C.

1.2.2 Fe-C-Cr system

In this section we illustrate our hybrid algorithm and discuss its efficiency in terms of CPU time in the ternary Fe-C-Cr system, more complex than the previous binary Fe-C system, but where the convex hull and its projection on the Gibbs simplex can still be easily visualized.

In Figs. 1.10 and 1.11, the projections on the Gibbs simplex of the approximate convex hulls found with QH are plotted at two temperatures 600 and 800°C and for different discretizations (N ranging from 2 to 55). The boundaries of the phase fields computed with Thermo-Calc are superimposed with thick lines: black for ferrite and red for austenite. Ferrite exhibits a low carbon solubility all along the x_{Cr} axis ($x_C^\alpha \lesssim 1.2 \cdot 10^{-2}$). At 600°C, the miscibility gap observed in α on the Fe-Cr binary axis at about $x_C \approx 0.5$ spreads along the carbon axis and splits the phase field in three parts (insets in Fig. 1.11). Austenite extends over carbon rich regions. At 800°C, a miscibility gap is observed around $x_C \approx 0.3$ and $x_{Cr} \approx 0.15$. At 600°C this miscibility gap merges with the α/γ two-phase field. Hence, whereas the α/γ two-phase field is narrow at 800°C for low Cr contents, it is very large at 600°C for $x_{Cr} \gtrsim 5 \cdot 10^{-2}$.

As expected, the greater the number of nodes in the grid (increasing with N), the better the agreement between quickhull and Thermo-Calc *tcs*. There is indeed a better fit of the two-phase field boundaries with facets located at the borders of one-phase fields as N increases. It is worth noting that this is very dependent on the density of nodes with respect to (i) the extension of one-phase fields (the distance between the boundaries calculated with thermocalc and those calculated with QH is at most equal to the local distance between neighboring nodes); (ii) the local shape of the boundaries (curvature, inclination with respect

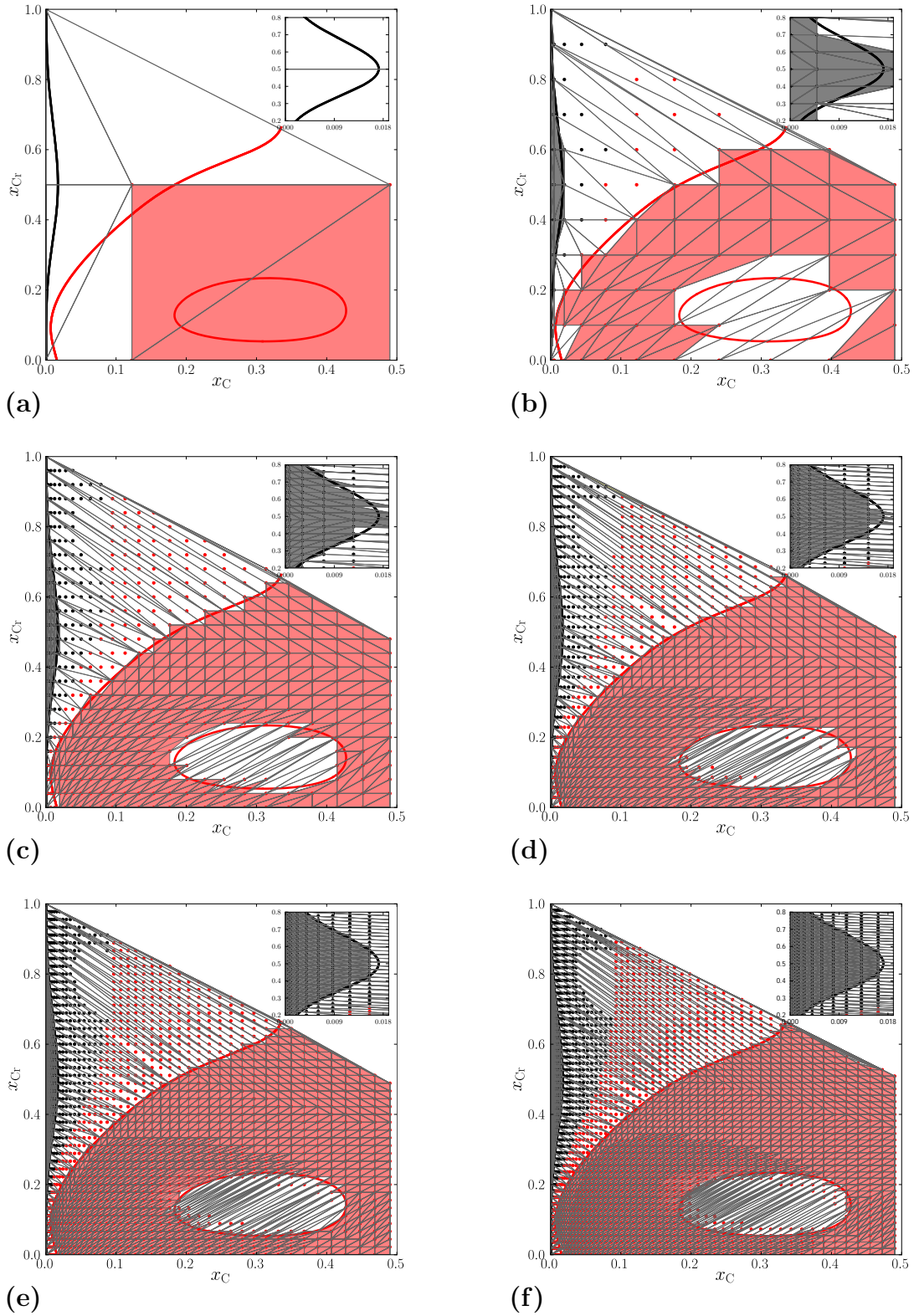


Figure 1.10: Projections of the final convex hulls (triangles) of the Gibbs energies of α (black dots) and γ (red dots) in Fe-C-Cr at 800°C, for $N = 2$ (a), $N = 10$ (b), $N = 25$ (c), $N = 35$ (d), $N = 45$ (e) and $N = 55$ (f).

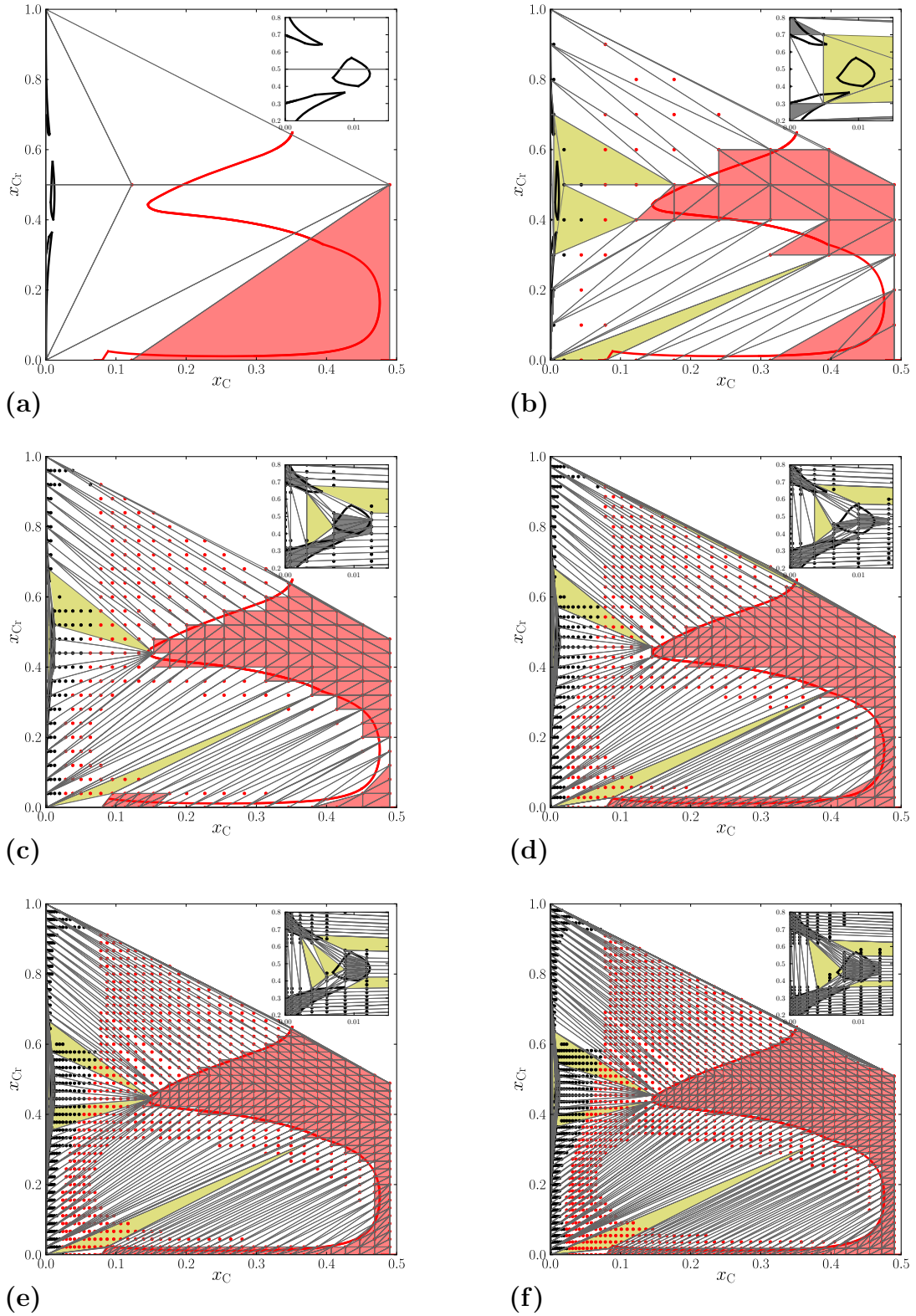


Figure 1.11: Projections of the final convex hulls (triangles) of the Gibbs energies of α (black dots) and γ (red dots) in Fe-C-Cr at 600°C, for $N = 2$ (a), $N = 10$ (b), $N = 25$ (c), $N = 35$ (d), $N = 45$ (e) and $N = 55$ (f).

to the meshing . . .). Moreover, it must be noted that the detection of three-phase fields depends on the quality of the description of one-phase fields.

For $N = 2$, very crude descriptions of the isothermal sections are obtained (Figs 1.10a and 1.11a). For $N = 10$, the description is still approximate, but some non trivial features are already captured, such as the miscibility gap in γ at 800°C (Fig. 1.10b), or the four three-phase fields (yellow facets) at 600°C (Fig. 1.11b). At 800°C, the agreement is satisfactory for $N = 35$ (Fig. 1.10c), and increasing N improves only quantitatively the matching between the results of QH and tcs (Fig. 1.10d-f). At 600°C, a good overall agreement is also achieved for $N = 35$ (Fig. 1.11c) except for the splitting of the α domain near the x_{Cr} axis around $x_{Cr} \approx 0.5$. As a consequence of this misdescription, one particular three-phase field has not been detected. This three-phase field is found for $N = 45$. However, the three-phase field connecting the three α domains is split spuriously into two parts for this nodes density (inset in Fig. 1.11e). A good description is finally achieved for $N = 55$ (Fig. 1.11f).

Similar observations have been done at various temperatures and for different ternary Fe-C-X systems ($X = Cr, Ni, Mo, Mn$) with α and γ , see Appendix C. Next, for illustrating the benefit to choose the approximate tie-line deduced from the convex hull as the initial guess for NR , we have considered an alloy with the following nominal composition: $x_C^0 = 0.92$, $x_{Cr}^0 = 2.66$ in mol.% (red dots in Figs 1.12-1.14).

First, Fig. 1.12 shows the evolution at 600°C of the tie-line during the NR iterations, starting from a random initial tie-line (violet). The successive iterations are shown in black, and superimposed to the isothermal section calculated with Thermo-Calc tcs : boundaries of α and γ are plotted respectively in black and red, and tie-lines in the two-phase field are drawn in light grey. The black tie-lines converge to the bold yellow tie-line, obviously very far from the good solution. It must be stressed that NR fails because the Jacobian of system (1.39) goes to zero whereas the system itself does not. Similar failures have been observed for many other random initial tie-lines.

Then, we have used the approximate tie-line determined from the convex hull: it is drawn in Figs. C.2 as a white line in the blue facet containing the red dot of the nominal composition. Contrary to the previous calculation, NR converges

to the real equilibrium tie-line in bold yellow (predicted by Thermo-Calc *tcs*), in a few iterations demonstrating the reliability of our approach. It is noteworthy that good convergence is achieved whatever the discretization, for the particular case investigated. However, the evolution of the intermediate tie-lines obtained in the course of the *NR* process is less erratic as N increases, i.e. as the convex hull is better described. Indeed, as N increases, the initial tie-line deduced from the initial facet (in blue) gets closer to the good final tie-line. This trend has been systematically observed for different nominal compositions in Fe-C-Cr at 600°C. The same kind of investigation has been carried out at 800°C, as shown in Figs. 1.14. At that temperature, $(x_{\text{C}}^0, x_{\text{Cr}}^0)$ is located in a narrow region of the α/γ two-phase field. Again, convergence is achieved whatever the discretization ($N \geq 2$). However, it has been observed that this behaviour depends on the grid refinement, which must be sufficient for the initial tie-line in the relevant facet not to be too far from the equilibrium tie-line: e.g. using a regular grid with $N = 2$, *NR* fails to converge to the good tie-line. The discretization issue is all the more critical that the two-phase field involved is narrow. In the present example, this happens above 655°C, as shown in Fig. 1.15, where x_{C}^γ is plotted versus temperature: for $N = 2$, the initial tie-line (black dots) is far from the final one (red line). Rapidly, i.e. for $N \geq 10$, the initial tie-line given by the convex hull construction gets closer to the final one. For $N = 95$, a very good approximation is achieved.

Our hybrid scheme *QH* + *NR* has then been examined in terms of computational cost, comparing the CPU times of both steps, *QH* and *NR*, for the particular nominal composition previously investigated.

In Fig. 1.16, the CPU times have been plotted vs. N for the successive steps, *QH* (white) and *NR* (black), at 600°C (triangles) and 800°C (dots). For both steps, the CPU times are greater at 800°C than at 600°C. For *QH*, the difference increases with N because the γ phase field becomes larger (and so, contains a larger number of facets) as T increases. For *NR*, the difference is larger for intermediate N ($N \in [4; \sim 35]$) due to a the relatively poor approximation of the initial tie-line with *QH* (Fig. 1.15). However, trends are similar for both temperatures. The CPU time for *QH* increases with N following roughly a power law with an exponent between 1.5 and 2. On the contrary, the CPU time for *NR*

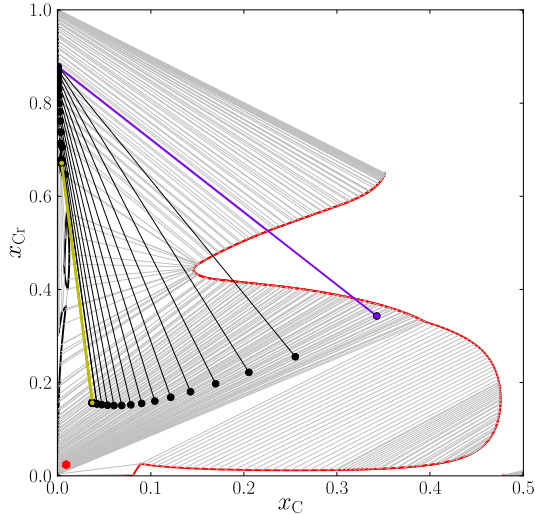


Figure 1.12: Tie-line search process with NR for Fe-0.92 mol.%C-2.66 mol.%Cr (red dot) at 600°C , starting with an arbitrary tie-line (violet). Intermediate, and final tie-lines are in black and yellow respectively.

exhibits a slight decrease, down to a constant value of 0.01 s for large N . At 600°C , this decrease is quite progressive for $N < 20$. At 800°C , a sharp decrease is observed at $N = 35$. Hence, for small N ($N \leq 10$ at 600°C and $N \leq 15$ at 800°C), the CPU time of NR is longer than the CPU time of QH : the overhead due to QH is negligible even for a single equilibrium calculation. The best compromise seems to be around $N \sim 10$. Similar trends have been observed for other nominal compositions in Fe-C-Cr and in other multicomponent systems (Fe-C-X and F-C-X₁-X₂).

It is worth stressing that, for successive equilibrium calculations at the same temperature, our hybrid algorithm can be efficient even for refined grids ($N > 10$). Indeed, the first QH step is carried out once, and only the search for approximate tie-lines in the convex hull has to be performed before successive NR steps. Moreover, advantage can be taken from the convex hull to rationalize the mapping process in an isothermal section by spanning all the two-phase facets.

Finally, for determining full phase diagrams, successive calculations must be performed at different temperatures and at different overall concentrations, following a prescribed mapping pattern. Usually, the equilibrium tie-line at the previous

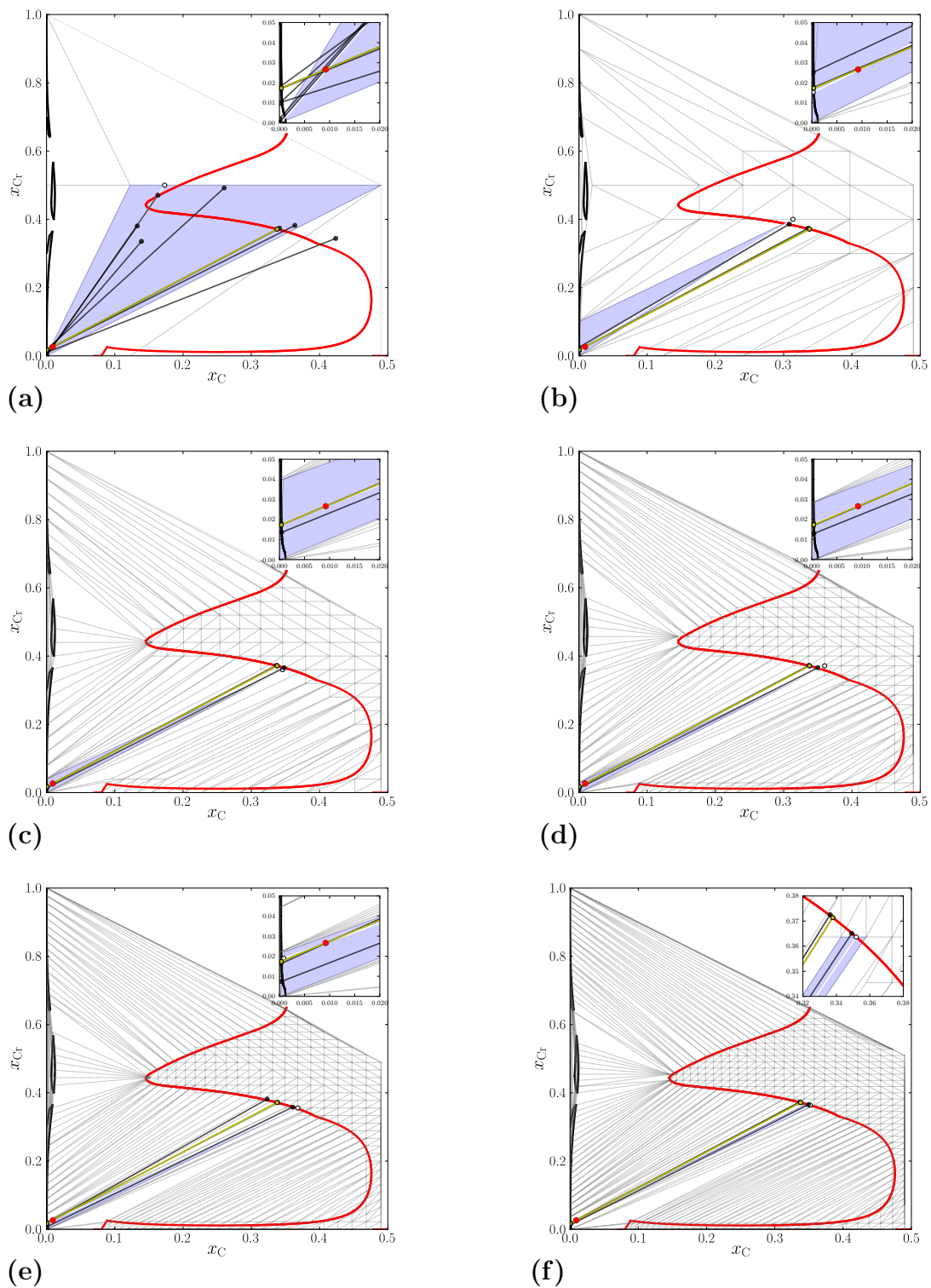


Figure 1.13: Tie-line search process with NR for Fe-0.92 mol.%C-2.66 mol.%Cr (red dot), starting with the tie-lines obtained from the convex hulls at 600°C (white line in the blue triangle) for $N = 2$ (a), $N = 10$ (b), $N = 25$ (c), $N = 35$ (d), $N = 45$ (e), $N = 55$ (f). Intermediate, and final tie-lines are in black and yellow respectively.

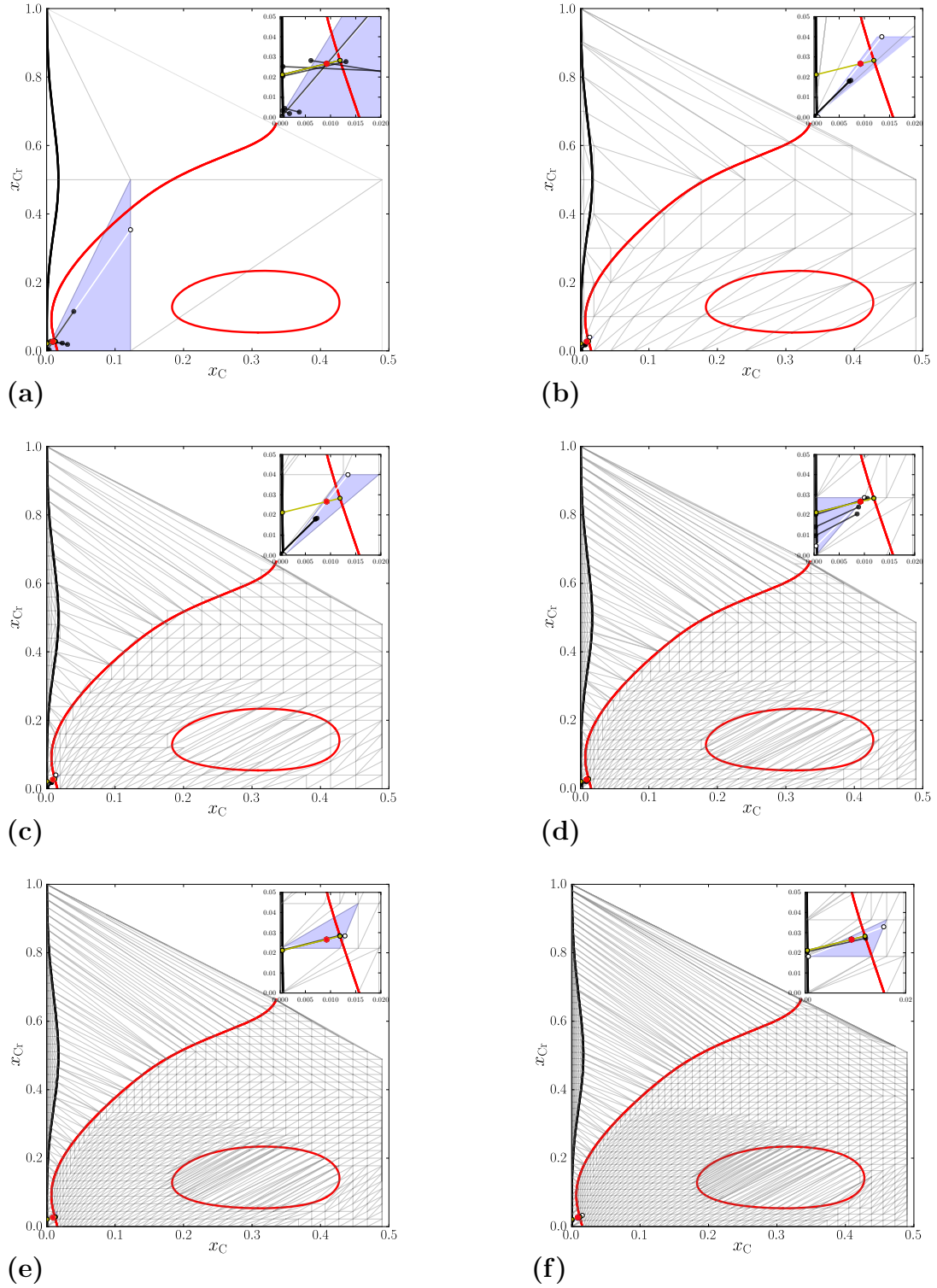


Figure 1.14: Tie-line search process with NR for Fe-0.92 mol.%C-2.66 mol.%Cr (red dot), starting with the tie-lines obtained from the convex hulls at 800°C (white line in the blue triangle) for $N = 2$ (a), $N = 10$ (b), $N = 25$ (c), $N = 35$ (d), $N = 45$ (e), $N = 55$ (f). Intermediate, and final tie-lines are in black and yellow respectively.

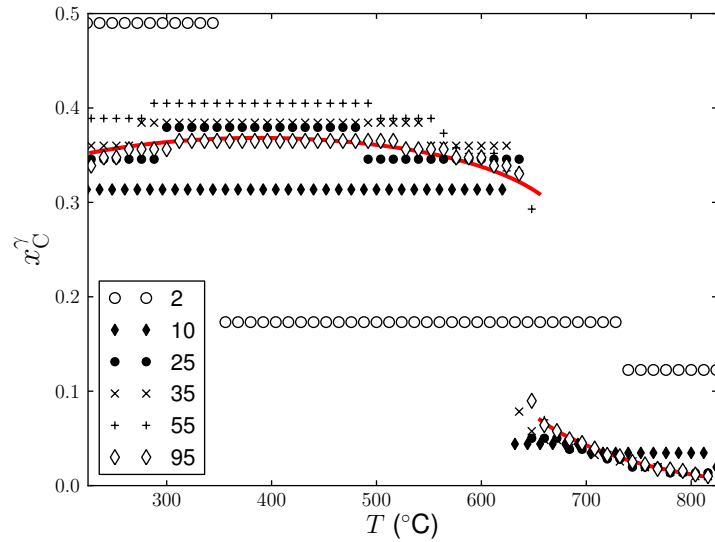


Figure 1.15: Approximate equilibrium x_C^γ vs. temperature obtained with Quickull for Fe-0.92 mol.%C-2.66 mol.%Cr with different discretizations N (red line obtained with Thermo-Calc *tcs*).

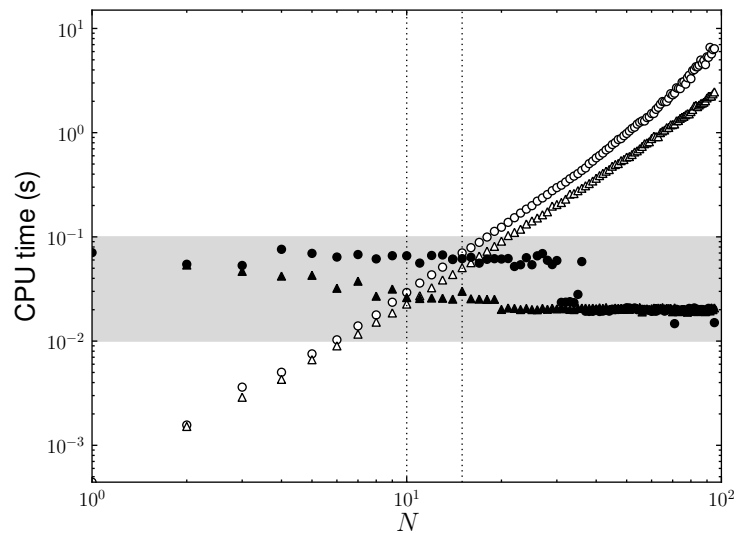


Figure 1.16: CPU times vs. N of QH (white) and subsequent NR (black) for Fe-0.92 mol.%C-2.66 mol.%Cr at 600°C (triangles) and 800°C (dots).

step is chosen as the initial guess for the current NR . When the topology of the phase boundaries does not change drastically, NR quickly converges to the correct tie-line. But in some cases, when sharp changes occur in the phase diagram due to bifurcations of the global minimum, taking the previous tie-line as the initial guess can be misleading for NR . Indeed, the previous global minimum may change into a local one and NR then converges towards a metastable equilibrium. This kind of problem, and its solution relying on our hybrid algorithm, are illustrated with the calculation of the phase fraction of α versus temperature in the ternary alloy Fe-0.92C-2.66Cr (mol.%).

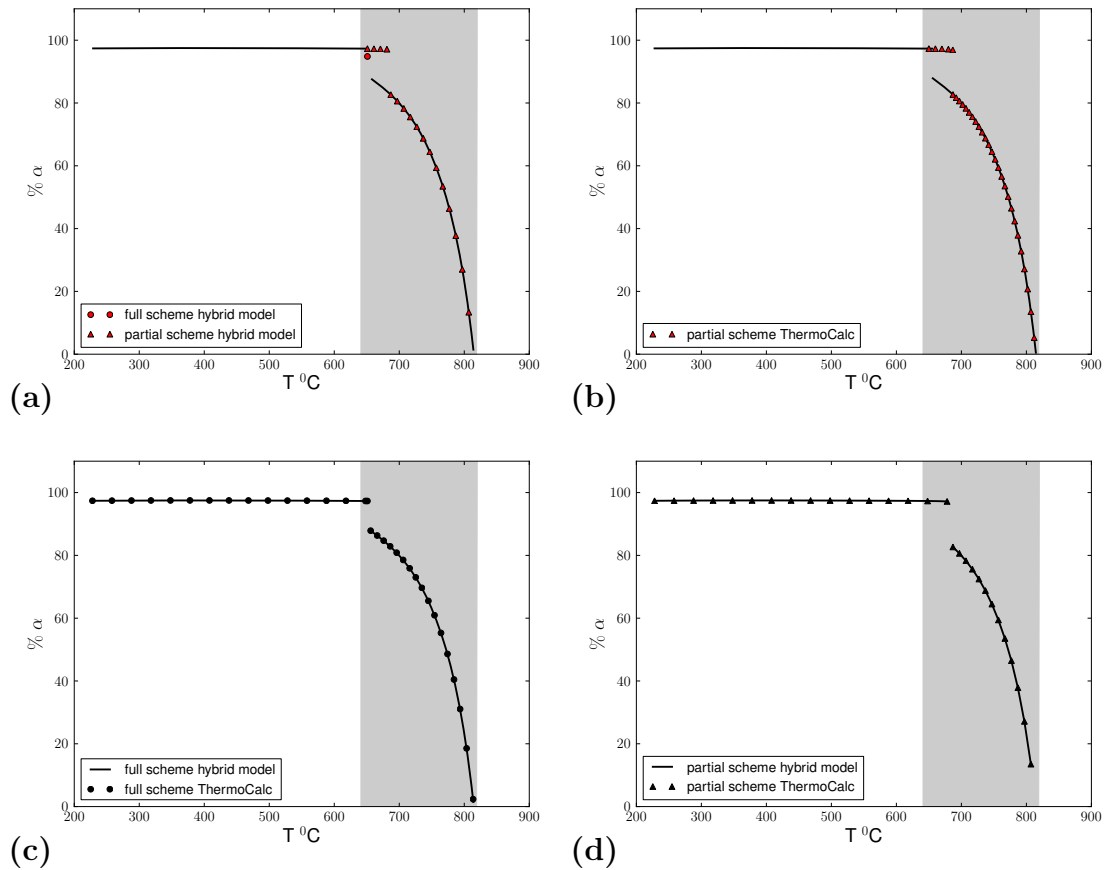


Figure 1.17: Phase fraction of α vs. temperature in a Fe-0.92 C-2.66 Cr (mol.%) alloy, full scheme (dots) partial scheme (triangles): hybrid model (a), ThermoCalc (b), hybrid and ThermoCalc full scheme (c), hybrid and ThermoCalc partial scheme (d).

For that purpose, we have considered the two different schemes mentioned above (*partial scheme* and *full scheme*) for the stepping process over a large temperature range [200°C;900°C] and with $N = 35$. As shown in Fig. 1.17a, the two schemes differ for $T \in [\sim 650^\circ\text{C}; \sim 800^\circ\text{C}]$ (grey domain): when the partial scheme predicts that the fraction of ferrite does not change drastically when increasing temperatures (red triangles), a disjointed decreasing branch appears with the full scheme relying on convex hulls (red dots). Obviously, the partial scheme has missed the bifurcation of the global minimum and has followed a metastable local minimum. Indeed, as shown previously for the Fe-C-Cr system (Figs. 1.10-1.11), there is a temperature below which the miscibility gap in γ merges with the α/γ two-phase field. Below this temperature, the particular tie-line corresponding to Fe-0.92 mol.%C-2.66 mol.%Cr links α with some γ at the border of the miscibility gap, with large concentrations in C (see e.g. Fig. C.2). On the contrary, above this temperature, the nominal composition is within the α/γ narrow two-phase field and γ is poor in C (see e.g. Fig. 1.14). But the partial scheme has been mistaken by the metastable equilibrium between α and the miscibility gap in γ which is disjointed from the narrow α/γ two-phase field.

We have also compared both schemes with Thermo-Calc *tcs*, performing calculations with this software along two ways: first, the calculations have been carried out using the step procedure in the full temperature range [200°C; 900°C] (Thermo-Calc *partial scheme*). Second, we have performed the calculations using the step procedure in two temperature ranges: [200°C; 640°C] and [640°C; 900°C] (called Thermo-Calc *full scheme*). The results from these calculations have been plotted in Fig. 1.17b and compared to both schemes of our hybrid algorithm (Fig. 1.17c-d). As can be seen, there is a perfect matching between the partial schemes and between the full schemes. In terms of computational cost, the *partial scheme* is better than the *full scheme*. However, for $T \in [640^\circ\text{C}; 700^\circ\text{C}]$ where there is a bifurcation of the global minimum, the total Gibbs energy of the system calculated with Thermo-Calc using the *partial scheme* is larger than that of the *full scheme*.

This example clearly demonstrates the superior reliability of our algorithm over those relying only on *NR*, to the detriment of the computational cost associated with the convex hull construction, which can however be limited by using coarse irregular grids.

1.2.3 Fe-C-Cr-Mo system

Finally, we have examined the more complex system Fe-C-Cr-Mo with 4 species. We have considered an alloy with the following nominal composition: $x_C^0 = 0.92$, $x_{Cr}^0 = 2.66$, $x_{Mo}^0 = 0.81$ in mol.%.

Fig. 1.18 shows the equilibrium concentrations x_C^γ , x_{Cr}^γ , x_{Mo}^γ versus temperature estimated with the convex hull algorithm. The equilibrium from Thermo-Calc *tcs* was computed in two temperature range for avoiding the failures of *NR* algorithm, as discussed in the previous section: [$\sim 200^\circ\text{C}$; $\sim 700^\circ\text{C}$] and [$\sim 700^\circ\text{C}$; $\sim 1600^\circ\text{C}$]. Then, phase field boundary computed with Thermo-Calc is superimposed with red line. For $N = 2$, the approximate equilibrium (in cross) is enough far from the final one (red line) in all temperature range. For $N = 10$, the initial approximate equilibrium given by the convex hull construction gets closer to the final solution and have a perfect agreement for x_{Cr}^γ at the higher temperature range. Rapidly, i.e. for $N > 10$, the approximate equilibrium gets more and more closer with increasing N to the final solution. For $N = 35$, a very good approximation is obtained.

In Fig. 1.19, the CPU times have been plotted vs. N for the successive steps, *QH* (white) and *NR* (black), at 600°C (triangles) and at 800°C (dots). For both steps, the CPU times are greater at 800°C than at 600°C . As expected, the CPU time for *QH* increases with N . On the contrary, the CPU time for *NR* decreases not progressively and, finally, down to a constant value for large N . The best compromise seems to be around $N = [3 \sim 10]$.

Finally, we have determined full phase diagram doing the successive calculations at different temperatures and at different overall concentrations, following a prescribed mapping pattern. We have illustrated this kind of calculations with the phase fraction of α versus temperature in the quaternary alloy Fe-0.92 C-2.66 Cr-0.81 Mo (mol.%). In order to avoid the misleading for *NR*, we have taken into account the topology of the phase boundaries. For that purpose, we have again resorted to the two different schemes, *partial scheme* and *full scheme*, over a large temperature range [200°C ; 1600°C]. As shown in Fig. 1.20a, both schemes differ for $T \in [\sim 600^\circ\text{C}; \sim 850^\circ\text{C}]$ (grey domain): when the *partial scheme* predicts the limit of phase fraction of α which increases continuously in the temperature range

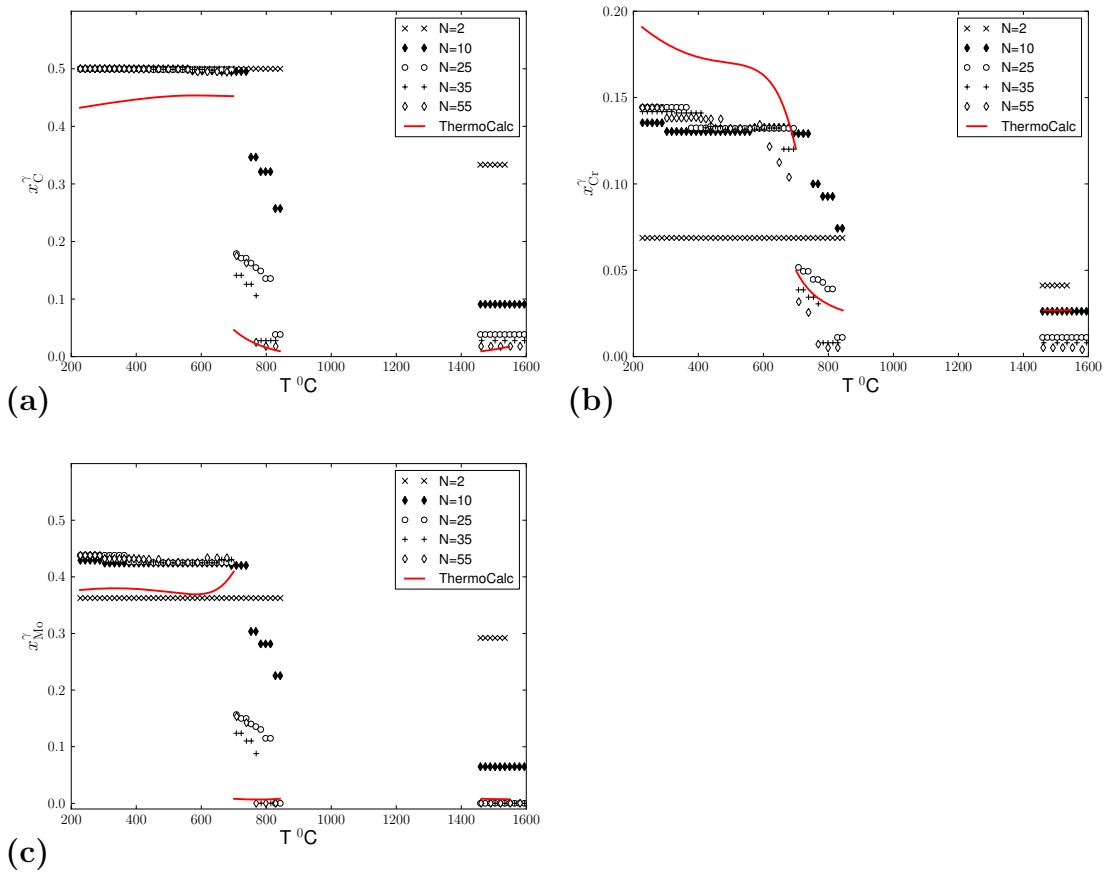


Figure 1.18: Equilibrium x_C^γ (a), x_{Cr}^γ (b), x_{Mo}^γ (c) vs. temperature estimated with Quickhull for Fe-0.92 mol% C-2.66 mol% Cr-0.81 mol% Mo with different discretizations N and with Thermo-Calc (red line).

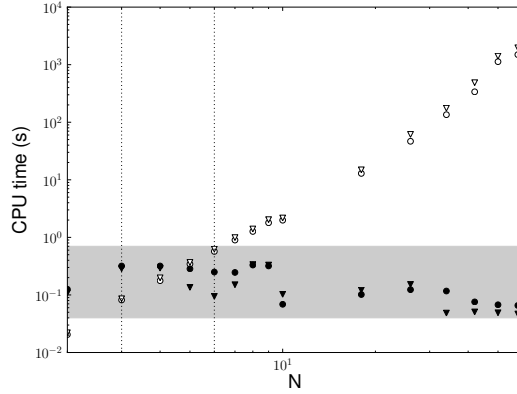


Figure 1.19: CPU times vs. N of QH (white) and subsequent NR (black) for Fe-0.92 mol% C-2.66 mol.% Cr-0.81 mol.% Mo at 600°C (triangles) and 800°C (dots).

[$\sim 600^\circ\text{C}$; $\sim 850^\circ\text{C}$] (red triangles), another disjointed branch decreasing in the same temperature range appears with the *full scheme* relying on convex hulls (red dots). Finally, the phase fraction of α from two schemes increases continuously in the higher temperature range [$\sim 1500^\circ\text{C}$; $\sim 1600^\circ\text{C}$]. The description of quaternary system relates on ternary system Fe-C-Cr (Figs. 1.11-1.10), where there is temperature below which the miscibility gap in γ merges with the α/γ two-phase field. Below this temperature, the particular tie-line corresponding to Fe-0.92 C-2.66 Cr-0.81 Mo (mol.%) relates α with some γ at the border of the miscibility gap, with large concentrations in C (see e.g. Fig. C.2). Once again, the partial scheme is trapped by a metastable equilibrium between α and the miscibility gap in γ , and miss the stable one. In Fig. 1.20b, we have compared the results computed with Thermo-Calc *tcs* using two the schemes already introduced for Fe-C-Cr. For the *partial scheme*, the calculations have been carried out with Thermo-Calc in the full temperature range [200°C ; 1600°C]. For the *full scheme*, the calculations with Thermo-Calc have been performed in two temperature ranges: first in [200°C ; $\sim 650^\circ\text{C}$]; then in [$\sim 650^\circ\text{C}$; $\sim 1600^\circ\text{C}$]. We observe the same tendencies as in Fig. 1.20a: both schemes differ for $T \in [\sim 600^\circ\text{C}; \sim 850^\circ\text{C}]$ (grey domain). Figs. 1.20c-d compare the results of the full schemes of our hybrid model and used to run Thermo-Calc *tcs*. A perfect agreement is found like for the Fe-C-Cr system.

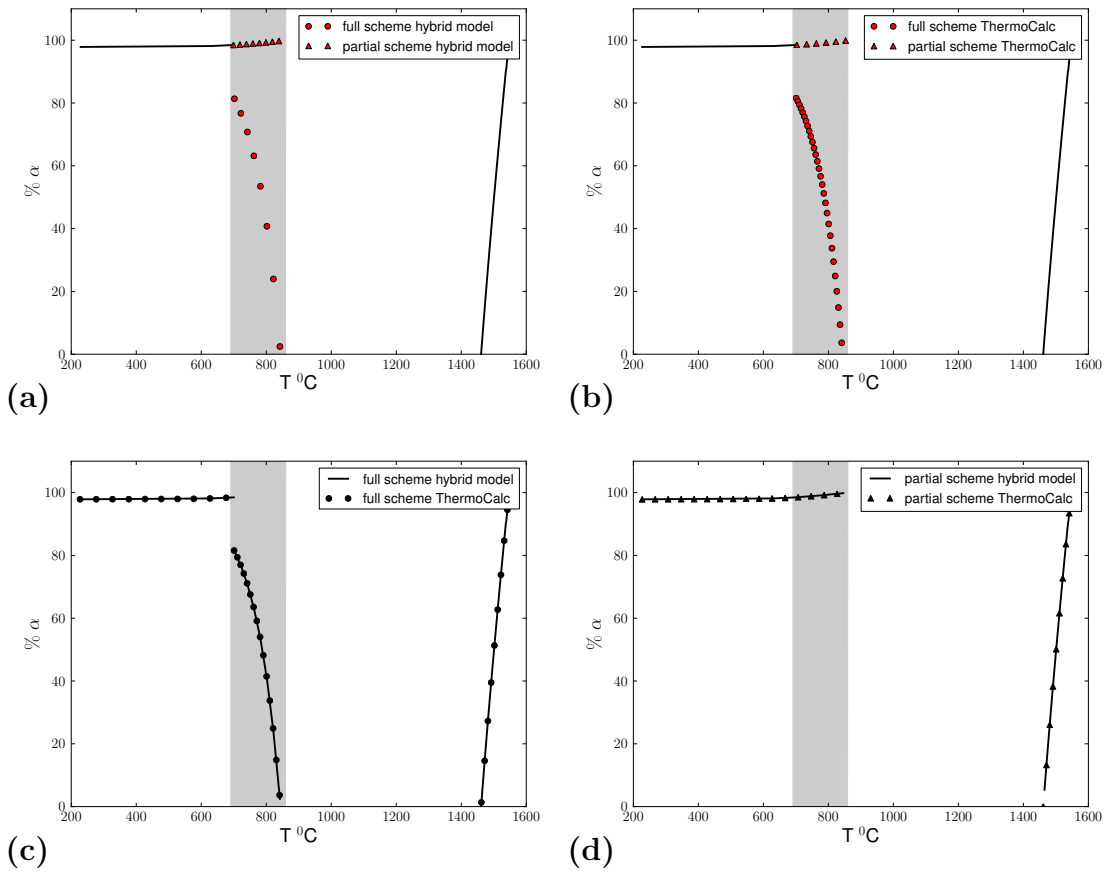


Figure 1.20: Phase fraction of α vs. temperature in a Fe-0.92 C-2.66 Cr -0.81 Mo (mol.%) alloy, full scheme (dots) partial scheme (triangles): hybrid model (a), Thermo-Calc (b), hybrid and Thermo-Calc full scheme (c), hybrid and Thermo-Calc partial scheme (d).

1.3 Conclusion

A hybrid algorithm has been designed to compute two-phase equilibria in multicomponent alloys with two sublattices relying on the convex hull construction of the Gibbs energy based on the Quick Hull algorithm, prior to the classical Newton-Raphson search procedure. We have applied our method to ternary Fe-C-Cr, Fe-C-Ni and quaternary Fe-C-Cr-Mo systems, for illustrating the benefit of our approach. The convex hull construction has been tested against two isothermal sections in Fe-C-Cr computed with Thermo-Calc *tcs* exhibiting different features. Even if the description of the isothermal sections is improved with refined grids used in the Quick hull algorithm, coarse discretizations can give satisfactory results depending on the complexity of the phase diagram. The selection of an approximate tie-line in the convex hull has permitted Newton-Raphson to converge quickly and safely to the real equilibrium, especially avoiding Newton-Raphson to be trapped by metastable equilibria. Although grid refinement leads to a better description of the convex hull, there is an upper number of nodes depending on the temperature above which refining does not seem to decrease the number of Newton-Raphson iterations. This trend has been confirmed by investigating the CPU times of the successive Quick Hull and Newton-Raphson steps versus the number of nodes. An optimal number of nodes has been found for the particular cases investigated which gives the better compromise between Quick Hull and Newton Raphson. This optimal number is likely to be relevant in other systems because it has revealed to be operative in several cases with different phase field topologies. Finally, it is worth mentioning that the algorithm proposed in this work is general and can easily be applied to other phases and alloys. It could also be extended to undertake multiphase equilibria.

Chapter 2

Thick interface model for the $\gamma \rightarrow \alpha$ transformation

The $\gamma \rightarrow \alpha$ transformation in steel is the most studied diffusion controlled transformation. Besides the works concerning the mechanisms at the atomic scale (growth ledges, disconnections etc., e.g. [4]), the most common approach for predicting the kinetics of diffusion controlled phase transformations relies on the so-called sharp interface concept: interfaces are reduced to mathematical surfaces with intrinsic thermodynamic and kinetic properties, following the seminal work of Gibbs [63]. If this is not the only way to deal with interfaces as will be shown in the next chapter, it has proved to be the most practical way for developing models handling microstructures at the millimeter scale, i.e. in a Representative Volume Element (RVE) for structural mechanics (e.g. [17, 95]).

Two steps are intrinsically implied by this approach. First, the transport problem in the bulk phases must be solved accounting for the moving interface through the local solute balances, relating the jumps in solute concentrations, the velocity, and the jumps in the flux [142]. Second, some conditions must be prescribed at the interface (sometimes called response functions [18]) which are the necessary boundary conditions for the diffusion problem in the bulks.

Early works have generally considered local equilibrium at the interfaces because it is the simplest case to envisage. Moreover, it makes the moving boundary problem analytically tractable, because for some particular simple geometries (plane,

cylinder, sphere ...) the interface is a concentration level set. Hence, similarity solutions to the diffusion problems can be used to find solutions as pioneered by Stefan [145], Zener [163], Frank [60], Ivantsov [91] and Horvay and Cahn [83]. If this is generally a good assumption when dealing with the solidification of metals and metallic alloys in normal conditions (those prevailing in most of the industrial casting processes), it is less clear whether it is still relevant at the solid state. Indeed, (i) there exists very often crystallographic constraints between coexisting solid phases [43, 44]. Growth ledges have been observed even at high temperatures at the interface generally considered implicitly as incoherent (e.g. [5]). Moreover, (ii) diffusivities in solid are generally much smaller than in liquid. As well, as temperature decreases at values where solid phases prevail, atomic mobilities also decrease and the equilibrium is less prone to be achieved. However, in many cases the local equilibrium hypothesis gives satisfying results, in particular in dilute binary metallic alloys exhibiting precipitation, e.g. [157]. This is also the case for transformations in multicomponent alloys at high temperatures i.e. not too far from equilibrium, and when all diffusivities are of the same order of magnitude, e.g. [66, 120]. In other cases, this assumption fails to predict the correct kinetics. Thus, different refinements have been proposed to the description of the diffusion processes in the bulks: diffusion in finite system with soft impingement [57], short circuit diffusion (e.g. by the collector plate mechanism) [2], or geometrical complexities (in that case by relying on numerical models) [154]. But all those refinements revealed to be not sufficient to explain many observed features, in particular slow kinetics and stases at fractions below equilibrium [6]. The most promising way which would give a consistent account of all these puzzling features relies on the description of the interfacial phenomena. This is not a new trend, since interface controlled transformations have been put forward very early as the opposite case to diffusion controlled transformations [44]. In the context of multicomponent steels, non-equilibrium conditions have been suggested early by Hultren for the slow substitutional elements only, a situation called paraequilibrium [86]. However, because paraequilibrium constitutes a limit case with no partition at all for the substitutional species, the conditions at the interface can be expressed without any knowledge of the interfacial processes involved. In parallel, works on the solute drag by grain boundaries have shed light

on the role that diffusion within interfaces/grain boundaries may play to explain significant but puzzling variations in the kinetics of moving boundaries [32, 81]. Similar concepts applied to rapid solidification [82] as well as to massive transformations [79, 81] have benefited from the consistent framework elaborated progressively by Hillert for handling non-equilibrium interfaces [71, 76]. Applying classical irreversible thermodynamics (e.g. [68]), Hillert first proposed to split the dissipated Gibbs energy into different contributions identified in the different problems mentioned above: dissipation by the so-called interface friction (interface controlled transformations) and dissipation by trans-interface diffusion (rapid solidification and solute drag). Recent advances along this line have been obtained by Odqvist in a series of studies [124, 125, 127] which constitute great improvements over previous approaches (e.g. [56, 136]).

The first aim of the present chapter is to enrich sharp interface models used commonly to handle microstructure evolutions in large scales problems [120, 121]. Hence, we have preserved the structure of this kind of model relying on solving local equilibrium coupled with bulk diffusion with simple analytical models. However, the assumption of local equilibrium has been relaxed thanks to the description of the irreversible processes inside the interface, in the framework proposed by Hillert [73] and inspired by the model of Odqvist [127]. Second, this model is intended to be used to investigate particularly puzzling kinetics associated with ternary Fe-C-X steels that have not been fully explained and predicted so far.

Hence, the chapter is organized as follows. First, the general framework of the model is detailed (§2.1). Then, it is applied to the simplest case exhibiting significant interface dissipation, i.e. the massive transformation $\gamma \rightarrow \alpha$ in binary Fe-Ni alloys, in order to illustrate some specific features of the model (§2.2). Finally, the last section is devoted to ternary Fe-C-X alloys, aiming at investigating the capabilities of the thick interface model to address puzzling kinetics (§2.3).

2.1 The model description

The model is a variation of the model of Odqvist [125]. It relies on two major assumptions. Despite its atomic scale, the interface is considered as a continuum with a prescribed thickness, where continuum thermodynamics can still apply. Moreover, contrary to the phase field approach (§3), a clear separation is hold between the properties and behaviours of the interface and of the abutting phases. Additional reasonable assumptions are also made which transforms partial differential equations into ordinary differential equations easier to integrate: (i) fields are varying only along the direction normal to the interface (the problem becomes 1D in space); (ii) the interfacial processes are assumed to be steady because the interface is so small that the fields can adjust immediately to the boundary conditions imposed by the bulks (the problem does not depend on time anymore). Finally, the coupling with the bulk is achieved in a transparent way through simple analytical expressions for the gradients in the bulks.

In the sequel, the following conventions will be used: the growing phase is denoted as α , the parent phase as γ , and the substitutional element as X .

2.1.1 α/γ interface

Concentration profiles

At a first step, the concentration profiles of the $n - 1$ alloying species i are determined through the interface. For that purpose, the solute balances are recast in the moving frame of the interface, assuming that a steady state prevails because processes are sufficiently fast to adapt instantaneously:

$$-v \frac{du_i}{dz} = V_m \frac{d}{dz} J_i \quad (2.1)$$

where z is the distance running normal to the interface, v is the interface velocity (positive for growth, i.e. in the direction of increasing z), V_m the molar volume of the substitutional elements forming the crystalline lattice and J_i is the density of flux of species i . u_i is the u -fraction defined as the number of moles of i per

mole of substitutional elements¹. When there is no interstitial elements, it can be noted that $u_i = x_i$.

Integrating (2.1) from the α side of the interface at $z = 0$, assuming that $J_i^\alpha = 0$ (e.g. u_i is flat in α), gives:

$$(u_i(z) - u_i^\alpha) v = V_m J_i(z) \quad (2.2)$$

The densities of flux J_i can be expressed as linear functions of gradients of some appropriate potentials [130]:

$$J_i = -\frac{1}{V_m} \sum_{j=1}^{n-1} L_{ij} \nabla \Phi_j \quad (2.3)$$

where L_{ij} are some phenomenological parameters (in $\text{m}^2\text{mol}/\text{J}/\text{s}$), entering the Onsager positive definite matrix of mobilities. Φ_i is the diffusion potential of species i . For substitutional elements $\Phi_i = \mu_i - \mu_{\text{ref}}$, where ref denotes the reference element, generally the major one (i.e. Fe in our case). For interstitial elements $\Phi_i = \mu_i$.

Using the chain rule, Eq. (2.3) becomes:

$$J_i = -\frac{1}{V_m} \sum_{j=1}^{n-1} L_{ij} \sum_{k=1}^{n-1} \frac{\partial \Phi_j}{\partial u_k} \nabla u_k \quad (2.4)$$

or alternatively:

$$J_i = -\frac{1}{V_m} \sum_{j=1}^{n-1} D_{ij}^* \nabla u_j \quad (2.5)$$

where we have introduced the diffusivities D_{ij}^* (in m^2/s):

$$D_{ij}^* = \sum_{k=1}^{n-1} L_{ik} \frac{\partial \Phi_k}{\partial u_j} \quad (2.6)$$

¹ The use of u -fractions relies implicitly on a constant molar volume. Indeed, in that case $c_i = u_i/V_m$ where c_i is the concentration in mole per unit volume.

or in vector notation¹:

$$\mathbf{D}^* = \mathbf{\tilde{L}} \cdot \mathbf{\tilde{\Phi}}_u \quad (2.7)$$

Inserting Eq. (2.4) into Eq. (2.2), the following system of $n - 1$ differential equations must be integrated to determine the concentration profiles within the interface:

$$- (u_i(z) - u_i^\alpha) v = \sum_{j=1}^{n-1} L_{ij}(z) \sum_{k=1}^{n-1} \partial_{u_k} \Phi_j(z) \frac{du_k}{dz} \quad (2.8)$$

or in vector notation:

$$- (\mathbf{u}(z) - \mathbf{u}^\alpha) v = \mathbf{\tilde{L}}(z) \cdot \mathbf{\tilde{\Phi}}_u(z) \cdot \frac{d\mathbf{u}}{dz} \quad (2.9)$$

From a mathematical point of view, Eqs. (2.9) constitute a boundary value problem which can be solved numerically by any methods relying on space discretization, such as Euler method or Runge-Kutta method [42] as proposed in different works [126, 148]. However, the benefit of using such methods is small because very little is known about the real variations of L_{ij} and Φ_i in the interface. Only an analysis of the processes at the atomic scale would provide such information. Moreover, we have found that the resulting algorithm is not robust in agreement with some comment in [149]. Hence, we have found more profitable to assume a simple linear profiles for Φ_i so as to obtain directly explicit expressions. In that case, on the γ side ($z = \delta^*$)

$$J_i(\delta^*) = -\frac{1}{V_m} \sum_{j=1}^{n-1} L_{ij}^\gamma \frac{\Delta\Phi_j}{\delta^*} \quad (2.10)$$

where $\Delta\Phi_i = \Phi_i^\gamma - \Phi_i^\alpha$ denotes the jump of diffusion potential across the interface for species i , δ^* is the interface thickness, and where L_{ij}^γ is the mobility matrix assessed on the γ side of the interface. Combining Eq. (2.10) with Eq. (2.1) at $z = \delta^*$ gives:

$$(u_i^\gamma - u_i^\alpha) v \delta^* = - \sum_{j=1}^{n-1} L_{ij}^\gamma \Delta\Phi_j \quad (2.11)$$

¹ Vectors with $n - 1$ elements are in bold face and $(n - 1) \times (n - 1)$ matrix are in bold face with \sim as a subscript.

Eqs. (2.11) can easily be inverted to give explicit expressions for the jumps of diffusion potentials at the interface (in vector notation):

$$\Delta\Phi = -v\delta^* \underline{\mathbf{L}}^{\gamma^{-1}} \cdot \Delta\mathbf{u} \quad (2.12)$$

where $\underline{\mathbf{L}}^{\gamma^{-1}}$ is the inverse of the mobility matrix at $z = \delta^*$, and $\Delta\mathbf{u} = (u_i^\gamma - u_i^\alpha)$ with $i = 1, n-1$. For Fe-C-X, neglecting the cross mobilities, i.e. $L_{XC}^\gamma = L_{CX}^\gamma = 0$, Eqs. (2.12) gives two simple expressions between the jumps of diffusion potentials and the jumps of concentrations across the α/γ interface:

$$\begin{cases} \Delta\Phi_C = -\frac{v\delta^*}{L_{CC}} (u_C^\gamma - u_C^\alpha) \\ \Delta\Phi_X = -\frac{v\delta^*}{L_{XX}} (u_X^\gamma - u_X^\alpha) \end{cases} \quad (2.13)$$

In the following sections, we will mention interfacial diffusivities $D_i^{\gamma*}$ (denoting $D_{ii}^{\gamma*}$) instead of mobilities to compare with bulk diffusivities (§2.1.2). When cross mobilities are neglected, inverting (2.7) is trivial to relate mobilities to diffusivities:

$$L_{CC}^\gamma = \frac{D_{CC}^{\gamma*}}{\partial\phi_C/\partial u_C} \quad (2.14)$$

$$L_{XX}^\gamma = \frac{D_{XX}^{\gamma*}}{\partial\phi_X/\partial u_X} \quad (2.15)$$

where the partial derivatives are performed on the γ side of the interface.

Balance of Gibbs energy

The second step consists in determining the balance of Gibbs energy in the interface, i.e. how the interfacial driving force is dissipated by the different phenomena operating at the interface. Hillert has proposed very early [77] to split the interfacial driving force (≥ 0 when α is growing) into two contributions for diffusion controlled transformations, as shown in Fig. 2.1:

$$DF^* = \Delta G_m^{\text{diff}} + \Delta G_m^{\text{friction}} \quad (2.16)$$

The driving force reads:

$$\begin{aligned}
 DF^* &= \sum_{i=1}^n u_i^\alpha (\mu_i^\gamma(\mathbf{u}^\gamma) - \mu_i^\alpha(\mathbf{u}^\alpha)) \\
 &= \underline{\mathbf{u}}^\alpha \cdot \underline{\Delta\boldsymbol{\mu}}
 \end{aligned} \tag{2.17}$$

where underlined vectors contain n elements, i.e. contain the contribution from the major species (e.g. Fe in Fe-C-X alloys)¹.

In Eq. (2.16), $\Delta G_m^{\text{friction}} \geq 0$ is associated with the interface migration itself involving the movement of all the substitutional atoms, responsible for the change in crystalline structure². $\Delta G_m^{\text{diff}} \geq 0$ is associated with the diffusion process, also called trans-interface diffusion, which gives rise to the solute partition between both sides of the interface.

It is worth emphasizing that this separation implicitly assumes that both processes are independent, as clearly shown by Hillert in [73], following the works of Baker and Cahn [19] and Caroli et al. [34]³.

Dissipation by trans-interface diffusion

Combining the first and second laws of thermodynamics, it can be shown that the local production rate of entropy \dot{s}_m^{irr} by the chemical diffusion of $n - 1$ solute elements in a system with uniform temperature and pressure writes [68]:

$$T \dot{s}_m^{\text{irr}} = -V_m \sum_{i=1}^{n-1} J_i \cdot \nabla \Phi_i \tag{2.18}$$

where the rate is per mole of substitutional species. In the moving frame of the interface, in stationary conditions, integration of Eq. (2.18) over the thickness of the interface gives:

$$\Delta G_m^{\text{diff}} = -\frac{V_m}{v} \sum_{i=1}^{n-1} \int_0^{\delta^*} J_i \frac{\partial \Phi_i}{\partial z} dz \tag{2.19}$$

¹ In contrast with $n - 1$ vectors in bold face.

² The change in crystalline structure is often referred to as interface friction.

³ See also the illuminating electrical analogy given in [118].

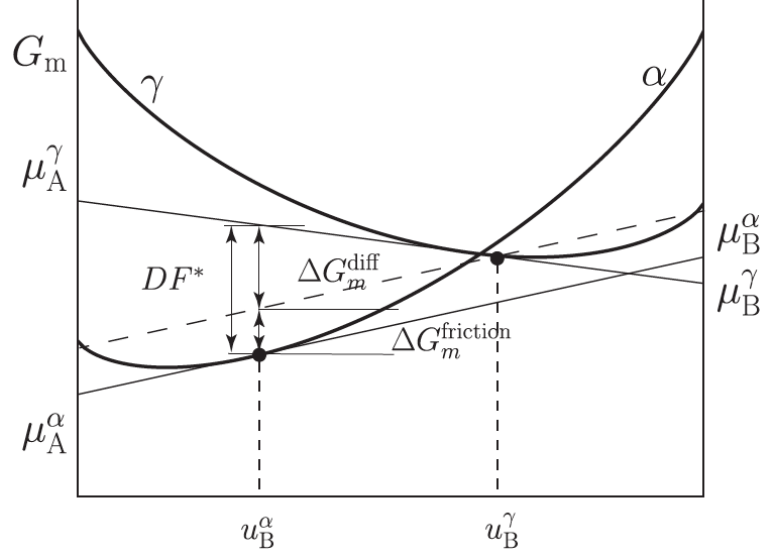


Figure 2.1: Additive contributions to the dissipation of the driving force at a moving α/γ interface with concentrations u_B^α and u_B^γ in an A-B binary alloy.

Using Eq. (2.10) to approximate the fluxes, Eq. (2.19) reads in vector notation:

$$\Delta G_m^{\text{diff}} = -\frac{V_m}{v \delta^*} (\tilde{\mathbf{L}}^\gamma \cdot \Delta \Phi) \cdot \Delta \Phi \quad (2.20)$$

where we have assumed constant mobilities within the interface, i.e. $\tilde{\mathbf{L}}(x) = \tilde{\mathbf{L}}^\gamma$. Neglecting cross mobilities leads to a simple expression for the dissipation by trans-interface diffusion (written for Fe-C-X):

$$\Delta G_m^{\text{diff}} = \frac{V_m}{v \delta^*} [L_{CC}^\gamma \Delta \Phi_C^2 + L_{XX}^\gamma \Delta \Phi_X^2] \quad (2.21)$$

Dissipation by interface friction

The change of crystalline lattice from parent to product phase is often referred to as interface friction. This cannot be an infinitely fast process and in some cases like massive transformations, it has been proposed to be the limiting kinetic factor (e.g. [110]). In such cases, the interface motion is then termed as interface controlled as opposed to diffusion controlled. In interface controlled transformations, the interface velocity is observed to be constant in isothermal

conditions, and related to some driving force involving the Gibbs energies of the parent and product phases. Specific relationships depend on the real mechanisms at the atomic scale which proceed at the interface, e.g. either involving diffusion-like atomic jumps, or involving lateral movements of growth ledges [31, 44]. The model proposed by Turnbull [153] for the migration of grain boundaries is generally adopted for its simplicity and the few parameters to be determined indirectly from experimental kinetics. It assumes that the grain boundary is a disordered region which migrates by uncoordinated atomic jumps described by the absolute rate theory [104]. If the difference in Gibbs energy between both sides of the interface is small with respect to thermal fluctuations, a linear relationship holds between the rate of migration and the driving force (corresponding to $\Delta G_m^{\text{friction}}$ if it is the only source of dissipation):

$$v = \frac{M}{V_m} \Delta G_m^{\text{friction}} \quad (2.22)$$

where M is the interface mobility (in $\text{m}^4/\text{J}/\text{s}$) which generally depends on temperature. If the absolute reaction rate really applies to the process, M follows an Arrhenius law $M = M_0 \exp(-Q/RT)$, with Q the activation energy for the migration.

In composition invariant transformations, it is obvious that $\Delta G_m^{\text{friction}} = G_m^\gamma(\mathbf{u}^0) - G_m^\alpha(\mathbf{u}^0)$ where \mathbf{u}^0 is the nominal composition of the alloy. When there is some partition between α and γ as shown in Fig. 2.1, the Gibbs energy per mole of substitutional elements corresponding to α with the same composition as the parent γ phase is:

$$G_m^\alpha = \sum_{i=1}^n u_i^\gamma \mu_i^\alpha(\mathbf{u}^\alpha) \quad (2.23)$$

Hence, in Fig. 2.1, $\Delta G_m^{\text{friction}}$ is the vertical distance between the dot corresponding to γ and the tangent to G_m^α . Shifting this tangent up to the dot for γ gives the dashed line which splits the driving force DF^* into ΔG_m^{diff} and G_m^{friction} .

2.1.2 Coupling with the bulks

The system of n non linear equations (2.16) and (2.12) for the $2n - 1$ variables $(u_i^\alpha, u_i^\gamma, v)$ derived in the previous section must be supplied with $n - 1$ equations, as already noted in [127]. Those equations are given by the $n - 1$ solute balances at the interface where the fluxes in α and γ at the boundaries of the thick interface ensure the coupling with the bulks:

$$(u_i^\gamma - u_i^\alpha) v = - \sum_{j=1}^{n-1} D_{ij}^\gamma \nabla u_j |^\gamma \cdot \vec{n} + \sum_{j=1}^{n-1} D_{ij}^\alpha \nabla u_j |^\alpha \cdot \vec{n} \quad (2.24)$$

where $|^\psi$ indicates that the gradient is in the bulk phase $\psi = \alpha, \gamma$ at the interface, \vec{n} is the normal to the interface pointing from α to γ , and D_{ij}^ψ is the matrix of diffusivities in bulk ψ ¹.

Instead of relying on a numerical method to compute the concentration profiles and determine the fluxes as in e.g. [67] or [35], we have chosen to use analytical solutions derived for the growth of self-preserving shapes. This is the reason why the solute balances (2.24) have not been expressed using the diffusion potentials like in the interface. The analytical solutions obtained in the seminal works of Zener [163], Frank [60] and Horvay & Cahn [83] (see also [27, 69]) rely on the following simplifying assumptions:

- (i) γ is semi-infinite or infinite;
- (ii) D_{ij}^γ is constant;
- (iii) there is no diffusion in α (either $D_{ij}^\alpha = 0$ or $\nabla u_i |^\alpha = 0$);
- (iv) the γ side of the interface is an iso-concentration, i.e. any variations induced by curvature or elasticity are neglected.

To fulfill these conditions, we have considered constant diffusivities D_i^γ , neglecting cross terms for simplicity (i.e. $D_i^\gamma = D_{ii}^\gamma$ and $D_{ij}^\gamma = 0$ for $i \neq j$), and we have assumed that $\nabla u_i |^\alpha = 0$. Hence, Eqs. (2.24) becomes:

$$v = \frac{D_i^\gamma}{\Delta_i} \Omega_i \quad (2.25)$$

¹ It must be noted that the vector notation has been used to indicate real space vectors, instead of vectors of unknowns as in the previous sections

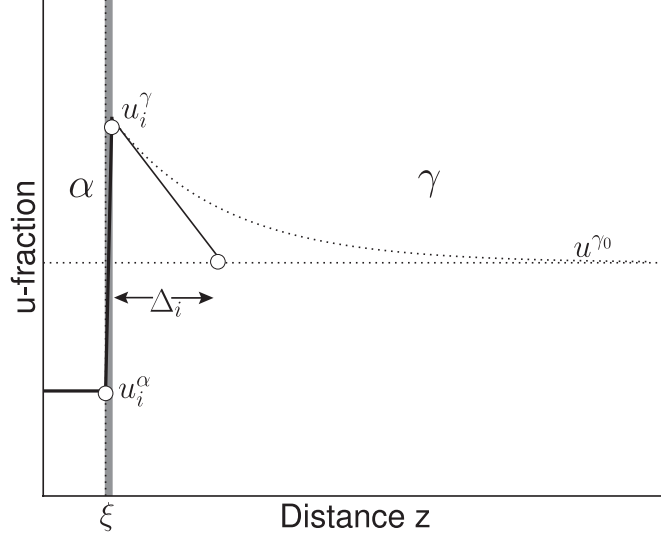


Figure 2.2: Schematic concentration profile during the growth of α in γ .

where (i) we have introduced the characteristics diffusion lengths Δ_i , as illustrated in Fig. 2.2:

$$\nabla u_i|^\gamma \cdot \vec{n} = \frac{u_i^{\gamma 0} - u_i^\gamma}{\Delta_i} \quad (2.26)$$

with $u_i^{\gamma 0}$ the concentration of the γ phase far from the interface (corresponding to the nominal concentration for an infinite γ matrix); and where (ii) we have introduced the supersaturations in the γ matrix $\Omega_i = (u_i^\gamma - u_i^{\gamma 0}) / (u_i^\gamma - u_i^\alpha)$.

For all shape preserving diffusion controlled growth, Δ_i is solution of a nonlinear equation involving the supersaturation Ω_i and exponential integrals of the Péclet number $Pe_i = v\xi/D_i^\gamma$ where ξ is the interface position [27]. For a planar interface, Zener [162] has proposed an approximate solution much simpler, based on a solute balance and a linear profile in γ , which fits very well the real solution:

$$\Delta_i = 2\xi \frac{1 - \Omega_i}{\Omega_i} \quad (2.27)$$

When $\Omega_i \rightarrow 0$, i.e. when approaching equilibrium, $\Delta_i \rightarrow \infty$ corresponding to a flat concentration profile and no interface movement. When $\Omega_i \rightarrow 1$, i.e. when the supersaturated γ matrix falls on the $\alpha/\alpha + \gamma$ boundary, $\Delta_i \rightarrow 0$ corresponding to a steep profile and a velocity going to infinity.

2.1.3 Governing equations

The full system of $2n - 1$ nonlinear equations necessary to find the interfacial concentrations and the interface velocity (entering the vector of unknowns \mathbf{Y}) is thus composed of Eqs. (2.12), (2.16) and (2.22):

$$\begin{cases} \Delta\Phi + \underline{\mathbf{P}} \cdot \Delta\mathbf{u} = 0 \\ V_m (\underline{\mathbf{P}}^{-1} \cdot \Delta\Phi) \cdot \Delta\Phi + \frac{V_m v}{M} - \underline{\mathbf{u}}^\alpha \cdot \underline{\Delta\mu} = 0 \\ v - \underline{\mathbf{D}}^\gamma \cdot \underline{\Omega}' = 0 \end{cases} \quad (2.28)$$

where we have introduced matrix $\underline{\mathbf{P}} = v\delta^* \underline{\mathbf{L}}^{\gamma-1}$ and vector $\underline{\Omega}' = (\Omega_i/\Delta_i)$, and where element n in vector $\underline{\mathbf{u}}^\alpha$ can easily be expressed with the other elements using the definition of u -fractions. The Calphad description of the Gibbs energies with the Compound Energy approach in §1 has been used for the chemical potentials and diffusion potentials. u -fractions are thus expressed with site fractions \mathbf{y}^α and \mathbf{y}^γ which are the quantities used together with v in the vector of unknowns¹. Because there are $2(n + 1)$ site fractions instead of $2(n - 1)$ u -fractions (y_{ref} and y_{va} for each phases are the 4 additional quantities), Eqs. (2.28) must be supplied with the four constraints on site fractions Eqs. (1.17).

2.1.3.1 Limit cases

Local equilibrium (LE)

Models assuming local equilibrium at the interface are easily recovered by the thick interface model as a limit case. Indeed, considering that $\underline{\mathbf{P}} \rightarrow 0^2$, Eq. (2.28)₁ can be replaced by $\Delta\Phi = 0$. Moreover, the first term in Eq. (2.28)₂ tends also to 0, since the numerator tends to 0 as v^2 when the denominator tends to 0 as v . Assuming that $M \rightarrow \infty$, Eqs. (2.28) reduce to the same nonlinear system as

¹ It is worth stressing that there is no ambiguity in substituting u -fractions to site fractions in the case of α and γ in Fe-C-X alloys.

² Equivalent to assume that growth rate is much slower than diffusion rates of all species.

in [119]:

$$\begin{cases} \Delta\Phi_i = 0 & i = 1, n-1 \\ \Delta\mu_n = 0 \\ v = D_i^\gamma \Omega'_i & i = 1, n-1 \end{cases} \quad (2.29)$$

where s and t are respectively for substitutional and interstitial lattices. It can be noted that the equilibrium conditions of equal chemical potentials in α and γ are the same as in Eqs. (1.39) except that the solute balances are local here, instead of global. However, both types of balance have similar mathematical shapes because they both involve the remaining variable, either v or f_α , linearly. Hence, we have taken advantage of this similarity for implementing the numerical resolution of Eqs. (2.29).

Paraequilibrium (PE)

Paraequilibrium can also easily be recovered as a particular case of Eqs. (2.28). To proceed in a more transparent way, we specialize Eqs. (2.28) to Fe-C-X alloys with simplifying assumptions used in Eqs. (2.13) and (2.21):

$$\begin{cases} \Delta\Phi_C + P_C \Delta u_C = 0 \\ \Delta\Phi_X + P_X \Delta u_X = 0 \\ V_m \left(\frac{\Delta\Phi_C^2}{P_C} + \frac{\Delta\Phi_X^2}{P_X} \right) + \frac{V_m v}{M} - (u_{\text{Fe}}^\alpha \Delta\mu_{\text{Fe}} + u_X^\alpha \Delta\mu_X + u_C^\alpha \Delta\mu_C) = 0 \\ v - D_C^\gamma \Omega'_C = 0 \end{cases} \quad (2.30)$$

where $P_i = v\delta^*/L_{ii}$ ($i = \text{C}, \text{X}$).

Setting $P_C \rightarrow 0$ and $P_X \rightarrow \infty$, and assuming that $M \rightarrow \infty$, one obtains:

$$\begin{cases} \Delta\Phi_C = 0 \\ \Delta u_X = 0 \\ u_{\text{Fe}}^\alpha \Delta\mu_{\text{Fe}} + u_X^\alpha \Delta\mu_X = 0 \\ v - D_C^\gamma \Omega'_C = 0 \end{cases} \quad (2.31)$$

where we have used the fact that $\Delta u_X = 0$ implies $\Delta u_{\text{Fe}} = 0$, and where $u_{\text{Fe}}^\alpha =$

$$u_{\text{Fe}}^\gamma = u_{\text{Fe}} \text{ and } u_{\text{X}}^\alpha = u_{\text{X}}^\gamma = u_{\text{X}}.$$

Mixed mode

Considering $\tilde{P} \rightarrow 0$ as for full equilibrium but keeping a finite interface mobility M , the mixed-mode model of Sietsma and van der Zwaag [144] can be recovered for a binary alloy (concentrations in that case are for the solute element, e.g. C). Indeed, $\Delta\Phi_{\text{C}} = 0$ implies that the tangents to G_{m}^α and G_{m}^γ at the interfacial concentrations, respectively u^α and u^γ , are parallel. In that case, the dashed line would merge with the tangent to G_{m}^α in Fig. 2.1, and the driving force is just the vertical distance between the parallel tangents: $DF^* = \mu_{\text{Fe}}^\gamma(u^\gamma) - \mu_{\text{Fe}}^\alpha(u^\alpha)$. The nonlinear system (2.28) becomes:

$$\begin{cases} \Phi_{\text{C}}^\gamma(u^\gamma) - \Phi_{\text{C}}^\alpha(u^\alpha) = 0 \\ \mu_{\text{Fe}}^\gamma(u^\gamma) - \mu_{\text{Fe}}^\alpha(u^\alpha) = \frac{V_{\text{m}} v}{M} \\ v = D^\gamma \Omega / \Delta \end{cases} \quad (2.32)$$

Expanding the chemical potentials with respect to the concentrations around their equilibrium values (indicated by eq in the sequel) gives:

$$\begin{cases} \frac{\partial\Phi_{\text{C}}^\gamma}{\partial u} \Big|_{\text{eq}} du^\gamma - \frac{\partial\Phi_{\text{C}}^\alpha}{\partial u} \Big|_{\text{eq}} du^\alpha = 0 \\ \left(\frac{\partial\mu_{\text{Fe}}^\gamma}{\partial u} \Big|_{\text{eq}} - \frac{\partial\mu_{\text{Fe}}^\alpha}{\partial u} \Big|_{\text{eq}} \frac{\partial\Phi^\gamma/\partial u|_{\text{eq}}}{\partial\Phi^\alpha/\partial u|_{\text{eq}}} \right) du^\gamma = \frac{V_{\text{m}} v}{M} \end{cases} \quad (2.33)$$

Where the equilibrium condition $\mu_{\text{C}}^\alpha(u_{\text{eq}}^\alpha) = \mu_{\text{C}}^\gamma(u_{\text{eq}}^\gamma)$ has been used.

Assuming that α is stoichiometric ($u^\alpha = u_{\text{eq}}^\alpha$) $\partial\Phi^\alpha/\partial u|_{\text{eq}} \rightarrow \infty$ and the balance of Gibbs energy Eq. (2.33)₂ becomes:

$$\frac{\partial\mu_{\text{Fe}}^\gamma}{\partial u} \Big|_{\text{eq}} du^\gamma = \frac{vV_{\text{m}}}{M} \quad (2.34)$$

which is exactly Eq. (3) in [144] with $\chi = \partial\mu_{\text{Fe}}^\gamma/\partial u|_{\text{eq}} \times 1/V_{\text{m}}$ and $du^\gamma = u^\gamma - u_{\text{eq}}^\gamma$.

Hence:

$$\begin{cases} v = M \chi (u^\gamma - u_{\text{eq}}^\gamma) \\ v = \frac{D^\gamma}{2\xi} \frac{\Omega^2}{1 - \Omega} \end{cases} \quad (2.35)$$

where the Zener approximation Eq. (2.27) of the diffusion length has been used in the solute balance Eq. (2.32)₃. Using the definition of supersaturation, $u^\gamma = (u^{\gamma 0} - u^\alpha \Omega)/(1 - \Omega)$ which can be substituted into Eq. (2.35)₁. Combining the resulting equation and (2.35)₂ gives a simple quadratic equation in Ω :

$$Z \Omega^2 - (u_{\text{eq}}^\gamma - u^\alpha) \Omega + (u_{\text{eq}}^\gamma - u^{\gamma 0}) = 0 \quad (2.36)$$

where $Z = 2\xi M \chi / D$ [144].

2.1.3.2 Data

The thermodynamic data entering the Calphad description have been retrieved from the non-encrypted *FEDAT* database. As well, the bulk diffusion coefficients in ferrite and austenite phases have been obtained with the mobilities in the *MOBFE1* database of DICTRA, see Tab. D.2 in Appendix D

Values for the quantities in interface are much more difficult to assess. First, the interface thickness has been assumed to be a few atomic distances, e.g. $\delta^* = 1$ nm. Because C is a very fast diffusing species in both α and γ which normally features local equilibrium at interfaces, we have chosen $D_C^{\gamma*} = D_C^\alpha$. Concerning the interfacial diffusivities $D_X^{\gamma*}$ of substitutional elements X, they have been taken as free parameters to investigate their influence on the growth kinetics regime. A similar methodology has been applied in [155] using the phase field model discussed in §3, but changing the interface thickness instead of the interfacial diffusivities.

Finally, when a finite interface mobility M is accounted for, the value suggested by Hillert [71] for steels has been used: $M = 0.035 \exp(-17700/T)$ in $\text{m}^4/\text{J/s}$ (with T the absolute temperature).

2.2 Massive transformation in Fe-Ni alloys

In Fe-Ni alloys, if austenite is quenched down to sufficiently low temperatures, but still above the martensite start temperature M_s , it will be decomposed by a massive transformation that yields to a characteristic blocky or massive microstructure. The massive transformation is partitionless like the martensitic transformation, i.e. it does not involve any composition change of the bulk phases, and thus long-range diffusion is unnecessary. Massive ferrite grows at a constant rate that is more or less independent of crystallographic orientation relationships, as opposed to martensite. A partitionless transformation $\gamma \rightarrow \alpha$ is thermodynamically possible only below T_0 temperature, at which α and γ have the same composition and the same Gibbs energy. However, at what temperature the massive transformation really becomes kinetically possible has been a matter of considerable controversy over the years. It may be argued that if the interfacial reactions of the migrating α/γ interface are rapid enough the interface will be in local thermodynamic equilibrium. In that case the transition to a massive mode of transformation would occur when the undercooling is so large that the composition of the parent γ phase falls on the $\alpha/\alpha + \gamma$ boundary in the binary Fe-X phase diagram. On the other hand it has been claimed that the massive transformation may occur far inside the $\alpha + \gamma$ two-phase field. As already explained thoroughly in [75], this can be achieved only if the interactions between solutes and the migrating phase interface are accounted for, as done in the model of Odqvist [127].

Since the model presented in this chapter is very similar to this model, it should also be able to predict such kind of transformation. Moreover, it is worth stressing that there are two major benefits for starting with a binary system. First, the solution of the nonlinear system is straightforward by means of conventional algorithms such as Newton-Raphson. Second, the results are more transparent and will make easier the understanding of the following section on Fe-C-X alloys.

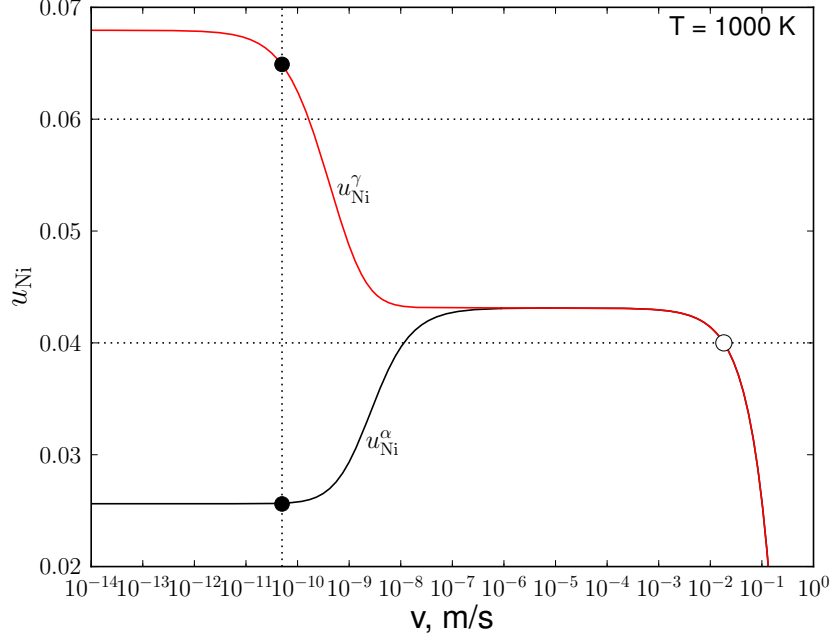


Figure 2.3: Interfacial concentrations versus growth rate in Fe-Ni at 727°C.

In the sequel, the calculations have been performed assuming a ratio $D_{\text{Ni}}^{\gamma^*}/D_{\text{Ni}}^{\gamma} = 10^4$, which has given the best results with respect to experiments, as discussed at the end of the section.

First, a series of calculations have been performed at $T = 727$ °C solving only Eqs. (2.28)_{1,2} with prescribed growth rates v so as to investigate the conditions for partitionless growth. In Fig. 2.3 the interface compositions u_{Ni}^{α} and u_{Ni}^{γ} are plotted vs. v respectively in black and red. For $v \lesssim 10^{-7}$ m/s the interfacial concentration exhibits a jump, i.e. $u_{\text{Ni}}^{\alpha} \neq u_{\text{Ni}}^{\gamma}$. For $v \gtrsim 10^{-7}$ m/s the transformation would be partitionless since $u_{\text{Ni}}^{\alpha} = u_{\text{Ni}}^{\gamma}$. Moreover, as $v \rightarrow \mathcal{O}(1$ m/s) the partitionless transformation exhibits a strong decrease of the interfacial concentrations with v . It is clear that for $u_{\text{Ni}}^0 \leq 0.043$, where 0.043 is the concentration corresponding to the plateau where u_{Ni}^{α} and u_{Ni}^{γ} are joining, a partitionless transformation is possible.

In order to illustrate the role played by the dissipation processes entering the Gibbs energy balance in the determination of the interfacial concentrations, Eqs. (2.28)_{1,3} have been solved with prescribed growth rates v and for a given ferrite

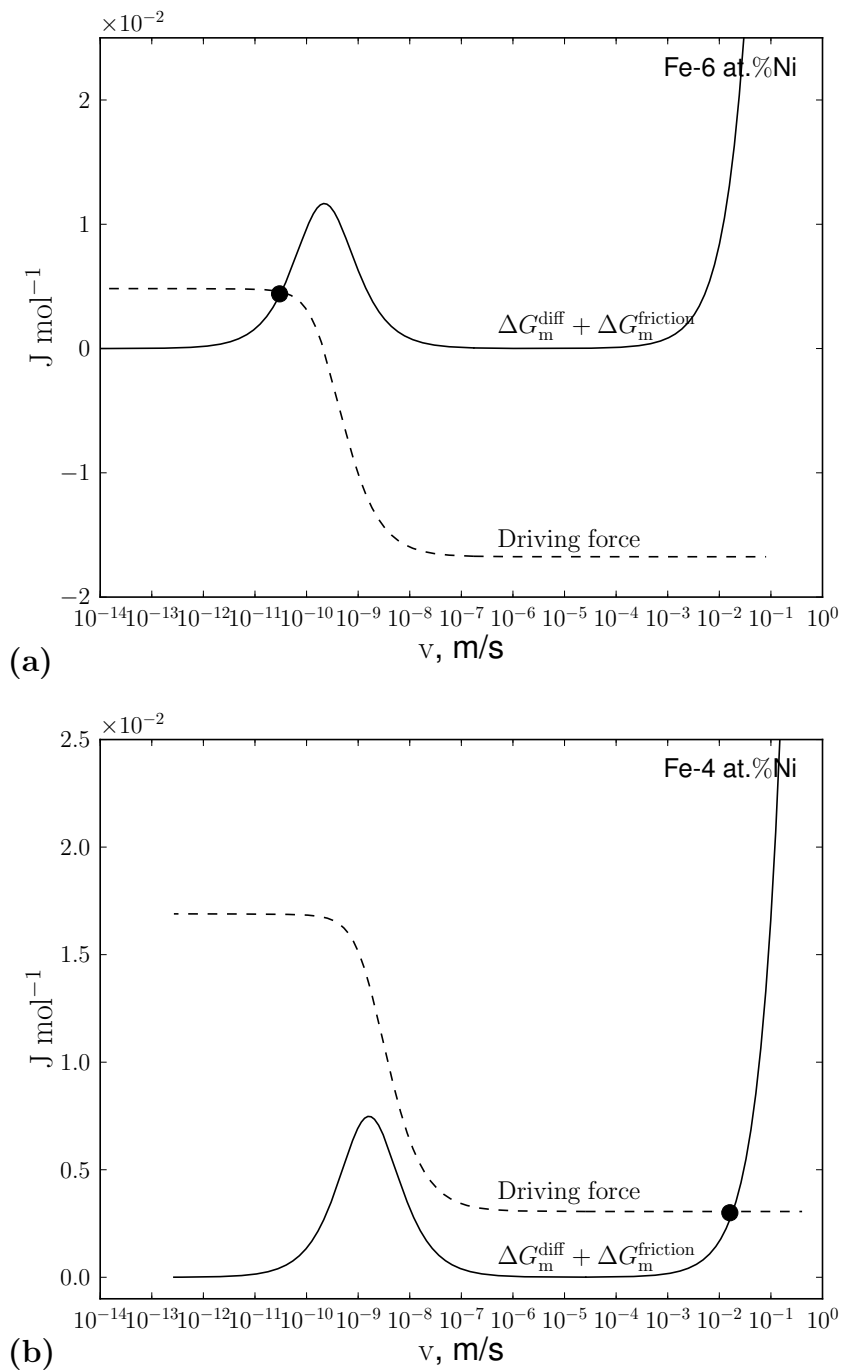


Figure 2.4: Dissipation of Gibbs energy (continuous line) and driving force (dashed line) in (a) Fe-6 at.%Ni and (b) Fe-4 at.%Ni at 727°C.

thickness $\xi = 10$ nm. Two alloys have been considered: (i) a first one with $u_{\text{Ni}}^0 = 0.06 > 0.043$, i.e. above the plateau in Fig. 2.3; (ii) a second one with $u_{\text{Ni}}^0 = 0.04 < 0.043$, i.e. below the plateau, where it has been claimed that a partitionless transformation is possible.

In Fig. 2.4a, the total dissipation $\Delta G_{\text{m}}^{\text{friction}} + \Delta G_{\text{m}}^{\text{diff}}$ is plotted with a continuous line whereas the driving force is plotted with a dashed line for alloy (i). The driving force is larger than 0 for velocities larger than ~ 1 nm/s and drops suddenly below 0 between 1 nm/s and 100 nm/s. The total dissipation tends to 0 when v tends to 0. Between 0.1 nm/s and 100 nm/s the total dissipation exhibits a bump with a maximum around 1 nm/s, caused mainly by $\Delta G_{\text{m}}^{\text{diff}}$. Then, it drops to 0 before starting to increase quickly at large velocities due to $\Delta G_{\text{m}}^{\text{friction}}$. The black dot indicates the location where curves are crossing: it corresponds to the Gibbs energy balance Eq. (2.28)₂. For that particular alloy and the chosen ferrite thickness ξ , the driving force is balanced by the dissipation at the beginning of the bump due to solute drag. It corresponds to the partitioning transformation indicated by the black dots in Fig. 2.3. As ξ increases, the curve for the driving force shifts down with respect to the total dissipation. For large precipitates, both curves cross at smaller growth rates and the corresponding interfacial concentrations get closer to equilibrium concentrations. Thus, it is clear that the $\gamma \rightarrow \alpha$ transformation cannot be partitionless in alloy (i) at 727°C. In Fig. 2.4b, the same analysis is carried out for alloy (ii). The driving force (dashed line) exhibits the same step shape but it remains always positive. As well, the total dissipation features a bump at velocities between 0.1 nm/s and 100 nm/s due to the trans-interface diffusion, and a steep increase at high velocities due to the friction term. Contrary to the previous case, both curves cross at the black dot located on the increasing branch of the dissipation. It corresponds to the partitionless transformation indicated by the white dot in Fig. 2.3. As ξ increases, the curve for the driving force shifts down with respect to the dissipation curve. The Gibbs energy balance (black dot) shifts to the left at lower growth rates. The transformation remains partitionless as long as the black dot has not reached the bump due to the trans-interface diffusion. This occurs at very large thicknesses in alloy (ii) at 727°C, and the $\gamma \rightarrow \alpha$ transformation is partitionless. It is worth noting that without the dissipation associated with friction (increasing branch

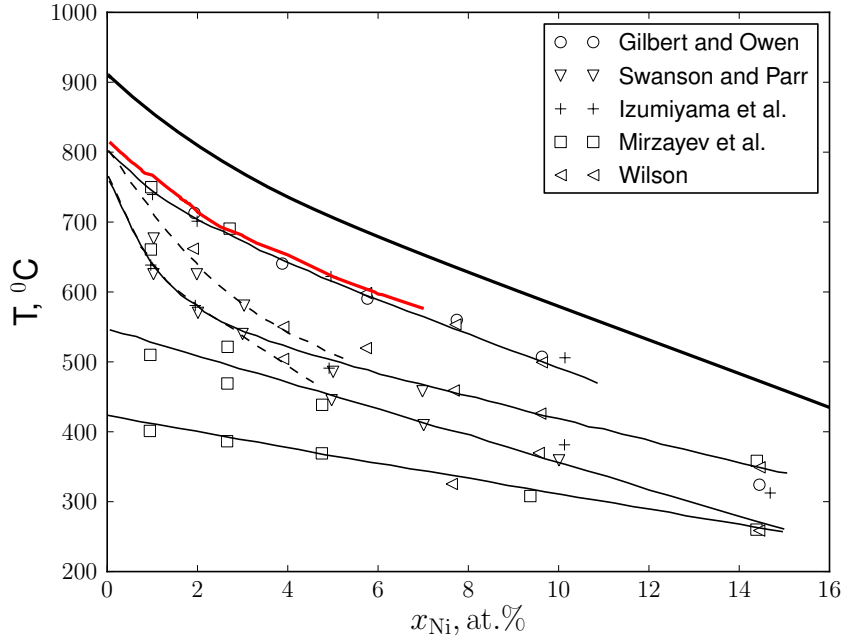


Figure 2.5: Start temperatures (symbols) of various partitionless transformations in the Fe-Ni system: Gillbert and Owen [64], Swanson and Parr [150], Izumiya et al. [92], Mirzayev et al. [116], Wilson [159]. Limit for massive transformation calculated with the present model (red line). T_0 temperature (thick black line).

at high growth rates), there is no solution for thicknesses smaller than a critical value when both curves cross.

Calculations similar to those presented above at $T = 727^\circ\text{C}$ have been performed at different temperatures ($T \in [600^\circ\text{C}; 800^\circ\text{C}]$) to determine the upper limit of the concentration range where partitionless transformations are possible (i.e. the plateau in Fig. 2.3). All results have been plotted with a red line in the Fe-Ni phase diagram in Fig. 2.5. In the same figure, experimental measurements of partitionless transformations determined from rapid cooling experiments [64, 92, 116, 150, 159] have also been plotted with symbols. They all lie well below the T_0 temperature (thick black line). The lower curves correspond to martensite whereas only the upper curve is associated with massive ferrite. The calculations match the measurements at the upper temperatures, deep inside the binary $\alpha + \gamma$ field. It is worth stressing that this agreement would have

not been achieved (i) if the dissipation due to the trans-interface diffusion had been neglected, and (ii) with a different ratio $D_{\text{Ni}}^{\gamma^*}/D_{\text{Ni}}^{\gamma}$. Indeed, a smaller ratio predicts a limit to partitionless transformations at lower temperatures. On the contrary, a larger ratio gives a limit much closer to T_0 . Hence, provided that the ratio $D_{\text{Ni}}^{\gamma^*}/D_{\text{Ni}}^{\gamma}$ is judiciously selected, a good description of partitionless transformations can be obtained.

2.3 Fe-C-X alloys

Most steels of practical importance contain not only C. Other alloying elements are generally substitutional and modify drastically the $\gamma \rightarrow \alpha$ kinetics, as already mentioned. In that case, the essential difference with the previous section is the concomitant presence of fast diffusing C and a slow diffusing substitutional element X¹. Indeed, this very difference induces different growth regimes with transitions which still remain puzzling and, up to now, difficult to fully rationalize with a single model.

In this section, we will first recall the limit cases, i.e. local full equilibrium and paraequilibrium, which have been proposed very early to predict the kinetics in different Fe-C-X alloys (§2.3.1). These models will serve as a basis in all the discussions concerning the subsequent results of our model. Then, we will discuss shortly some experimental evidences of deviations from the limit cases (§2.3.2), before justifying our choice for a particular ternary system (§2.3.3). Because $D_C \gg D_X$, Eqs. (2.28) are very stiff in many cases: algorithms have thus been developed specifically to handle ternary Fe-C-X systems, which will be presented in §2.3.4 together with their analysis. We will discuss first the different growth regimes in a Fe-C-Ni alloy predicted by our model (§2.3.5); second the predictions concerning the isothermal growth at 700°C of ferrite in different Fe-C-Ni alloys (§2.3.6). We will conclude this section with a summary of the main results together with a short discussion (§2.3.7).

¹ Only replacing Ni by C does not change the analysis of §2.2 (e.g. [93, 107]): massive transformations have indeed been observed in Fe-C either for $\delta \rightarrow \gamma$ [161] or $\gamma \rightarrow \alpha$ [106].

2.3.1 Limit cases

As stated in the introduction, the first models applied to the diffusion controlled $\gamma \rightarrow \alpha$ transformation in ternary Fe-C-X steels rely either on the assumption of full local equilibrium at the interface (orthoequilibrium) [46, 47, 48, 135, 138], or on partial equilibrium for C and non-partitioning for X (paraequilibrium) [86]. Before investigating general non-equilibrium conditions with our model, it is useful to recall the particular features associated with those limit cases, which can easily be recovered by our model as particular cases (§2.1.3).

Local equilibrium (Orthoequilibrium)

Contrary to the case of binary alloys where the interfacial concentrations depend only on temperature and can be trivially retrieved from the phase diagram¹, in multi-component systems the interfacial tie-line, called operative, does not match generally the final equilibrium tie-line passing through the nominal composition as imposed by the overall solute balances Eq. (1.39)₅. By contrast, it is the solute balances at the interface involving the interface velocity v , Eq. (2.28)₃ that determine the operative tie-line. To find the operative tie-line among all the equilibrium tie-lines (given by Eqs. (1.34)) for a given nominal composition, one can proceed as proposed by Coates [46] or Dehoff [52]. Assuming that growth is shape-preserving in an infinite matrix (nominal composition reduces to the matrix composition), and provided that diffusivities are constant without cross terms ($D_{CX}^\gamma = 0$), the concentrations at the interface remain constant during growth. Recall that the solute balances at interface reads:

$$\begin{cases} v = D_C^\gamma \frac{\Omega_C}{\Delta(\Omega_C)} \\ v = D_{Mn}^\gamma \frac{\Omega_X}{\Delta(\Omega_X)} \end{cases} \quad (2.37)$$

¹ neglecting the Gibbs-Thomson effect and elasticity.

where the dependencies of the diffusion lengths with respect to supersaturations have been explicitly stated. Or, introducing the Péclet numbers $\mathcal{P}e_i = v\xi/D_i^\gamma$:

$$\begin{cases} \mathcal{P}e_C = \mathcal{F}(\Omega_C) \\ \mathcal{P}e_X = \mathcal{F}(\Omega_X) \end{cases} \quad (2.38)$$

where \mathcal{F} is a function depending on the particular shape of the growing precipitate. Because both Eq. (2.38)₁ and Eq. (2.38)₂ involve the same velocity and size, the following equality must hold:

$$D_X^\gamma \mathcal{P}e_X = D_C^\gamma \mathcal{P}e_C \quad (2.39)$$

Using Eqs. (2.38) above:

$$D_C^\gamma \mathcal{F}(\Omega_C) = D_X^\gamma \mathcal{F}(\Omega_X) \quad (2.40)$$

where \mathcal{F} can be inverted to explicit the supersaturations in X in γ :

$$\Omega_X = \mathcal{F}^{-1}(1/r \mathcal{F}(\Omega_C)) \quad (2.41)$$

where $r = D_X^\gamma/D_C^\gamma$. For a planar precipitate \mathcal{F}^{-1} is defined as follows [60]:

$$\mathcal{F}^{-1}(\mathcal{P}e) = \sqrt{\pi\mathcal{P}e} \exp(\mathcal{P}e) \operatorname{erfc}(\sqrt{\mathcal{P}e}) \quad (2.42)$$

In Fig. 2.6, the relationship between Ω_C and Ω_X given by Eq. (2.41) together with Eq. (2.42) has been plotted for different ratios r . The corresponding curves have been called Interface Composition contours or IC contours by Coates [46, 47] for reasons explained below. When $r = 1$, $\Omega_C = \Omega_X$ and the operative tie-line is the final equilibrium tie-line. When $r \rightarrow 0$, corresponding to the relevant case in Fe-C-X steels, the relation between both supersaturations features two branches corresponding to two growth regimes as discussed below: a steep increase of Ω_X at $\Omega_C \approx 0$ (vertical branch); an horizontal branch at $\Omega_X = 1$.

The IC contours can be reported on each tie-line in an isothermal section of the Fe-C-X diagram, as illustrated schematically in Fig. 2.7 for a γ -stabilizer substitutional element. Because $r \approx 10^{-6}$ (C is interstitial and X is substitutional) the

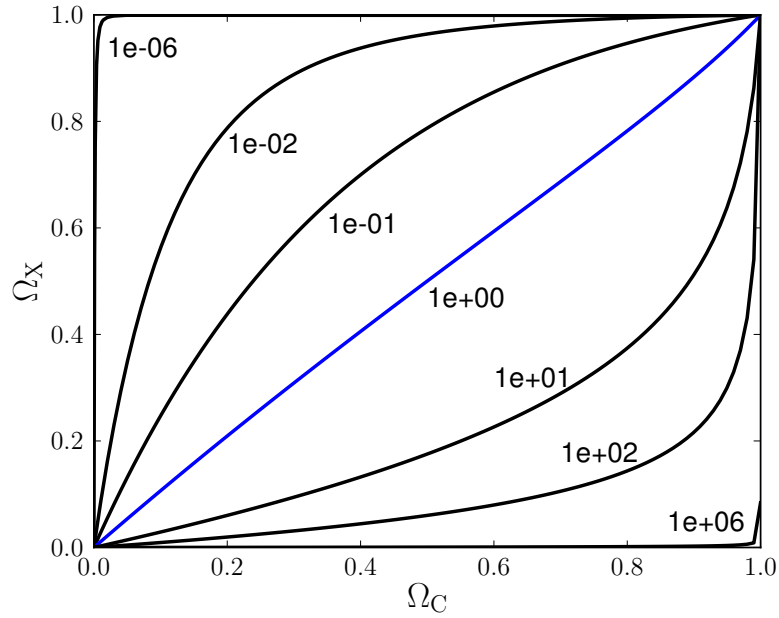


Figure 2.6: Supersaturation in X vs. supersaturation in C for various D_X^γ/D_C^γ ratios for a planar ferrite precipitate.

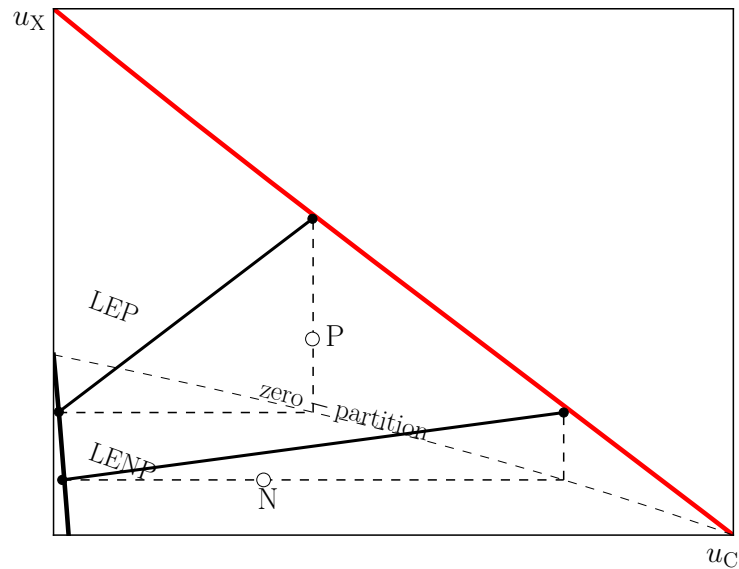


Figure 2.7: Isothermal section of a schematic Fe-C-X phase diagram with solubility limits of α (thick black) and of γ (red). Tie-lines (thin black) with IC contours (dashed), and zero-partition line (dashed).

IC contours (dashed) make right-angled triangles with the tie-lines (continuous line). All nominal compositions belonging to a given IC contour correspond to the same operative tie-line. It must be noted that the growth rates are however different along the IC contours, ranging from ∞ on the α boundary to 0 on the γ boundary. A line passing through the right angles of all the IC contours, called zero-partition line, split the $\alpha + \gamma$ two-phase field into two domains. (i) The upper domain above the zero-partition line contains the vertical branches of the IC contours and is called LEP for Local Equilibrium Partitioning. (ii) The lower domain below the zero-partition line contains the horizontal branches of the IC contours and is called LENP for Local Equilibrium Non Partitioning.

To illustrate the difference between the two domains, we have considered two particular alloys with nominal compositions P and N in Fig. 2.7. Profiles of C and X for both alloys are superimposed to the ternary section in Fig. 2.8. For alloy P in the LEP domain, both C and X partition between α and γ . The profile of C is flat in γ whereas the profile of X exhibits a gradient. Growth is thus controlled by diffusion of X and proceeds slowly. For alloy N in the LENP domain, C is still partitioning between α and γ . However, this is not the case for X: content of bulk γ in X is the same as content of bulk α , despite a spike in X pushed ahead the interface. Growth is controlled by C diffusion and is much faster than in LEP domain.

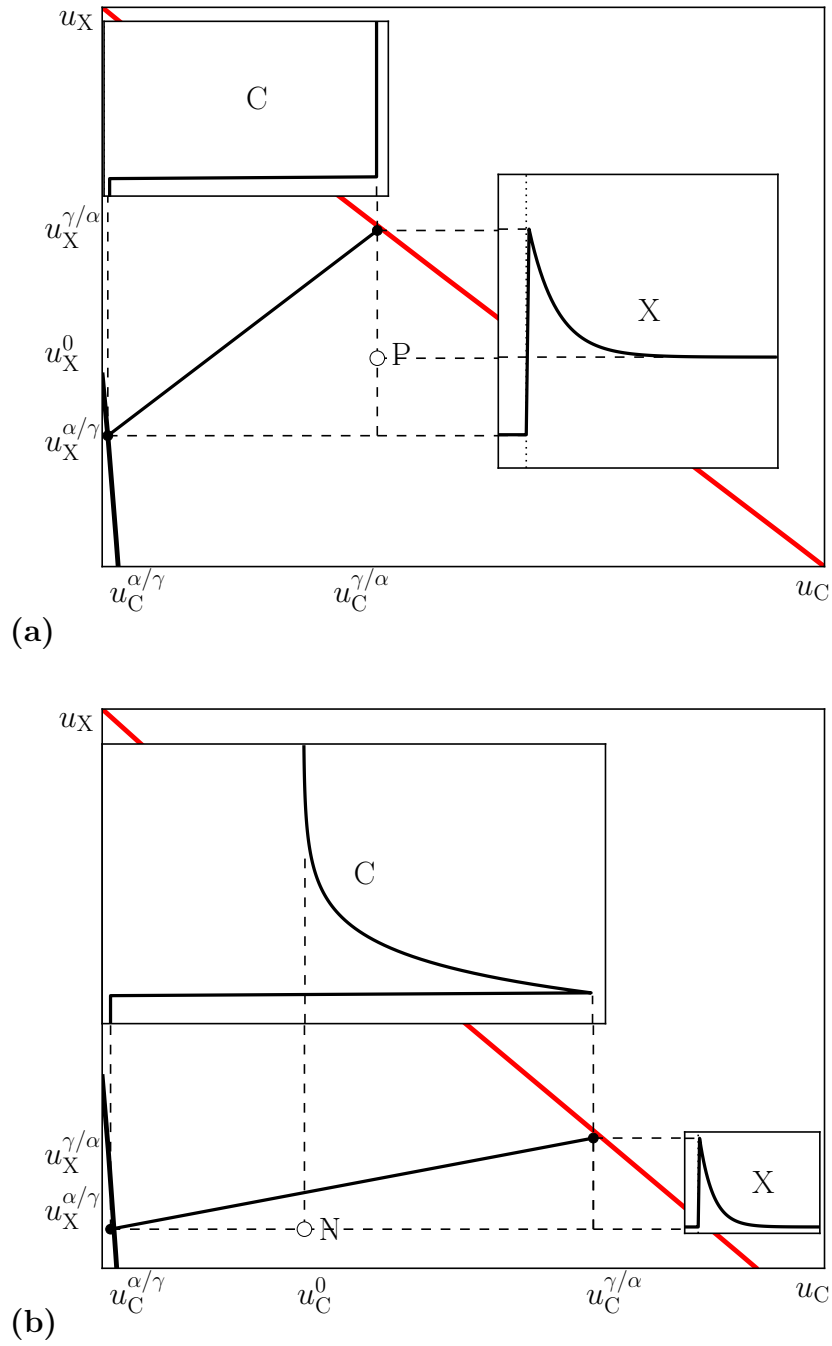


Figure 2.8: Isothermal sections of a schematic Fe-C-X phase diagram with C and X profiles: (a) for alloy P in the LEP domain; (b) for alloy N in the LENP domain.

Paraequilibrium

Under paraequilibrium (PE), local equilibrium is established only for C and the substitutional elements X are assumed to remain frozen. This partial equilibrium expressed by Eqs. (2.31)_{1,2} defines a pseudo phase diagram (paraequilibrium diagram) with horizontal tie-lines in isothermal sections, as shown in Fig. 2.9. It can be shown [72] that the boundaries of the paraequilibrium diagram are located within the $\alpha + \gamma$ two-phase field, joining the T_0 line on the Fe-X binary to the equilibrium binary Fe-C diagram (grey region in Fig. 2.9). Growth under paraequilibrium is a fast process because it is controlled by C diffusion only. When X is a γ -stabilizer element, paraequilibrium is generally faster than LENP [59]. Moreover, it is worth noting that LENP (below the zero-partition line) and paraequilibrium domains are generally overlapping.

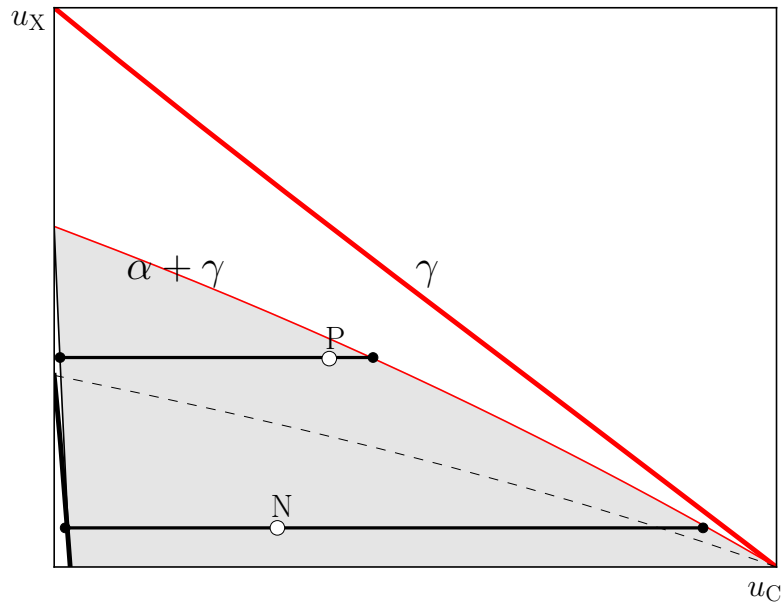


Figure 2.9: Isothermal section of a schematic Fe-C-X phase diagram with solubility limits of α (thick black) and of γ (red). Paraequilibrium two-phase field in grey with paraequilibrium tie-lines for alloys N and P.

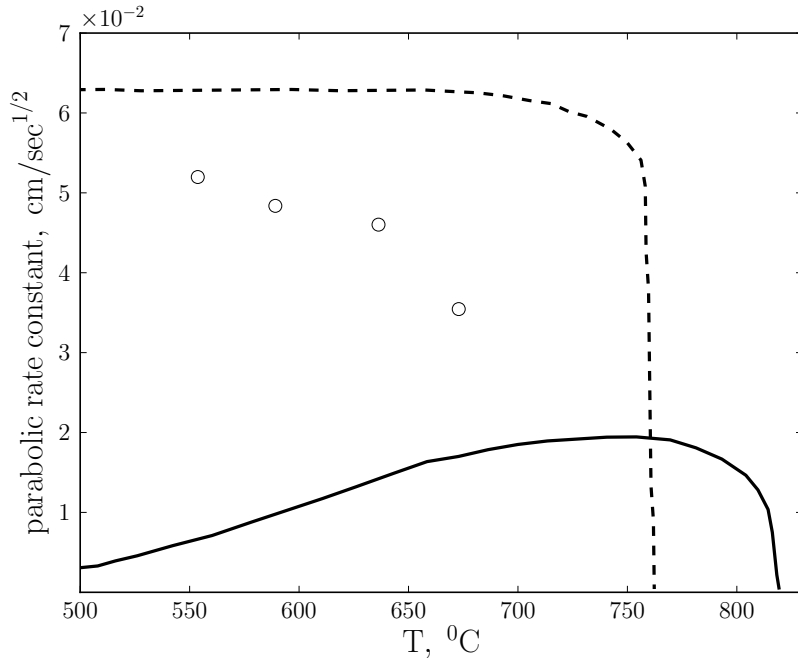


Figure 2.10: Parabolic growth rate constants vs. temperature in a Fe-0.56at.%C-3.1at.%Mn alloy: measurements (dots) and calculations (LE: continuous; PE: dashed) [59].

2.3.2 Deviations from the limit cases

The local concentrations at the α/γ interface are likely to deviate from equilibrium or paraequilibrium values. This statement is generally done indirectly by comparing the predictions of the limit cases discussed above and experimental measurements of ferrite thickness vs. time, usually obtained during isothermal treatments [29, 87, 89].

First, Enomoto [59] has performed such comparisons in various Fe-C-X systems at different temperatures with data collected in literature. As illustrated in Fig. 2.10 for a particular Fe-C-Mn alloy, the measured $\gamma \rightarrow \alpha$ kinetics can largely deviate from the limit cases LE (continuous line) and PE (dashed line), still remaining bounded by those limits. The largest deviations have been reported on for Mn, Cr and Mo, with some kinetics even slower than LE [21, 89].

Second, the growth kinetics can exhibit changes of regime, either progressive or sharp, as shown by Hutchinson et al. [87]. Indeed, these authors have performed

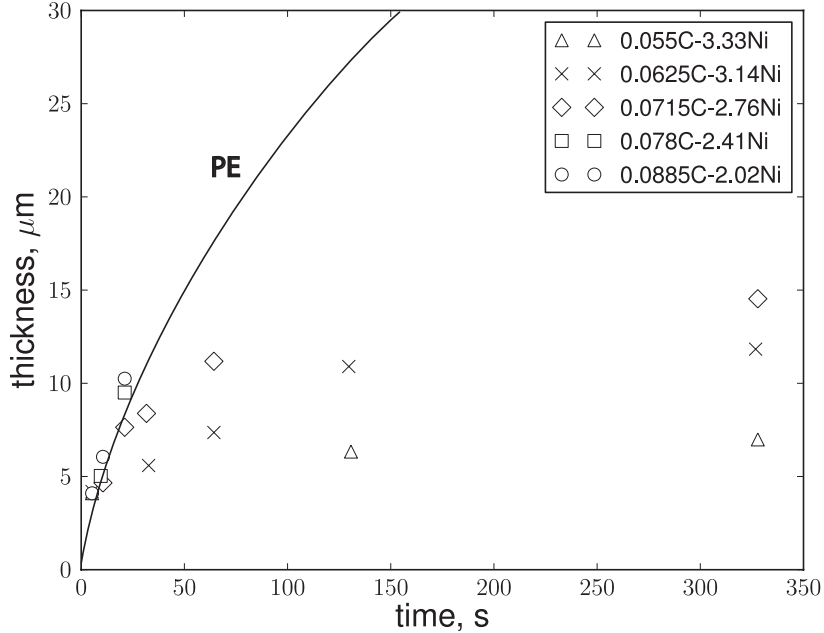


Figure 2.11: Ferrite thickness vs. time in different Fe-C-Ni alloys (wt.%) held at 700°C: experiments (symbols) and calculated PE (continuous line) (from [87, 89]).

isothermal treatments at 700°C in different Fe-C-Ni alloys, showing such features as illustrated in Fig. 2.11. For the five alloys investigated, PE matches very well the first stage during about 25 s. Then, different behaviours are observed depending on whether the alloy is above or below the zero-partition line. For alloys below the zero-partition line, a smooth transition to LEP is observed. For alloys above the zero-partition line, stases are observed which have been attributed to transitions to slow LEP regimes. By contrast, similar experiments by Thuillier in a Fe-C-Mn alloy have shown a stasis below the zero-partition line [151], reproduced by phase field calculations in [155]. It is worth mentioning that stases, called stagnant stages, have also been observed during recent experiments based on cyclic heat treatments [35], which may be due as well to some transitions from fast to slow growth regime [36].

Third, if it was admitted that fast growth prevails generally at large supersaturations (i.e. low temperatures) whereas slow LEP concerns small supersaturations (i.e. high temperatures), the frontiers both in temperature and concentrations

between the fast and slow growth do not coincide with the theoretical limits (§2.1.3.1) as shown early in [3] or more recently in [129]: they have been found to lie significantly above the LENP/LEP limit, but well inside the PE boundary. Fourth, recent decarburization experiments designed to obtain perfectly plane α/γ interfaces (growth kinetics are thus easier to measure) have provided new puzzling results concerning the temperature ranges where the different regimes can be observed [131]. Contrary to the common statement that PE prevails at low temperatures when LE does at high temperatures (still observed in Fe-C-Ni alloys [87]), it has been found that ferrite would grow under LE at low temperatures and under PE at high temperatures in Fe-C-Mn [165], at least when controlled by diffusion of C in α . However, in classical conditions (i.e. growth of grain boundary allotriomorphs), the usual hierarchy between LENP and PE seems to give results in agreement with the cycling experiments [36].

Finally it should be mentioned that measuring directly the concentrations at the interface has been attempted using the three-dimensional atom probe technique in an Fe-C-Mn alloy partially transformed at 700°C [152]. No significant partitioning has been detected, an observation which seems to discard LENP at least.

2.3.3 Choice of a relevant ternary system

At first sight, to identify the most relevant description among the limit cases discussed above may appear a trivial task: it would be just a matter of (i) performing interrupted isothermal experiments for different alloys spanning the whole $\alpha + \gamma$ two-phase field; and (ii) comparing the experimental kinetics to the predictions of the different models. However, this is a huge amount of work, very time consuming, with many experimental difficulties, in particular for determining ferrite thicknesses with accuracy. It is worth mentioning some alternative ways to investigate the different regimes in single experiments: either by using diffusion couples for spanning large range of X concentrations [88]; or by performing cyclic heat treatments in the intercritical temperature range [35, 36, 37].

For this kind of examination to be possible and meaningful, there are several requisites which cannot be all fulfilled at the same time. Depending on which

item prevails over the other, one may prefer a particular ternary alloy.

- (i) First, the $\gamma \rightarrow \alpha$ transformation must not be hindered by other transformations, such as carbide precipitation, in any form. The largest the intercritical region (both in temperature and X concentration ranges), the best it is.
- (ii) Second, there must be some significant differences between the growth kinetics. If this is generally the case between LEP and the other regimes, fast kinetic regimes may be difficult to discriminate.
- (iii) Third, the intermediate kinetics (§2.3.2) which are observed in between the limit cases are likely to involve interfacial dissipation as already shown by previous modeling works [124, 125]. Thus, the interactions, thermodynamic (Φ in Eqs. (2.28)) or kinetic (\mathcal{L} in Eqs. (2.28)) between X species and the interface should be significant for observing any intermediate kinetics. However, it must be kept in mind that elements which interact strongly with the interface are more prone to form carbides, as discussed in [89].

At first sight, the Fe-C-Cr system studied in chapter §1 would be an interesting candidate with respect to the last item, as suggested by Hillert in [76]. However items (i) and (ii) cannot be fulfilled together in that system. Indeed, 700°C would give sufficient differences between PE and LENP as shown for a particular alloy P in Fig. 2.12. However, carbides precipitate at this temperature. At 800°C, carbides do not precipitate, but the tie-lines for PE and LENP are very close, as shown in Fig. 2.13.

Mn could appear as a better candidate because it is not a carbide stabilizer element. However, as mentioned in the previous section, opposite trends have been observed in Fe-C-Mn between decarburization experiments on one hand, and isothermal and cyclic experiments on the other hand. Consequently, we have chosen Ni as the substitutional element because it fulfills at least the first two items, despite its weak interactions with interface [89].

Finally, to simplify the analysis, we will assume that the interface mobility is large enough so that the free energy dissipated by friction is negligible.

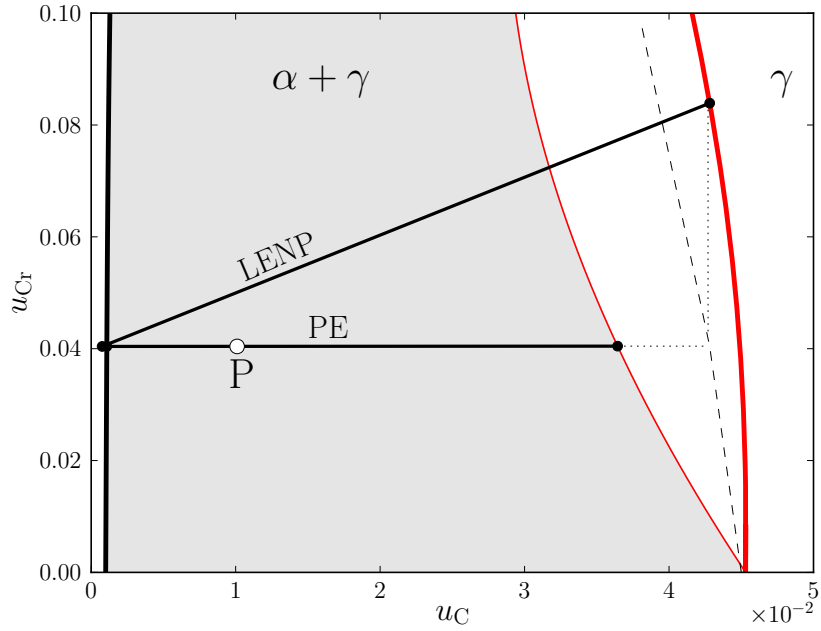


Figure 2.12: Isothermal section at 700°C of Fe-C-Cr with only α and γ (dashed line: zero-partition line; grey region: paraequilibrium region).

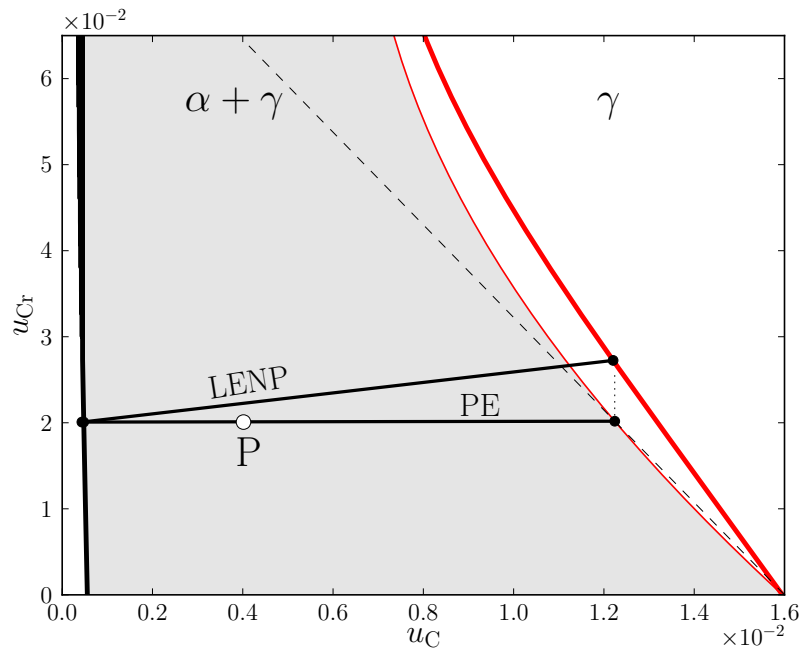


Figure 2.13: Isothermal section at 800°C of Fe-C-Cr with only α and γ (dashed line: zero-partition line; grey region: paraequilibrium region).

2.3.4 Specific algorithms

The large difference between D_C and D_X makes the nonlinear system Eqs. (2.28) particularly stiff to solve, using blindly Newton-Raphson with local equilibrium, or even paraequilibrium in some cases, as starting conditions. Indeed, as will be shown in the sequel, there can be several solutions which cannot be detected by a local method such as Newton-Raphson. Unfortunately, the dissipation terms preclude the use of the global minimization algorithm proposed in chapter §1, and algorithms have been designed specifically for Fe-C-X to guess “intelligent” starting conditions for Newton-Raphson, in particular when performing successive calculations as in parameter studies (§2.3.5) or during growth (§2.3.6).

The two algorithms that are proposed below rely on the following trick: one variable is removed from the vector of unknowns as well as one equation. The new nonlinear system is consequently less stiff and can be solved more easily with Newton-Raphson for a prescribed value of the removed variable. Such a calculation is performed spanning a large range of values for the removed variable, and an auxilliary quantity which initially appeared in the removed equation is calculated correspondingly. The solution to the full initial nonlinear system Eqs. (2.28) is finally obtained when the value of the auxilliary variable matches some prescribed physical value.

“ u -algorithm”

The nonlinear system Eqs. (2.28) is simplified by removing u_C^α from the vector of unknowns (§2.1.3), i.e. the vector of unknowns becomes $\tilde{\mathbf{Y}} = \{u_X^\alpha, u_X^\gamma, u_C^\gamma, v\}$ and u_C^α is given a prescribed value. Accordingly, the solute balance for X is removed, and Eqs. (2.28) become:

$$\begin{cases} \Delta\Phi_C + P_C\Delta u_C = 0 \\ \Delta\Phi_X + P_X\Delta u_X = 0 \\ V_m \left(\frac{\Delta\Phi_C^2}{P_C} + \frac{\Delta\Phi_X^2}{P_X} \right) + \frac{V_m v}{M} - (u_{\text{Fe}}^\alpha \Delta\mu_{\text{Fe}} + u_X^\alpha \Delta\mu_X + u_C^\alpha \Delta\mu_C) = 0 \\ v - D_C^\gamma \Omega_C / \Delta_C = 0 \end{cases} \quad (2.43)$$

Solving Eqs. (2.43) for a series of prescribed u_C^α gives a series of tie-lines and interface velocities. The total dissipation can easily be extracted using the first two terms in Eq. (2.43)₃. The auxilliary variable which permits to find the solution(s) to the full nonlinear system Eqs. (2.28) is the nominal concentration¹ in X u_X^0 entering the removed solute balance for X. It can be explicitly computed as the solution of the following quadratic equation, using Zener approximation Eq. (2.27) for the diffusion length Δ_X :

$$\Omega_X^2 + 2Pe_X \Omega_X - 2Pe_X = 0 \quad (2.44)$$

with $Pe_X = v\xi/D_X^\gamma$ and where $u_X^0 = u_X^\gamma - \Omega_X (u_X^\gamma - u_X^\alpha)$. Finally, the solution to the full system is found when u_X^0 matches \tilde{u}_X^0 the real nominal concentration of the investigated alloy.

The u -algorithm is illustrated for three different ratios $D_X^{\gamma^*}/D_X^\gamma$, in the case of an alloy situated above the zero-partition line in a Fe-C-X system with X as a γ -stabilizer².

In Figs. 2.14-2.16 typical results are plotted as follows. (a) The isothermal section is shown with the same conventions as before, together with the series of tie-lines obtained for different u_C^α (each tie-line is corresponding to one dot on the curves in (b-d)). The considered alloy is indicated with a red dot. The two branches (dashed lines) of the IC contour, crossing at the zero-partition line (continuous black) are extended along the full axes as horizontal and vertical dashed lines. The nominal concentration u_X^γ (b) computed with Eq. (2.44), the total dissipation (c) calculated with the first two terms in Eq. (2.43)₃, and the growth rate v (d) are plotted vs. u_C^α . The solution(s) for the alloy (red dot) is obtained by looking for the intersection(s) between u_X^γ in (b) and the horizontal line at the ordinate of the red dot (horizontal continuous line in (b)). Four particular concentrations are worth to be noticed in (b):

- (i) $u_C^\alpha(eq)$, a lower bound for u_C^α , corresponds to the intersection between the

¹ In a finite system, this would rather be the average concentration in γ .

² The calculations have been carried out with $\xi = 10$ nm and the data of Fe-C-Ni at 700°C, but the results are generic and valid for any Fe-C-X system with a similar phase diagram. Changing the ferrite thickness would not change the three typical behaviours which are exemplified.

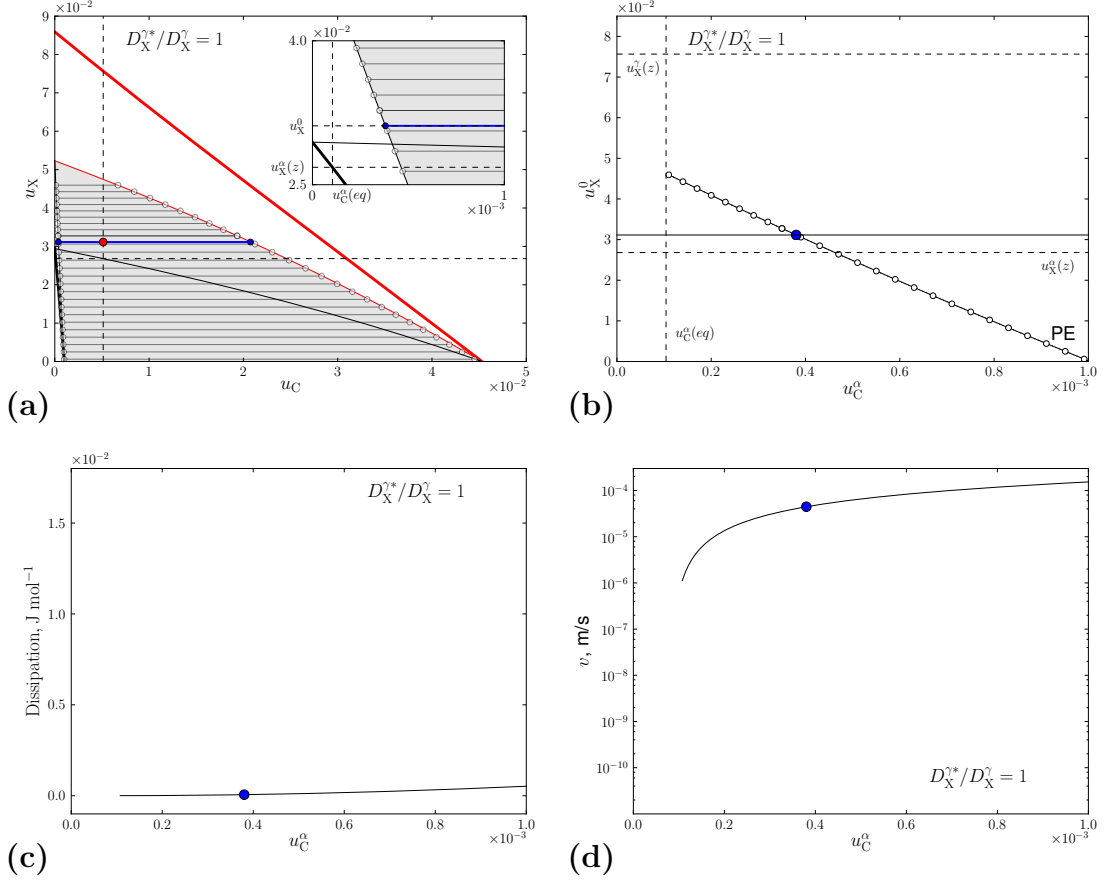


Figure 2.14: Results of the u -model (abscissae are u_C^α) for $D_X^{\gamma^*}/D_X^\gamma = 1$: (a) tie-lines; (b) nominal concentration u_X^0 ; (c) total dissipation; (d) growth rate.

horizontal branch of the IC contour and the solubility limit of α .

- (ii) $\max(u_C^\alpha)$, an upper bound for u_C^α , is determined with the solubility limit of C in α on the Fe-C binary system.
- (iii) $u_X^\alpha(z)$, a local lower limit for u_X^0 , corresponds to the ordinate of the horizontal branch of the IC contour.
- (iv) $u_X^\gamma(z)$, an upper bound for u_X^0 , is located at the ordinate of the intersection between the vertical branch of the IC contour and the solubility limit of γ .

For $D_X^{\gamma^*}/D_X^\gamma = 1$, u_X^0 extends from $u_C^\alpha(eq)$ to $\max(u_C^\alpha)$ and decreases linearly with u_C^α from some value between $u_X^\alpha(z)$ and $u_X^\gamma(z)$ down to 0. This is a PE branch because the corresponding tie-lines in Fig. 2.14a are paraequilibrium horizontal tie-lines. Accordingly, (i) there is almost no dissipation at the interface because

C is in local equilibrium and there is no partitioning (so no trans-interface diffusion) in X as shown in Fig. 2.14c; (ii) growth rates are large (Fig. 2.14d). One solution is found at the intersection of u_X^0 and \tilde{u}_X^0 (blue dot) corresponding to the paraequilibrium blue tie-line passing through the nominal composition (red dot) in Fig. 2.14a.

For $D_X^{\gamma^*}/D_X^\gamma = 10^4$, the u_X^0 curve changes drastically (Fig. 2.15b). At $u_C^\alpha(eq)$, a quasi-vertical branch goes from $u_X^\gamma(z)$ down to $u_X^\alpha(z)$ (LEP branch). The associated tie-lines in (a) are the LEP tie-line with a thick black line, with no dissipation in (c) and very small growth rates (< 1 nm/s) in (d). Then, u_X^0 increases up to some local maximum above \tilde{u}_X^0 . The corresponding tie-lines in (b) twist from the LEP tie-line to join the γ limit of the paraequilibrium diagram (grey). A spike

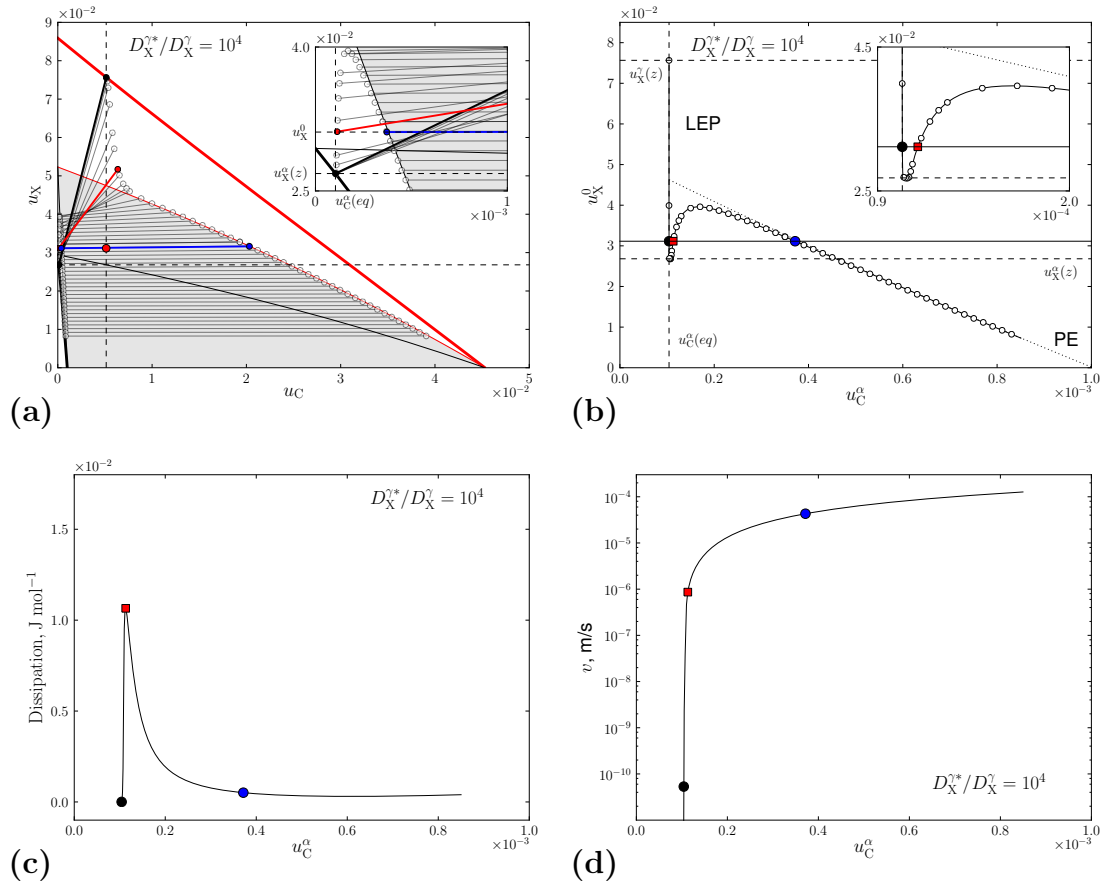


Figure 2.15: Results of the u -model (abscissae are u_C^α) for $D_X^{\gamma^*}/D_X^\gamma = 10^4$: (a) tie-lines; (b) nominal concentration u_X^0 ; (c) total dissipation; (d) growth rate.

in the dissipation curve as well as a steep increase of the velocity are observed concomitantly. Finally, u_X^0 decreases and joins rapidly the PE branch (dotted decreasing straight line), associated with the PE horizontal tie-lines in (a). Unexpectedly, three intersections are found between the u_X^0 curve and \tilde{u}_X^0 . (i) The intersection with the LEP branch (black dot) is related to the LEP tie-line (thick black line), no dissipation and a small velocity. (ii) The intersection with the PE branch (blue dot) is associated with the PE tie-line (blue line), nearly no dissipation and a very fast growth. Finally, (iii) the intersection with the increasing part (red dot) corresponds to the red intermediate tie-line, the maximum of dissipation and an intermediate growth rate.

For $D_X^{\gamma^*}/D_X^\gamma = 10^6$, u_X^0 still features the vertical LEP branch. The second branch does not exhibit anymore a local maximum, but decreases with a slope smaller than the PE branch (dotted). The tie-lines associated with this branch are nearly full equilibrium tie-lines. In that case, the only solution is the LEP tie-line (black dots and black thick line) with no dissipation and a very small velocity.

The “ u -algorithm” clearly shows that, for some values of the ratio $D_X^{\gamma^*}/D_X^\gamma$, there can be several tie-lines which are solutions to the full nonlinear system (2.28). This could explain the lack of robustness of Newton-Raphson to solve this problem, which has been observed in preliminary attempts.

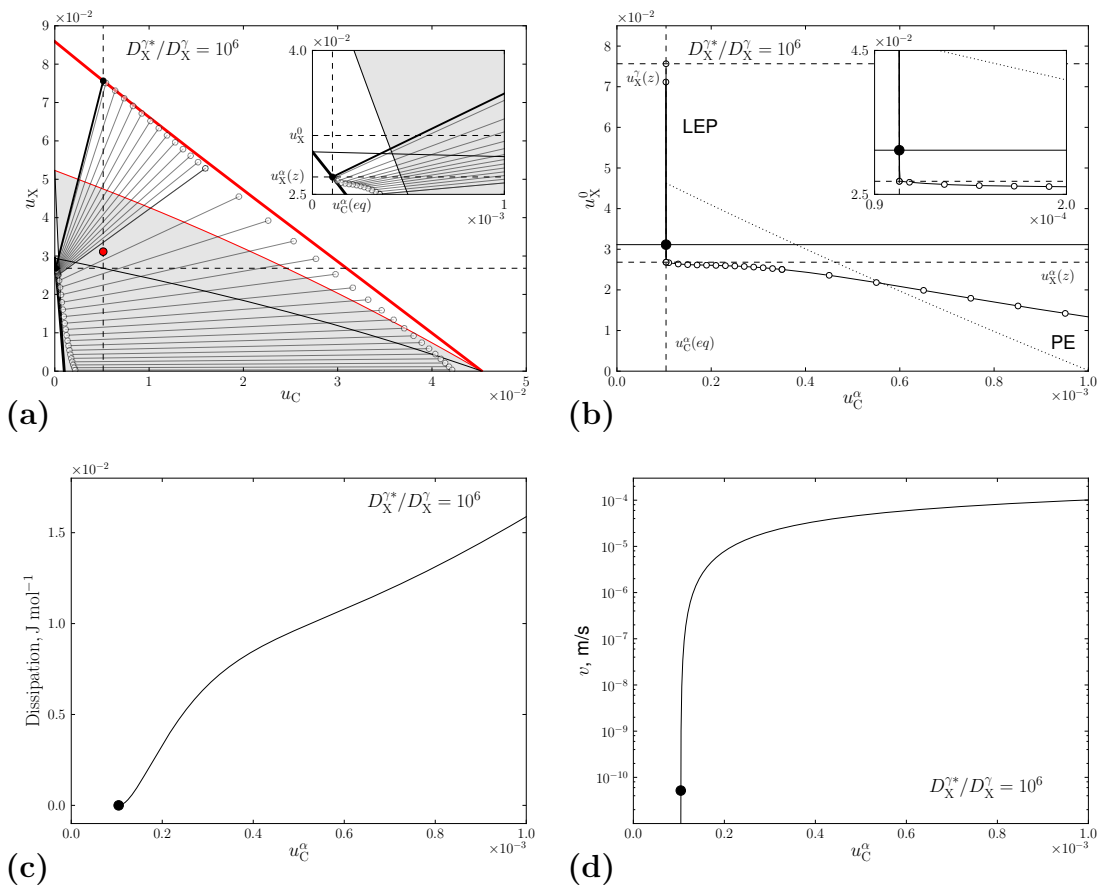


Figure 2.16: Results of the u -model (abscissae are u_C^α) for $D_X^{*\gamma}/D_X^\gamma = 10^6$: (a) tie-lines; (b) nominal concentration u_X^0 ; (c) total dissipation; (d) growth rate.

“ v -algorithm”

An alternative way to find the solution(s) to the full nonlinear system Eqs. (2.28) consists in removing v from the vector of unknowns (§2.1.3), i.e. the vector of unknowns becomes $\tilde{\mathbf{Y}} = \{u_C^\alpha, u_X^\alpha, u_X^\gamma, u_C^\gamma\}$ and v is given a prescribed value. Accordingly, the Gibbs energy balance is removed, and Eqs. (2.28) become:

$$\begin{cases} \Delta\Phi_C + P_C\Delta u_C = 0 \\ \Delta\Phi_X + P_X\Delta u_X = 0 \\ v - D_C^\gamma \Omega_C / \Delta_C = 0 \\ v - D_X^\gamma \Omega_X / \Delta_X = 0 \end{cases} \quad (2.45)$$

Solving Eqs. (2.45) for a series of prescribed v gives a series of tie-lines. The total dissipation as well as the driving force can easily be computed using Eqs. (2.21)-(2.22) and (2.17) respectively. The solution to the full nonlinear system Eqs. (2.28) can be found at the intersection between the curves dissipation and driving force.

To illustrate the kind of results which can be obtained with the v -algorithm, as well as to check that the results are the same as with the u -algorithm, we have performed computations for the same alloy and with the same three different ratios $D_X^{\gamma^*}/D_X^\gamma$ as those used previously.

In Figs. 2.17-2.19 typical results are plotted as follows. (a) The isothermal section is shown with the same conventions as before, together with only the tie-lines corresponding to the considered alloy indicated with a red dot. (b) The total dissipation (continuous line) and the driving force (dashed line) are plotted vs. v . For all $D_X^{\gamma^*}/D_X^\gamma$ ratios, the total dissipation exhibits a bump which shifts toward greater velocities when $D_X^{\gamma^*}/D_X^\gamma$. As well, the driving force vs. v features a particular shape with a bump at velocities where trans-interface dissipation is significant, added to an overall decrease with v which drops the driving force below zero at high velocities. It is worth noting that these curves are different from those shown in [137] and in [125]: for the total dissipation, the difference can easily be explained, because we have neglected the interface friction which would give a sudden increase at high velocity (see e.g. Fig. 2.4). For the driving

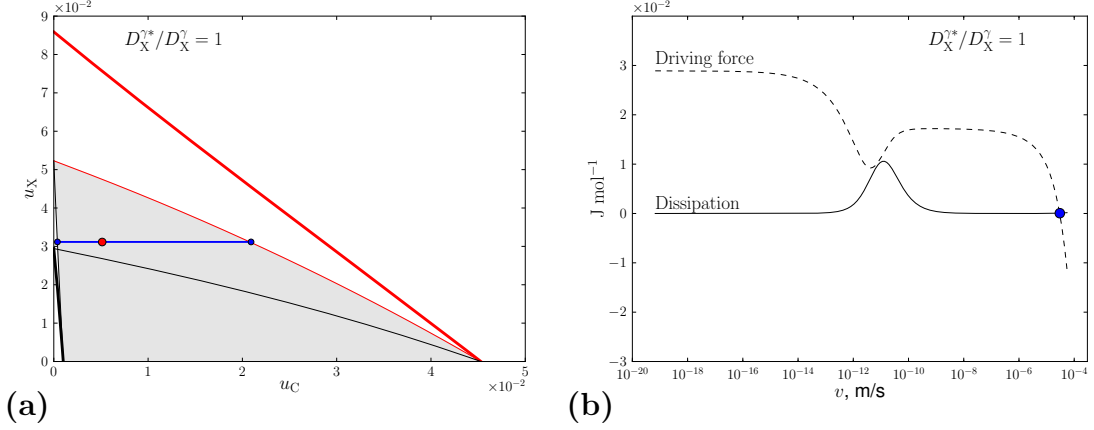


Figure 2.17: Results of the v -model (abscissae are v) for $D_X^{\gamma^*}/D_X^\gamma = 1$: (a) tie-lines; (b) Dissipation and driving force.

force, on the one hand the difference with Purdy and Bréchet [137] (see also Fig. 2 in [129]) can be attributed to their approximation by quadratic Gibbs energies (cf. their Eq. (11)). On the other hand, the difference with Odqvist [125] lies in their definition including the diffusion profile outside of the interface which is permitted only for non partitioning transformations.

For $D_X^{\gamma^*}/D_X^\gamma = 1$ (Fig. 2.17), the driving force is much higher than the dissipation at small velocities and the first drop is compensated for by the bump when trans-interface diffusion comes into play. Consequently, the driving force crosses the dissipation curve at large velocity, around $30 \mu\text{m/s}$ (blue dot). The corresponding blue tie-line in (a) is the horizontal paraequilibrium tie-line passing through the nominal composition (red dot), in perfect agreement with the u -algorithm (Fig. 2.14).

For $D_X^{\gamma^*}/D_X^\gamma = 10^4$ (Fig. 2.18), the driving force crosses the dissipation curve three times: at small velocities ($v < 0.1 \text{ nm/s}$) before the trans-interface diffusion bump (black dot); at the top of the bump around $v = 1 \mu\text{m/s}$ (red dot); at large velocities ($v > 20 \mu\text{m/s}$) after the bump (blue dot). It must be stressed that this unexpected situation is related to the peculiar shape of the driving force. The corresponding tie-lines are those already found with the u -algorithm: the LEP black tie-line, the paraequilibrium blue tie-line and a non-equilibrium intermediate red tie-line ending in between the equilibrium phase diagram and

the paraequilibrium diagram.

For $D_X^{\gamma^*}/D_X^\gamma = 10^6$ (Fig. 2.19), the bump in the driving force does not compensate for the overall decrease and the driving force crosses the dissipation before the trans-interface diffusion bump, at a small velocity ($v \approx 10^{-2}$ nm/s). The corresponding tie-line is simply LEP, in full agreement with the u -algorithm.

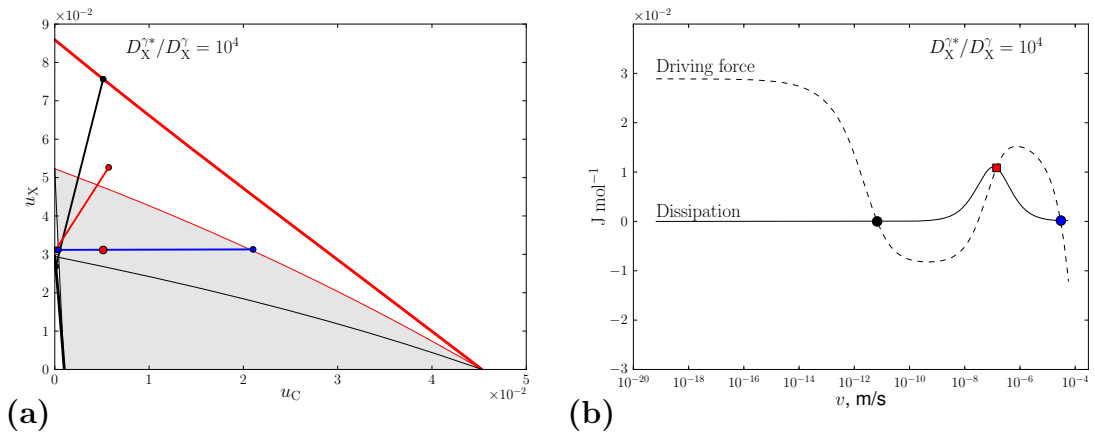


Figure 2.18: Results of the v -model (abscissae are v) for $D_X^{\gamma^*}/D_X^\gamma = 10^4$: (a) tie-lines; (b) Dissipation and driving force.

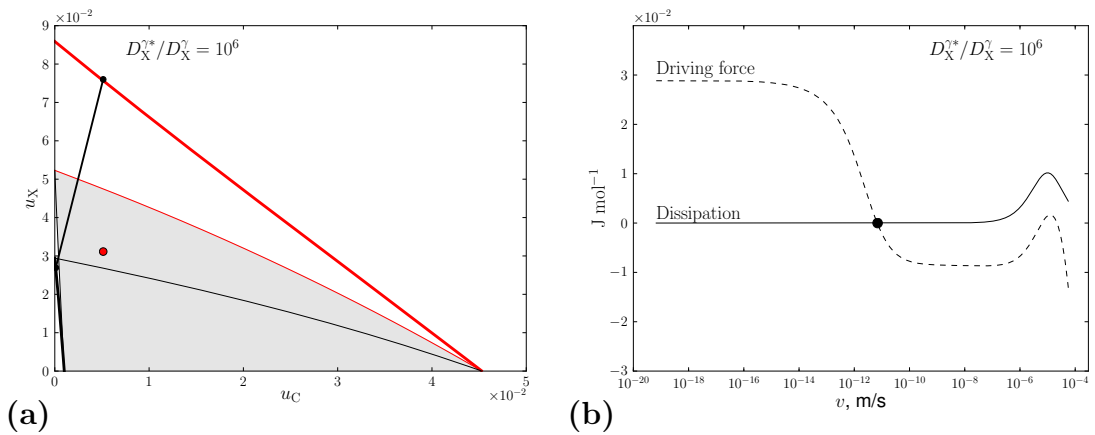


Figure 2.19: Results of the v -model (abscissae are v) for $D_X^{\gamma^*}/D_X^\gamma = 10^6$: (a) tie-lines; (b) Dissipation and driving force.

2.3.5 Growth regimes

Using any of the above algorithms which have been proved to be completely equivalent, the different growth regimes for a given alloy can be investigated with respect to temperature as in Enomoto [59] by plotting the parabolic growth rate constant $v\xi$ vs. temperature. The predictions of the thick interface model are illustrated in Fig. 2.20 for Fe-0.92 at.% C-2.4 at.% Ni, with the ratio $D_{\text{Ni}}^{\gamma^*}/D_{\text{Ni}}^{\gamma} = 10^4$ which exhibits three possible growth regimes under isothermal conditions.

First, two limit curves (black) have been computed. (i) The continuous line corresponding to local equilibrium with LENP and LEP, respectively below and above $\sim 720^\circ\text{C}$, has been obtained for $\xi \rightarrow \infty$ and very slow kinetics. Indeed, in that case, the growth kinetics is so slow that the time necessary for the interface to reach equilibrium is easily achieved. (ii) The dashed line corresponding to paraequilibrium (PE) not possible above $\sim 780^\circ\text{C}$ has been obtained for $\xi \rightarrow 0$ and very fast kinetics. In that case, Ni cannot diffuse across the interface to partition.

For intermediate sizes ξ (e.g. $\xi = 100 \mu\text{m}$, blue), three possible solutions have been obtained as discussed in the previous sections¹: two of them are located on the limit curves, either local equilibrium or paraequilibrium. A third one located in between, as shown with colored lines in Fig. 2.20, corresponds to the intermediate tie-lines associated with large dissipation by trans-interface diffusion. Peculiarities of the intermediate kinetics are: (i) the growth rate increases with temperature whereas it is the inverse for PE and LE; (ii) under isothermal conditions, the parabolic growth rate constant increases with the precipitate size whereas it remains constant under PE or LE regimes. Thus, growth accelerates under the intermediate regime, as will be shown in the following section §2.3.6.2. The temperature range where these intermediate kinetics are observed is delimited by the sharp transition between LEP and LENP and the upper limit for PE (780°C) at most. Below the lower limit, all the curves collapse to PE. Above the upper limit, all the curves collapse to LEP. Hence, our model predicts that there is an upper temperature, below 780°C , above which growth cannot proceed under PE anymore. This upper limit decreases down to the transition from LEP/LENP as the precipitate size ξ increases.

¹ Similar set of curves can be obtained by varying the ratio $D_{\text{Ni}}^{\gamma^*}/D_{\text{Ni}}^{\gamma}$ instead of ξ .

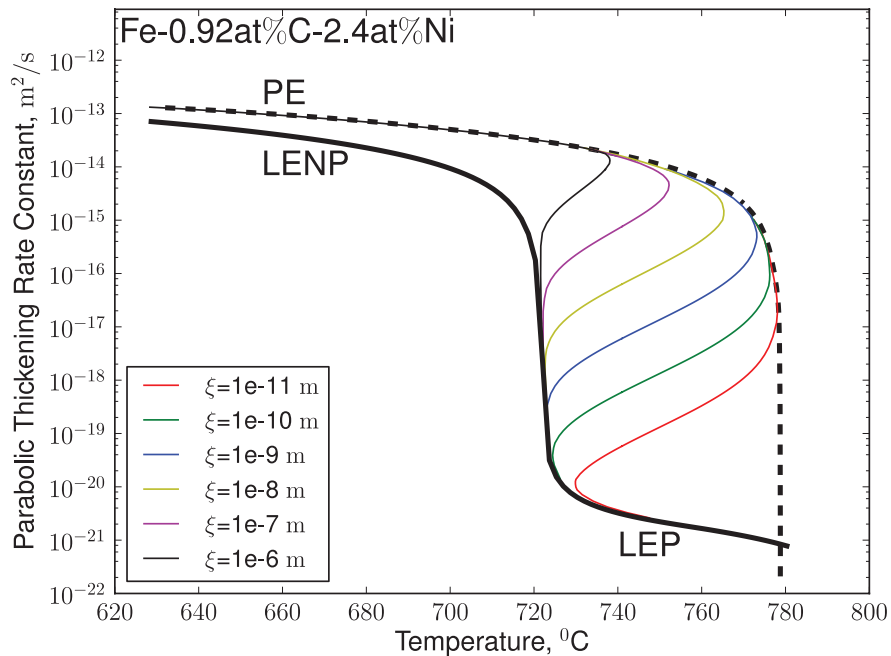


Figure 2.20: Growth rate constant: local equilibrium (continuous black); paraequilibrium (dashed); intermediate kinetics for different sizes (colored).

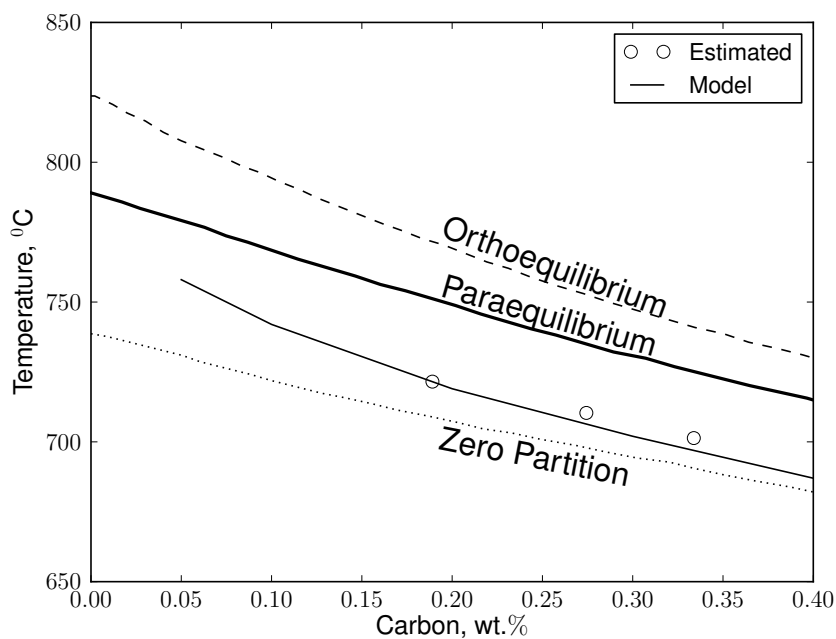


Figure 2.21: Isothermal section of the Fe-C-Ni ternary phase diagram at 700°C: calculations (thin line) and experiments (white dots) from [129].

These curves can be exploited to interpret some experimental measurements about the limit between fast and slow growth modes both in Fe-C-Mn and Fe-C-Ni [129], which has been found to lie above the zero-partition line, but well below the limit of the PE domain (Fig. 2.21). Indeed, consider that the Fe-0.92C-2.4Ni (mol.%) alloy concerned with Fig. 2.20 undergo an isothermal treatment at a temperature above the zero-partition line ($\sim 720^\circ\text{C}$) and below the limit of PE ($\sim 780^\circ\text{C}$). If one assumes that growth starts under PE, the growth rate is given by the upper branch of some S-shaped curve associated with a small precipitate size, e.g. $\xi = 1$ nm. As growth proceeds, the size increases and progressively, the growth rate changes smoothly to curves corresponding to larger sizes. At a given size, there is no longer any upper branch, i.e. possible fast growth, but only the slow LEP mode (there is neither any intermediate growth regime). If a size ξ of a few μm is chosen as a typical size for the sudden transition to occur, the limit between fast and slow growth is about 10°C above the zero-partition line, in agreement with the measurements of Oi et al. [129] in different alloys (Fig. 2.21).

2.3.6 Isothermal growth of α

In the present section, the isothermal growth of ferrite is investigated with the thick interface model. In particular, we focus on the transitions between the different growth regimes in Fe-C-Ni system. For that purpose and for the purpose of comparison, we have chosen the alloys studied in [125] (Tab. 2.1) at the same temperature, i.e. 700°C. These alloys are plotted in the corresponding ternary section in Fig. 2.22: all alloys are situated above the zero-partition line (dashed line) except the one with the lower carbon content.

Assuming that growth starts with a high growth rate, the PE tie-line obtained with the u or v -algorithm for $\xi = 10$ nm has been chosen as the initial condition for the calculations (except in one case where the intermediate tie-line has been selected). An explicit scheme is adopted for integrating the growth rate with time to get the size evolution:

$$\xi = \xi^0 + v(\xi^0) \Delta t \quad (2.46)$$

where 0 as a superscript denotes a value at the previous time step, i.e. at $t - \Delta t$. At time increments $i\Delta$ with $i > 0$, the full nonlinear system Eqs. (2.28) is solved with Newton-Raphson to provide the operative tie line and growth rate $\mathbf{Y} = (u_C^\alpha, u_X^\alpha, u_C^\gamma, u_X^\gamma, v)$. The stability of the calculations is ensured by the selection of a small time step ($\Delta t = 0.1$ s) and small successive changes of \mathbf{Y} .

All computations have been performed with a ratio $D_{\text{Ni}}^{\gamma^*}/D_{\text{Ni}}^\gamma = 4$, which has been adjusted to give the best agreement with the calculations of Odqvist et al. [125], as will be shown in the next sections. It is difficult to compare $D_{\text{Ni}}^{\gamma^*}$ in the present work with the interface diffusivity used in [125] because both models rely on different descriptions of the interface. However, it will be shown that similar results can still be obtained. Finally, it must be stressed that the agreement between Odqvist's model and experimental kinetics is not clearly established in [125], and has still to be established. Indeed, we will show that for our model to compare favorably to experiments of [87], a different $D_{\text{Ni}}^{\gamma^*}/D_{\text{Ni}}^\gamma$ ratio must be selected.

x_C (at.%)	u_C	x_{Ni} (at.%)
0.5	0.005	2.27
1.3	0.0134	2.27
1.47	0.0149	2.27
1.75	0.0178	2.27
2.1	0.021	2.27

Table 2.1: Compositions of Fe-C-Ni alloys investigated in the present work and in [125].

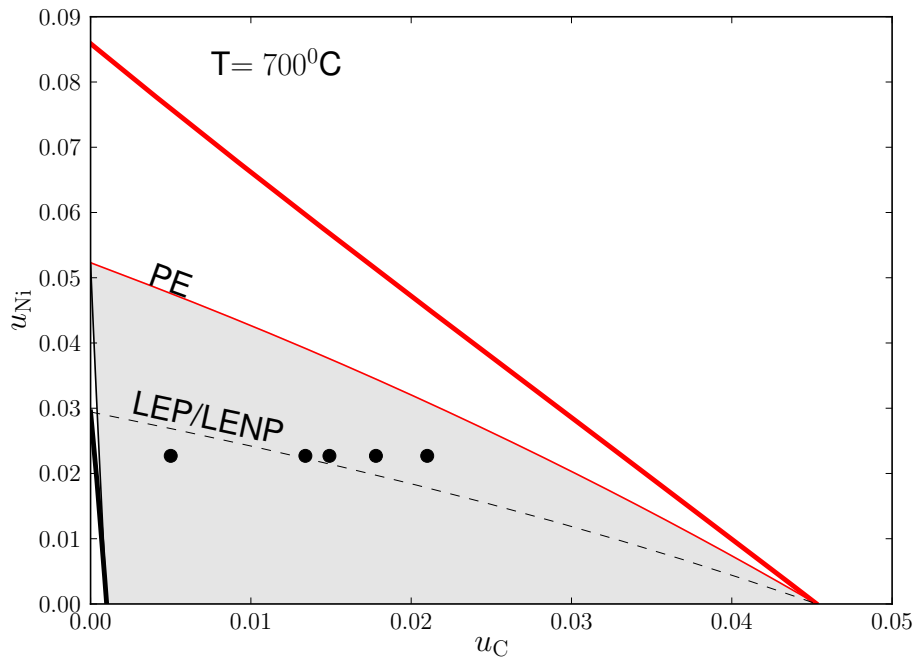


Figure 2.22: Isothermal section of the Fe-C-Ni ternary phase diagram at 700°C with the investigated alloys (black dots) in Tab. 2.1.

2.3.6.1 Below the zero-partition line

In Fig. 2.23, ferrite thickness is plotted vs. time for the Fe-0.5 at.%C-2.27 at.%Ni alloy, situated below the zero-partition line (Fig. 2.22). The thickness follows a \sqrt{t} growth law¹. Moreover, a good agreement is found with the results of [125] (Fig. 10) for the same alloy (dots).

As already mentioned, PE has been chosen as the initial condition as in [125]. PE remains the growth mode for more than 10^6 s, as clearly shown in Fig. 2.24 where the total dissipation is plotted vs. time. Indeed, there is no significant dissipation before $\sim 10^9$ s when the bump of trans-interface diffusion of Ni emerges. Before $\sim 10^9$ s, the operative tie-line is the horizontal paraequilibrium tie-line, as shown in Fig. 2.25.

For $t > 10^9$ s, dissipation is associated with the formation of a Ni spike in front of the interface while the transformation remains partitionless: the operative tie-line evolves smoothly toward the LEMP tie-line with a progressive increase of u_{Ni}^γ (white dots in Fig. 2.25) and an horizontal shift of u_{C}^α from the α boundary of the paraequilibrium diagram to the α boundary of the equilibrium diagram (inset of Fig. 2.25). It is worth noting that this transition from PE to LEMP is unlikely to be observed experimentally for the time scale selected by the small $D_{\text{Ni}}^{\gamma^*}/D_{\text{Ni}}^\gamma$ ratio, and that soft-impingement would stop the transformation at the fraction of paraequilibrium.

¹ The scale has been chosen to compare with alloys above the zero-partition line in the next section §2.3.6.2.

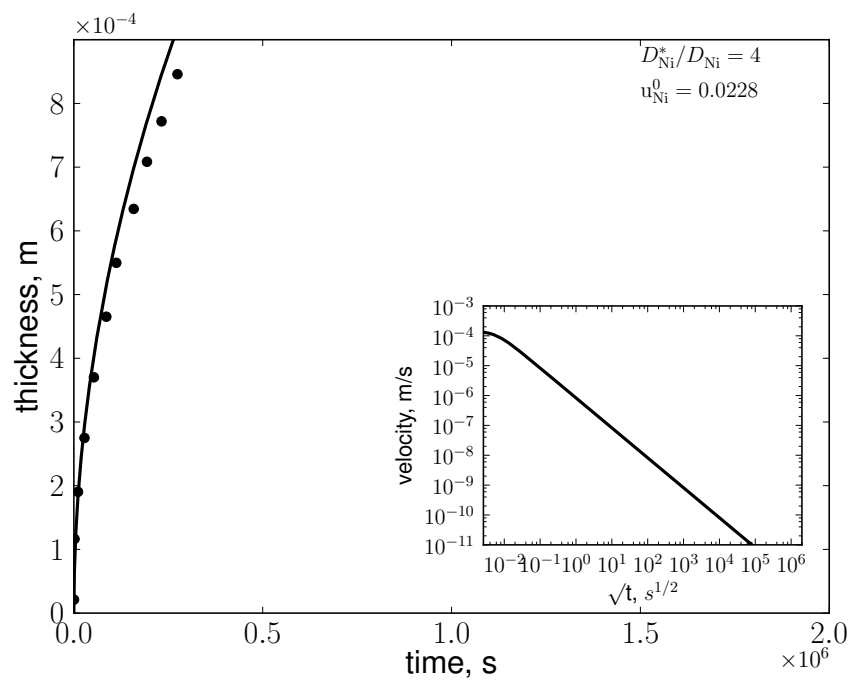


Figure 2.23: Ferrite growth kinetics in a Fe-0.5 at.%C-2.27 at.%Ni alloy at 700°C (inset: growth rate vs. time): present work (continuous line) and results from [124] (dots).

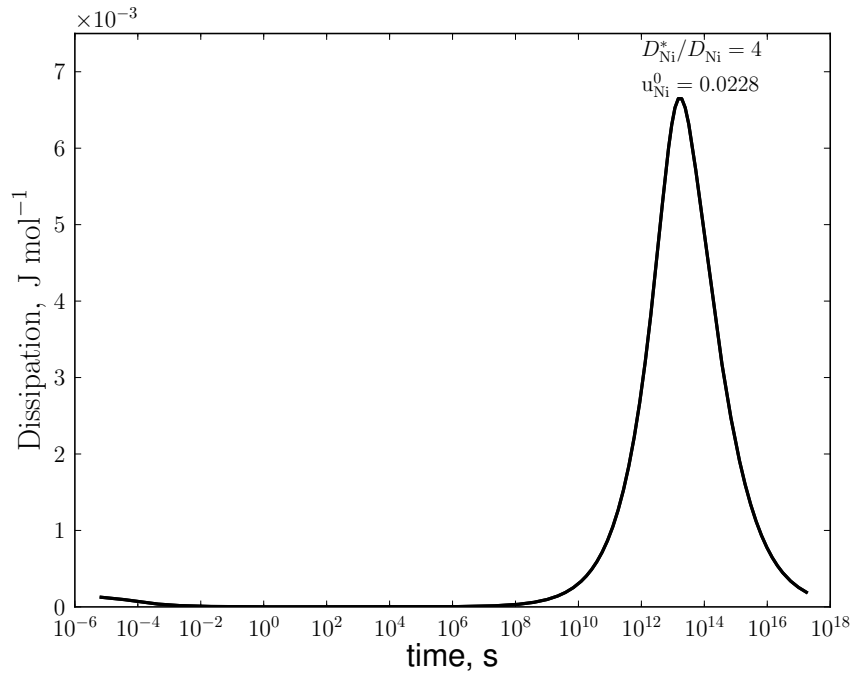


Figure 2.24: Evolution of the interfacial dissipation during growth of ferrite at 700°C in a Fe-0.5 at.%C-2.27 at.%Ni alloy.

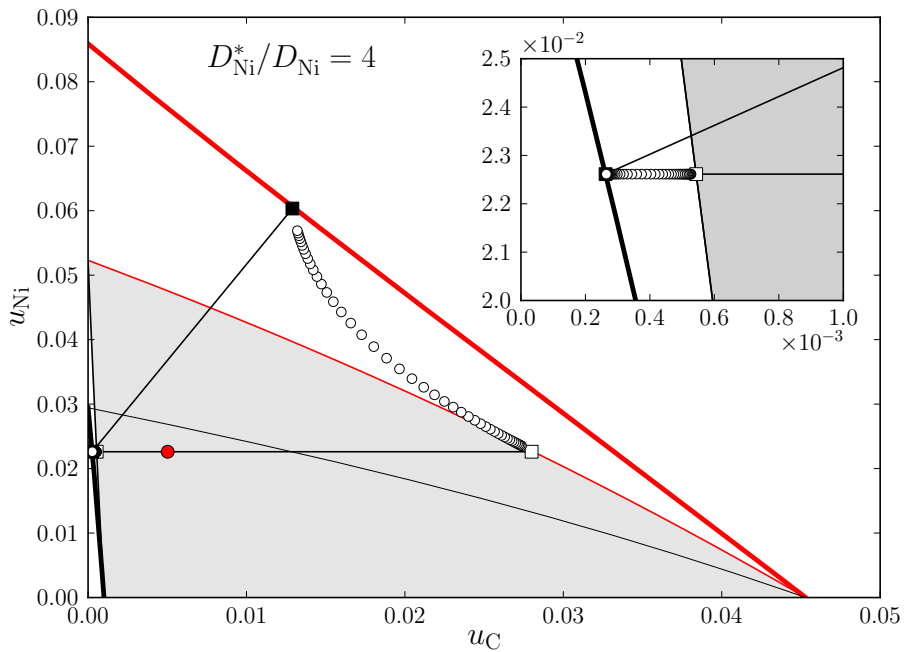


Figure 2.25: Isothermal section of the Fe-C-Ni phase diagram at 700°C. Evolution of the operative tie-line for a Fe-0.5 at.%C-2.27 at.%Ni alloy (red dot).

2.3.6.2 Above the zero-partition line

PE as initial condition

Next, we have investigated the growth of the four alloys in Tab. 2.1 above the zero-partition line (Fig. 2.22). The ferrite thicknesses vs. time are plotted in Fig. 2.26, together with the calculations of [125] (Figs. 7 and 10).

Our model predicts that for these alloys, growth proceeds in three stages which are more visible in the evolution of the total dissipation in Fig. 2.27.

For about 100 s, growth is very fast following a paraequilibrium \sqrt{t} law. This stage with no interfacial dissipation is exactly the same for all alloys because (i) they all have the same Ni content; (ii) growth is only controlled by carbon diffusion. In other words, all alloys share the same paraequilibrium tie-line (e.g. Fig. 2.28).

Then, a second stage is observed with a deviation from the paraequilibrium \sqrt{t} law and with an increase of the dissipation due to the trans-interface diffusion of Ni. The larger the carbon content, the shorter this stage, as clearly shown in Fig. 2.26. It must be noticed that our results agree quite well with the calculations of Odqvist et al. [125] whatever the alloy. The faster kinetics predicted by the present work can already be observed in Fig. 2.23 during the PE growth stage: slight differences in the diffusivity of C in γ might thus play a role, as well as the different descriptions of the interface. As shown in the ternary section in Fig. 2.28 for the alloy with 1.3 at.%C (very close to the zero-partition line), the second stage corresponds to the deviation of the operative tie-line from the PE tie-line: it twists toward the LEP tie-line.

For all alloys, growth stops suddenly at different times and thicknesses (Fig. 2.26), corresponding to a sudden drop to 0 of the interfacial dissipation (Fig. 2.27). In fact, the velocities are very small and determined by the LEP growth regime controlled by diffusion of Ni. As illustrated in Fig. 2.28, the change is associated with a jump of the operative tie-line from some intermediate tie-line to the LEP tie-line. The larger the C content, i.e. the closer the alloy to the γ boundary of the paraequilibrium diagram, the sooner the transformation is stopped and the smaller the ferrite thickness at the plateau. For all alloys, except the alloy with 1.3%at.C ($u_C = 0.0134$), a good agreement is found between the plateaus

predicted by our model and those inferred in [125]¹. Concerning the alloy with 1.3%at.C, very close to the zero-partition line, Odqvist et al. have found a smooth transition toward LENP, whereas we have found a sudden stop and a jump to LEP, consistently with the situation of the alloy above the zero-partition line. Finally, it must be stressed that Viardin [155, 156] has predicted with the phase field model discussed in chapter §3 that growth suddenly stops as soon as the C concentration of γ crosses the zero-partition line, due to soft impingement. The operative tie-line changes progressively from PE to some equilibrium tie-line during the plateau: the profile of concentration in X within the interface changes significantly and is obviously not steady. This gives a clue on why the tie-line changes suddenly, in a quite unrealistic manner.

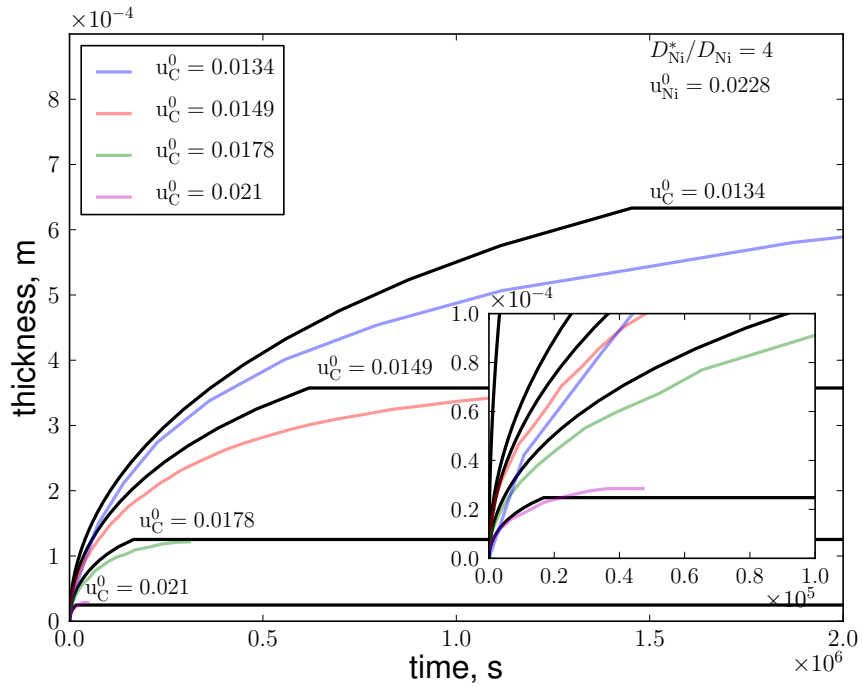


Figure 2.26: Ferrite growth kinetics in different Fe-C-Ni alloys (Tab. 2.22) at 700°C: present work (black lines) and results from [124] (colored lines).

¹ The plateaus have not been computed by Odqvist et al. [125] because they have constrained their model to non-partitioning transformations.

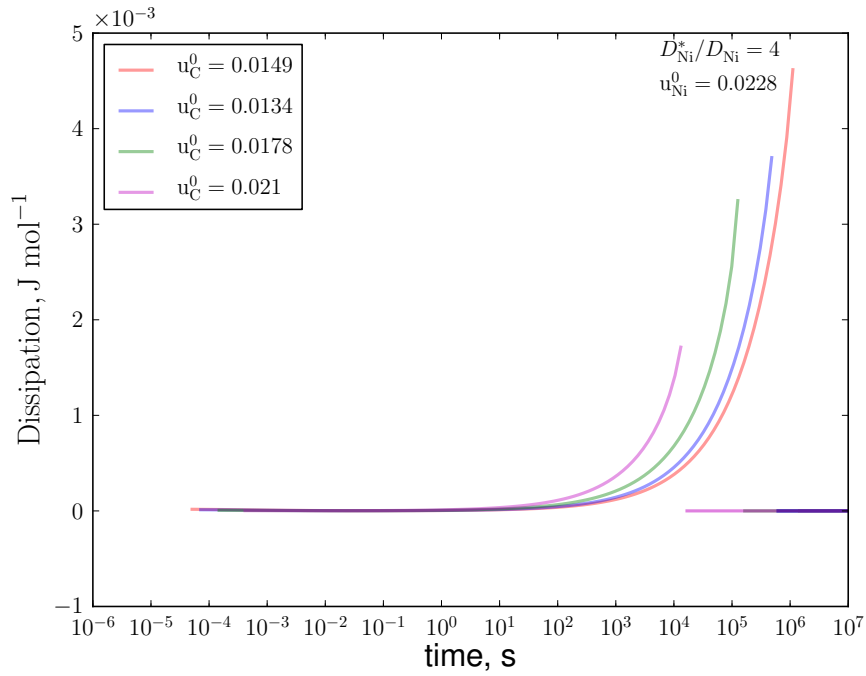


Figure 2.27: Evolution of the interfacial dissipation during the growth of ferrite at 700°C in different Fe-C-Ni alloys (Tab. 2.22).

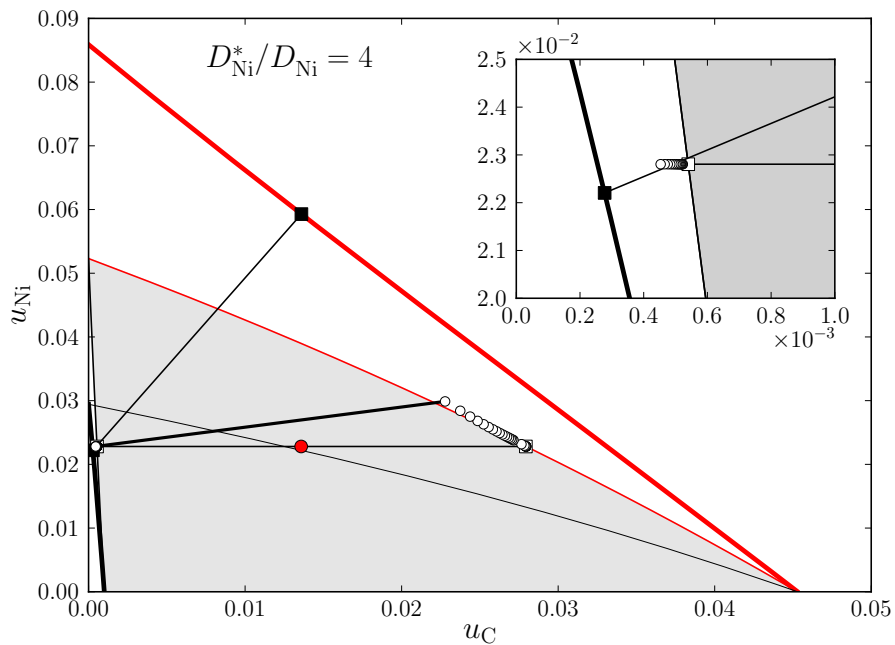


Figure 2.28: Isothermal section of the Fe-C-Ni phase diagram at 700°C. Evolution of the operative tie-line in a Fe-1.3 at.%C-2.27 at.%Ni alloy (red dot).

Intermediate tie-line as initial condition

As shown in §2.3.5, intermediate kinetics between PE and LEP can be obtained with the present model, as it is observed in some Fe-C-X systems (see §2.3.2), provided that an intermediate tie-line is selected. It is not clear how these intermediate tie-lines would be achieved after the nucleation step. However, we have investigated what kind of growth kinetics would be obtain if such a tie-line was selected as the initial condition for the calculations. For that purpose, we have chosen Fe-1.3 at.%C-2.27 at.%Ni, near the zero partition line (the three other alloys above the zero-partitioning line feature similar results, only quantitatively different).

Ferrite growth proceeds in two stages as shown in Fig. 2.29. For $\sim 2.5 \cdot 10^7$ s, growth accelerates and ferrite thickness vs. time exhibits a peculiar convex shape. This stage is associated with the intermediate operative tie-line twisting from the initial tie-line (thick black line) toward the LEP tie-line (ending with black squares), as shown in Fig. 2.3.6.2. It is quite remarkable that intermediate tie-lines which could not be achieved previously have now been obtained. From the very beginning of the transformation, a Ni spike is dragged by the interface with a significant dissipation due to trans-interface diffusion (not shown for brevity). Growth is still non-partitioning as shown in the inset of Fig. 2.29 where u_{Ni}^{α} shifts horizontally toward the equilibrium diagram and remains equal to u_{Ni}^0 . Although the growth kinetics is about one order of magnitude smaller than when starting with PE (consistently with the analysis of §2.3.4), ferrite achieves a larger size at the end of the first stage.

At $t \sim 2.5 \cdot 10^7$ s, growth stops suddenly: the operative tie-line jumps from some intermediate tie-line (ending with red squares) to LEP, similarly to the previous case in Fig. 2.28. It can be noticed that the jump occurs much later than when starting in PE mode, because the initial tie-line is very close to the final intermediate tie-line when starting in PE.

Finally, it must be concluded that the growth curve in Fig. 2.29 has never been reported on and is likely to be very unrealistic. As for the sudden jump already observed in the more realistic previous calculations, the missing feature which could explain such strange behaviours may possibly be that diffusion within the interface is strongly transient.

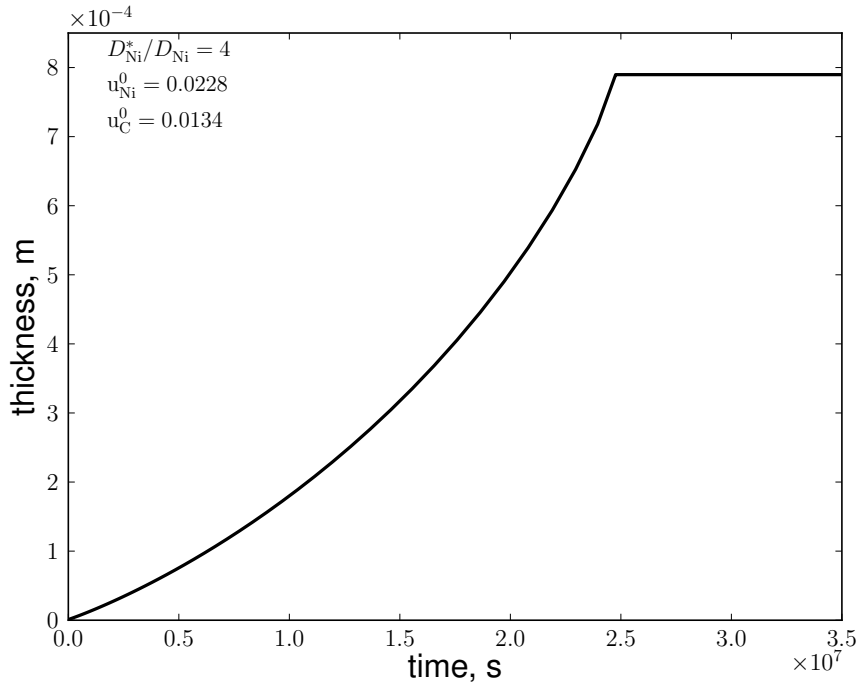


Figure 2.29: Ferrite growth kinetics in a Fe-1.3 at.%C-2.24 at.%Ni at 700°C, starting from an intermediate tie-line.

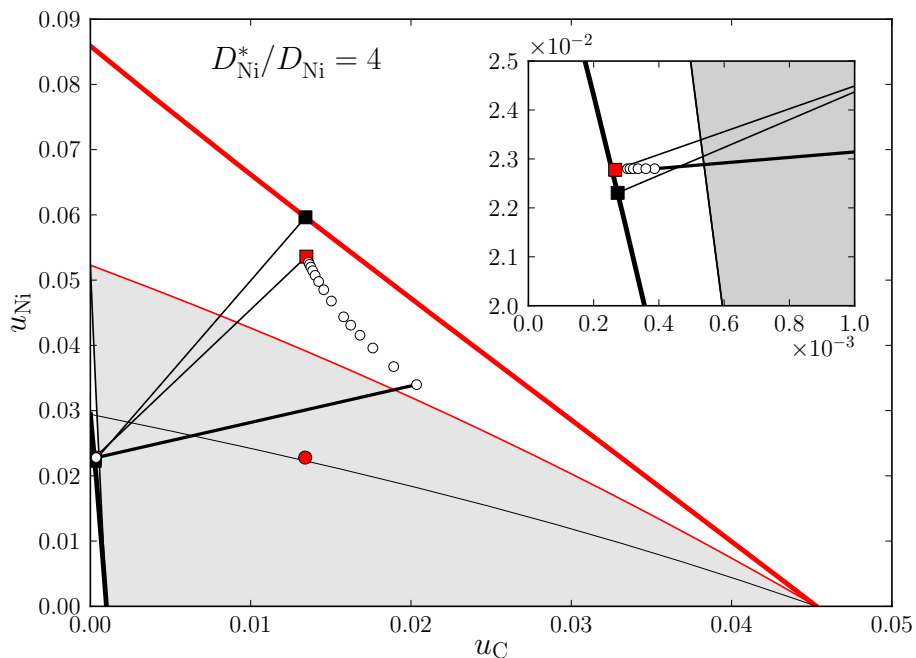


Figure 2.30: Isothermal section of the Fe-C-Ni phase diagram at 700°C. Evolution of the operative tie-line in a Fe-1.3 at.%C-2.27 at.%Ni alloy (red dot), starting from the intermediate tie-line (thick black line).

Comparison with some experimental results

The previous sections have shown that our model gives predictions similar to Odqvist's model, with some new features permitted by the relaxation of its unnecessary constraint confining growth to non-partitioning modes. However, as already mentioned, the previous calculations have not been compared favorably with experiments, except for massive transformations in Fe-Ni (Fig. 12 in [125] and §2.2). This is why we have considered the isothermal experiments of Hutchinson et al. [87] performed in different Fe-C-Ni alloys at 700°C (Tab. 2.2).

Following a trial and errors procedure¹, the ratio $D_{\text{Ni}}^{\gamma^*}/D_{\text{Ni}}^{\gamma} = 10^4$ gives the best agreement between our calculations and the experiments, as shown in Fig. 2.31. The initial conditions have been chosen to be PE because it has been shown to be the most realistic.

For the first ~ 20 s, the PE growth regime fits very well the experiments (taken from Fig. 8 in [87]), as already noted in [87]. Then, depending on the position of the alloy with respect to the zero-partition line (tab. 2.2), our model predicts either a smooth transition to LENP (alloys with 1.92 at.% and 2.62 at.% of Ni), or a sudden stop after a short transition to LEP (alloy with 2.98 at.% of Ni), consistently with the analysis above. The agreement with the experiments is also good during this second stage, in particular for the two alloys below the zero-partition line exhibiting the smooth transition. For the Fe-0.29at.%C-2.98at.%Ni alloy, the agreement is not perfect but better than with the model proposed by Hutchinson et al. [87]: the plateau is closer to the experiments.

¹ The same that was used in the previous sections.

x_C (at.%)	x_{Ni} (at.%)	w_{Ni} (wt.%)	position wrt. zero-partition line
0.3624	1.92	2.02	below
0.3323	2.62	2.76	below
0.2907	2.98	3.14	above

Table 2.2: Compositions of Fe-C-Ni alloys investigated in [87].

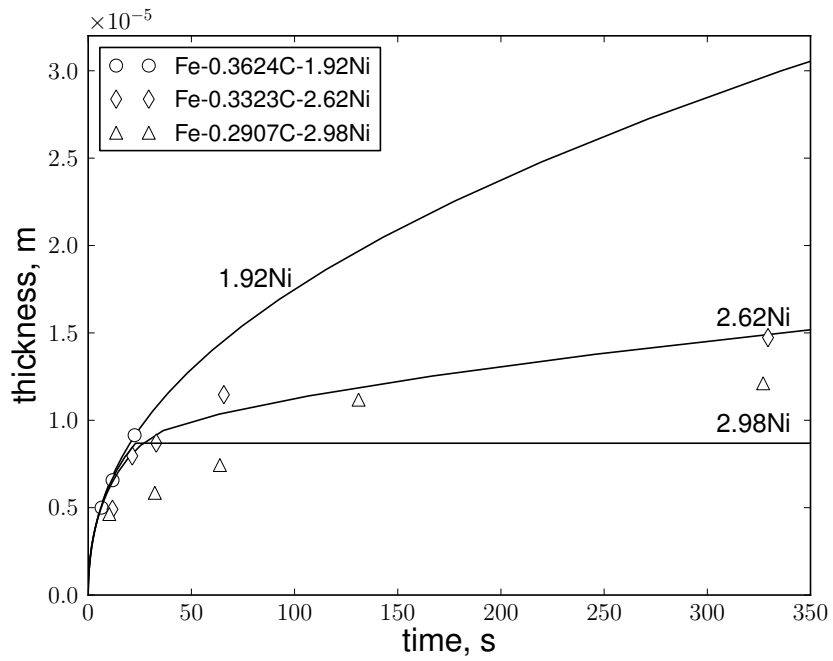


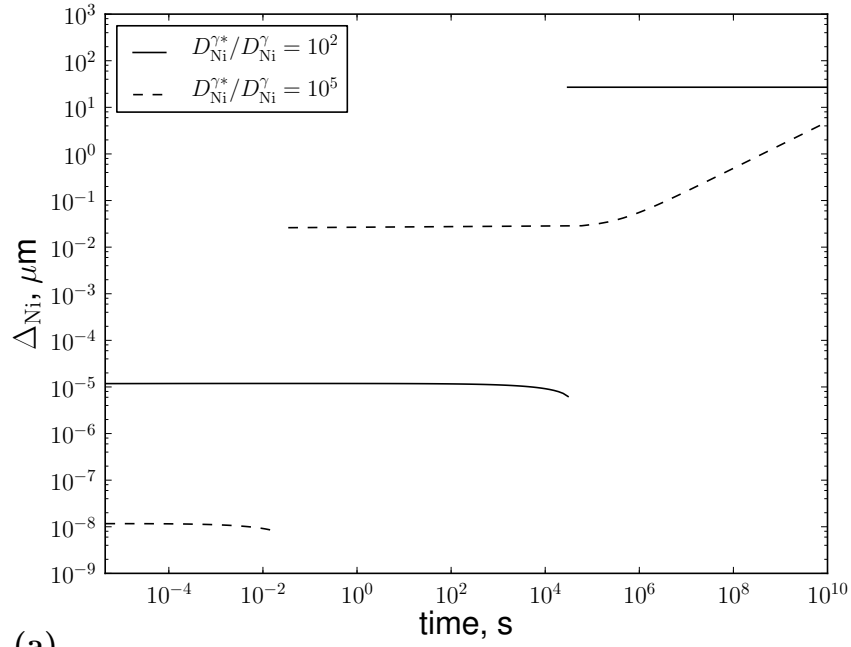
Figure 2.31: Ferrite growth kinetics in different Fe-C-Ni alloys (at.%) at 700°C (Tab. 2.2): present work (black lines) and experiments from [87] (symbols).

2.3.7 Discussion

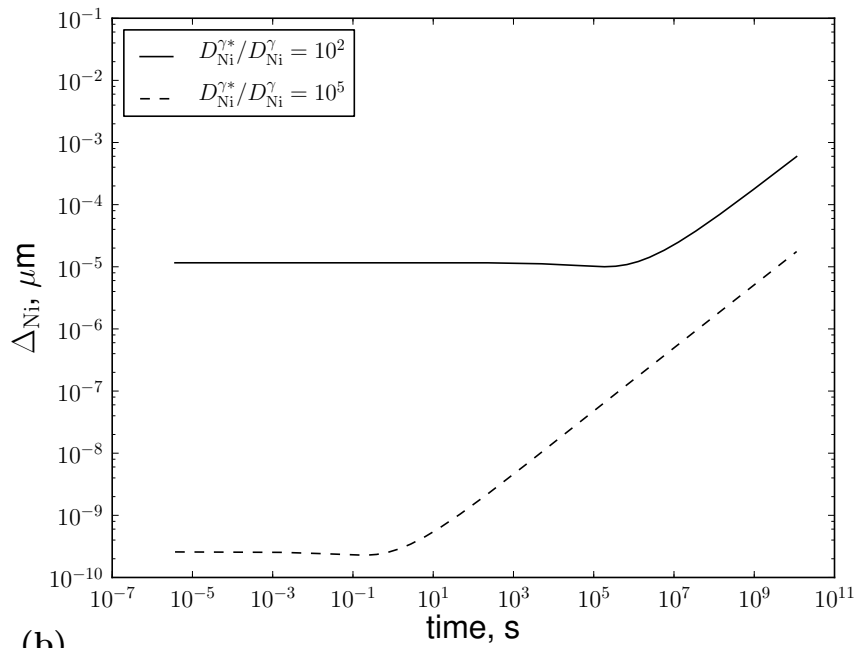
We have shown in the previous sections that some experimental facts can be explained in a consistent picture with the present model, despite the crude assumptions regarding the description of the interface as a continuum. The only parameter which has been adjusted is the ratio $D_{\text{Ni}}^{\gamma^*}/D_{\text{Ni}}^{\gamma}$ which is believed to encompass the most important interface property regarding kinetic transitions in Fe-C-X alloys. Indeed, it does not seem to be necessary to invoke any complicated interactions between the interface and the substitutional element, at least in Fe-C-Ni, contrary to the most common opinion [58, 59, 127, 136, 139]. If a complete consistent picture of the growth kinetics has not been achieved yet, these results can be considered as sufficiently convincing for having some confidence in the basic ingredients of the model.

There is however a delicate issue which may plague all models relying on a thick interface description, and which is worth to be discussed. The strong assumption of the model is not really that interface is a continuum, but that there is a strict separation between inside and outside the interface, for writing coupling conditions involving fluxes in the bulks to determine the growth velocity. Indeed, this assumption has important consequences on the values that the diffusion length Δ_{Ni} delivered by the Zener approximation Eq. (2.27) is able to adopt, in particular during the non-partitioning growth regimes, PE and LENP. Examples of such values are displayed in Figs. 2.32a and 2.32b, during the isothermal growth of ferrite in two Fe-C-Ni alloys, respectively above and below the zero-partition line (corresponding respectively to the lower and upper growth curves in Fig. 2.31). As it immediately appears with the scales of the y -axes, Δ_{Ni} shows generally unrealistically small values, except when growth becomes suddenly (jumps in Fig. 2.32a) partitioning. This behaviour is not a unique feature of Zener approximation, but would be encountered with any diffusion model where $\Delta_X \rightarrow 0$ when $\Omega_X \rightarrow 1$ ¹.

¹ There would be not problem with the usual diffusion length $\Delta_{XX} = \xi$ commonly used in precipitation models, but there would be no non-partitioning regime at all.



(a)



(b)

Figure 2.32: Evolution of the Ni spike width in γ at 700°C in (a) Fe-0.29C-2.98Ni (mol.%) above zero-partition and in (b) Fe-0.36C-1.92Ni (mol.%) below zero-partition, assuming PE as the initial condition.

This feature has already been pointed out in [79], and is in line with the early discussions about the size of the spike of substitutional element in front of the interface, predicted by the LENP model [48, 71]. At first sight, it may appear as an unacceptable flaw of the model. But in fact, $\Delta_x \approx 0$ would just indicate that the whole process is totally controlled by the phenomena taking place within the interface, where the linear concentration profiles mimic crudely either a more complex profile at a sub-interface scale, or atomistic processes. The most surprising is that such small values (i) are robustly managed by the solver and algorithms devised in the present work; and (ii) permit the prediction of realistic growth rates.

2.4 Conclusion

The model proposed in this chapter, despite its numerous simplifying assumptions to facilitate its numerical implementation, has provided several interesting features.

First, it encompasses as limit cases of a consistent framework different models proposed in the literature, such as the classical LEP/LENP solution, PE and the mixed-mode model of Sietsma and van der Zwaag [144]. The framework is ready to incorporate other features such as the intrinsic interface mobility, or thermodynamic interactions localized at the interface (e.g. segregation resulting in some extra solute drag). These possibilities have not been investigated so as to better highlight the consequences of the single trans-interface diffusion on the kinetics. It is worth stressing that a particular effort has been put to devise robust algorithms, necessary to handle the stiff nonlinear system which makes the model.

Despite the simplifying assumptions, our model has proved to be consistent with Odqvist's model [127]. Indeed, very similar results have been obtained for the massive transformation in Fe-Ni and for the allotriomorphic ferrite growth in Fe-C-X alloys. Only one parameter has been adjusted to match the results in [124, 127], the ratio between the diffusivities of the substitutional element in the interface and in bulk austenite D_X^*/D_X^γ . This parameter is indeed the essential parameter which controls the outcome of the model. If it is associated with a very simple picture of the real process, it has demonstrated that it is able to account for many kinetic regimes, in particular in Fe-C-X alloys.

Hence, we have shown that there exists a qualitative difference between the kinetics of alloys below and above the zero-partition line, in an infinite austenite grain. If both starts in PE mode, the first ones exhibit a smooth transition toward the LENP growth mode, whereas the second ones feature a sharp transition toward the LEP growth mode.

- (i) It is worth stressing that this last transition is an original outcome of our model since it has not been obtained so far with the other “thick interface” models. Indeed, the other models get round the difficult resolution of the general nonlinear systems by assuming explicitly or implicitly that the

transformations are non-partitioning [89, 125, 127, 165], discarding by this way the possibility to investigate the interesting transitions above the zero-partition line.

- (ii) Moreover, the sharp transitions from PE to LEP are consistent with the previous calculations of Viardin with a phase field model [155] (§3). Indeed, all his calculations ended by a stasis, whatever the alloy because of the enrichment of austenite due to soft-impingement, which drives the system into the LEP domain.
- (iii) The existence of sharp transitions from PE to LEP for alloys above the zero-partition line is also consistent with experimental measurements of the limit between fast and slow growth [129].
- (iv) Concerning the smooth transitions from PE to LENP for alloys situated below the zero-partition line, they are unlikely to be observed for allotriomorphic ferrite appearing at the γ/γ grain boundaries because of soft-impingement, as shown by Viardin [155]. However, situations where soft-impingement is not an issue could feature such transitions, such as during decarburization experiments [21, 164, 165].
- (v) Finally, it is worth mentioning that strange intermediate kinetics have been found in between PE and LEP growth modes, which feature unrealistic increasing growth rates corresponding to some high dissipation by trans-interface diffusion. Those kinetics have thus been discarded from the possible solutions, and should rather be seen as the consequence of supposing steady transport within the interface, an hypothesis obviously too stringent when transitions between different growth regimes are possible.

Many improvements and further analyses can be proposed for future works on the topics. First, it seems better a posteriori to adopt the most simple thermodynamic descriptions to improve numerical robustness, as well as to put forward more clearly the relevant ingredients responsible for the salient features. Indeed, if the Calphad description is mandatory for quantitative predictions of the equilibrium tie-lines, its validity for the intermediate tie-lines is questionable. Moreover, it must be stressed that the whole complicated machinery cannot be fully used within the interface because of the total lack of knowledge about what should be

the description of the interface in terms of bulk thermodynamics.

Second, in order to perform calculations in situations more comparable with experiments, one should incorporate soft-impingement accounting for the finite grain size of austenite with the presence of ferrite all along the grain boundaries. This could also permit a more direct comparison with the phase field modeling of the next chapter. As well, it would be desirable to account for diffusion in ferrite in order to investigate more complex situations, such as decarburization [21] or non-isothermal treatments (e.g. continuous cooling, or cyclic treatments [35]).

Finally, the decisive improvement from the point of view of model consistency would be to find an alternative to the integral solute balance which involve the coupling with the bulks. Indeed, it is responsible for the unrealistic diffusion length in γ necessary to mimic phenomena confined within the interface. In particular, this would necessitate to remove the too stringent assumption of linear profile in the interface, allowing for the continuity of fluxes at the boundaries of the thick interface, and mimicking in a simple way the behaviour of the phase field model of the next chapter.

Chapter 3

Diffuse interface model for the $\gamma \rightarrow \alpha$ transformation

As shown in the previous chapter, making a clear separation between the interface and the bulks may cause serious problems in terms of robustness in systems exhibiting very different kinetic regimes such as Fe-C-X alloys. The design of special algorithms has appeared to be mandatory §2.3.4 to overcome these problems and to obtain good initial conditions to proceed further §2.3.6. Moreover, it has been concluded that most of the interesting features are likely to happen within the interface §2.3.7. This is why we have switched to a phase field model which has previously provided interesting results for the $\gamma \rightarrow \alpha$ transformation in Fe-C-X alloys [155]. Indeed, although phase field models are much more demanding in terms of computational resources because they are “full field” models, they cannot be plagued by the problems encountered with the thick interface model. Indeed, coupling with the bulk is transparent and does not require any particular effort. Moreover, they deliver more realistic concentration profiles because

- (i) they naturally account for soft impingement which are very important for the changes in growth regimes as shown e.g. in [155, 156].
- (ii) They account naturally for diffusion in α which is likely to play a non negligible role during non isothermal treatments (see e.g. [35, 36, 37]).

However, the flexibility given by the diffuse interface must be analyzed in detail. Indeed, even if thermodynamic consistency is retained, the outcome of the model

in terms of interfacial concentrations deserves a particular attention. Indeed, the down side of the diffuse interface is that the different dissipative processes are more difficult to identify than in the thick interface model of chapter §2.

Therefore, the motivation of this third chapter is two-fold.

- (i) First, to provide a thorough analysis of the phase field mobility. On one hand, this will render possible the comparisons with the thick interface model in the future. On the other hand, this will firmly ascertain the expressions proposed previously in [155] to obtain relevant results in Fe-C-X.
- (ii) Second, to investigate one aspect which has been neglected in the previous chapter, as well as in [155]: the effect of a finite interface mobility. Indeed, there is still some active debate on whether the interface mobility is essential or not to predict the kinetics of the $\gamma \rightarrow \alpha$ transformation in Fe-C-X steels [1, 35, 61, 115, 139, 144]. Indeed, if the modeling is quite straightforward in binary alloys or multicomponent alloys with comparable diffusivities, it is much more challenging in Fe-C-X steels.

The present chapter is organized as follows.

First, the phase field model proposed in [155] and used in this work is shortly described (§3.1). Second, a full section is devoted to the analysis of the conditions at the interface, aiming at better understanding the outcome of the phase field model, in particular with respect to the phase field mobility (§3.2). Then, the influence of the interface mobility on the growth regimes will be investigated: in Fe-C (§3.3); and finally in Fe-C-X (§3.4).

3.1 Phase field model

These last two decades have seen a tremendous amount of work on the diffuse interface approach (phase field models) for moving boundary problems (e.g. [25, 38, 117, 146] for general reviews), for its unrivaled capabilities in morphological predictions. Indeed, one of the major advantage of this approach is that the moving interface needs not be numerically tracked. A second advantage is that many phenomena can easily be incorporated in a thermodynamically consistent manner. Hence, a large number of transformations and phenomena can be handled, such as solidification [97, 98]; phase transformations at the solid state, either displacive [141], or diffusive [11, 16, 155], involving elasticity [26, 28, 143] or plasticity [12, 13, 50]; dislocation dynamics [140]; or grain growth and recrystallization [7, 8], among others.

Different types of model have been proposed, mainly differing in the choice of the fields to describe the microstructure, and the way the free energy functional is built.

3.1.1 Model of Kim, Kim, Suzuki

In the present work, the formulation of Kim et al. [102] (thereafter sometimes referred to as KKS) has been used, following the work of Viardin [155]. The model relies classically on the so-called phase field $\phi(x, t)$ discriminating between two phases, here ferrite ($\phi = 1$) and austenite ($\phi = 0$). ϕ enters the free energy functional \mathcal{F} as follows:

$$\mathcal{F} = \int_{\Omega} \left[f_0(T, c_i, \phi) + \frac{\epsilon^2}{2} |\nabla\phi|^2 \right] d\Omega \quad (3.1)$$

where Ω is the volume of the system.

$f_0(T, c_i, \phi)$ is the homogeneous free energy density, depending on temperature T , and on the different fields characterizing the microstructure: ϕ and the solute concentrations $c_i = (c_C, c_X)^1$. The coefficient ϵ of the gradient term is assumed to be constant.

¹ c_i denote molar fractions.

Evolution equations

To obtain the evolution equations of the different fields, the free energy functional is derived with respect to time:

$$\frac{d\mathcal{F}}{dt} = \int_{x_{\min}}^{x_{\max}} \left[\left. \frac{\partial f_0}{\partial \phi} \right|_{c_i} \frac{\partial \phi}{\partial t} + \sum_i \left. \frac{\partial f_0}{\partial c_i} \right|_{\phi} \frac{\partial c_i}{\partial t} + \epsilon^2 \frac{\partial \phi}{\partial x} \times \frac{\partial}{\partial x} \left(\frac{\partial \phi}{\partial t} \right) \right] dx \quad (3.2)$$

where a 1D system with boundaries at x_{\min} and x_{\max} has been considered to render the derivation more transparent¹.

Applying the divergence theorem, the time derivative can be split into the contributions from the bulk and the surface:

$$\begin{aligned} \frac{d\mathcal{F}}{dt} = \int_{x_{\min}}^{x_{\max}} \left[\left(\frac{\partial f_0}{\partial \phi} - \epsilon \frac{\partial^2 \phi}{\partial x^2} \right) \frac{\partial \phi}{\partial t} + \sum_i \frac{\partial f_0}{\partial c_i} \frac{\partial c_i}{\partial t} \right] dx \\ + \left[\epsilon \frac{\partial \phi}{\partial x} \frac{\partial \phi}{\partial t} \right]_{x_{\min}}^{x_{\max}} \end{aligned} \quad (3.3)$$

Using the solute balances:

$$\frac{\partial c_i}{\partial t} = -\frac{\partial}{\partial x} J_i \quad (3.4)$$

where J_i is the density of flux of solute i (positive in the direction of increasing x , in m/s), together with the divergence theorem:

$$\begin{aligned} \frac{d\mathcal{F}}{dt} = \int_{x_{\min}}^{x_{\max}} \left[\left(\frac{\partial f_0}{\partial \phi} - \epsilon \frac{\partial^2 \phi}{\partial x^2} \right) \frac{\partial \phi}{\partial t} + \sum_i \frac{\partial}{\partial x} \left(\frac{\partial f_0}{\partial c_i} \right) J_i \right] dx \\ + \left[\epsilon \frac{\partial \phi}{\partial x} \frac{\partial \phi}{\partial t} + \sum_i \frac{\partial f_0}{\partial c_i} J_i \right]_{x_{\min}}^{x_{\max}} \end{aligned} \quad (3.5)$$

For a closed system ($J_i(x_{\min}) = J_i(x_{\max}) = 0$), assuming that $\partial \phi / \partial x = 0$ at the boundaries, Eq. (3.5) reduces to the bulk contribution:

$$\frac{d\mathcal{F}}{dt} = \int_{x_{\min}}^{x_{\max}} \left[\left(\frac{\partial f_0}{\partial \phi} - \epsilon \frac{\partial^2 \phi}{\partial x^2} \right) \frac{\partial \phi}{\partial t} + \sum_i \frac{\partial}{\partial x} \left(\frac{\partial f_0}{\partial c_i} \right) J_i \right] dx \quad (3.6)$$

¹ Extension to higher dimensions is straightforward.

At constant volume and temperature, \mathcal{F} must decrease with time according to the second principle of thermodynamics. Following the classical irreversible thermodynamics [68], linear relationships are assumed to hold between flows and thermodynamic forces, which ensure that dissipation is quadratic and thus always positive:

$$\frac{\partial \phi}{\partial t} = -M_\phi \left(\frac{\partial f_0}{\partial \phi} - \epsilon^2 \frac{\partial^2 \phi}{\partial x^2} \right) \quad (3.7)$$

$$\frac{\partial c_i}{\partial t} = \frac{\partial}{\partial x} \left[L_{ij} \frac{\partial}{\partial x} \left(\frac{\partial f_0}{\partial c_i} \right) \right] \quad (3.8)$$

where $M_\phi > 0$ (in $\text{m}^3\text{J/s}$) is the phase field mobility and L_{ij} (in $\text{m}^5\text{J/s}$) is the definite positive symmetric matrix of species mobilities (§3.1.2).

Homogeneous free energy density

Following Kim et al. [102], the homogeneous free energy density for multicomponent steels with α and γ phases has been postulated as follows (Fig. 3.1):

$$f_0(c_i, \phi) = W g(\phi) + f_{\text{ch}}(c_i, \phi) \quad (3.9)$$

$$f_{\text{ch}}(c_i, \phi) = h(\phi) f^\alpha(c_i^\alpha(c_i, \phi)) + \bar{h}(\phi) f^\gamma(c_i^\gamma(c_i, \phi)) \quad (3.10)$$

The first term on the right hand side is the so-called double well potential with height W proportional to the interface energy, as shown later in §3.1.2. The following particular double well potential has been chosen:

$$g(\phi) = \phi^2 (1 - \phi)^2 \quad (3.11)$$

The second and third term on the right hand side of Eq. (3.9) interpolate monotonously the free energy densities of ferrite f^α and austenite f^γ within the diffuse interface, with an odd polynomial, e.g.:

$$h(\phi) = \phi^3 (6\phi^2 - 15\phi + 10) \quad (3.12)$$

$$\bar{h}(\phi) = 1 - h(\phi)$$

which ensures that local minima remain on the axes $\phi = 0$ and $\phi = 1$.

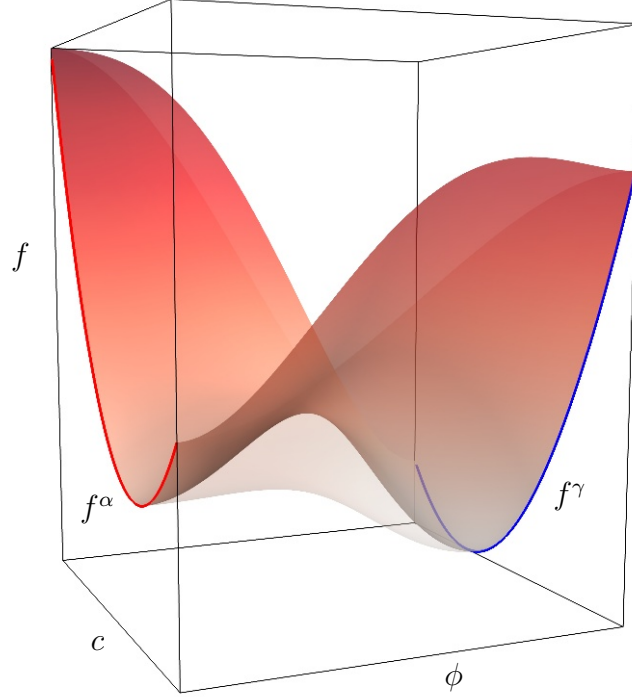


Figure 3.1: Homogeneous free energy density f_0 for a binary alloy (interpolation by $h(\phi)$ only in transparent grey).

It is worth stressing that f^α and f^γ are functions of auxiliary concentration fields c_i^α and c_i^γ , respectively. These auxiliary concentrations are linked to the real variables ϕ and c by two relationships. First, a kind of mixture law:

$$c_i = h(\phi) c_i^\alpha + \bar{h}(\phi) c_i^\gamma \quad (3.13)$$

Second, a relation, first proposed in [102] and called quasi-equilibrium in Eiken et al. [54], assuming that locally the diffusion potentials of both phases are equal:

$$\frac{\partial f^\alpha}{\partial c_i^\alpha} = \frac{\partial f^\gamma}{\partial c_i^\gamma} \quad (3.14)$$

Eq. (3.14) ensures (i) that the common tangent condition is fulfilled at equilibrium (in general situations, it enforces the parallel tangent condition); and (ii) that there is no extra contribution to the interface energy due to the concentration profile (see also [133] for a deep analysis of this problem). In addition,

Eq. (3.14) implies that $\partial f/\partial c_i = \partial f^\alpha/\partial c_i^\alpha = \partial f^\gamma/\partial c_i^\gamma$.

In general, Eqs. (3.13)-(3.14) constitute a nonlinear system (equivalent to Eqs. (1.39)_{1,5} if $h(\phi) = \phi$ and if ϕ is considered as the ferrite fraction). This nonlinear system must be solved as many times as there are nodes in the computational grid used to solve Eqs. (3.7)-(3.8). In some cases, there is little benefit to use a complicated description for the free energies, as used in the previous chapters: in particular, if the phase diagram is simple and well known, as it is the case for a number of Fe-C-X alloys in the Fe rich corner. Hence, to save some significant CPU time¹, a linearized phase diagram has been considered, following Viardin [155]. The following expressions for the free energies have been derived on the basis of regular dilute solutions:

$$V_m f^\psi = \mu_{\text{Fe}}^{\psi 0}(T, p) + \sum_i c_i^\psi \left[\mu_i^{\psi 0}(T_a, p) + RT_a (a_i \ln c_i^\psi - 1) + \epsilon_{\text{Fe};i}^\psi \right] - pV_m \quad (3.15)$$

where $\psi = \alpha, \gamma$, V_m is the molar volume supposed constant, T_a is a reference temperature chosen at the allotropic transformation $\alpha \leftrightarrow \gamma$ in pure Fe, $\mu_i^{\psi 0}$ is the reference chemical potential of species i , and $\epsilon_{\text{Fe};i}$ is the interaction parameter between Fe and solute i assumed constant. a_i are new parameters independent of phases: they have been introduced to linearize independently the binary sides Fe-C and Fe-X of the ternary phase diagram, which can be described with (i) the partition coefficients $k_i = c_i^\alpha/c_i^\gamma$ and (ii) the slopes m_i relating the temperature T^γ of the γ domain boundary to the concentrations c_i^γ :

$$k_i = \exp\left(\frac{\Delta\mu_i^0 + \Delta\epsilon_{\text{Fe};i}}{a_i RT_a}\right) \quad (3.16)$$

$$T^\gamma = T_a + \sum_i m_i c_i^\gamma \quad (3.17)$$

with $m_i = -a_i(1 - k_i)RT_a/\Delta s_{\text{Fe}}^0$. Δ denotes a difference between quantities in α and γ (e.g. $\Delta s_{\text{Fe}}^0 = s_{\text{Fe}}^{0\gamma} - s_{\text{Fe}}^{0\alpha}$ is the difference in entropy of Fe at T_a between both phases).

¹ An overhead of about 100% can easily be expended with Calphad free energies if no tricky algorithm is devised.

3.1.2 Phase field parameters

Equilibrium parameters

The magnitude of the double well W and the coefficient ϵ are related to the following physical parameters: the interface thickness δ and the interface energy γ ¹. To find these relations, the model is examined in the case of an equilibrium between two phases of infinite extensions separated by a planar interface [33, 158]: then, $\partial\phi/\partial t = 0$ and $\partial f_{\text{ch}}/\partial\phi = 0$, and Eq. (3.7) becomes:

$$\epsilon^2 \frac{d^2\phi}{dx^2} - W g'(\phi) = 0 \quad (3.18)$$

where ' stands for derivatives with respect to ϕ . Integrating twice (with the particular double well function g in Eq. (3.11)) and accounting for the boundary conditions $\lim_{x \rightarrow -\infty} \phi = 1$ and $\lim_{x \rightarrow +\infty} \phi = 0$ gives:

$$\phi(x) = \frac{1}{2} \left(1 - \tanh(2\alpha x/\delta) \right) \quad (3.19)$$

where δ is the interface thickness:

$$\delta = 2\alpha \frac{\epsilon}{\sqrt{2W}} \quad (3.20)$$

defined between two particular symmetric values of ϕ , ϕ_{min} and $\phi_{\text{max}} = 1 - \phi_{\text{min}}$, with $\alpha = \ln(\phi_{\text{max}}/\phi_{\text{min}})$.

Thanks to the introduction of the auxilliary concentrations c_i^α and c_i^γ , the interface energy accounts only for the contribution from the phase field (see [101, 102, 133]):

$$\gamma = \int_{-\infty}^{+\infty} \left(\frac{\epsilon^2}{2} \left| \frac{\partial\phi}{\partial x} \right|^2 + W g(\phi) \right) dx = \int_{-\infty}^{+\infty} \epsilon^2 \left| \frac{\partial\phi}{\partial x} \right|^2 dx \quad (3.21)$$

By combining Eq. (3.19) and Eq. (3.21), we obtain:

$$W = b\gamma/\delta \quad (3.22)$$

¹ There should be no confusion with austenite.

with $b = 6\alpha$. Hence, by inserting Eq. (3.22) into Eq. (3.20) the second phase field parameter can be written as:

$$\epsilon^2 = a \gamma \delta \quad (3.23)$$

with $a = \alpha/3$.

Kinetic parameters

As shown in [155], there are different ways to interpolate the mobilities L_{ij} within the interface between the values in the bulks. It has been shown that, for practical numerical reasons, it is better to follow [54]:

$$L_{ij}(\phi) = h(\phi) L_{ij}^\alpha + \bar{h}(\phi) L_{ij}^\gamma \quad (3.24)$$

rather than to directly interpolate diffusivities, i.e. $D_{ij}(\phi) = h(\phi) D_{ij}^\alpha + \bar{h}(\phi) D_{ij}^\gamma$ and plug back the interpolation into the mobilities as usually done for solidification (e.g. [102]). The mobilities of the bulk phases L_{ij}^α and L_{ij}^γ are deduced from their diffusivities D_{ij}^α and D_{ij}^γ respectively. By assuming that the cross terms in the mobilities are negligible (i.e. $L_{ij}^\phi = 0$), together with the linear dependency with c_i of the thermodynamic interaction parameters $\epsilon_{\text{Fe};i}$ (Eq. (3.15)), there is no cross diffusivities [155] and we get:

$$L_{ii}^\psi = \frac{V_m D_i^\psi}{\partial^2 f^\psi / \partial c_i^\psi \partial c_i^\psi} \quad (3.25)$$

The other kinetic parameter of the phase field model is the phase field mobility M_ϕ , to which the next section §3.2 is devoted.

3.2 Phase field Mobility

For achieving rapidly local equilibrium at the interface, Karma and Rappel have shown that a particular expression for M_ϕ can be derived [10, 96, 97, 98], taking advantage of the trans-interface diffusion to cancel interface friction, both scaling linearly with the interface thickness. This idea has been transposed to alloys in a crude manner by Kim et al. [102], without performing rigorously the asymptotic analysis at the basis of the expression of Karma. Instead, they have mixed both the first and second order terms to decisive, but quite intuitive, assumptions (e.g. Eq. (59) in [102]). If using the expression of [102] and its extension to multicomponent alloys [123], the result has been quite convincing from a practical point of view (e.g. [100, 122]), it deserves much more attention for at least two reasons (beside mathematical rigor).

- (i) The essential flaw when solute diffusivity is heterogeneous (so-called non-symmetric case), identified and cured by Karma [96] thanks to the ad-hoc addition of a non variational term, called anti-solute trapping current (see also the recent work in [128]). The formulation in the initial paper of Kim et al. [102] does not account properly for this flaw. More recently, an attempt to put on a firmer footing the initial expression by using arguments from Karma has been proposed in [99], but keeping the obscure mixed 1st and 2nd orders.
- (ii) Applying blindly the extension to multicomponent [123] to Fe-C-Mn does not give good results when compared to experimental kinetics, in particular when paraequilibrium is desired [155]. A modified expression must therefore be proposed [155, 156].

Moreover, contrary to solidification, at the solid state the phase field mobility is usually assigned a value taken from experiments [71, 108]. But to match the experimental kinetics, M_ϕ is most often considered as a fitting parameter [111, 112, 113, 160]. Even in that case, the need for an accurate control of the outcome of the phase field model is needed. This could be achieved by a deep analysis of the phase field mobility.

Before performing the matched asymptotic analysis §3.2.2 necessary to settle more rigorously the expression for the phase field mobility used in [155] and

in the present work, we will show in §3.2.1 the analogy between the particular phase field model used and the thick interface model of the previous chapter. In particular, we will derive the free energy balance¹ introduced in §2, a necessary step for the further analysis of the results.

3.2.1 Interface dissipation

Following the analysis of Ahmad et al. [9] and Loginova et al. [107], we have considered a planar diffuse interface, moving at velocity v , in a steady state. In that case, the partial differential equation (PDE) can be recast into an ordinary differential equation (ODE) of space only. For the phase field, Eq. (3.7) reads:

$$-\frac{v}{M_\phi} \frac{\partial \phi}{\partial x} = \epsilon^2 \frac{d^2 \phi}{dx^2} - W g' - \frac{df_{\text{ch}}}{d\phi} \quad (3.26)$$

Together with the boundary conditions:

$$\lim_{x \rightarrow -\infty} \phi = 1 \quad (3.27)$$

$$\lim_{x \rightarrow +\infty} \phi = 0 \quad (3.28)$$

$$\lim_{x \rightarrow \pm\infty} d\phi/dx = 0 \quad (3.29)$$

The last term on the right hand side of Eq. (3.26) can be expressed using df_{ch} , the full derivative of f_{ch} :

$$\frac{\partial f_{\text{ch}}}{\partial \phi} = \frac{df_{\text{ch}}}{d\phi} - \sum_i \frac{\partial f_{\text{ch}}}{\partial c_i} \frac{dc_i}{d\phi} \quad (3.30)$$

Inserting Eq. (3.30) in Eq. (3.26):

$$-\frac{v}{M_\phi} \frac{d\phi}{dx} = \epsilon^2 \frac{d^2 \phi}{dx^2} - W g' - \frac{df_{\text{ch}}}{d\phi} + \sum_i \frac{\partial f_{\text{ch}}}{\partial c_i} \frac{dc_i}{d\phi} \quad (3.31)$$

¹ same as the Gibbs energy balance provided that pV_m is negligible as it is the case.

Multiplying both sides by $d\phi/dx$ and integrating across the interfacial region over the thickness δ :

$$-\frac{v}{M_\phi} \frac{J}{\delta} = - \int_\delta df_{\text{ch}} + \sum_i \int_\delta \frac{\partial f_{\text{ch}}}{\partial c_i} \frac{dc_i}{dx} dx \quad (3.32)$$

where we have used the fact that ϕ outside $[-\delta/2; +\delta/2]$ decays sufficiently fast to assume the following:

$$\left[\left(\frac{d\phi}{dx} \right)^2 \right]_\delta \approx \left[\left(\frac{d\phi}{dx} \right)^2 \right]_\infty = 0 \quad (3.33)$$

$$[g]_\delta \approx [g]_\infty = 0 \quad (3.34)$$

$$\int_\delta \left(\frac{d\phi}{dx} \right)^2 dx \approx \int_\infty \left(\frac{d\phi}{dx} \right)^2 dx = \frac{J}{\delta} \quad (3.35)$$

where $[\Psi]_x = \Psi(+x/2) - \Psi(-x/2)$.

Integrating the last integral by parts leads to:

$$\frac{v}{M_\phi} \frac{J}{\delta} = \left[f_{\text{ch}} - \sum_i (c_i - c_i^\alpha) \frac{\partial f_{\text{ch}}}{\partial c_i} \right]_\delta + \sum_i \int_\delta (c_i - c_i^\alpha) \frac{d}{dx} \left(\frac{\partial f_{\text{ch}}}{\partial c_i} \right) dx \quad (3.36)$$

where it is assumed that $c_i(-\delta/2) \approx c_i^\alpha = \text{cste}$.

We recognize the balance of free energy Eq. (2.16) with

(i) on the right hand side, the driving force Eq. (2.17) (positive for $\gamma \rightarrow \alpha$):

$$DF^* = \left[f_{\text{ch}} - \sum_i (c_i - c_i^\alpha) \frac{\partial f_{\text{ch}}}{\partial c_i} \right]_\delta \quad (3.37)$$

(ii) on the right hand side, the dissipation (positive) by trans-interface diffusion (Eqs. (2.19),(2.2)):

$$\Delta G^{\text{diff}} = - \sum_i \int_\delta (c_i - c_i^\alpha) \frac{d}{dx} \left(\frac{\partial f_{\text{ch}}}{\partial c_i} \right) dx \quad (3.38)$$

(iii) on the left hand side, the dissipation by friction Eq. (2.22):

$$\Delta G^{\text{friction}} = \frac{v}{M_\phi} \frac{J}{\delta} \quad (3.39)$$

For assessing the dissipation due to friction from numerical results (§3.3.2), it is more convenient to resort to an alternative expression. For that purpose, $\partial f_{\text{ch}}/\partial\phi$ is explicitied using Eq. (3.10) and Eq. (3.26):

$$-\frac{v}{M_\phi} \frac{d\phi}{dx} = \epsilon^2 \frac{d^2\phi}{dx^2} - Wg' + h'\Delta w \quad (3.40)$$

where $\Delta w = f^\gamma(c^\gamma) - f^\alpha(c^\alpha) - \sum_i (c_i^\gamma - c_i^\alpha) df^\gamma/dc_i^\gamma$ is the local driving force for the transformation $\gamma \rightarrow \alpha$ (already introduced in §2.1, see Fig. 2.1). Multiplying again by $d\phi/dx$ and integrating over the interface thickness together with Eqs. (3.33)-(3.35) gives:

$$\frac{v}{M_\phi} \frac{J}{\delta} = - \int_\delta \Delta w \frac{dh}{dx} dx \approx - \int_\infty \Delta w \frac{dh}{dx} dx \quad (3.41)$$

Finally:

$$\Delta G^{\text{friction}} \approx - \int_\infty \Delta w \frac{dh}{dx} dx \quad (3.42)$$

3.2.2 2nd order matched asymptotic analysis

From the previous section, the relationship between M_ϕ and the interface mobility M seems straightforward: $M = M_\phi/\mathcal{J}$ (Eq. (3.39)). However, it is not clear how long this relation holds when the interface thickness δ is varied. Indeed, replacing integrals over δ by integrals on the whole system introduces errors which are not well controlled as δ changes, at least as long as any expression for this change is not proposed. To do so, we have followed the method of matched asymptotic analysis up to second order proposed by Almgren [10] (see also [62]). The analysis is carried out for the binary Fe-C system, and c denotes c_C . Generalization to multicomponent alloys (e.g. Fe-C-X) is straightforward provided that the mobilities L_i for the additional solute elements i do not scale as δ , i.e. $L_i^{(0)} \neq 0$. Consequently, this kind of generalization cannot apply to paraequilibrium and intermediate regimes, unfortunately.

To simplify the analysis, we have only considered a flat interface, reducing the equations of evolution to 1D PDE (neglecting any effect of the curvature such as the stretch interface term or the tangential diffusion [10]).

$$\beta \frac{\partial \phi}{\partial t} = a\gamma\delta \frac{\partial^2 \phi}{\partial x^2} - \frac{b\gamma}{\delta} g' + h' \Delta w \quad (3.43)$$

$$\frac{\partial c}{\partial t} = \frac{\partial}{\partial x} \left(L \frac{\partial}{\partial x} f_c \right) \quad (3.44)$$

where the phase field parameters ϵ^2 and W have been replaced by their expressions with respect to γ and δ , respectively Eqs. (3.22),(3.23), and where $\beta = 1/M_\phi$. For brevity, f_c is used to denote $\partial f/\partial c|_\phi$.

Then, the equations are non dimensionalized with respect to the following scales: a length Λ for space, typical of the microstructure dimensions (e.g. $\sim 1 \mu\text{m}$); a time scale defined with the fastest diffusivity, e.g. D_C^α , i.e. Λ^2/D_C (e.g. $\sim 10^{-3}$ s); a typical energy, chosen here related to the interface energy, γ/Λ

(e.g. $\sim 10^5$ J/m³). Hence:

$$\tilde{\beta} \tilde{\delta} \frac{\partial \phi}{\partial \tilde{t}} = a \tilde{\delta}^2 \frac{\partial^2 \phi}{\partial \tilde{x}^2} - b g' + \tilde{\delta} h' \Delta \tilde{w} \quad (3.45)$$

$$\frac{\partial c}{\partial \tilde{t}} = \frac{\partial}{\partial \tilde{x}} \left(\tilde{L} \frac{\partial}{\partial \tilde{x}} \tilde{f}_c \right) \quad (3.46)$$

where \sim denotes dimensionless quantities: $x = \tilde{x} \Lambda$, $\delta = \tilde{\delta} \Lambda$, $t = \tilde{t} \Lambda^2 / D_C^\alpha$, $\Delta w = \Delta \tilde{w} \gamma / \Lambda$, $f_c = \tilde{f}_c \gamma / \Lambda$, $\beta = \tilde{\beta} \gamma \Lambda / D_C^\alpha$ and $L = \tilde{L} D_C^\alpha \Lambda / \gamma$.

A Taylor expansion can be applied to the kinetic parameters β with the interface thickness δ as a the small parameter:

$$\tilde{\beta} = \tilde{\beta}^{(1)} \tilde{\delta} + \tilde{\beta}^{(2)} \tilde{\delta}^2 + \mathcal{O}(\tilde{\delta}^3) \quad (3.47)$$

where it has been assumed that (i) the chemical mobilities L^α and L^γ are independent of δ (for alternative cases see [65]); (ii) ϕ and c are evolving on comparable time scales whatever the interface thickness (hence $\beta^{(0)} = 0$).

The last step before performing the asymptotic expansions is to recast the evolution equations into the moving frame of the interface. Neglecting the transient terms [97, 98]:

$$-\delta^2 v (\beta^{(1)} + \delta \beta^{(2)}) \frac{d\phi}{dx} = a \delta^2 \frac{d^2 \phi}{dx^2} - b g' + \delta h' \Delta w \quad (3.48)$$

$$-v \frac{dc}{dx} = \frac{d}{dx} \left(L \frac{\partial}{\partial x} f_c \right) \quad (3.49)$$

where tildes have been dropped for clarity, because all quantities are now dimensionless and there will be no ambiguity; and where x is now centered at the interface.

The associated boundary conditions are:

$$\lim_{x \rightarrow -\infty} \phi = 1 \quad (3.50)$$

$$\lim_{x \rightarrow +\infty} \phi = 0 \quad (3.51)$$

As it will appear below, it is not necessary to specify the boundary conditions for the concentration field c .

3.2.2.1 Outer expansion

Now, we proceed to the asymptotic expansion per se. First, a regular expansion, called outer because the behaviors of the bulk will be recovered, is undertaken. All fields are expanded in series of functions with δ as the small parameter of the expansion:

$$\psi(x) = \bar{\psi}^{(0)}(x) + \delta \bar{\psi}^{(1)}(x) + \delta^2 \bar{\psi}^{(2)}(x) + \mathcal{O}(\delta^3) \quad (3.52)$$

with ψ any function of space entering Eqs. (3.48)-(3.49) (e.g. $\phi(x)$, $c(x)$...).

Inserting the expansions into the evolution equations, keeping second order terms at most, gives:

$$\begin{aligned} -\beta^{(1)} \delta^2 v \frac{d\bar{\phi}^{(0)}}{dx} &= a \delta^2 \frac{d^2 \bar{\phi}^{(0)}}{dx^2} - b g^{(0)} - b g''^{(0)} \delta \bar{\phi}^{(1)} \\ &\quad - \delta^2 b \left(g''^{(0)} \bar{\phi}^{(2)} + \frac{1}{2} g'''^{(0)} (\bar{\phi}^{(1)})^2 \right) \\ &\quad + \delta \left(h^{(0)} + \delta h''^{(0)} \bar{\phi}^{(1)} \right) \left(\Delta \bar{w}^{(0)} + \delta \Delta \bar{w}^{(1)} \right) \end{aligned} \quad (3.53)$$

$$\begin{aligned} -v \left(\frac{d\bar{c}^{(0)}}{dx} + \delta \frac{d\bar{c}^{(1)}}{dx} + \delta^2 \frac{d\bar{c}^{(2)}}{dx} \right) \\ = \frac{d}{dx} \left((\bar{L}^{(0)} + \delta \bar{L}^{(1)} + \delta^2 \bar{L}^{(2)}) \frac{d}{dx} (\bar{f}_c^{(0)} + \delta \bar{f}_c^{(1)} + \delta^2 \bar{f}_c^{(2)}) \right) \end{aligned} \quad (3.54)$$

where¹ $\psi^{(n)} = \psi(\phi^{(n)})$ for any function $\psi(\phi)$ and any order n .

Now terms of equal order in δ are collected and the resulting hierarchy of equations is solved order by order, exploiting the fields at the previous orders.

Order 0

For the phase field ϕ , we simply get:

$$\bar{g}'^{(0)} = 0 \quad (3.55)$$

¹ In this section, it is implicitly considered that $g^{(n)}$ and $h^{(n)}$ are functions of the order n outer expansion $\bar{\phi}^{(n)}$

which has three possible solutions: $\bar{\phi}^{(0)} = 0$, $\bar{\phi}^{(0)} = 1$ and $\bar{\phi}^{(0)} = 1/2$. Among these solutions, only the first two are compatible with the boundary conditions Eqs. (3.50)-(3.51):

$$\bar{\phi}^{(0)} = 1 \quad \text{for } x < 0 \quad (3.56)$$

$$\bar{\phi}^{(0)} = 0 \quad \text{for } x > 0 \quad (3.57)$$

At order 0, the outer expansion of ϕ is a trivial step function. For the concentration field c , we get:

$$-v \frac{d\bar{c}^{(0)}}{dx} = \frac{d}{dx} \left(L^{(0)} \frac{d}{dx} f_c^{(0)} \right) \quad (3.58)$$

where $L^{(0)} = h^{(0)}L^\alpha + \bar{h}^{(0)}L^\gamma$.

Using Eqs. (3.56)-(3.57), together with the conditions relating the auxilliary concentrations to ϕ and c Eqs. (3.13)-(3.14), we obtain:

$$-v \frac{d\bar{c}^{\alpha(0)}}{dx} = \frac{d}{dx} \left(L^\alpha \frac{df_c^{\alpha(0)}}{dx} \right) \quad \text{for } x < 0 \quad (3.59)$$

$$-v \frac{d\bar{c}^{\gamma(0)}}{dx} = \frac{d}{dx} \left(L^\gamma \frac{df_c^{\gamma(0)}}{dx} \right) \quad \text{for } x > 0 \quad (3.60)$$

which are the usual diffusion equations in the bulk.

Orders 1 and 2

For ϕ , Eq. (3.54) gives at first order:

$$-b g''^{(0)} \bar{\phi}^{(1)} + h'^{(0)} \Delta \bar{w}^{(0)} = 0 \quad (3.61)$$

Eqs. (3.56)-(3.57) together with Eq. (3.12) imply that $h'^{(0)} = 0$. Then, Eq. (3.61) reads: $\bar{\phi}^{(1)} = 0$, i.e. there is no correction at first order to the step function $\bar{\phi}^{(0)}$. This has many simplifying consequences. Indeed, $L^{(1)} = 0$ and the diffusion

equations are also recovered at first order:

$$-v \frac{d\bar{c}^{(1)}}{dx} = \frac{d}{dx} \left(L^\alpha \frac{df_c^{(1)}}{dx} \right) \quad \text{for } x < 0 \quad (3.62)$$

$$-v \frac{d\bar{c}^{(1)}}{dx} = \frac{d}{dx} \left(L^\gamma \frac{df_c^{(1)}}{dx} \right) \quad \text{for } x > 0 \quad (3.63)$$

It is straightforward to show that similar results are obtained at order 2, i.e. there is no correction to the step function $\bar{\phi}^{(2)} = 0$, and the diffusion equations still hold in the bulk.

3.2.2.2 Inner expansion

As shown previously with the outer expansion, the structure of the fields within the interface is lost because the small parameters of the regular expansion multiply the highest order derivative in Eq. (3.45) [22, 24, 105]. To recover the inner structure, one must proceed to a rescaling of space by the interface thickness $z = x/\delta$. Then, when $\delta \rightarrow 0$ the new space coordinate is stretched such that the detail of the inner boundary layer is preserved.

First the governing equations in the moving frame of the interface Eqs. (3.48)-(3.49) are recast in the stretched frame:

$$-\delta v (\beta^{(1)} + \delta \beta^{(2)}) \frac{d\phi}{dz} = a \frac{d^2\phi}{dz^2} - b g' + \delta h' \Delta w \quad (3.64)$$

$$-\delta v \frac{dc}{dz} = \frac{d}{dz} \left(L \frac{df_c}{dz} \right) \quad (3.65)$$

All fields are then expanded with new series of functions depending on z :

$$\psi(z) = \psi^{(0)}(z) + \delta \psi^{(1)}(z) + \delta^2 \psi^{(2)}(z) + \mathcal{O}(\delta^3) \quad (3.66)$$

where ψ stands for all fields appearing in Eqs. (3.64) and (3.65). Because f_c and ω are related to f and c , their respective expansions are related by (at most at

first order):

$$f = f^{(0)} + \delta f_c^{(0)} c^{(1)} + \mathcal{O}(\delta^2) \quad (3.67)$$

$$w = f - f_c c = (f^{(0)} + \delta f^{(1)}) - (f_c^{(0)} + \delta f_c^{(1)})(c^{(0)} - \delta c^{(1)}) + \mathcal{O}(\delta^2) \quad (3.68)$$

such that

$$w^{(0)} = f^{(0)} - f_c^{(0)} c^{(0)} \quad (3.69)$$

$$w^{(1)} = f^{(1)} - f_c^{(1)} c^{(0)} - f_c^{(0)} c^{(1)} \quad (3.70)$$

Inserting all expansions into Eqs. (3.64)-(3.65) gives (keeping terms of second order at most):

$$\begin{aligned} -\delta v (\beta^{(1)} + \delta \beta^{(2)}) \left(\frac{d\phi^{(0)}}{dz} + \delta \frac{d\phi^{(1)}}{dz} \right) &= a \left(\frac{d^2\phi^{(0)}}{dz^2} + \delta \frac{d^2\phi^{(1)}}{dz^2} + \delta^2 \frac{d^2\phi^{(2)}}{dz^2} \right) \\ &- b \left(g^{(0)} + g^{(0)}\phi^{(1)}\delta + \delta^2 \left[g^{(0)}\phi^{(2)} + \frac{1}{2} g^{(0)}(\phi^{(1)})^2 \right] \right) \\ &+ \delta (h^{(0)} + h^{(0)}\phi^{(1)}\delta) (\Delta w^{(0)} + \delta \Delta w^{(1)}) \quad (3.71) \end{aligned}$$

$$\begin{aligned} -\delta v \left(\frac{dc^{(0)}}{dt} + \delta \frac{dc^{(1)}}{dt} \right) \\ = \frac{d}{dz} \left(\left(L^{(0)} + \delta L^{(1)} + \delta^2 L^{(2)} \right) \left(\frac{df_c^{(0)}}{dz} + \delta \frac{df_c^{(1)}}{dz} + \delta^2 \frac{df_c^{(2)}}{dz} \right) \right) \quad (3.72) \end{aligned}$$

There are no boundary conditions per se necessary to determine the integration constants when solving the equations order by order, because there are no real boundaries. It is the conditions relating the outer and inner expansions, called matching conditions, which play this role.

Those conditions read for any field ψ :

$$\lim_{z \rightarrow \pm\infty} \psi^{(0)}(z) \sim \lim_{x \rightarrow 0^\pm} \bar{\psi}^{(0)}(x) \quad (3.73)$$

$$\lim_{z \rightarrow \pm\infty} \psi^{(1)}(z) \sim \lim_{x \rightarrow 0^\pm} \left(\frac{d\bar{\psi}^{(0)}}{dx}(x) \times z + \bar{\psi}^{(1)}(x) \right) \quad (3.74)$$

Next, as for the outer expansion, we collect terms order by order and solve sequentially the resulting hierarchy of equations using the solutions at the previous order.

Order 0

For the phase field:

$$a \frac{d^2 \phi^{(0)}}{dz^2} - b g'^{(0)} = 0 \quad (3.75)$$

Integration of Eq. (3.75) together with the matching conditions for $\phi^{(0)}$ give the equilibrium solution for $\phi^{(0)}$ (cf. Eq. (3.19)):

$$\phi^{(0)} = \frac{1}{2}(1 - \tanh(az/b)) \quad (3.76)$$

For the concentration field:

$$\frac{d}{dz} \left(L^{(0)} \frac{d}{dz} f_c^{(0)} \right) = 0 \quad (3.77)$$

which leads to:

$$\frac{d}{dz} f_c^{(0)} = \frac{\text{const}}{L^{(0)}} \quad (3.78)$$

The matching conditions:

$$\lim_{z \rightarrow \pm\infty} f_c^{(0)}(z) = \bar{f}_c^{(0)}(0^\pm) \quad (3.79)$$

imply that $f_c^{(0)}$ remains bounded as $z \rightarrow \pm\infty$: the integration constant must be 0 and $f_c^{(0)} = \text{const}$. In the most general case, $f_c^{(0)} = \text{const}$ corresponds to parallel tangents, as in the Mixed mode model of Sietsma and van der Zwaag [144] (§2.3.1). Local equilibrium is a particular case with $f_c^{(0)} = 0$. In any case, $c^{\alpha(0)}$, $c^{\gamma(0)}$, $f^{\alpha(0)}$ and $f^{\gamma(0)}$ are all constant: finally, we obtain a constant driving force over the interface at order 0, matching the outer expansion at $x = 0$:

$$\Delta w^{(0)} = \Delta \bar{w}^{(0)}(0) \quad (3.80)$$

Order 1

Rearranging the first order term in Eq. (3.71) and introducing the following self-adjoint linear differential operator:

$$\mathcal{L}(\psi) = a \frac{d^2\psi}{dz^2} - b g''^{(0)}\psi \quad (3.81)$$

gives:

$$\mathcal{L}(\phi^{(1)}) = -v \beta^{(1)} \frac{d\phi^{(0)}}{dz} - h'^{(0)} \Delta w^{(0)} \quad (3.82)$$

The derivation of Eq. (3.75) with respect to z reads:

$$\mathcal{L}\left(\frac{d\phi^{(0)}}{dz}\right) = 0 \quad (3.83)$$

Therefore $d\phi^{(0)}/dz$ belongs to the kernel of \mathcal{L} , and must be orthogonal to the right hand side of Eq. (3.82) [51, 166]. The resulting solvability condition reads:

$$\int_{-\infty}^{+\infty} \frac{d\phi^{(0)}}{dz} \left(-v \beta^{(1)} \frac{d\phi^{(0)}}{dz} - h'^{(0)} \Delta w^{(0)} \right) dz = 0 \quad (3.84)$$

Using Eqs. (3.80) and $\int_{-\infty}^{\infty} (h'^{(0)} d\phi^{(0)}/dz) dz = -1$, one obtains:

$$v \beta^{(1)} \mathcal{J} = \Delta \bar{w}^{(0)}(0) \quad (3.85)$$

with $\mathcal{J} = \int_{-\infty}^{+\infty} (d\phi^{(0)}/dz)^2 dz$.

Hence, the phase field equation at order 1 balances the dissipation by interface friction with the interface driving force at order 0, as found in the approximate analysis Eq. (3.41) in §3.2.1. If the asymptotic analysis is stopped at first order, the phase field mobility is simply proportional to the interface mobility, as:

$$M_\phi = M \mathcal{J} / \delta \quad (3.86)$$

At order 1, Eq. (3.72) gives for concentration:

$$-v \frac{dc^{(0)}}{dz} = \frac{d}{dz} \left(L^{(0)} \frac{df_c^{(1)}}{dz} \right) \quad (3.87)$$

Integrating from $z = 0$ leads to:

$$-v c^{(0)} + A = L^{(0)} \frac{df_c^{(1)}}{dz} \quad (3.88)$$

where A is an integration constant.

Integrating once again to express $f_c^{(1)}$:

$$f_c^{(1)} = B + \int_0^z \left(\frac{A}{L^{(0)}} - \frac{v}{L^{(0)}} c^{(0)} \right) d\rho \quad (3.89)$$

The integral diverges as $z \rightarrow \pm\infty$ because the limits of the integrand are constants (e.g. $\lim_{+\infty} L^{(0)} = L^\gamma$ and $\lim_{-\infty} c^{(0)} = c^{\gamma(0)}$). So, we split the integral in two parts as follows.

- For $z \rightarrow +\infty$ (on the austenite side):

$$\begin{aligned} f_c^{(1)} = B + & \left(\frac{A}{L^\gamma} - \frac{v}{L^\gamma} c^{\gamma(0)} \right) z \\ & + A \int_0^z \left(\frac{1}{L^{(0)}} - \frac{1}{L^\gamma} \right) d\rho - v \int_0^z \left(\frac{c^{(0)}}{L^{(0)}} - \frac{c^{\gamma(0)}}{L^\gamma} \right) d\rho \end{aligned} \quad (3.90)$$

With the matching conditions at first order Eq. (3.74), we identify the linear part easily and the remaining:

$$\frac{d}{dx} \bar{f}_c^{(0)}(0^-) = \frac{A}{L^\alpha} - \frac{v}{L^\alpha} c^{\alpha(0)} \quad (3.91)$$

$$\bar{f}_c^{(1)}(0^-) = B + A \int_0^{-\infty} \left(\frac{1}{L^{(0)}} - \frac{1}{L^\alpha} \right) d\rho - v \int_0^{-\infty} \left(\frac{c^{(0)}}{L^{(0)}} - \frac{c^{\alpha(0)}}{L^\alpha} \right) d\rho \quad (3.92)$$

- For $z \rightarrow -\infty$ (on the ferrite side):

$$\begin{aligned} f_c^{(1)} = B + & \left(\frac{A}{L^\alpha} - \frac{v}{L^\alpha} c^{\alpha(0)} \right) z \\ & + A \int_0^z \left(\frac{1}{L^{(0)}} - \frac{1}{L^\alpha} \right) d\rho - v \int_0^z \left(\frac{c^{(0)}}{L^{(0)}} - \frac{c^{\alpha(0)}}{L^\alpha} \right) d\rho \end{aligned} \quad (3.93)$$

The matching conditions give:

$$\frac{d}{dx} \bar{f}_c^{(0)}(0^+) = \frac{A}{L^\gamma} - \frac{v}{L^\gamma} c^{\gamma(0)} \quad (3.94)$$

$$\bar{f}_c^{(1)}(0^+) = B + A \int_0^{+\infty} \left(\frac{1}{L^{(0)}} - \frac{1}{L^\gamma} \right) d\rho - v \int_0^{+\infty} \left(\frac{c^{(0)}}{L^{(0)}} - \frac{c^{\gamma(0)}}{L^\gamma} \right) d\rho \quad (3.95)$$

We introduce the following notations to simplify Eqs. (3.91)-(3.95):

$$G^\alpha = \int_{-\infty}^0 \left(\frac{1}{L^{(0)}} - \frac{1}{L^\alpha} \right) d\rho \quad (3.96)$$

$$G^\gamma = \int_0^{+\infty} \left(\frac{1}{L^\gamma} - \frac{1}{L^{(0)}} \right) d\rho \quad (3.97)$$

$$F^\alpha = \int_{-\infty}^0 \left(\frac{c^{(0)}}{L^{(0)}} - \frac{c^\alpha}{L^\alpha} \right) d\rho \quad (3.98)$$

$$F^\gamma = \int_0^{+\infty} \left(\frac{c^\gamma}{L^\gamma} - \frac{c^{(0)}}{L^{(0)}} \right) d\rho \quad (3.99)$$

Eqs. (3.92) and (3.95) then read:

$$\bar{f}_c^{(1)}(0^-) = B - A G^\alpha + v F^\alpha \quad (3.100)$$

$$\bar{f}_c^{(1)}(0^+) = B - A G^\gamma + v F^\gamma \quad (3.101)$$

And Eqs. (3.91) and (3.94) become:

$$L^\alpha \frac{d\bar{f}_c^{(0)}}{dx}(0^-) = A - v c^{\alpha(0)} \quad (3.102)$$

$$L^\gamma \frac{d\bar{f}_c^{(0)}}{dx}(0^+) = A - v c^{\gamma(0)} \quad (3.103)$$

It is worth stressing that the left hand sides of Eqs. (3.102) and (3.103) involve outer expansions whereas the right hand sides involve outer expansions.

If we subtract Eq. (3.102) from Eq. (3.103), the solute balance at a sharp interface

is recovered at order 0:

$$-L^\gamma \frac{d}{dx} \bar{f}_c^{\gamma(0)} + L^\alpha \frac{d}{dx} \bar{f}_c^{\alpha(0)} = v (\bar{c}^{\gamma(0)} - \bar{c}^{\alpha(0)}) \quad (3.104)$$

where we have used the matching conditions at order 0 to relate the inner concentrations to the outer ones.

Moreover, by subtracting Eq. (3.100) from Eq. (3.101), we obtain the jump of diffusion potential at the interface at first order:

$$\llbracket \bar{f}_c^{(1)} \rrbracket = \bar{f}_c^{(1)}(0^+) - \bar{f}_c^{(1)}(0^-) = A (G^\alpha - G^\gamma) + v (F^\gamma - F^\alpha) \quad (3.105)$$

where A can be expressed with the outer concentration fields by adding Eqs. (3.102) and (3.103):

$$A = \frac{1}{2} \left(L^\alpha \frac{d\bar{f}_c^{\alpha(0)}}{dx} + L^\gamma \frac{d\bar{f}_c^{\gamma(0)}}{dx} \right) + \frac{1}{2} v (\bar{c}^{\alpha(0)} + \bar{c}^{\gamma(0)}) \quad (3.106)$$

As mentioned above, the tangents to f^γ and f^α are parallel at order 0 ($\bar{f}_c^{\gamma(0)} = \bar{f}_c^{\alpha(0)}$). However, Eq. (3.105) indicates that there is a deviation from the common tangent condition at the interface scaling as δ , which involves the difference in chemical mobilities between the bulk phases.

In the particular symmetric case where $L^\alpha = L^\gamma = L$, we get trivially $G^\alpha = G^\gamma = 0$, as well as:

$$F^\alpha = \frac{1}{L} (c^{\gamma(0)} - c^{\alpha(0)}) \int_{-\infty}^0 \bar{h}^{(0)} dz \quad (3.107)$$

$$F^\gamma = \frac{1}{L} (c^{\gamma(0)} - c^{\alpha(0)}) \int_0^{+\infty} h^{(0)} dz \quad (3.108)$$

where we have used the mixture law at order 0: $c^{(0)} = h^{(0)} c^{\alpha(0)} + \bar{h}^{(0)} c^{\gamma(0)}$.

It follows that $F^\alpha = F^\gamma$, and the first order jump in diffusion potential at the interface Eq. (3.105) vanishes, as found initially in [97, 98] for a symmetric model.

Order 2

Collecting all terms at order 2 in Eq. (3.71) for ϕ gives:

$$\begin{aligned}
& -v\beta^{(1)} \frac{d\phi^{(1)}}{dz} - v\beta^{(2)} \frac{d\phi^{(0)}}{dz} \\
& = a \frac{d^2\phi^{(2)}}{dz^2} - b \left(g''^{(0)} \phi^{(2)} + \frac{1}{2} g'''^{(0)} (\phi^{(1)})^2 \right) \\
& \quad + h''^{(0)} \phi^{(1)} \Delta w^{(0)} + h'^{(0)} \Delta w^{(1)} \quad (3.109)
\end{aligned}$$

where we recognize the self-adjoint linear operator \mathcal{L} (Eq. (3.81)):

$$\begin{aligned}
\mathcal{L}(\phi^{(2)}) = & -v\beta^{(1)} \frac{d\phi^{(1)}}{dz} - v\beta^{(2)} \frac{d\phi^{(0)}}{dz} + b \frac{1}{2} g'''^{(0)} (\phi^{(1)})^2 \\
& - h''^{(0)} \phi^{(1)} \Delta w^{(0)} - h'^{(0)} \Delta w^{(1)} \quad (3.110)
\end{aligned}$$

Then, the right hand side of Eq. (3.110) must be orthogonal to its kernel $d\phi^{(0)}/dz$, i.e.:

$$\int_{-\infty}^{+\infty} \mathcal{L}(\phi^{(2)}) \frac{d\phi^{(0)}}{dz} dz = I_1 + I_2 + I_3 = 0 \quad (3.111)$$

where I_1 gathers all terms involving $\phi^{(1)}$:

$$I_1 = \int_{-\infty}^{+\infty} \left(-v\beta^{(1)} \frac{d\phi^{(1)}}{dz} + b \frac{1}{2} g'''^{(0)} (\phi^{(1)})^2 - h''^{(0)} \phi^{(1)} \Delta w^{(0)} \right) \frac{d\phi^{(0)}}{dz} dz \quad (3.112)$$

where I_2 is related to friction:

$$I_2 = \int_{-\infty}^{+\infty} -v\beta^{(2)} \left(\frac{d\phi^{(0)}}{dz} \right)^2 dz = -v\beta^{(2)} \mathcal{J} \quad (3.113)$$

and where I_3 is related to the trans-interface diffusion contribution:

$$I_3 = \int_{-\infty}^{+\infty} -h'^{(0)} \Delta w^{(1)} \frac{d\phi^{(0)}}{dz} dz \quad (3.114)$$

First, we assume that $\phi^{(1)}$ is even because \mathcal{L} is an even operator and because the right hand side of Eq. (3.82) is also even [10]. Second $\phi^{(0)}$ is odd. Consequently

$I_1 = 0$, and the solvability condition Eq. (3.111) becomes:

$$v \beta^{(2)} \mathcal{J} = - \int_{-\infty}^{+\infty} h^{(0)} \Delta w^{(1)} \frac{d\phi^{(0)}}{dz} dz \quad (3.115)$$

$\Delta w^{(1)}$ can be written explicitly using Eqs. (3.67)-(3.70):

$$\Delta w^{(1)} = f_c^{\gamma(1)} c^{\gamma(0)} - f_c^{\alpha(1)} c^{\alpha(0)} = f_c^{(1)} (c^{\gamma(0)} - c^{\alpha(0)}) \quad (3.116)$$

Then:

$$\begin{aligned} v \beta^{(2)} \mathcal{J} &= - \int_{-\infty}^{+\infty} h^{(0)} \frac{d\phi^{(0)}}{dz} f_c^{(1)} (c^{\gamma(0)} - c^{\alpha(0)}) dz \\ &= - (c^{\gamma(0)} - c^{\alpha(0)}) \int_{-\infty}^{+\infty} \frac{dh^{(0)}}{dz} f_c^{(1)} dz \end{aligned} \quad (3.117)$$

Splitting the integral to make possible the integration by parts gives:

$$\int_{-\infty}^{+\infty} \frac{dh^{(0)}}{dz} f_c^{(1)} dz = -B + \int_{-\infty}^0 \bar{h}^{(0)} \frac{df_c^{(1)}}{dz} dz - \int_0^{+\infty} h^{(0)} \frac{df_c^{(1)}}{dz} dz \quad (3.118)$$

Using Eq. (3.88) to express $df_c^{(1)}/dz$, Eq. (3.118) becomes:

$$\begin{aligned} \int_{-\infty}^{+\infty} \frac{dh^{(0)}}{dz} f_c^{(1)} dz &= -B + A \int_{-\infty}^0 \frac{\bar{h}^{(0)}}{L^{(0)}} dz - v \int_{-\infty}^0 \frac{\bar{h}^{(0)}}{L^{(0)}} c^{(0)} dz \\ &\quad - A \int_0^{+\infty} \frac{h^{(0)}}{L^{(0)}} dz + v \int_0^{+\infty} \frac{h^{(0)}}{L^{(0)}} c^{(0)} dz \end{aligned} \quad (3.119)$$

Finally Eq. (3.117) reads:

$$v \beta^{(2)} \mathcal{J} = (c^{\gamma(0)} - c^{\alpha(0)}) \left[B + A(\tilde{G}^\gamma - \tilde{G}^\alpha) - v(\tilde{F}^\gamma - \tilde{F}^\alpha) \right] \quad (3.120)$$

where

$$\tilde{G}^\gamma = \int_0^{+\infty} \frac{h^{(0)}}{L^{(0)}} dz \quad (3.121)$$

$$\tilde{G}^\alpha = \int_{-\infty}^0 \frac{\bar{h}^{(0)}}{L^{(0)}} dz \quad (3.122)$$

$$\tilde{F}^\gamma = \int_0^{+\infty} \frac{h^{(0)}}{L^{(0)}} c^{(0)} dz \quad (3.123)$$

$$\tilde{F}^\alpha = \int_{-\infty}^0 \frac{\bar{h}^{(0)}}{L^{(0)}} c^{(0)} dz \quad (3.124)$$

Eq. (3.92) can be added to Eq. (3.95) to express B :

$$B = \frac{1}{2} \left(\bar{f}_c^{(1)}(0^+) + \bar{f}_c^{(1)}(0^-) \right) + \frac{A}{2} (G^\alpha + G^\gamma) - \frac{v}{2} (F^\alpha + F^\gamma) \quad (3.125)$$

Finally:

$$v \beta^{(2)} \mathcal{J} = \langle \Delta \bar{w}^{(1)} \rangle + (c^{\gamma(0)} - c^{\alpha(0)}) (A G - v F) \quad (3.126)$$

where

$$\langle \Delta \bar{w}^{(1)} \rangle = \frac{1}{2} (\Delta \bar{w}^{(1)}(0^+) + \Delta \bar{w}^{(1)}(0^-)) \quad (3.127)$$

$$G = \tilde{G}^\gamma - \tilde{G}^\alpha + \frac{1}{2} (G^\alpha + G^\gamma) \quad (3.128)$$

$$F = \tilde{F}^\gamma - \tilde{F}^\alpha + \frac{1}{2} (F^\alpha + F^\gamma) \quad (3.129)$$

Hence, the phase field equation at order 2 delivers a correction, scaling as δ , to the relationship between the friction term and the driving force Eq. (3.85):

$$v (\beta^{(1)} + \delta \beta^{(2)}) \mathcal{J} = (\Delta \bar{w}^{(0)}(0) + \delta \langle \Delta \bar{w}^{(1)} \rangle) + \delta (c^{\gamma(0)} - c^{\alpha(0)}) (A G - v F) \quad (3.130)$$

We recover the free energy balance Eq. (3.36) with the friction term (left hand side), the driving force (first on right hand side), and a third term associated with the dissipation by trans-interface diffusion.

The correction of the driving force at first order involves both sides of the interface

because $f_c^{(1)}$ varies across the interface (Eq. (3.106)), contrary to the order 0 contribution. Beside integrals F^ψ and G^ψ , the jump in $\Delta\omega^{(1)}$ resulting from the variation increases with the interface velocity as well as with the gradients of diffusion potentials in the bulk on both side of the interface. As already mentioned, in the particular case of homogeneous mobility L , differences in F^ψ and G^ψ vanishes and the first order correction is removed.

To quantify the importance of the dissipation due to trans-interface diffusion (third term), we have performed a parametric study of the integrals entering F and G . $G^\gamma + G^\alpha$ and $\tilde{G}^\gamma - \tilde{G}^\alpha$ entering G in Eq. (3.128), scaled by L^α , are plotted in Fig. 3.2 versus the ratio of mobilities $\kappa = L^\gamma/L^\alpha$. At $\kappa = 1$, both quantities vanish (black dots). For $\kappa > 1$, they both remain around 0, whereas they increase strongly as κ decreases below 1. Unfortunately, for Fe-C, $\kappa \ll 1$, as illustrated by the red dots ($\kappa = 0.026$) at 776°C. $F^\gamma + F^\alpha$ and $\tilde{F}^\gamma - \tilde{F}^\alpha$ entering L in Eq. (3.129), scaled by L^α , are mapped in Fig. 3.2 versus the ratio of mobilities κ and the partition coefficient k : the darkest (blue), the highest. The red lines indicate the zero level sets, located at the same position on the (κ, k) maps. For both quantities, the largest absolute values are observed at the bottom left corner corresponding to small ratios L^γ/L^α and small partition coefficients. This is generally the case in Fe-C, as illustrated by the dashed line corresponding to the partition coefficient at 776°C, and by the red dot corresponding to the ratio between mobilities at the same temperature. The resulting G and F entering Eq. (3.126) are plotted in Fig. 3.4. As expected from the inspection of each integrals Eqs. (3.96)-(3.99) and (3.121)-(3.124), the contribution of trans-interface diffusion is likely to increase at small ratios κ , and to vanish quite surprisingly at ratios greater than 1.

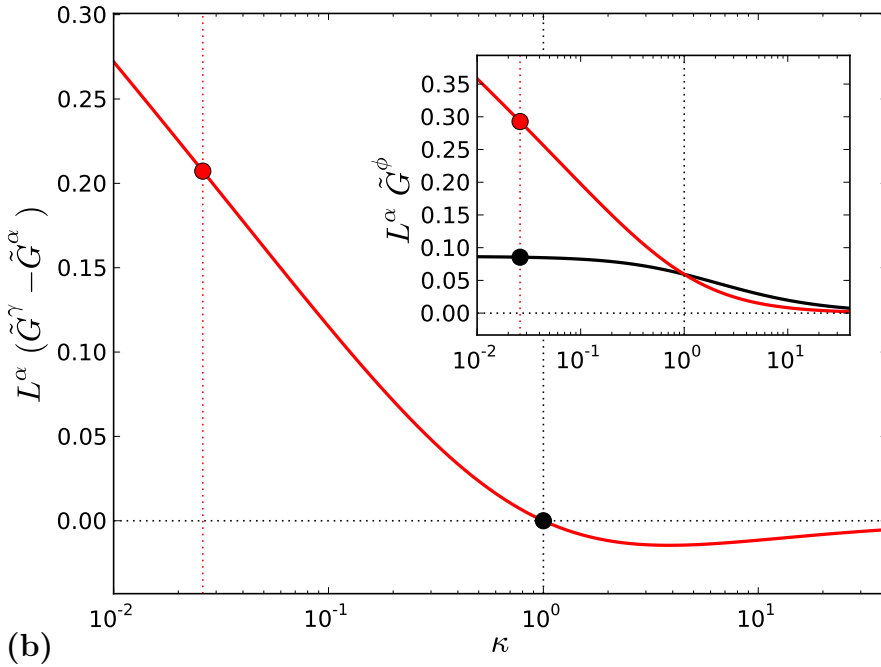
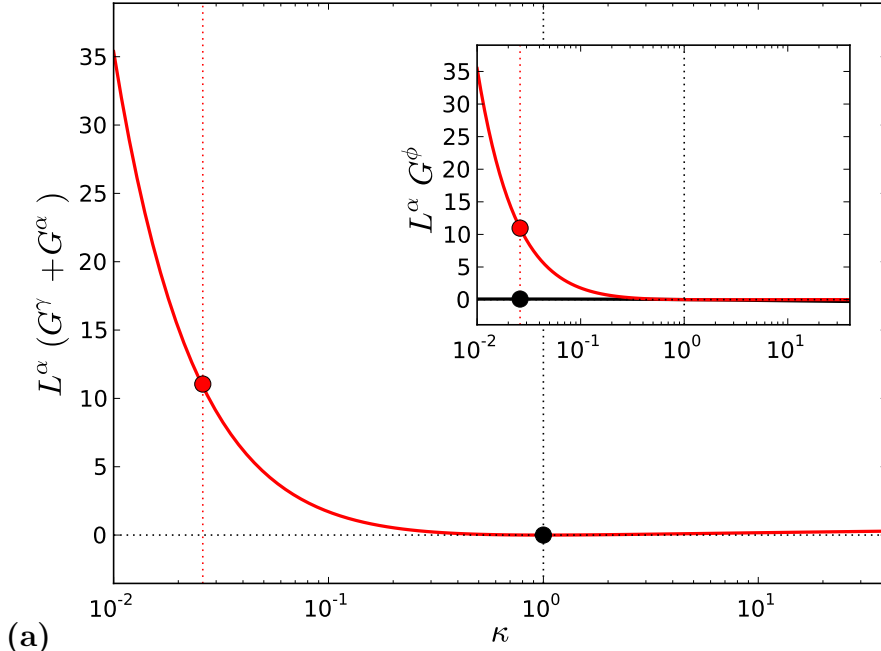


Figure 3.2: (a) $(G^\gamma + G^\alpha)$ and (b) $(\tilde{G}^\gamma - \tilde{G}^\alpha)$ vs. $\kappa = L^\gamma/L^\alpha$. Insets: γ in red and α in black.

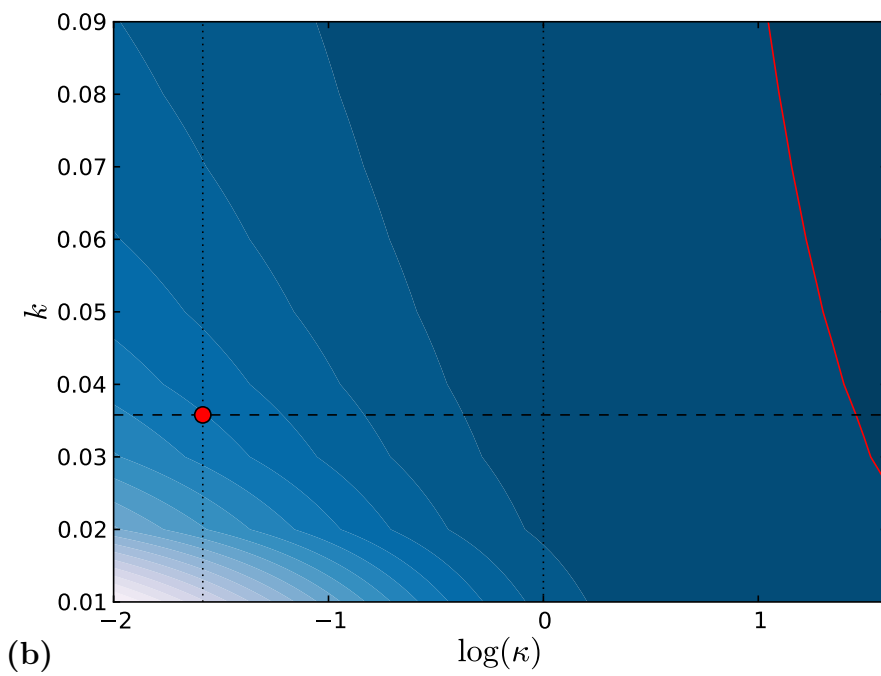
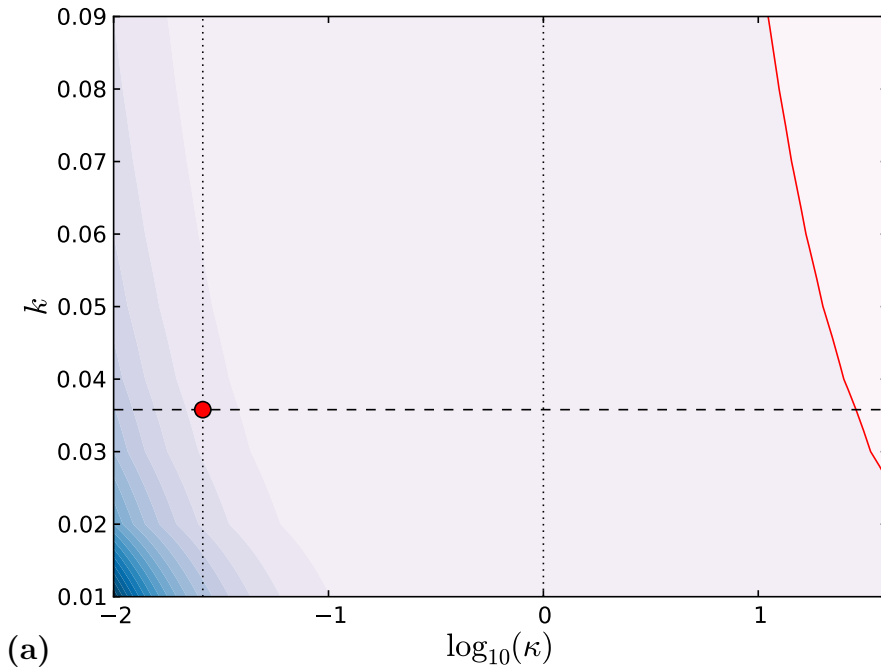


Figure 3.3: Projection of (a) $(F^\gamma + F^\alpha)$ and (b) $(\tilde{F}^\gamma - \tilde{F}^\alpha)$ on $(k, \log(\kappa))$.

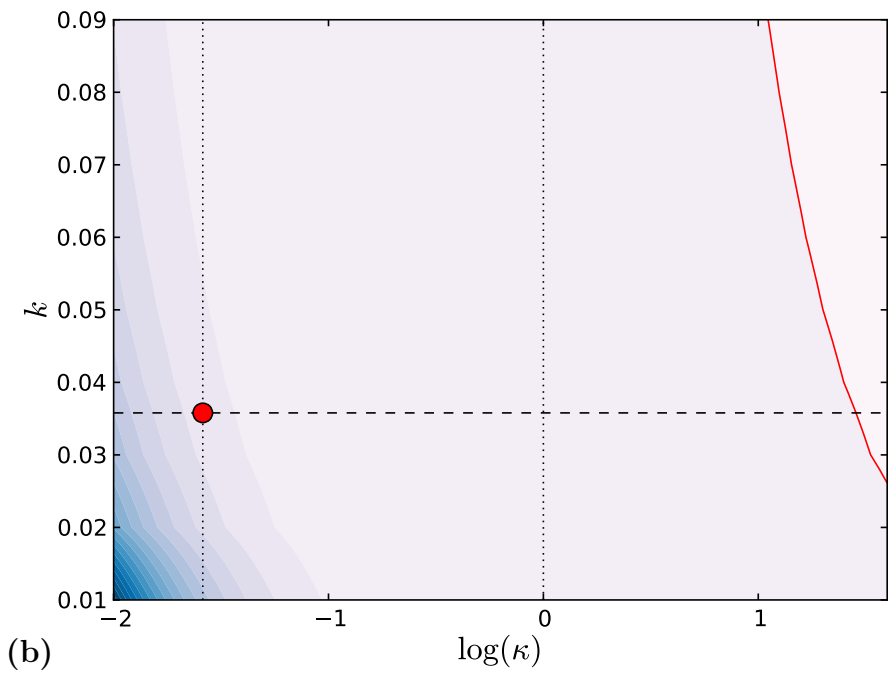
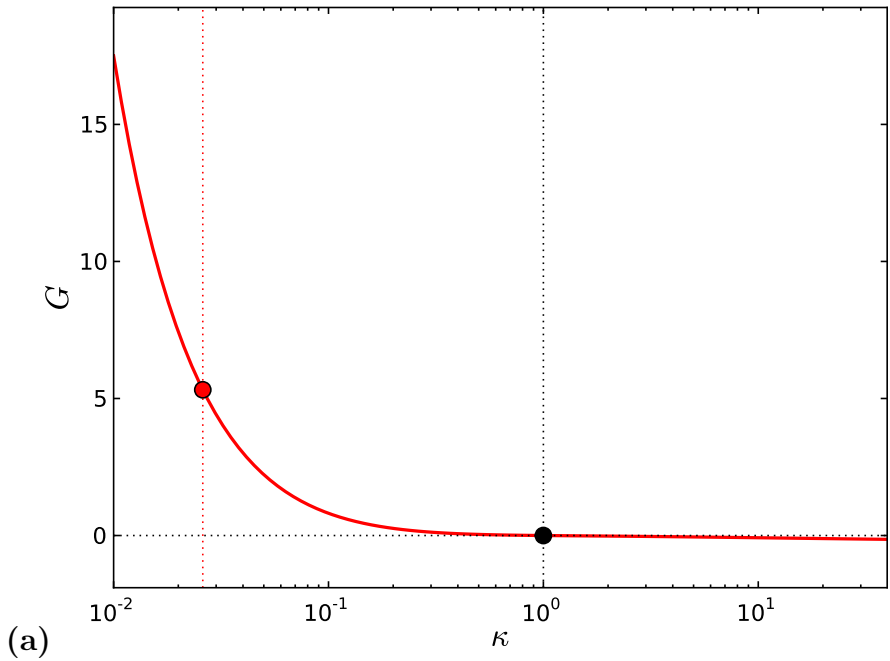


Figure 3.4: Projection of (a) G and (b) F on $(k, \log(\kappa))$.

3.2.2.3 Particular cases

Homogeneous mobility L

Considering the symmetric case with a constant mobility over the whole system ($L^\alpha = L^\gamma = L$), the expressions are considerably simplified. Indeed:

$$G^\alpha = G^\gamma = 0 \quad (3.131)$$

$$\tilde{G}^\alpha = \tilde{G}^\gamma \quad (3.132)$$

$$F^\alpha = F^\gamma = (c^{\gamma(0)} - c^{\alpha(0)}) \frac{1}{L} \int_0^{+\infty} h^{(0)} dz \quad (3.133)$$

Then $G = 0$ and $F = \tilde{F}^\gamma - \tilde{F}^\alpha + F^\alpha$, and Eq. (3.126) becomes:

$$\beta^{(2)} \mathcal{J} = (c^{\gamma(0)} - c^{\alpha(0)}) (\tilde{F}^\alpha - \tilde{F}^\gamma - F^\alpha) \quad (3.134)$$

Using $\int_0^{+\infty} h^{(0)} dz = \int_{-\infty}^0 \bar{h}^{(0)} dz$, tedious calculations give:

$$F = (c^{\gamma(0)} - c^{\alpha(0)}) \Upsilon \quad (3.135)$$

with $\Upsilon = \int_{-\infty}^{+\infty} h^{(0)} \bar{h}^{(0)} dz$. Finally, Eq. (3.134) reads:

$$\beta^{(2)} = \frac{(c^{\gamma(0)} - c^{\alpha(0)})^2}{L} \Upsilon / \mathcal{J} \quad (3.136)$$

It is worth stressing that in this simple case, the trans-interface diffusion term is very similar to the expression in the thick interface model of chapter §2. Indeed, it is quadratic in the jump of concentration at the interface and inverse to the mobility L (cf. Eqs. (2.13) and (2.21)).

The balance of free energy at the interface reads:

$$v(\beta^{(1)} + \delta\beta^{(2)}) \mathcal{J} = \Delta\bar{\omega}^{(0)}(0) + \frac{(c^{\gamma(0)} - c^{\alpha(0)})^2}{L} \Upsilon \quad (3.137)$$

It is clear from Eq. (3.137) that β (or M_ϕ) can judiciously be chosen to preserve

local equilibrium at the interface at order 1, contrary to the first order analysis. Indeed, by choosing:

$$\frac{1}{M_\phi} = \delta\beta = \delta^2\beta^{(2)} = \delta^2 \frac{(c^{\gamma(0)} - c^{\alpha(0)})^2}{L} \Upsilon/\mathcal{J} \quad (3.138)$$

Eq. (3.137) becomes trivially $\Delta\bar{\omega}^{(0)} = 0$ with a finite value for M_ϕ , i.e. for some finite time steps. This is the feature exploited by Karma to obtain quantitative calculations of dendritic solidification in pure materials [97, 98] with reasonable computation resources, and which has made the success of second order analysis in the phase field literature (e.g. [10, 14, 45, 62, 70, 128]).

Homogeneous diffusivity D

The assumptions in the previous case are different from the assumptions in Kim et al. [102]. Indeed, rather than an homogeneous mobility, they have considered an homogeneous diffusivity D_i , at least in the interface. Unfortunately, they have not discussed the consequences of this simplification on the validity of the expression for the phase field mobility. In particular, it is not possible to have any clue about the best choice for D_i when the diffusivities are not the same in the abutting phases. Therefore, in this section, we intend to render more explicit the hidden assumptions necessary for the expression proposed by Kim et al. [102] to hold. Indeed, inspecting Eq. (3.130), we were unable to recover the expression of KKS involving only one integral over the whole interface, even with a constant D : for this integral to converge (avoiding the necessary split into negative and positive integrals, Eqs. (3.96)-(3.99) and (3.121)-(3.124)), one essential condition must be assumed (not stated clearly in [102]). This condition is $\lim_{z \rightarrow -\infty} df_c^{(1)}/dz = 0$. Then, from Eq. (3.88), $A = v c^{\alpha(0)}$. This simple relation has two important consequences.

(i) First, the whole trans-interface diffusion term is proportional to v , and Eq. (3.126) becomes:

$$v\beta^{(2)}\mathcal{J} = \langle \Delta\bar{w}^{(1)} \rangle - v(c^{\gamma(0)} - c^{\alpha(0)}) (\tilde{H}^\gamma - \tilde{H}^\alpha + H^\alpha + \Delta H/2) \quad (3.139)$$

with

$$\Delta H = H^\gamma - H^\alpha \quad (3.140)$$

$$\tilde{H}^\gamma = \tilde{F}^\gamma - \tilde{G}^\gamma c^{\alpha(0)} = (c^{\gamma(0)} - c^{\alpha(0)}) \int_0^{+\infty} \frac{\bar{h}^{(0)} h^{(0)}}{L^{(0)}} dz \quad (3.141)$$

$$\tilde{H}^\alpha = \tilde{F}^\alpha - \tilde{G}^\alpha c^{\alpha(0)} = (c^{\gamma(0)} - c^{\alpha(0)}) \int_{-\infty}^0 \frac{(\bar{h}^{(0)})^2}{L^{(0)}} dz \quad (3.142)$$

$$H^\alpha = F^\alpha - G^\alpha c^{\alpha(0)} = (c^{\gamma(0)} - c^{\alpha(0)}) \int_{-\infty}^0 \frac{\bar{h}^{(0)}}{L^{(0)}} dz \quad (3.143)$$

$$H^\gamma = F^\gamma - G^\gamma c^{\alpha(0)} = (c^{\gamma(0)} - c^{\alpha(0)}) \int_0^{+\infty} \left(\frac{1}{L^\gamma} - \frac{\bar{h}^{(0)}}{L^{(0)}} \right) dz \quad (3.144)$$

(ii) Second, the jump in the driving force at order 1 is also proportional to v . Using Eq. (3.116) and Eq. (3.105) one obtains:

$$[[\Delta \bar{w}^{(1)}]] = v (c^{\gamma(0)} - c^{\alpha(0)}) \left[c^{\alpha(0)} (G^\alpha - G^\gamma) + (F^\gamma - F^\alpha) \right] \quad (3.145)$$

Thus

$$\langle \Delta \bar{w}^{(1)} \rangle = \Delta \bar{w}^{(1)}(0^-) + \frac{1}{2} [[\Delta \bar{w}^{(1)}]] = \Delta \bar{w}^{(1)}(0^-) + v (c^{\gamma(0)} - c^{\alpha(0)}) \Delta H / 2 \quad (3.146)$$

Inserting Eq. (3.146) into Eq. (3.139) gives:

$$v\beta^{(2)}\mathcal{J} = \Delta \bar{w}^{(1)}(0^-) - v (\tilde{H}^\gamma - \tilde{H}^\alpha + H^\alpha) \quad (3.147)$$

$$= \Delta \bar{w}^{(1)}(0^-) + v (c^{\gamma(0)} - c^{\alpha(0)})^2 \mathcal{K} \quad (3.148)$$

with $\mathcal{K} = \int_{-\infty}^{+\infty} \frac{\bar{h}^{(0)} h^{(0)}}{L^{(0)}} dz$.

$L^\alpha \mathcal{K}$ is plotted versus the ratio of mobilities κ to illustrate that the conclusions obtained in the general case (Fig. 3.4) are not drastically changed: trans-interface diffusion does not vanish at constant L (black dot, with the value given by $L\mathcal{K} = \Upsilon$) and increases as κ decreases. The red dot indicates the value of $L^\alpha \mathcal{K}$ for the ratio obtained in Fe-C at 776°C.

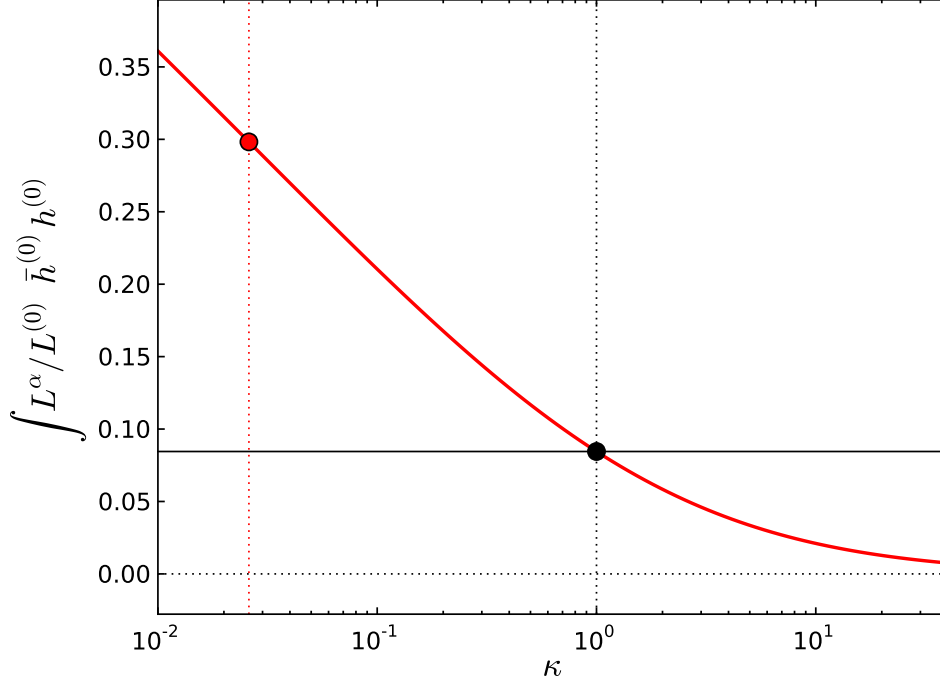


Figure 3.5: Integral \mathcal{K} entering Eq. (3.147) vs. ratio $\kappa = L^\gamma/L^\alpha$.

Finally, the balance of free energy reads:

$$v (\beta^{(1)} + \delta \beta^{(2)}) \mathcal{J} = \Delta \bar{w}^{(0)}(0) + \delta \Delta \bar{w}^{(1)}(0^-) + v \delta (c^{\gamma(0)} - c^{\alpha(0)})^2 \mathcal{K} \quad (3.149)$$

It has a shape very similar to Eq. (3.137), thanks to the condition of vanishing gradient of diffusion potential in α ($\lim_{z \rightarrow -\infty} df_c/dz = 0$). Moreover, it is exactly Eq. (62) in [102], (i) provided that the conversion to equivalent parameters is performed using the relationships Eqs. (3.22),(3.23) between the phase field parameters and the physical quantities; (ii) recognizing the equivalence $(c^{\gamma(0)} - c^{\alpha(0)})^2 \mathcal{K} = \epsilon \zeta / (D_i \sqrt{2W})$ with ζ defined in [102] as follows:

$$\zeta = (c^{\gamma(0)} - c^{\alpha(0)})^2 \int_0^1 \frac{\bar{h}^{(0)} h^{(0)}}{h^{(0)}/f_{cc}^\alpha + \bar{h}^{(0)}/f_{cc}^\gamma} \times \frac{d\phi^{(0)}}{\phi^{(0)}(1 - \phi^{(0)})} \quad (3.150)$$

with $f_{cc}^\psi = d^2 f^\psi / d(c^\psi)^2$

But contrary to KKS, Eq. (3.149) shows explicitly that the driving force at the

interface (i) is defined asymmetrically on the precipitate side; (ii) depends on the interface thickness. Consequently, the kinetics predicted by the phase field model of KKS is likely to deviate from the sharp interface predictions as δ increases. Defining the interface mobility M as usual with the following linear relation (see also Eq. (2.22)):

$$v = M \Delta\omega \approx M (\Delta\bar{w}^{(0)}(0) + \delta\Delta\bar{w}^{(1)}(0^-)) \quad (3.151)$$

we can replace the approximate driving force in Eq. (3.149) by v/M . Thus, the phase field mobility reads:

$$\frac{1}{M_\phi} = \delta\beta^{(1)} + \delta^2\beta^{(2)} = \frac{\delta}{\mathcal{J}} \left[\frac{1}{M} + \delta(c^{\gamma(0)} - c^{\alpha(0)})^2 \mathcal{K} \right] \quad (3.152)$$

As already mentioned for the previous assumption $L = \text{cst}$, it is possible to select M_ϕ such that the driving force vanishes and that local equilibrium is achieved. In the present case, one may choose:

$$\frac{1}{M_\phi} = \delta^2\beta^{(2)} = \delta^2 (c^{\gamma(0)} - c^{\alpha(0)})^2 \mathcal{K}/\mathcal{J} \quad (3.153)$$

However, contrary to the previous case, this expression does not ensure fully that local equilibrium can hold because of the first order correction to the driving force.

3.3 Interface mobility in Fe-C alloys

In this section we focus on the consequence of a finite interface mobility on the kinetics of the $\gamma \rightarrow \alpha$ transformation in Fe-C alloys. It must be mentioned that a similar study has been carried out recently [114] but with a more crude analysis. Instead of using experimental values for the interface mobility as usually done in the thick interface models [107, 124, 125], or values obtained by fitting experimental kinetics as done in some phase field calculations [111, 112, 113], we have used the expression derived in the previous section §3.2.2.3 to perform a parametric study. In particular, Eq. (3.152) has been recast to match the expression proposed by KKS [102]:

$$M_\phi = \frac{\gamma}{\epsilon^2} \left(\frac{1}{M} + \frac{\epsilon}{\sqrt{2W}} \frac{\zeta_C}{D_C^\gamma} \right)^{-1} \quad (3.154)$$

where D_C^γ has been chosen for D_i , although L and D are varying within the interface, by trial and error on the calculation in §3.3.1. For the free energies Eq. (3.15) describing the linearized equilibrium between ferrite and austenite in Fe-C, integral ζ_C simply reads:

$$\zeta_C = \frac{RT}{V_m} (1 - k_C) \int_0^1 \frac{\bar{h}^{(0)} h^{(0)}}{\bar{h}^{(0)} k_C + h^{(0)}} \times \frac{d\phi^{(0)}}{\phi^{(0)} (1 - \phi^{(0)})} \quad (3.155)$$

Fig. 3.6 shows two different expressions for M_ϕ with respect to M , depending on the order of the analysis. The first order (Eq. (3.86) or Eq. (3.154) with $\zeta_C = 0$) yields a linear relationship (triangles), usually invoked to choose a phase field mobility (e.g. [114]). The second order (Eq. (3.152) or (3.154)) gives the curve with black dots exhibiting a crossover between the linear relationship similar to first order for small interfacial mobilities and the horizontal blue line for large interfacial mobilities, corresponding to the particular expression Eq. (3.153) ensuring approximately local equilibrium. All values of M_ϕ above this upper limit give also local equilibrium but at a highest computational cost due to time steps Δt getting smaller as M_ϕ increases ($\Delta t \propto 1/M_\phi$). For that reason, all subsequent calculations are performed using Eq. (3.155) for the phase field mobility.

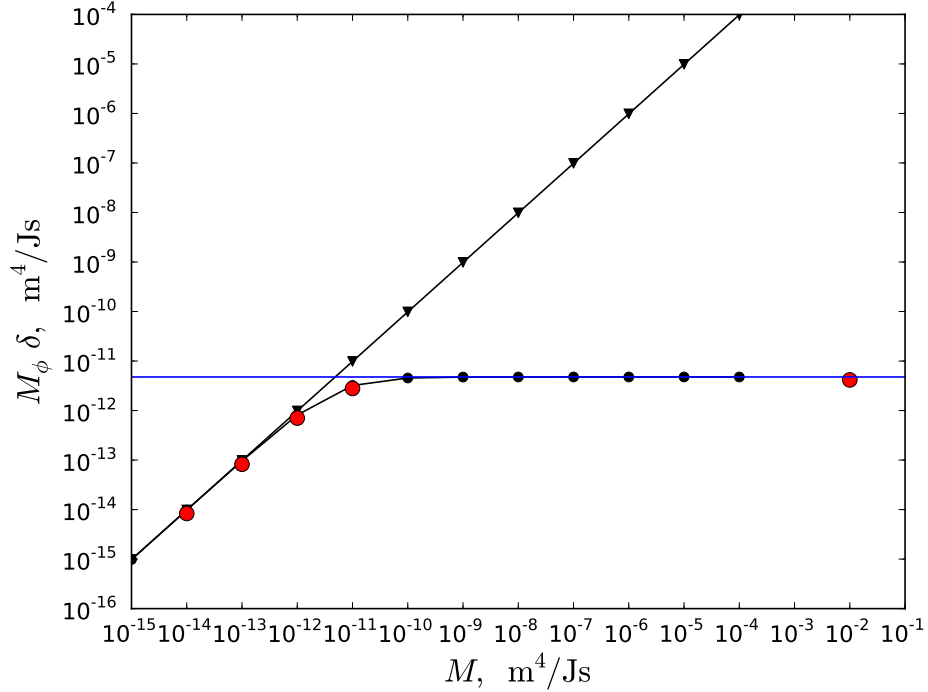


Figure 3.6: Phase field mobility vs. interface mobility in Fe-C at 776°C: first order asymptotics (triangles), second order asymptotics (black dots), calculations of §3.3.1 and §3.3.2 (red dots).

A series of calculations have been performed in a Fe-0.3 C (wt.%) steel, hold at 776°C. The data for the linearized phase diagram and for the diffusivities in α and γ are reported in Appendix D.

A system of 5 μm has been discretized with 512 nodes, resulting in a 59 nm thick interface (containing 6 nodes). A 100 nm ferrite nucleus is settled at the left side, which corresponds to an initial ferrite fraction $f_\alpha^0 = 0.02$. The initial concentration in austenite c_0^γ and in ferrite $c_0^\alpha = k_C c_0^\gamma$ are set such that the average concentration matches the nominal concentration of the alloy, i.e.:

$$c_0^\gamma = \frac{c_0}{1 - (1 - k_C) f_\alpha^0} \quad (3.156)$$

where c_0 is the nominal concentration.

3.3.1 Local equilibrium at the interface

At first, we illustrate the outcome of the model with a value of $M = 10^{-2}$ sufficiently large for M_ϕ to be very close to the blue upper limit in Fig. 3.6 (right-most red dot).

For this value, the growth kinetic is fast and a total duration of 4 s is sufficient to reach equilibrium. The evolution of the ferrite fraction is plotted in Fig. 3.7 with white dots. The corresponding growth rate is plotted in the inset. During the first 1.5 s, growth follows a \sqrt{t} law in excellent agreement with the sharp interface solution in a semi-infinite system (thin line). After 1.5 s, the equilibrium fraction is achieved (dashed line) and growth stops.

In Fig. 3.8, a few profiles of carbon concentration are plotted to illustrate the diffusion-controlled process. Very rapidly, the carbon concentration rises on the γ side of the interface and a concentration gradient develops in γ which drives the growth of the precipitate. At first sight, there seems to be some deviation between the interface concentration in γ and the equilibrium concentration (horizontal dotted line). But as discussed in [155], the concentration at the maximum of the profile is not the interface concentration in γ because of the diffuse interface. Indeed, as shown in Fig. 3.9, the extrapolation of the bulk concentration profiles in the interface to the position of the level-set $\phi = 0.5$ may give some values which are different from the values, either taken at the limit of the diffuse interface, or at the maximum of the curve for the γ side as done in [84]. By performing systematically such an extrapolation on all the successive profiles, we are able to extract better values for the interface concentrations. This is clearly shown in Fig. 3.10 where the maxima (dots) and the extrapolated values (red dots) are compared to the equilibrium concentration (dashed horizontal): when the maxima seem not to have reached equilibrium before the end of the transformation, the extrapolated values converge rapidly to equilibrium after a transient stage of about 0.3 s, in agreement with the kinetics.

Although the mobility has been chosen so as to achieve fast local equilibrium at interface, during the transient stage there is a substantial deviation from equilibrium (Fig. 3.10). It must be noted that the input mobility has not been chosen to be infinite. Consequently, there can be some small interface friction associated

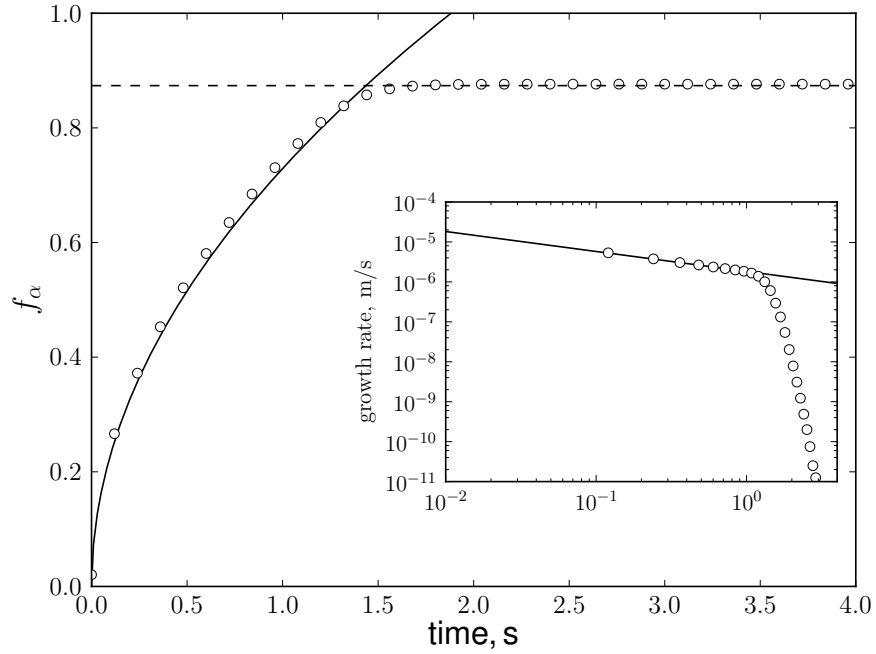


Figure 3.7: Ferrite fraction vs. time in Fe-0.3C (wt.%) at 776°C: phase field (white dots), sharp interface (continuous line) and equilibrium (dashed line).

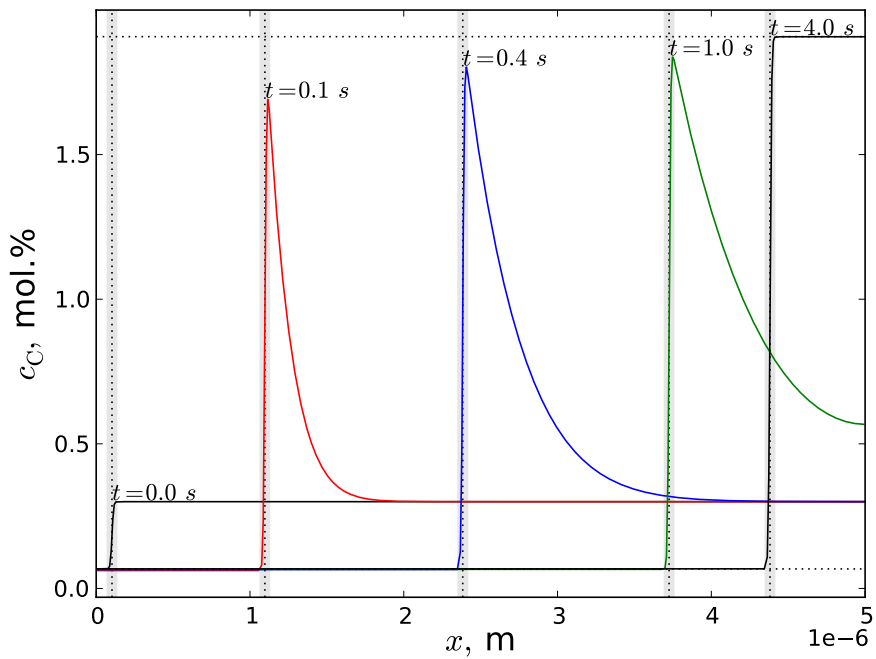


Figure 3.8: Concentration profiles of carbon at successive time steps (diffuse interface located by grey slabs).

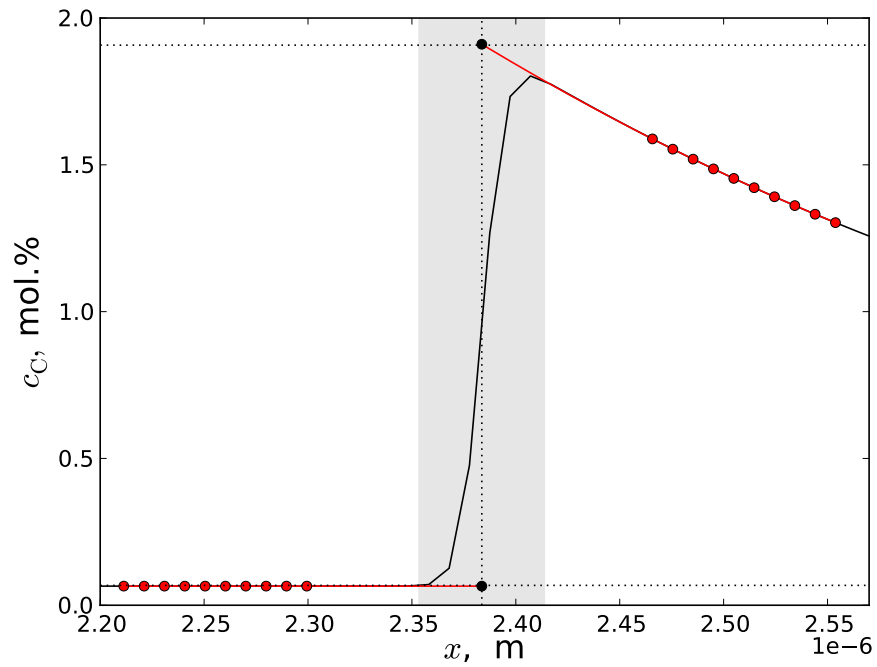


Figure 3.9: Zoom of the concentration profile at 0.4 s close to the interface (grey slab). Extrapolations (red) from the bulks to the position of the level-set $\phi = 0.5$.

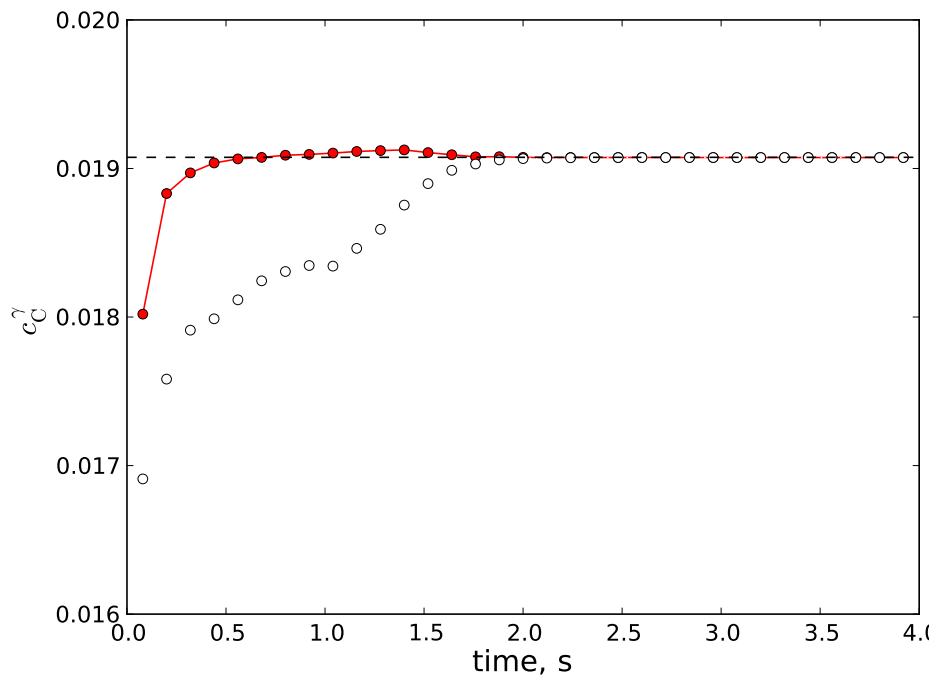


Figure 3.10: Evolution of the carbon concentration at the interface in γ : Maximum concentrations (white dots); extrapolated at $\phi = 0.5$ (red dots).

with this finite value. As well, we have stressed in §3.2.2.3 that due to the difference in mobilities between α and γ a first order correction to the driving force does not vanish when $v > 0$. Then, there must be some small additional interface friction which has been quantified using Eqs. (3.39),(3.42) in the approximate analysis in §3.2.1. First, we have determined the interface velocity v by deriving the growth curve with respect to time using 1st order finite differences. Second, we have checked that, in agreement with the asymptotic analysis, the profile of ϕ keeps the same tanh shape with a constant thickness δ , such that J/δ remains constant. Third, we have computed $\Delta G^{\text{friction}}$ according to Eq. (3.42), using the profiles of $\Delta\omega$, as shown in Fig. 3.11a. In order to compare the magnitude of the driving forces, all profiles have been centered at the interface positions before superposition. As expected, the driving force decreases during the transformation down to 0 at 2 s (black triangles). Moreover, as stressed in the asymptotic analysis, Δw is not flat across the interface, except when equilibrium is achieved: the deviation from the baseline made by the flat profile in α depends on the interface thickness and is the largest at the beginning when v is the largest (white dots). As well, the magnitude of $\Delta\omega$ in α is related to the first order correction $\delta\Delta\bar{\omega}^{(1)}(0^-)$ which decreases as the transformation proceeds and slows down. The corresponding densities of dissipation by friction are plotted in Fig. 3.11b. They are slightly asymmetric due to the variation of $\Delta\omega$ across the interface, and decrease to 0 with $\Delta\omega$. The integration of these densities over the interface thickness provides $\Delta G^{\text{friction}}$ which can be plotted against velocity, as shown in Fig. 3.12 with white dots. A linear regression is then performed discarding the first time step (right-most dot). A very good fit is obtained, and the slope gives the effective interface mobility which may be different from the input value (10^{-2} m⁴/J/s). If friction would have been perfectly cancelled by trans-interface diffusion, the driving force would have remained zero and the resulting effective mobility infinite. Unfortunately, as shown in Fig. 3.11b, this is not the case. In fact, the effective mobility obtained from the linear regression is exactly the value of $M_\phi\delta$, i.e. the value in Fig. 3.6 at the intersection between the 1st order linear relationship (Eq. (3.86)) and the upper limit given by Eq. (3.153).

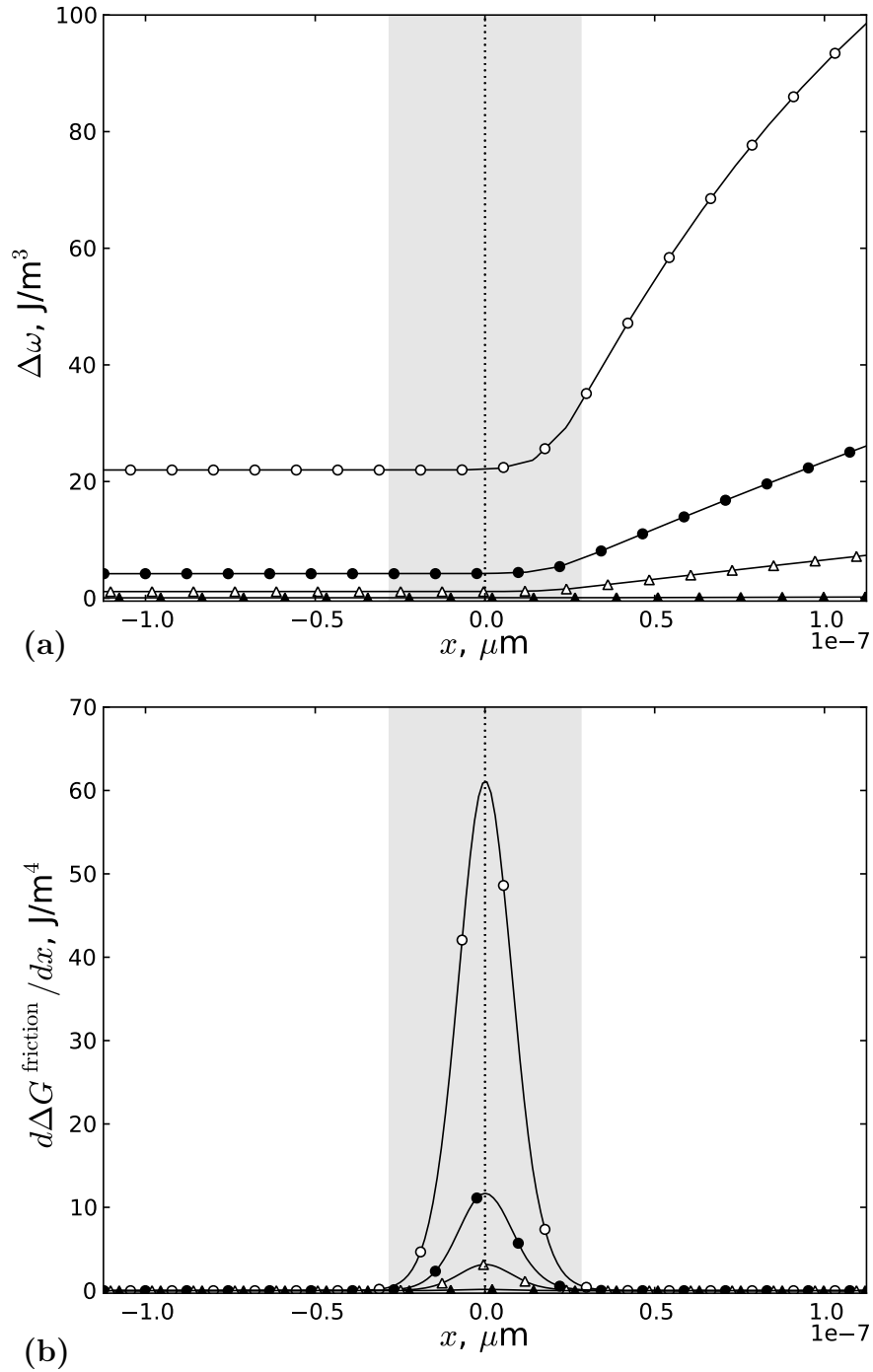


Figure 3.11: Profiles of (a) driving force Δw and (b) dissipation by friction $h'(\phi)\Delta w$ at the interface (grey slab) at 10^{-2} s (white dots), 1 s (black dots), 1.5 s (white triangles) and 2 s (black triangles).

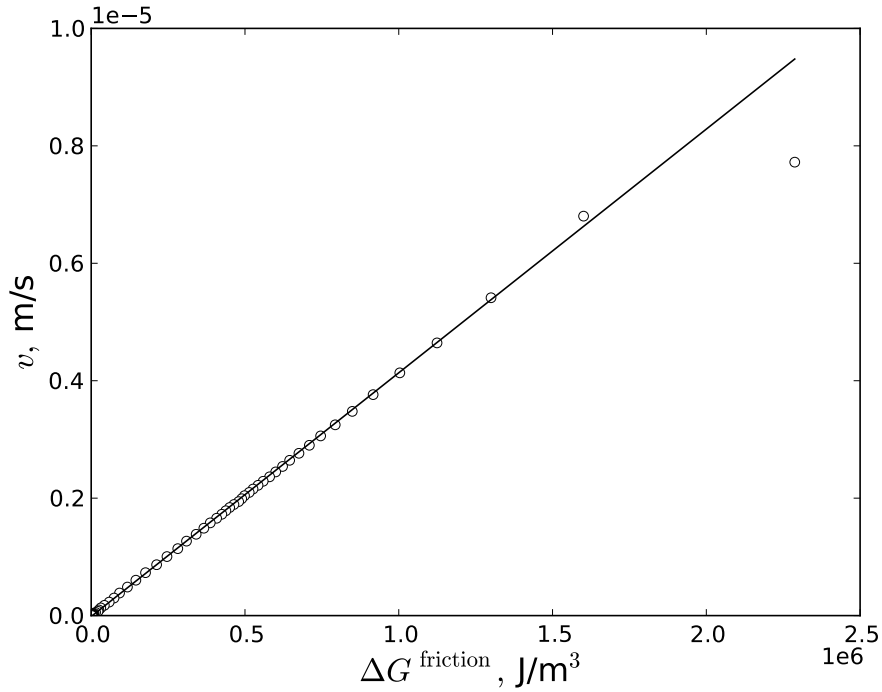


Figure 3.12: Growth rate (dots) vs. $\Delta G^{\text{friction}}$ with a best linear fit excluding the right-most dot (line).

It seems that removing the first order jump in the driving force is mandatory to obtain perfect local equilibrium at the interface, and that the phase field mobility proposed by KKS is not sufficient when the abutting phases have different chemical diffusivities. This is not a new result and only one remedy has been proposed so far, the so-called anti-solute trapping term, by Karma [96] (see also [53, 99, 128]). But fortunately, the deviation from local equilibrium is quite small and has practically no incidence on the kinetics. Hence, the expression proposed in KKS [102] puts a upper limit for M_ϕ and consequently a practical lower bound for the time step, sufficient to get results very close to local equilibrium.

3.3.2 Mixed-mode growth

We have carried out the same calculation with a series of smaller mobilities so as to investigate the influence of the interface mobility M on the $\gamma \rightarrow \alpha$ transformation kinetics. The following values have been used: 10^{-11} , 10^{-12} , 10^{-13} and 10^{-14} $\text{m}^4/\text{J}/\text{s}$ (resp. in green, blue, red and black in Fig. 3.13).

In Fig. 3.13a we have compared the evolutions of the ferrite fraction, together with the corresponding growth rates (inset). As expected, the smallest M , the slowest the transformation. $M = 10^{-11}$ $\text{m}^4/\text{J}/\text{s}$ gives results quantitatively very similar to the local equilibrium case (thick black in the same figure), with a \sqrt{t} growth law which is the signature of a diffusion-controlled process. At the opposite, for $M = 10^{-14}$ $\text{m}^4/\text{J}/\text{s}$, the transformation is complete only after about 70 s, instead of 2 s for the local equilibrium case. Moreover, it can be observed that the growth law is linear, before soft-impingement occurs, as confirmed by the constant growth rate (thin black in inset). In that case, growth is interface controlled with a constant velocity given by $v = M \Delta G^{\text{friction}}$. For the intermediate values (in particular $M = 10^{-12}$ $\text{m}^4/\text{J}/\text{s}$, blue curves), it is interesting to notice a change in the growth regime, starting with an interface-controlled growth and switching to a \sqrt{t} diffusion-controlled growth, before soft-impingement. This is in agreement with the results of the mixed-model of Sietsma and van der Zwaag [144].

Inspecting the successive concentration profiles in the different cases (Figs. E.1-E.2 in Appendix E) which are flatter when M are smaller and kinetics slower, we have retrieved the evolutions of the interfacial concentrations c^γ using the method presented in the previous section §3.3.1. They are compared in Fig. 3.13b (with a zoom of the first seconds in the inset). Consistently with the kinetics, the greatest the interface mobility, the fastest the interface concentration goes from the nominal concentration to the equilibrium value (horizontal dashed line). For $M \leq 10^{-12}$ $\text{m}^4/\text{J}/\text{s}$, the evolutions exhibit inflections. After a concave initial stage corresponding to a constant growth velocity (linear growth), the increase of c^γ toward equilibrium concentration accelerates when soft impingement has significantly enriched austenite in C and started to slow down the process. Then, when approaching equilibrium, the evolution of the interfacial concentration slows down again until it reaches equilibrium.

We have also analyzed the different contributions entering the balance between the driving force and the dissipation by friction in Eqs. (3.39),(3.42). The different profiles used to compute the right hand side of Eq. (3.42) are plotted in Figs. E.3-E.4, for the different interface mobilities. As M decreases, the magnitude of the driving force $\Delta\omega$ increases and remains at a high level for a longer time. Moreover, it is worth noting that the variation of $\Delta\omega$ across the interface (left in Figs. E.3-E.4) is much less pronounced when M is small because v is small. Then, the 1st order error is likely to be less important when M is smaller. To determine the effective interface mobility, it has been checked that the phase field always exhibits a tanh profile with a constant interface thickness, ensuring that the integral \mathcal{J} in Eq. (3.39) remains constant (center in Figs. E.3-E.4). Finally, integrals of $\Delta\omega dh/dx$ (right in Figs. E.3-E.4) over the interface thickness plotted versus the growth rate v can be used to determine the effective mobility, as previously in §3.3.1. Indeed, the effective mobility is the slope of the line obtained by fitting these curves by linear regression. The resulting mobilities are located on the master curve in Fig. 3.6 (red dots), as expected. Therefore, it seems that the phase field model of Viardin [155] together with the phase field mobility of KKS [102] give a very good control of the interface mobility, in contrast with the recent work of [114]. Furthermore, it must be stressed that our results for Fe-C are not very sensitive to the interface thickness (remaining in the same order of magnitude, i.e. below a few hundreds of nm).

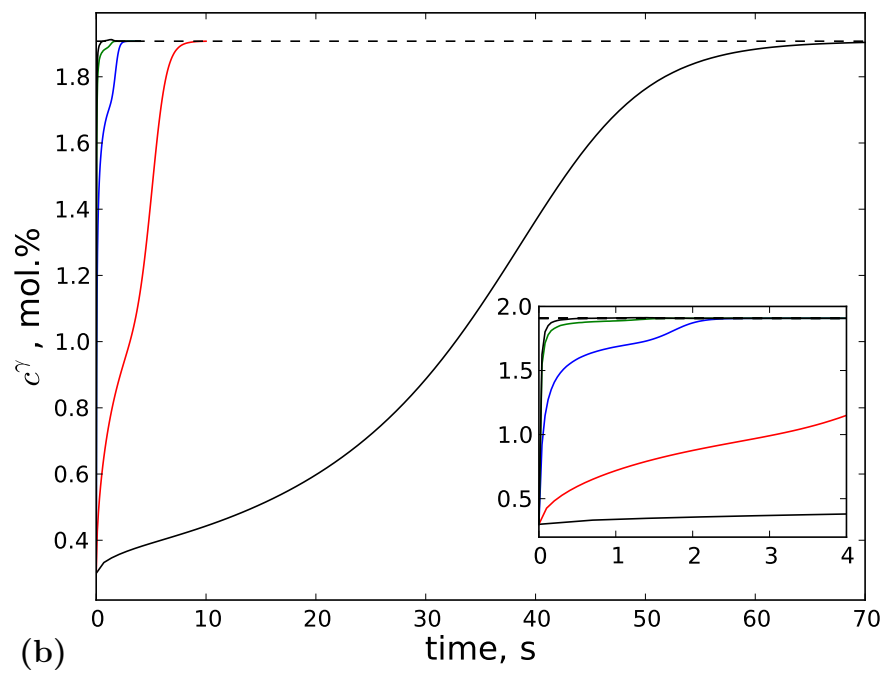
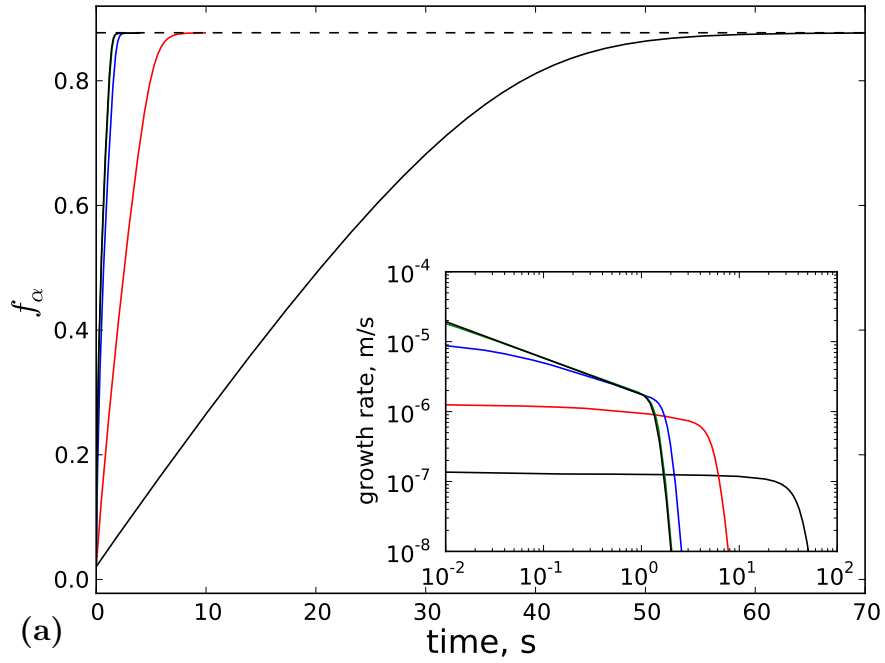


Figure 3.13: (a) Ferrite fraction and (b) interface concentration in γ vs. time in Fe-0.3C (wt.%) at 776°C, for different M (in $\text{m}^4/\text{J/s}$): 10^{-2} , 10^{-11} , 10^{-12} , 10^{-13} , 10^{-14} (from fastest to slowest).

3.4 Interface mobility in Fe-C-X alloys

In this section, the kinetics of the $\gamma \rightarrow \alpha$ transformation in ternary Fe-C-Mn system is investigated with the phase field model of [155, 156], accounting for both C and Mn diffusion, and a finite interface mobility.

As shown in Viardin [155], proposing an expression for the phase field mobility in a ternary Fe-C-X alloy is not a trivial task. One may be tempted to propose the following extension of Eq. (3.154), which can straightforwardly be obtained by extending the asymptotic analysis of §3.2.2 (just putting sums over i where necessary):

$$M_\phi = \frac{\gamma}{\epsilon^2} \left(\frac{1}{M} + \frac{\epsilon}{\sqrt{2W}} \sum_i \frac{\zeta_i}{D_i^\gamma} \right)^{-1} \quad (3.157)$$

where $i = C, X$, and integrals ζ_i still given by Eq. (3.155) (with k_i replacing k_C). But this expression does not give satisfying results when compared to experimental kinetics. In particular, it is unable to capture PE for alloys deep inside the PE region, as observed usually in experiments (§2). A quick inspection of Eq. (3.157) shows why PE is unlikely to be obtained with such an expression. Setting $M \rightarrow \infty$, the dominant term is $1/D_X$ since $D_C \gg D_X$ and the phase field mobility scales as D_X . The typical time scale over which the phase field varies is the time scale for X diffusion, i.e. much longer than typical time for PE, controlled by C diffusion. To remedy this flaw, Viardin [155] has proposed to remove the contribution of X and to use Eq. (3.154). If this can be justified on the basis of a crude analysis as in §3.2.1, considering PE, the asymptotic analysis at second order is much more involved because the driving force $\Delta\omega$ at order 0 is non homogeneous due to the flat concentration profile in X.

In Fig. 3.14, we have plotted both expressions for M_ϕ Eqs. (3.154),(3.157) with respect to the interface mobility M , for the particular Fe-C-Mn alloy studied below (§3.4.1). Both feature the same shape with a linear part corresponding to the interface-controlled regime and an horizontal branch where trans-interface diffusion is supposed to balance the interface friction. The difference of six decades between the horizontal branches simply comes from the ratio D_C/D_{Mn} . If M_ϕ is selected on the lower horizontal branch, one could expect to obtain local equi-

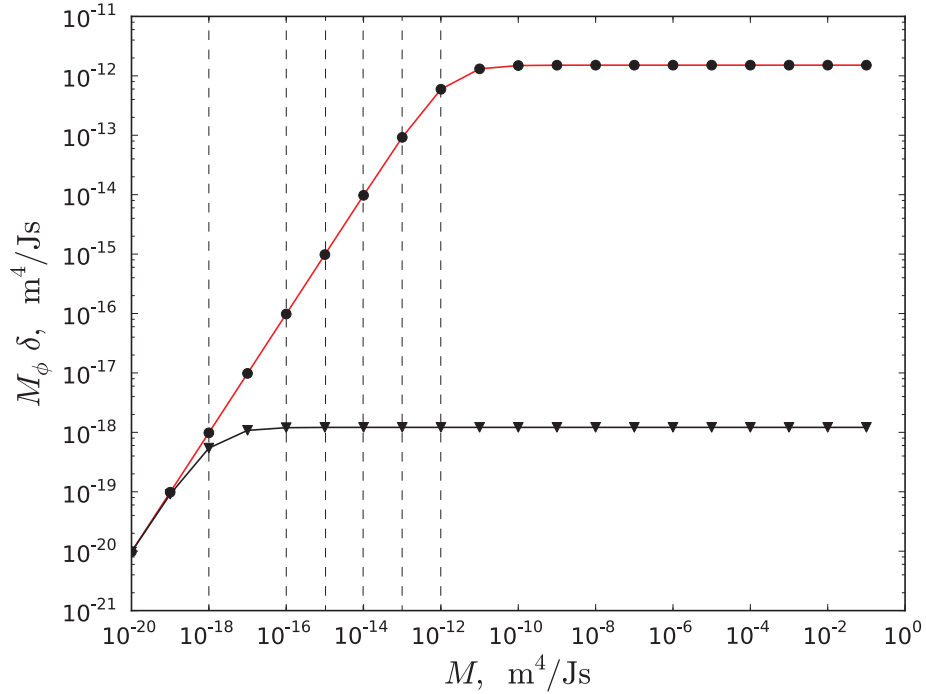


Figure 3.14: Phase field mobility vs. interface mobility in Fe-0.15 C-1.5 Mn (wt.%) at 650°C: accounting for C and Mn (triangles); accounting for C only (red line with dots).

librium, but on a time scale much larger than what is experimentally relevant. Hence, besides the upper branch, already investigated by Viardin [155, 156], the intermediate phase field mobilities between the two branches are likely to be relevant with respect to experimental kinetics. This is the main motivation of the following parametric study spanning the whole intermediate branch of Eq. (3.154) (vertical dashed lines in Fig. (3.14)): $M = 10^{-18}, 10^{-16}, 10^{-15}, 10^{-14}, 10^{-13}$ and $10^{-12} \text{ m}^4/\text{J/s}$.

3.4.1 Kinetic pathways in isothermal condition

The case of a Fe-0.15C-1.5Mn (wt.%) alloy (white dot in Fig. 3.16) hold at 650°C has been considered. At this temperature, the alloy is situated below the zero partition line deep inside the LENP and PE domains, and is likely to feature a fast growth regime, at least for high interface mobilities. It can be mentioned that results similar to what will be shown below have also been obtained in the Fe-C-Ni system. The data for the linearized phase diagram and for the diffusivities in α and γ are reported in Appendix D, and the general configuration (system size, discretization and initial conditions) is the same as in §3.3.

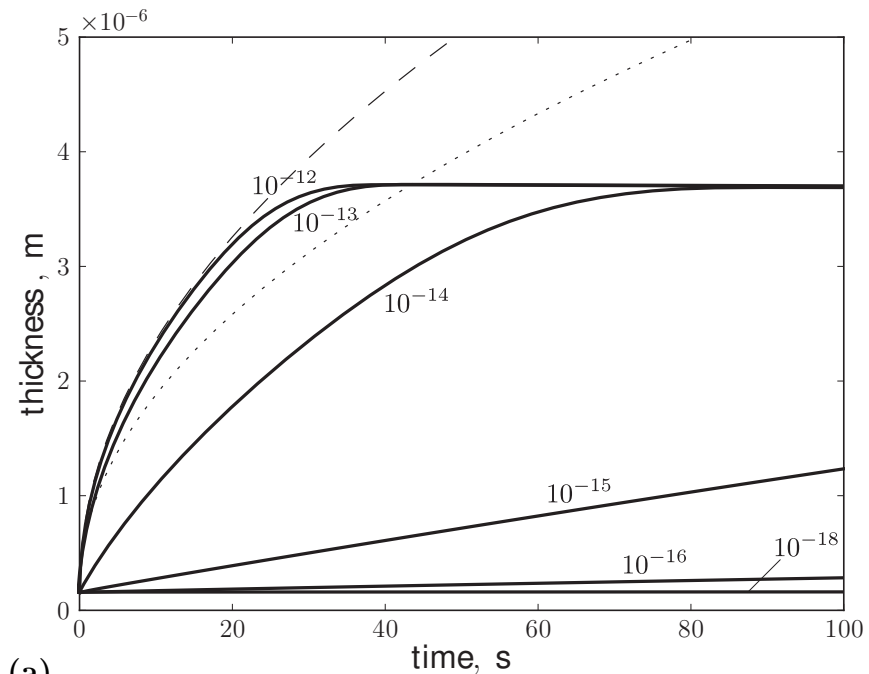
The time evolutions of ferrite thickness are shown in Fig. 3.15a for all the mobilities investigated (together with the growth rate in Fig. 3.15b). The analytical solutions in semi-infinite systems are also plotted for comparison: the slowest LENP (dotted line), and the fastest PE (dashed line). For $M = 10^{-12}$ m⁴/J/s, corresponding to M_ϕ very close to the upper branch in Fig. 3.14, the kinetics features three stages, in agreement with [155]. The first stage is fast and very close to the \sqrt{t} growth law under PE predicted analytically. The second stage around 20 s is a smooth transition to the third stage ($t > 30$ s) where the transformation seems to have stopped (stasis), slightly below the paraequilibrium fraction. Apart from the smooth transition, this result is qualitatively similar to the results of the thick interface model for alloys situated above the zero-partition line, in the LEP region (§2.3.6.2). This apparent contradiction will fade away when discussing below about the evolution of the operative tie-lines. The same kind of kinetics is observed for 10^{-13} m⁴/J/s, with a slightly slower first stage. Indeed, at the very beginning, the growth rate deviates from a purely diffusion-controlled growth rate as shown in Fig. 3.15b. The ferrite thickness at the stasis is almost identical to the highest mobility. For $M = 10^{-14}$ m⁴/J/s, the kinetics is significantly slower and it is not easy to separate the first and second stages. Moreover, it is not clear whether growth still follows a \sqrt{t} law. The stasis achieved after about 80 s (i.e. on an experimental time scale for this kind of alloy) is very close to the stases of the highest mobilities. For the three smallest mobilities, growth is much slower than previously, with durations of the order of $10^5 - 10^6$ s to achieve a stasis a bit smaller than for the highest mobilities (for the full curves, see the small insets

in Fig. 3.18). On the scale of a few hundreds of seconds, or more for the smallest mobility, growth is linear in agreement with an interface-controlled growth mode (the growth rates are almost constant before the stases). From a purely kinetic point of view, the slow substitutional species does not change drastically the picture with respect to the binary case.

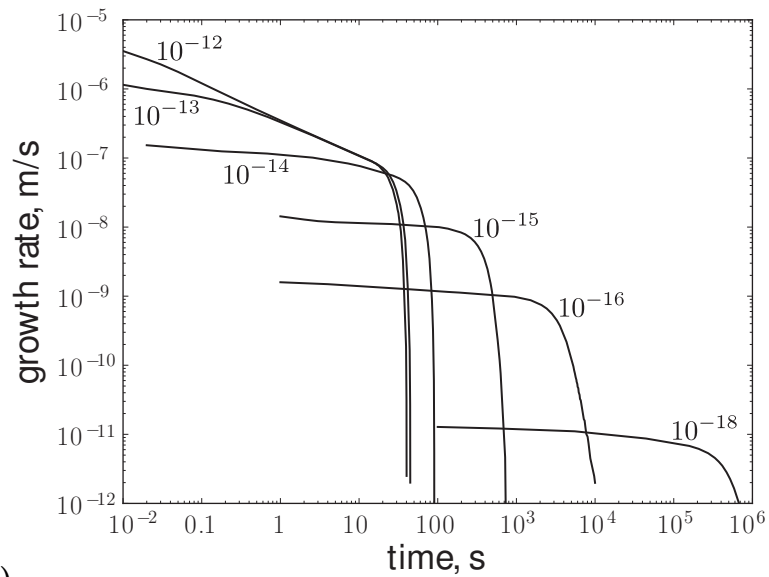
The same conclusion will not be drawn for the tie-lines. To determine those tie-lines the bulk concentration fields of C in the vicinity of the interface have been extrapolated up to the level set $\phi = 0.5$, as in the binary case §3.3. On the contrary, we have taken the extrema for Mn because of the steep gradients, very often confined to the interface, which prevent any relevant extrapolation of the bulk fields (except for the very slow transformations at the very long times). For clarity, we have plotted only the evolutions of the γ side of the tie-lines (blue lines) in the isothermal section in Fig. 3.16. The white dot represents the initial homogeneous composition of γ , whereas the red dots indicate the final (i.e. at the end of the calculations) compositions at the right boundary of the system, for the different mobilities.

For the three highest interface mobilities (10^{-14} , 10^{-13} and 10^{-12} m⁴/J/s), a similar behaviour is observed, already discussed in [155, 156]. During the first kinetic stage, the operative tie-line reaches rapidly the PE tie-line (dotted line ended by white squares). Whereas it is quite instantaneous for the highest mobility, for 10^{-13} m⁴/J/s it takes about 0.1 s for c^γ to move horizontally along the PE tie-line, the time necessary to switch from a mixed mode regime to a diffusion-controlled regime (Fig. 3.15b). For $M = 10^{-14}$ m⁴/J/s, c^γ goes very close to the PE tie-line (in about 80 s) but never reaches PE. Then, during the transient stage toward the stasis, the C concentration in γ at the right boundary of the system increases gradually (Fig. 3.17) due to the soft-impingement of the C concentration fields. It is notable that the profile of Mn remains almost flat (c^γ moving only horizontally in the ternary section, along the PE tie-line) even for $M = 10^{-14}$ m⁴/J/s. Finally, the stases (third stage) correspond to flat C profiles in γ (Fig. 3.17), defining the position of the red dots in Fig. 3.16: Mn spikes are developing and the corresponding c^γ go vertically toward the LEP tie-lines, at the abscissae of the red dots.

For the smallest M (10^{-18} m⁴/J/s), at the level of the lower branch for M_ϕ



(a)



(b)

Figure 3.15: (a) Ferrite thickness and (b) growth rate vs. time in a Fe-0.15C-1.5Mn (wt.%) alloy at 650°C for different mobilities.

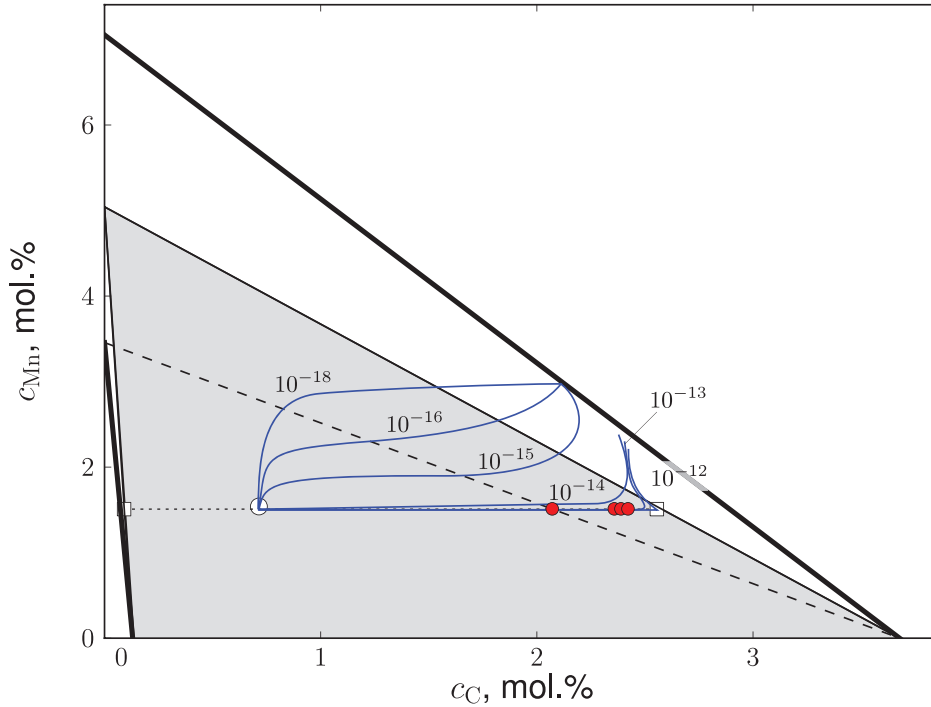


Figure 3.16: Evolutions of c^γ (blue curves) in the isothermal section of the Fe-C-Mn diagram at 650 °C for different mobilities M (in $\text{m}^4/\text{J/s}$).

(Fig. 3.14), i.e. corresponding to a time scale set by manganese diffusion (Eq. (3.157)), the kinetic pathway of the operative tie-line is surprising and opposite to the previous cases. Indeed, during about $5 \cdot 10^4$ s, the profiles of C remain flat, at the initial nominal carbon concentration, as shown in Fig. 3.17c: the growth is so slow that C has enough time to get homogenized in γ by soft-impingement (finite size effect). At the same time, a large Mn spike increases, as well as the Mn concentration in ferrite, both to reach the Mn content of the LEMP tie-line. Therefore, during this stage, c^γ climbs vertically remaining very close to the initial C concentration. After about $2 \cdot 10^5$ s, once the transformation has become nearly non-partitioning for Mn, the carbon concentration raises up in γ as the transformation proceeds. It slows down seriously when the tie-line gets close to the LEMP tie-line.

The two remaining mobilities, 10^{-16} and 10^{-15} $\text{m}^4/\text{J/s}$, are also very surprising and feature strange kinetic pathways in between the previous cases. Both start as for the lowest mobility, developing Mn spikes when the carbon con-

centrations remain flat in γ and equal to the initial nominal C concentration: consequently, c^γ starts to climb vertically in the ternary section. But contrary to $M = 10^{-18} \text{ m}^4/\text{J/s}$, c^γ turns right to move horizontally when an unusual non-partitioning growth mode is established in between PE and LENP: with a small spike but with Mn concentrations at the foot higher than the nominal Mn concentration. Finally, when c^γ approaches the γ boundary of the two-phase field because γ has been enriched in C due to growth, the Mn spike develop and c^γ climbs again toward the γ side of the LENP tie-line.

If the relevance of these calculations are not certain due to the lack of accurate experimental data on the kinetic pathway followed by the operative tie-lines during the $\gamma \rightarrow \alpha$ transformation in ternary steels, we have shown that the introduction of a finite mobility in a phase field model may give rise to a rich array of behaviours.

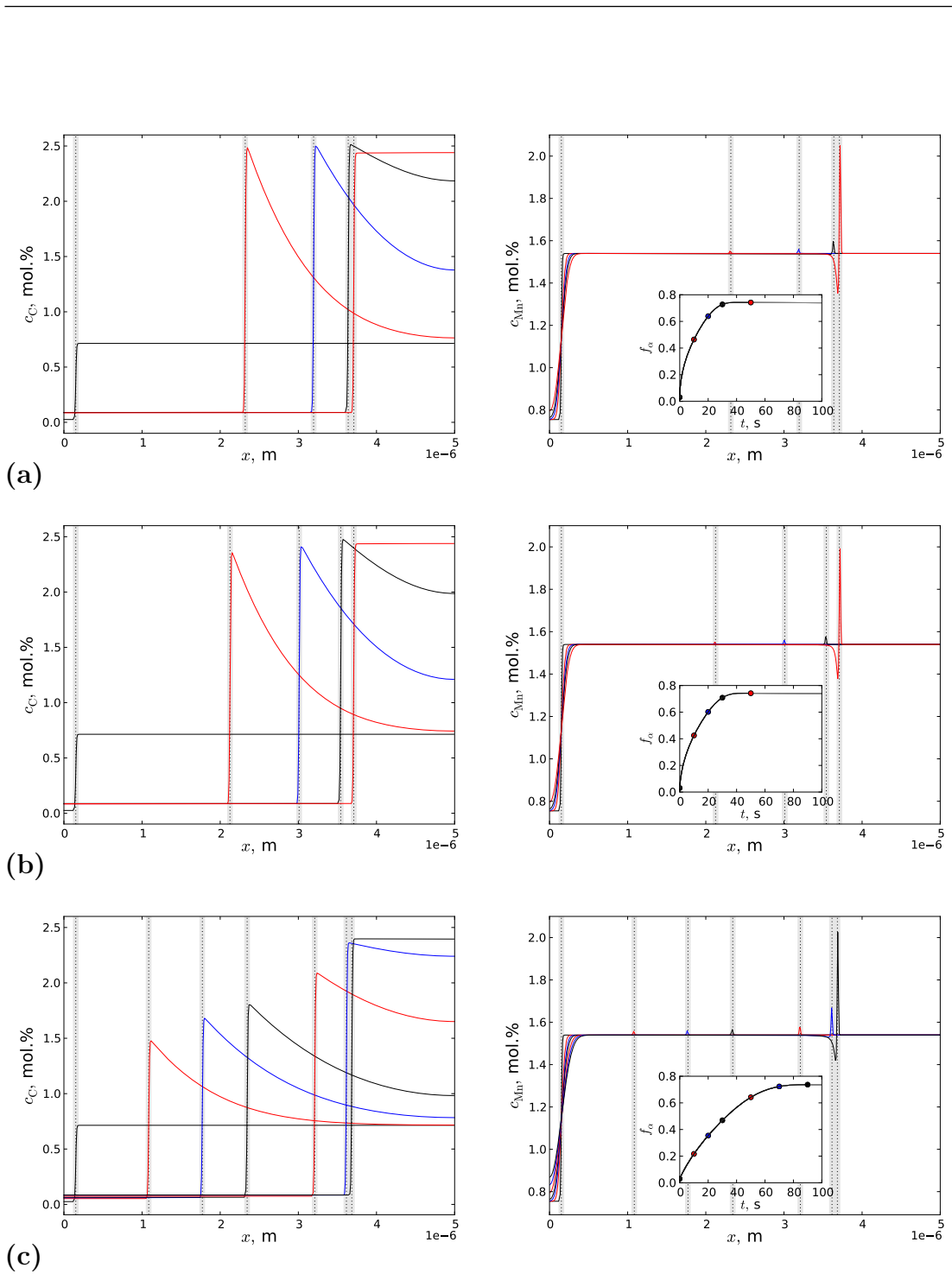


Figure 3.17: Fe-0.15C-1.5Mn (wt.%) alloy at 650°C. Profiles of C (left) and Mn (right) with (a) $M = 10^{-12}$, (b) $M = 10^{-13}$, (c) $M = 10^{-14}$ (diffuse interfaces in grey slabs).

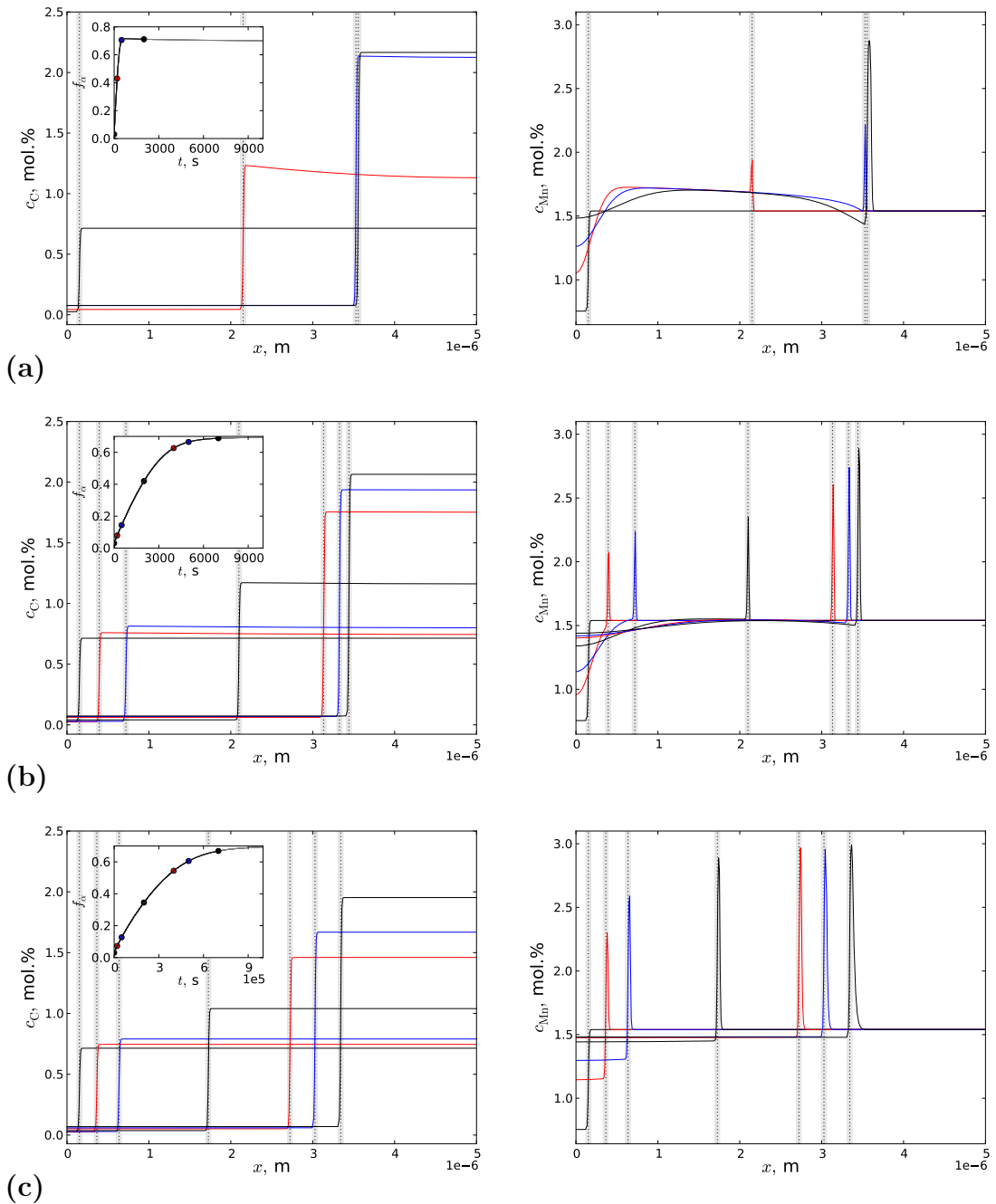


Figure 3.18: Fe-0.15C-1.5Mn (wt.%) alloy at 650°C. Profiles of C (left) and Mn (right) with (a) $M = 10^{-15}$, (b) $M = 10^{-16}$, (c) $M = 10^{-18}$ (diffuse interfaces in grey slabs).

3.5 Conclusion

In this chapter, we have performed a deep analysis of the mobility of the phase field model developed previously by Viardin [155] for investigating the kinetics of the $\gamma \rightarrow \alpha$ transformation in Fe-C-Mn alloys. Indeed, this parameter had appeared to be very crucial for predicting realistic kinetics in ternary Fe-C-X steels, in particular PE, as discussed in [156]. The analysis which uses the technique of matched asymptotic expansions, has been carried out up to second order following the work of Karma and Rappel [97, 98] and Almgren [10]. It has permitted to identify the declared advantages and the hidden disadvantages of the expression proposed initially by Kim et al. [102] (KKS), on the basis of a more rigorous derivation. In particular, some subtle hidden assumptions have been found which explain why the KKS mobility is not working perfectly in the case of unequal diffusivities in the coexisting phases (asymmetric model), as already identified in [96]. This puts on a firmer footing the use of such an expression, and prepare future, and more involved, rigorous derivations for the case of Fe-C-X alloys.

Then, we have analyzed the influence of the interface mobility on the kinetics, first in binary Fe-C alloys, second in ternary Fe-C-Mn alloys. In binary alloys, we have put into evidence the essential flaw of the KKS expression for obtaining perfect local equilibrium conditions because of the different diffusivities in α and γ , as already pointed out in the asymptotic analysis. Fortunately, the predictions with were still very good in terms of kinetics and interfacial concentrations, when compared to the solution of the corresponding sharp interface model. When the interface mobility is reduced, growth is interface-controlled with a constant velocity at the beginning of the transformation, and can change to diffusion-controlled with a velocity scaling as $1/\sqrt{t}$, if soft impingement does not occur too early. When the mobility is further reduced, growth can remain interface-controlled, featuring a linear growth law until the occurrence of soft impingement. These trends are consistent with the mixed mode model of Sietsma and van der Zwaag [144].

In ternary alloys, decreasing the interface mobility has featured a variety of scenarios, with some of them quite unexpected. When the phase field mobilities

are close to some upper limit calculated with the expression of KKS accounting for carbon diffusivity only, the kinetic pathway is close to what Viardin has obtained [155]. Growth starts as PE until the enrichment of γ in C moves the system close to the zero-partition line. Then, growth stops and the ferrite fraction vs. time exhibits a stasis below the paraequilibrium fraction. Correlatively, the tie-line moves toward some LEP tie-line. For the mobility close to the expression of KKS using both C and Mn diffusivities, i.e. with a very small value, the pathway followed by the operative tie-line is very different and accompany a very slow growth process. A Mn spike starts to develop when the carbon content of γ remains flat at its initial level. Then, when the Mn profile has adopted the LENP configuration, the flat carbon profile in γ increases to reach its LENP configuration. For mobilities in between, the kinetic pathways are a mix of both.

In prospect, we could propose first to improve the asymmetric model by removing the spurious jump of driving force at first order to recover perfect local equilibrium at the interface. If the introduction of a so-called anti-solute trapping has already been proposed in [96] for that purpose, the arguments of Plapp [132] about the relevance of this correction indicate that other solutions could be proposed.

The comparison of the phase field model with the mixed mode model remains to be performed in the binary case. Although it has already been done with another kind of phase field model in [114], the authors have reported difficulties to get quantitative agreement which have not been encountered with the present model and the present analysis.

As already mentioned, a rigorous derivation of the mobility following an asymptotic analysis in Fe-C-X for recovering PE is still lacking. Indeed, the main difficulty to overcome is associated with the variation of the driving force at the lowest order. Along the same line, it would be interesting to perform an asymptotic analysis considering that diffusivities may scale with the interface thickness, in the spirit of [65]. This would indeed give access to PE independently of the interface thickness.

Finally, the results concerning the peculiar kinetic pathway in the ternary alloys when mobilities are small deserve to be analyzed further, following the methodology used for the binary case, i.e. quantifying the dissipation and the driving force.

Appendix A

CalPhaD thermodynamic database for Fe-C-Cr

The thermodynamic parameters entering the *CalPhaD* expressions of the Gibbs energies have taken from *FEDAT* database of Thermo-Calc software.

For an illustrative purpose, we present in this appendix a basic thermodynamic database in the same format as the non-encrypted Thermo-Calc databases. We have chosen the Fe-Cr-C system, containing the solution phase BCC_A2 (bcc structure of A2 type) and FCC_A1 (fcc structure of A1 type). The lines in the database are displayed in typewriter font.

```
$Thermodynamic database for Fe-Cr-C
```

```
ELEMENT VA VACUUM      0.0000E+00  0.0000E+00  0.0000E+00 !  
ELEMENT C  GRAPHITE    1.2011E+01  1.0540E+03  5.7400E+00 !  
ELEMENT CR BCC_A2     5.1996E+01  4.0500E+03  2.3560E+01 !  
ELEMENT FE BCC_A2     5.5847E+01  4.4890E+03  2.7280E+01 !
```

The first few lines include a comment about the origin of the database and four lines that define the elements that are included in the database. The three numeric values represent the molar weight of the element in grams as well as the enthalpy and entropy at a temperature of 298 K and a pressure of 1 atm.

\$definition of some functions

```
FUNCTION GHSECC 298.15 -17368.441+170.73*T-24.3*T*LN(T)
-4.723E-04*T**2+2562600*T**(-1) -2.643E+08*T**(-2)+1.2E+10*T**(-3);
6000.00 N !
```

```
FUNCTION GHSECR 298.15 -8856.94+157.48*T-26.908*T*LN(T)+.00189435*T**2
-1.47721E-06*T**3+139250*T**(-1);2180.00 Y -34869.344+344.18*T-50*T*LN(T)
-2.88526E+32*T**(-9); 6000.00 N !
```

```
FUNCTION GHSEFE 298.15 +1225.7+124.134*T -23.5143*T*LN(T)-.00439752*T**2
-5.8927E-08*T**3+77359*T**(-1);1811.00 Y -25383.581+299.31255*T-46*T*LN(T)
+2.29603E+31*T**(-9); 6000.00 N !
```

Each of these functions starts with the keyword "FUNCTION" and its name. Functions are defined for convenience, if quantities are used multiple times, or for clearer structuring. In the preceding case they represent the pure element states as previously described in Chapter 2. The function name is followed by the lower temperature limit for the next polynomial, which describes the quantity as a function of temperature and/or pressure. The polynomial ends with a semicolon ";". Next is the upper temperature limit and an "N" if no further data follows or "Y" if data for another temperature interval is defined.

```
TYPE_DEFINITION & GES A_P_D BCC_A2 MAGNETIC -1.0 0.4
TYPE_DEFINITION & GES A_P_D BCC_A2 MAGNETIC -3.0 0.28
```

These lines define the magnetic properties of the bcc and fcc solution phases. The next to the last number represent the antiferromagnetic factor n from Chapter 2 and the last number represent the parameter p from equations (1.6) and (1.7).

\$definition of the bcc phase

PHASE BCC_A2 & 2 1.0 3.0 !

CONSTITUENT BCC_A2 : CR%, FE% : C, VA% : !

The keyword "PHASE" starts the phase definition. The phase name is followed by symbols, which have been defined after the keyword "TYPE_DEFINITION", then the number of sublattices and the number of moles on these sublattices ($a_s = 1.0$ and $a_t = 3.0$ from equations). The keyword "CONSTITUENT" defines the elements on the individual sublattices separated with a colon ":". The percent sign "%" after an element indicates major constituents.

\$thermodynamic parameters of the bcc phase

PARAMETER G(BCC_A2,FE:VA;0) 298.15+GHSERFE#; 6000.00 N !

PARAMETER G(BCC_A2,FE:C;0) 298.15+322050+75.667*T+GHSERFE#+3*GHSERCC#;
6000.00 N !

PARAMETER G(BCC_A2,CR:VA;0) 298.15 +GHSERCR#; 6000.00 N !

PARAMETER G(BCC_A2,CR:C;0) 298.15 +416000+GHSERCR# +3*GHSERCC#;
6000.00 N !

\$interaction parameters

PARAMETER L(BCC_A2,CR,FE:VA;0) 298.15 +20500-9.68*T; 6000.00 N !

PARAMETER L(BCC_A2,CR,FE:C;0) 298.15 -1250000+667.7*T; 6000.00 N !

PARAMETER L(BCC_A2,CR:C,VA;0) 298.15 -190*T; 6000.00 N !

PARAMETER L(BCC_A2,FE:C,VA;0) 298.15 -190*T; 6000.00 N !

\$thermodynamic parameters for magnetic ordering

\$TC: Curie temperature

\$BMAG: Bohr magneton number

PARAMETER TC(BCC_A2,CR:VA;0) 298.15 -311.5; 6000.00 N !

PARAMETER TC(BCC_A2,CR:C;0) 298.15 -311.5; 6000.00 N !

PARAMETER TC(BCC_A2,FE:VA;0) 298.15 +1043; 6000.00 N !

PARAMETER TC(BCC_A2,FE:C;0) 298.15 +1043; 6000.00 N !

```

PARAMETER TC(BCC_A2,CR,FE:VA;0) 298.15 +1650; 6000.00 N !
PARAMETER TC(BCC_A2,CR,FE:VA;1) 298.15 +550; 6000.00 N !
PARAMETER TC(BCC_A2,CR,FE:C;0) 298.15 +1650; 6000.00 N !
PARAMETER TC(BCC_A2,CR,FE:C;1) 298.15 +550; 6000.00 N !
PARAMETER BMAGN(BCC_A2,CR:VA;0) 298.15 -.01; 6000.00 N !
PARAMETER BMAGN(BCC_A2,CR:C;0) 298.15 -.008; 6000.00 N !
PARAMETER BMAGN(BCC_A2,FE:VA;0) 298.15 2.22; 6000.00 N !
PARAMETER BMAGN(BCC_A2,FE:C;0) 298.15 2.22; 6000.00 N !
PARAMETER BMAGN(BCC_A2,CR,FE:VA;0) 298.15 -.85; 6000.00 N !
PARAMETER BMAGN(BCC_A2,CR,FE:C;0) 298.15 -.85; 6000.00 N !

```

The keyword "PARAMETER" is followed by the type of parameter (G, TC or BMAG), with the phase name and the elements. Again, sublattice are separated by a colon. After the semicolon comes the exponent k of the Redlich-Kister polynomials in equations (1.4), (1.5), (1.21). This parameter is only relevant for the interaction parameters. Finally, the definition of the thermodynamic data for the carbide phases is:

\$definition of the fcc phase

```
PHASE FCC_A21 & 2 1.0 1.0 !
```

```
CONSTITUENT BCC_A2 : CR, FE% : C, VA% : !
```

```
PARAMETER G(FCC_A1,CR:VA;0) 298.15 +GCRFCC#; 6000.00 N !
```

```
PARAMETER G(FCC_A1,CR:C;0) 298.15 +GHSERCR#+GHSERCC#+1200-1.94*T;
6000.00 N !
```

```
PARAMETER G(FCC_A1,FE:VA;0) 298.15 +GFEFCC#; 6000.00 N !
```

```
PARAMETER G(FCC_A1,FE:C;0) 298.15 +77207-15.877*T+GFEFCC#+GHSERCC#;
6000.00 N !
```

```
PARAMETER L(FCC_A1,CR,FE:VA;0) 298.15 +10833-7.477*T; 6000.00 N !
```

```
PARAMETER L(FCC_A1,CR,FE:VA;1) 298.15 +1410; 6000.00 N !
```

```
PARAMETER L(FCC_A1,CR,FE:C;0) 298.15 -74319+3.2353*T; 6000.00 N !
```

PARAMETER L(FCC_A1,CR:C,VA;0) 298.15 -11977+6.8194*T; 6000.00 N !
PARAMETER L(FCC_A1,FE:C,VA;0) 298.15 -34671; 6000.00 N !
PARAMETER TC(FCC_A1,FE:VA;0) 298.15 -201; 6000.00 N !
PARAMETER TC(FCC_A1,FE:C;0) 298.15 -201; 6000.00 N !
PARAMETER BMAGN(FCC_A1,FE:VA;0) 298.15 -2.1; 6000.00 N !
PARAMETER BMAGN(FCC_A1,FE:C;0) 298.15 -2.1; 6000.00 N !

Appendix B

Main function of convex hull building in numerical language

In the algorithm of Qhull [20] for building the convex hull we enumerate here some of the most important classes that we are used, as: `point`, `pointList`, `hyperplane`, `qhull`.

The class of `point` contains the pointer to the massif of coordinates; constructors (copy, creation of point in n-dimension using the massif of coordinates); destructors (delete of point and liberate the allocated memory); operators (comparison of points, subtraction).

Concerning the class of `pointList` we are created the list of points; pointer to the first item in the list of points; pointer to the last item in the list of points; functions (addition of point in the list of points, delete an element from list).

The class of `hyperplane` contains the hyperplane constructors; calculation of distance from point to hyperplane; definition of visibility conditions of hyperplane from point; pointer to the neighbors; delete of hyperplanes; operators

The class of `qhull` contains the following set of operations:

```
int numPoints // number of points in the hull
int numPlanes // number of hyperplanes in the hull
pointList sourcePoints // list of source points
pointList qhullPoints // list of points the hull
```

```

hyperplane *firstplane // pointer to the initial
    hyperplane
hyperplane *start // pointer to the first item in the
    list of set of hyperplanes
hyperplane *last // pointer to the last item in the list
    of set of hyperplanes
hyperplane *addPlane(hyperplane *plane, hyperplane *
    previousPlane) // addition of the hyperplane into the
    hull with inclusion of it in the list of hyperplanes
hyperplane *deletePlane(hyperplane *plane) // delete of
    the hyperplane from the list of hyperplanes
point *nextPoint(hyperplane &plane) // searching of the
    next point to be added into the hull
void setOFneighbors() // list of the neighbors for all
    hyperplanes of hull
hyperplane *addPoint(hyperplane} *plane, point *point)
    // adding point into the hull
hyperplane *findVisible(hyperplane *plane, point *point)
    // visibility conditions of hyperplane from point

```

Function of convex hull building (void `qhull :: buildQhull()`):

```

int noPoints = 0; // counter of planes for which there is no outside points
hyperplane *cur = start; // set the current plane as the first in the list of
planes
while true do
    // if for this plane there are no points
    if (cur → inNOpoints()) then
        noPoints ++ ; // increment counter of planes without external points
        // if the number of planes in the hull is equal to the number of planes
        without external points
        if (noPoints == numPlanes) then
            break; // exit from the cycle, the hull is built
        end if

```

```

cur = cur → next; // in the case of existence planes with external points, then
proceed to the next plane in the list
// if the pointer to this plane is equal zero this means that previous plane
is the last in the list
if ( !cur ) then
    noPoints = 0; // counter of planes without external points is zero
    cur = strat; // current plane becomes the first plane in the list
end if
continue; // to the beginning of the cycle
end if
point *pt = nextPoint( *cur ); // obtain a point to add to the plane
// if there is no point
if ( !pt ) then
    cur → setNOpoints(); // this plane has no exterior points
    noPoints ++ ; // counter increment
    // if the number of planes in the hull is equal to the number of planes
    without external points
    if ( noPoints == numPlanes ) then
        break; // exit from the cycle, the hull is built
    end if
    cur = cur → next; // in the case of existence planes with external points, then
    proceed to the next plane in the list
    // if the pointer to this plane is equal zero this means that previous plane
    is the last in the list
    if ( !cur ) then
        noPoints = 0; // counter of planes without external points is zero
        cur = start; // current plane becomes the first plane in the list
    end if
    continue; // to the beginning of the cycle
end if
cur = addPoint( cur, pt ); // add current point pt to the plane, returns the
plane following the current
removeInnerPoints(); // delete an interior points

```

```
if ( !cur ) then  
    noPoints = 0; // counter of planes without external points is zero  
    cur = start; // current plane becomes the first plane in the list  
end if  
end while
```

Appendix C

The hybrid algorithm applied to Fe-C-Ni

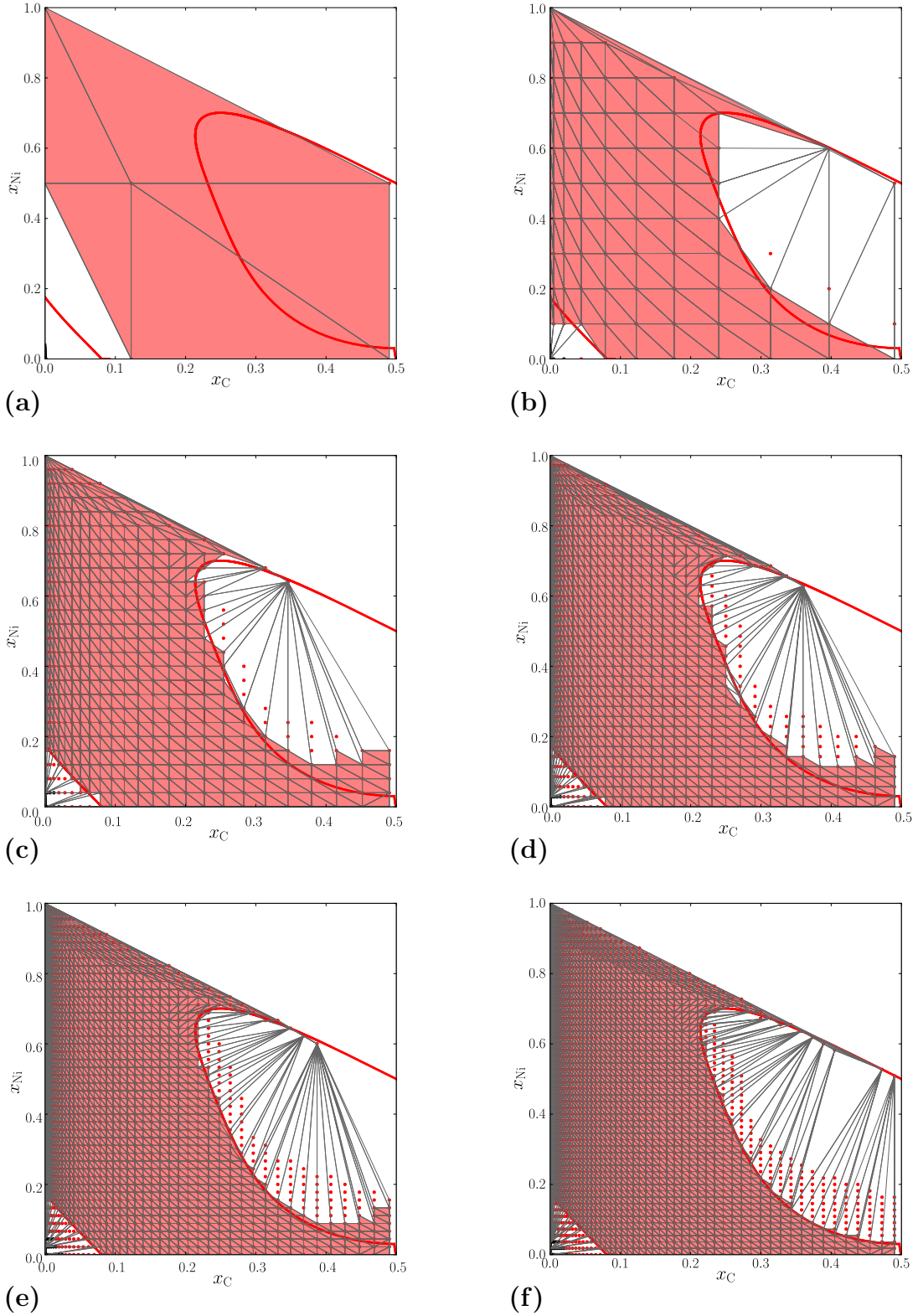


Figure C.1: Projections of the final convex hulls (triangles) of the Gibbs energies of α (black dots) and γ (red dots) in Fe-C-Ni at 600°C, for $N = 2$ (a), $N = 10$ (b), $N = 25$ (c), $N = 35$ (d), $N = 45$ (e) and $N = 55$ (f).

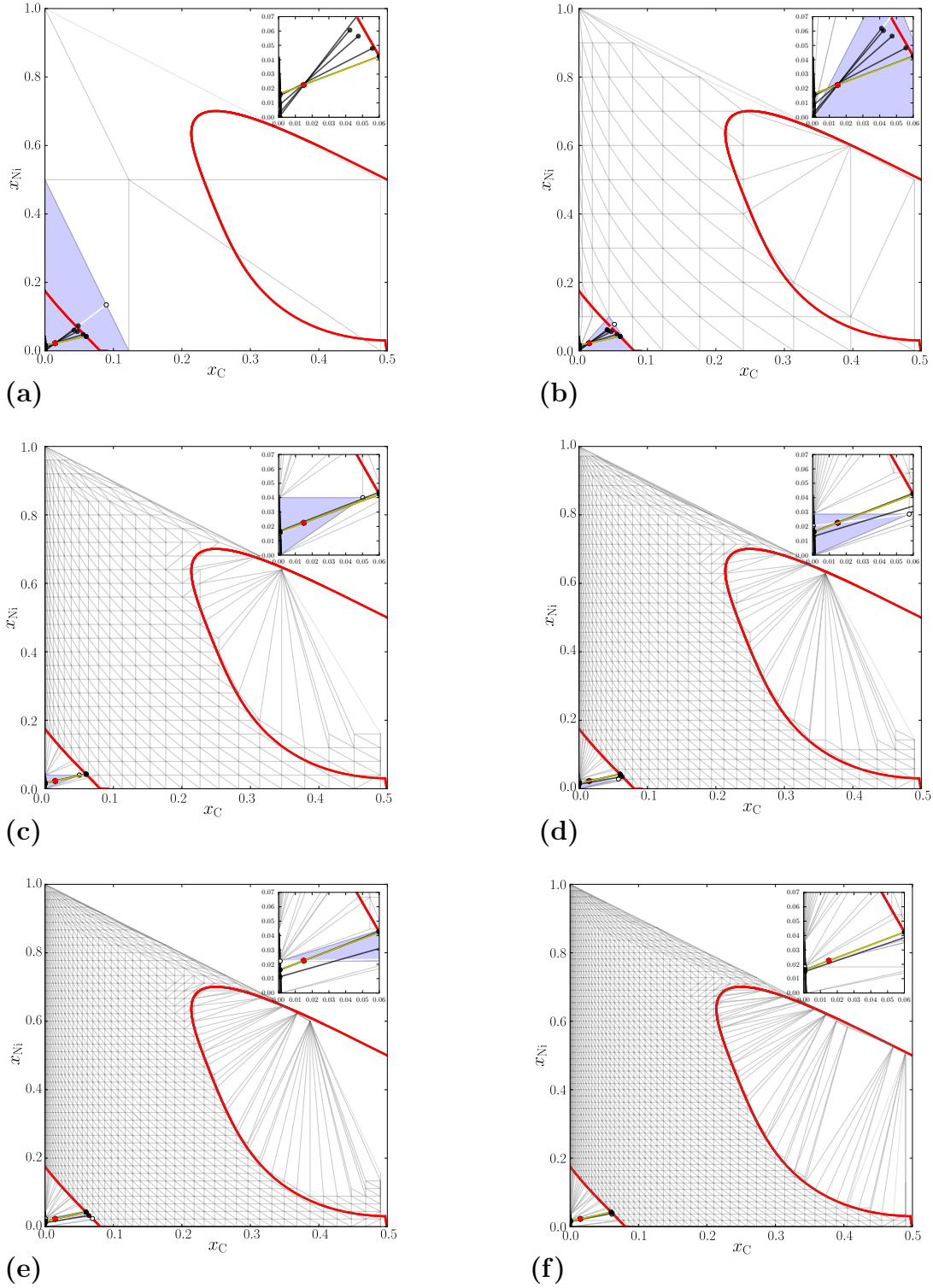


Figure C.2: Tie-line search process with NR for Fe-1.5 mol.%C-2.25 mol.%Ni (red dot), starting with the tie-lines obtained from the convex hulls at 600°C (white line in the blue triangle) for $N = 2$ (a), $N = 10$ (b), $N = 25$ (c), $N = 35$ (d), $N = 45$ (e), $N = 55$ (f). Intermediate, and final tie-lines are in black and yellow respectively.

Appendix D

Data for the kinetic calculations

	T_{ref} (K)	m_i	k_i
C	911.76	-7116.61	0.035
Mn		-3711.0	0.049

Table D.1: Parameters for the linearized Fe-C-Mn phase diagram.

Elements		γ	α
C	D^0 (m ² /s)	$2.5 \cdot 10^{-5}$	$2 \cdot 10^{-5}$
	Q (kJ/mol)	144.21	84.018
Ni	D^0 (m ² /s)	$3.5 \cdot 10^{-5}$	—
	Q (kJ/mol)	286	—
Mn	D^0 (m ² /s)	$1.6 \cdot 10^{-5}$	$1.27 \cdot 10^{-1}$
	Q (kJ/mol)	261.25	271

Table D.2: Diffusion coefficients of carbon, nickel and manganese in austenite and ferrite from the MOBFE database.

Alloy	T (°C)	$D_{\text{C}}^{\gamma^*}$	$D_{\text{Ni}}^{\gamma^*}$	$D_{\text{Mn}}^{\gamma^*}$
<i>a</i>	[630-780]	D_{C}^{α}	10^{-1}	—
<i>b</i>	[700-900]	D_{C}^{α}	—	10^{-2}

Table D.3: Diffusion coefficients inside the interface in Fe-C-Ni and Fe-C-Mn systems.

Appendix E

Interface mobility in Fe-C

This appendix contains additional materials related to the calculations in §[3.3.2](#).

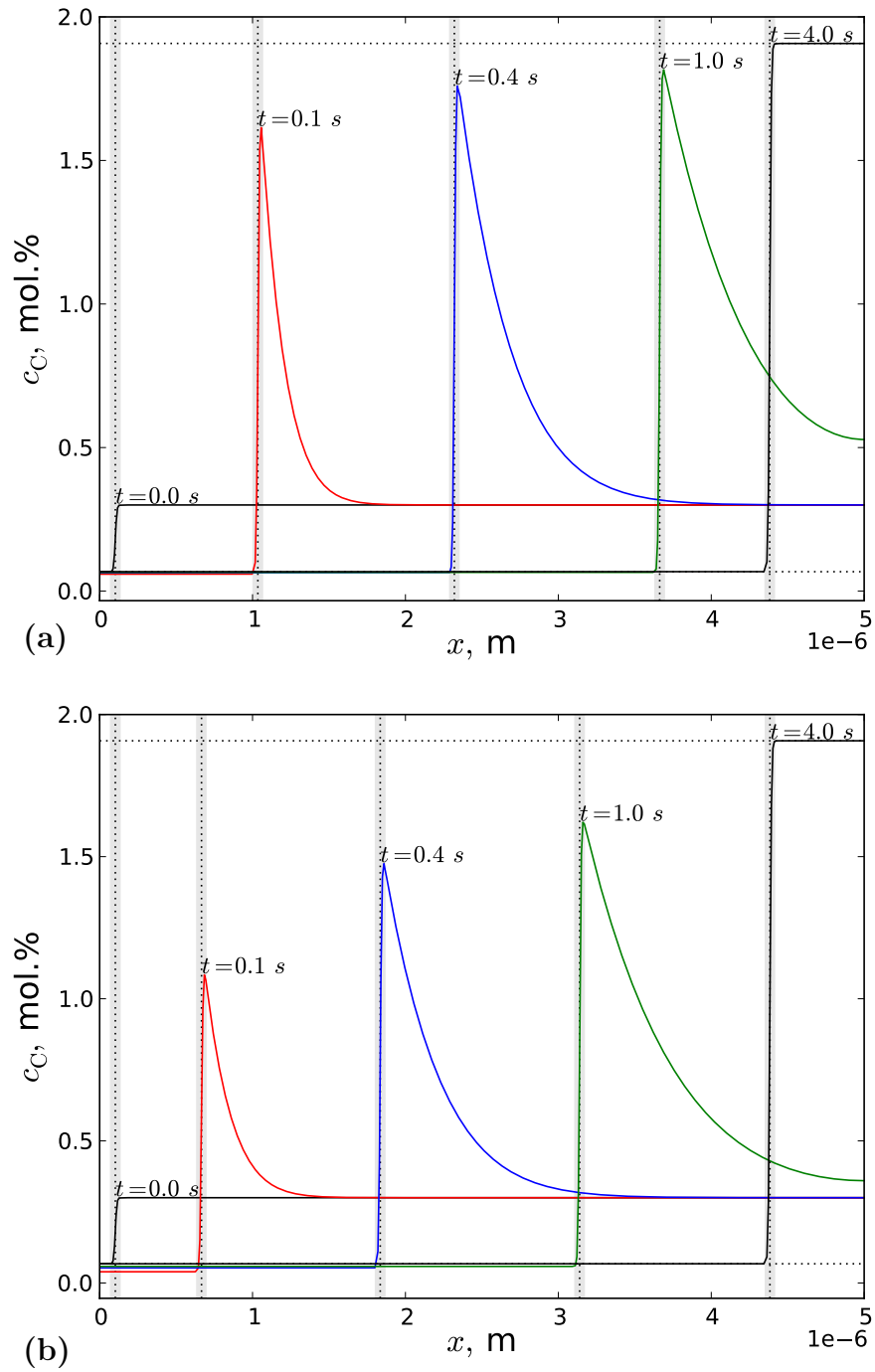


Figure E.1: Carbon concentration profiles: (a) $M = 10^{-11} \text{ m}^4/\text{J/s}$; (b) $M = 10^{-12} \text{ m}^4/\text{J/s}$.

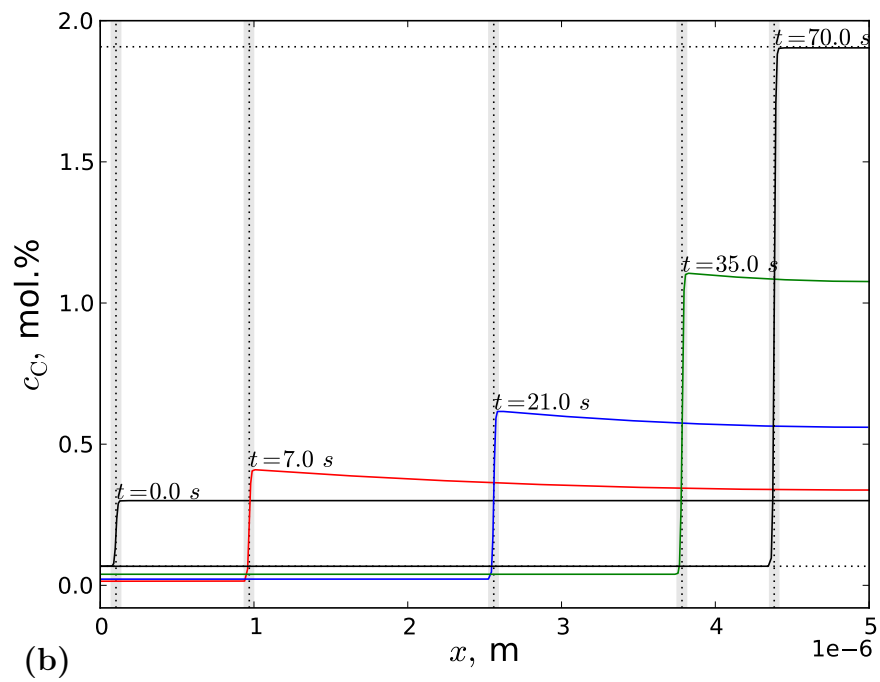
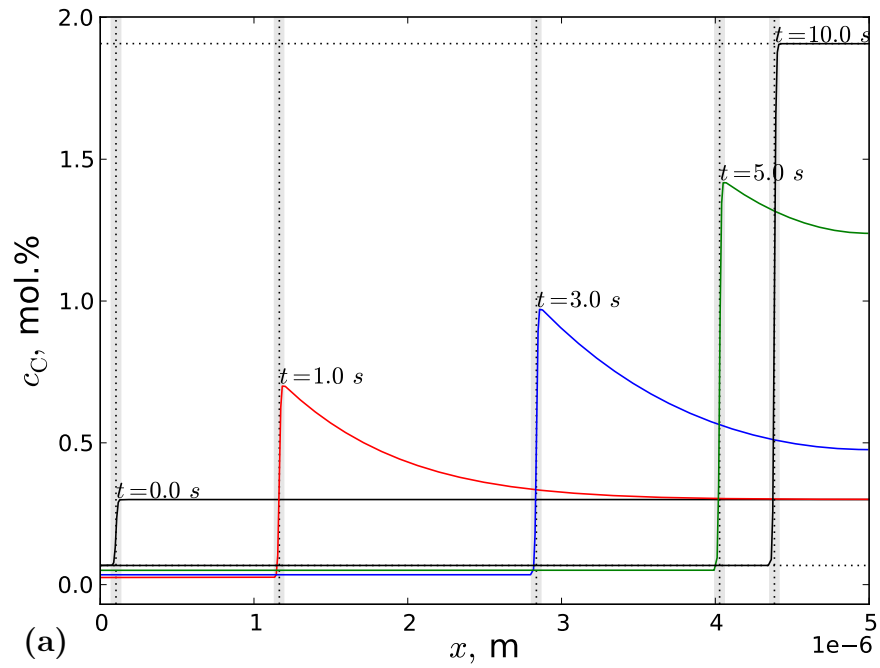


Figure E.2: Carbon concentration profiles: (a) $M = 10^{-13} \text{ m}^4/\text{J/s}$; (b) $M = 10^{-14} \text{ m}^4/\text{J/s}$.

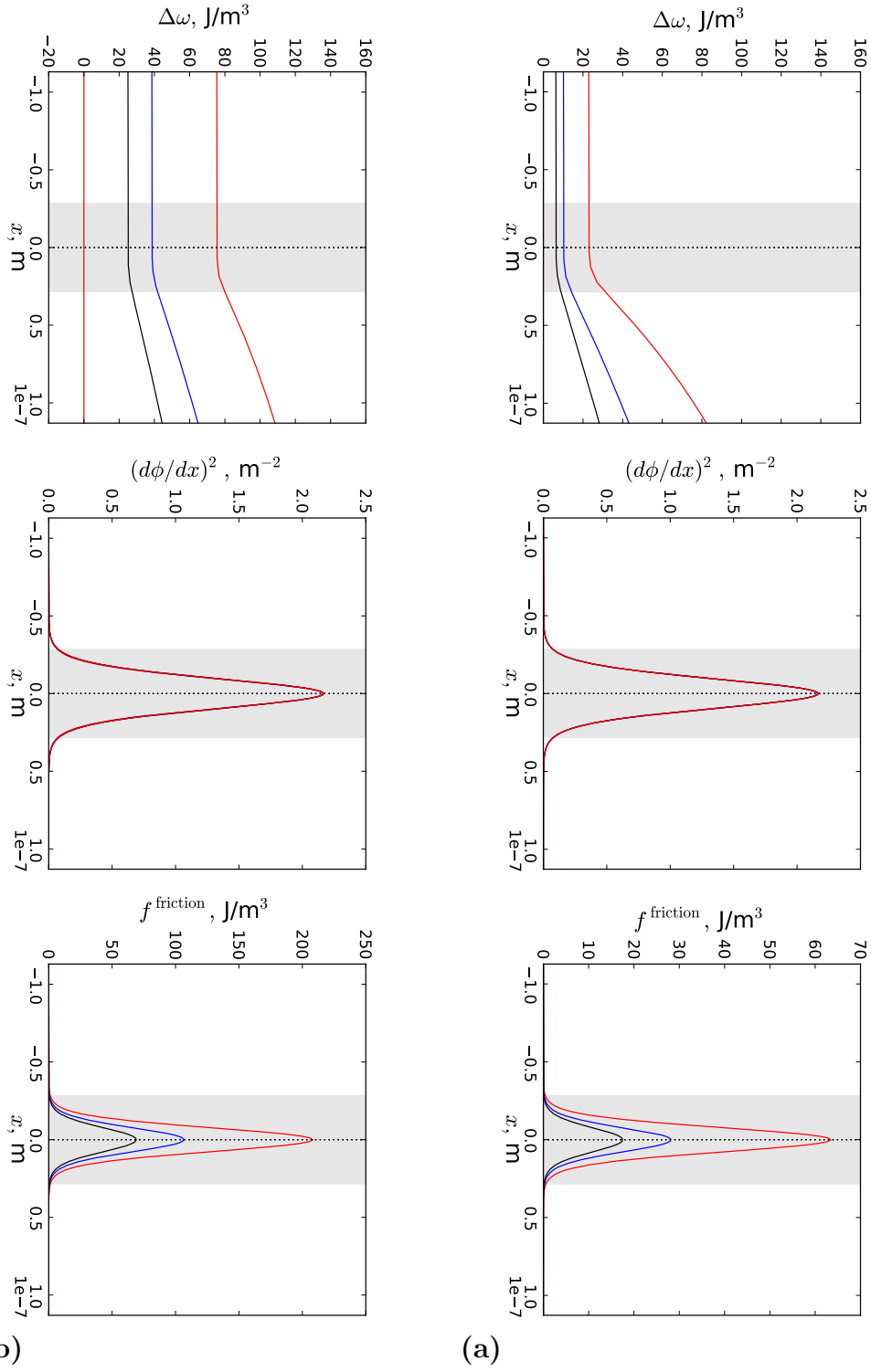


Figure E.3: $\Delta\omega$, $(d\phi/dx)^2$ and $f^{\text{friction}} = h' \Delta\omega d\phi/dx$ versus x at increasing time (top to bottom): (a) $M = 10^{-11}$; (b) $M = 10^{-12}$.

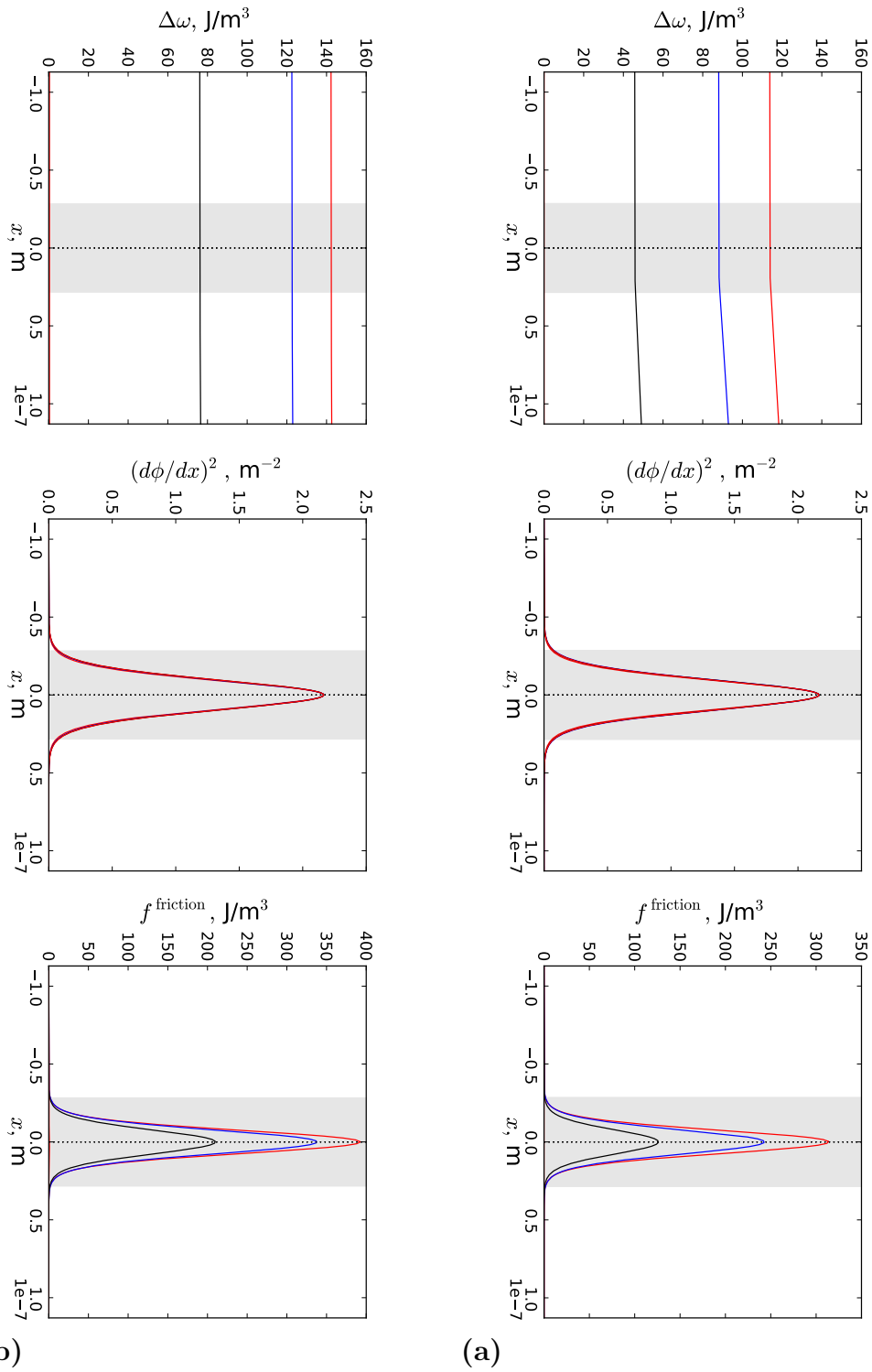


Figure E.4: $\Delta\omega$, $(d\phi/dx)^2$ and $f^{\text{friction}} = h' \Delta w d\phi/dx$ versus x at increasing time (top to bottom): (a) $M = 10^{-13}$; (b) $M = 10^{-14}$.

References

- [1] Ferrite formation in Fe-C alloys during austenite decomposition under non-equilibrium interface conditions. *Mat. Sci. Eng. A*, 237(2):216 – 223, 1997. [11](#), [126](#)
- [2] H.B. Aaron and H.I. Aaronson. Growth of grain boundary precipitates in al-4% cu by interfacial diffusion. *Acta Met.*, 16:789–798, 1968. [8](#), [62](#)
- [3] H.I Aaronson and H.A. Domian. Partitioning of alloying elements between austenite and proeutectoid ferrite and bainite. *Trans. TMS-AIME*, 236: 781–796, 1966. [92](#)
- [4] H.I. Aaronson, T. Furuhashi, J.M. Rigsbee, W.T. Reynolds Jr., and J.M. Howe. Crystallographic and mechanistic aspects of growth by shear and by diffusional processes. *Met. Trans. A*, 21:2369–2409, 1990. [7](#), [61](#)
- [5] H.I. Aaronson, B.C. Muddle, J.F. Nie, and J.P. Hirth. Comparison of interfacial structure-related mechanisms in diffusional and martensitic transformations. *Met. Mat. Trans. A*, 33(8):2541–2547, 2002. [8](#), [62](#)
- [6] H.I. Aaronson, W.T. Reynolds Jr., and G.R. Purdy. The incomplete transformation phenomenon in steel. *Met. Mat. Trans. A*, 37:1731–1745, 2006. [8](#), [62](#)
- [7] G. Abrivard, E.P. Busso, S. Forest, and B. Appolaire. Phase field modelling of grain boundary motion driven by curvature and stored energy gradients. Part I: theory and numerical implementation. *Phil. Mag.*, iFirst, 2012. [127](#)

-
- [8] G. Abrivard, E.P. Busso, S. Forest, and B. Appolaire. Phase field modelling of grain boundary motion driven by curvature and stored energy gradients. Part II: Application to recrystallisation. *Phil. Mag.*, iFirst, 2012. [127](#)
- [9] N.A. Ahmad, A.A. Wheeler, W.J. Boettinger, and G.B. McFadden. Solute trapping and solute drag in a phase-field model of rapid solidification. *Phys. Rev. E*, 58(3):3436–3450, 1998. [135](#)
- [10] R.F. Almgren. Second-order phase field asymptotics for unequal conductivities. *SIAM J. Appl. Math.*, 59(6):2086–2107, 1999. [134](#), [138](#), [149](#), [157](#), [181](#)
- [11] K. Ammar, B. Appolaire, G. Cailletaud, F. Feyel, and S. Forest. Finite element formulation of a phase field model based on the concept of generalized stresses. *Comp. Mat. Sci.*, 45:800–805, 2009. [127](#)
- [12] K. Ammar, B. Appolaire, G. Cailletaud, and S. Forest. Combining phase field approach and homogenization methods for modelling phase transformation in elastoplastic media. *Eur. J. Comp. Mech.*, 18(5-6):485–523, 2009. [127](#)
- [13] K. Ammar, B. Appolaire, G. Cailletaud, and S. Forest. Phase field modeling of elasto-plastic deformation induced by diffusion controlled growth of a misfitting spherical precipitate. *Phil. Mag. Lett.*, 91(3):164–172, 2011. [127](#)
- [14] D.M. Anderson, G.B. McFadden, and A.A. Wheeler. A phase-field model with convection: sharp-interface asymptotics. *Physica D*, 151(2-4):305, 2001. [157](#)
- [15] J.-O. Andersson, T. Helander, L. Hoglund, P. Shi, and Bo. Sundman. Thermo-Calc & DICTRA, computational tools for materials science. *CAL-PHAD*, 26(2):273–312, 2002. [41](#)
- [16] B. Appolaire and E. Gautier. Modelling of phase transformations in titanium alloys with a phase field model. In H. Emmerich, B. Nestler, and M. Schrekenberg, editors, *Interface and Transport Dynamics*, volume 32, pages 196–202. Springer, 2003. [127](#)

REFERENCES

- [17] B. Appolaire, L. Hélicher, and E. Aeby-Gautier. Modelling of phase transformation kinetics in Ti alloys – Isothermal treatments. *Acta Mat.*, 53: 3001–3011, 2005. [7](#), [61](#)
- [18] M.J. Aziz. Interface response functions for rapid alloy solidification: theory and experiment. In E.W. Collings and C.C. Koch, editors, *Undercooled alloy phases*. TMS, March 1986. [7](#), [61](#)
- [19] J.C. Baker and J.W. Cahn. *Solidification*, page 23. ASM, 1971. [68](#)
- [20] C.B Barber, D.P Dobkin, and H. Hundanpaa. The Quickhull algorithm for convex hulls. *ACM Trans. Math. Soft.*, 22:469–483, 1995. [6](#), [19](#), [33](#), [35](#), [189](#)
- [21] A. Beche, H.S. Zurob, and C.R. Hutchinson. Quantifying the solute drag effect of Cr on ferrite growth using controlled decarburization experiments. *Met. Mat. Trans. A*, 38(12):2950–2955, 2007. [90](#), [123](#), [124](#)
- [22] R. Bellman. *Perturbation Techniques in Mathematics, Physics, Engineering*. Holt, Rinehart and Winston, Inc., 1966. [142](#)
- [23] G.V Belov, A.L Emelina, V.I Goriacheva, I.A Uspenskaya, and G.F Voronin. An algorithm of calculation of phase diagrams based on convex hulls approach and its implementation. *J. Alloys Comp.*, 452(133-135), 2007. [5](#), [18](#)
- [24] C.M. Bender and S.A. Orszag. *Advanced Mathematical Methods for Scientists and Engineers*. McGraw-Hill, 1978. [142](#)
- [25] W.J. Boettinger, J.A. Warren, C. Beckermann, and A. Karma. Phase-field simulation of solidification 1. *Ann. Rev. Mat. res.*, 32:163–194, 2002. [127](#)
- [26] Y. Le Bouar and A.G. Khachaturyan. Mechanism and modeling of saw-tooth structure formation in the $l1_2$ - $l1_0$ two-phase system. *Acta Mat.*, 48: 1705–1717, 2000. [127](#)
- [27] J.P. Bourne, C. Atkinson, and R.C. Reed. Diffusion-controlled growth in ternary systems. *Met. Mat. Trans. A*, 25(12):2683–2694, 1994. [71](#), [72](#)

REFERENCES

- [28] G. Boussinot, A. Finel, and Y. Le Bouar. Phase-field modeling of bimodal microstructures in nickel-based superalloys. *Acta Mat.*, 57(3):921–931, 2009. [127](#)
- [29] J.R Bradley, J.M Rigsbee, and H.I Aaronson. Growth kinetics of grain boundary ferrite allotriomorphs in Fe-C alloys. *Met. Trans. A*, 8(2):323–333, 1977. [90](#)
- [30] W.L. Bragg and E.J. Williams. The effect of thermal agitation on atomic arrangement in alloys. *Proc. R. Soc. Lond. A*, 145(699-730), 1934. [21](#)
- [31] J.W. Cahn. Theory of crystal growth and interface motion in crystalline materials. *Acta Mat.*, 8:554–562, 1960. [70](#)
- [32] J.W Cahn. The impurity-drag effect in grain boundary motion. *Acta Met.*, 10(9):789–798, 1962. [8](#), [63](#)
- [33] J.W. Cahn and J.E. Hilliard. Free energy of a nonuniform system. i. interfacial free energy. *J. Chem. Phys.*, 28(2):258–267, 1958. [132](#)
- [34] B. Caroli, C. Caroli, and B. Roulet. Interface kinetics and solidification of alloys: A discussion of some phenomenological models. *Acta Met.*, 34(9):1867–1877, 1986. [68](#)
- [35] H. Chen and S. van der Zwaag. Application of the cyclic phase transformation concept for investigating growth kinetics of solid-state partitioning phase transformations. *Comp. Mat. Sci.*, 49:801–813, 2010. [10](#), [11](#), [71](#), [91](#), [92](#), [124](#), [125](#), [126](#)
- [36] H. Chen, B. Appolaire, and S. van der Zwaag. Application of cyclic partial phase transformations for identifying kinetics transitions during solid-state phase transformations: Experiments and modeling. *Acta Mat.*, 59(6751-6760), 2011. [10](#), [91](#), [92](#), [125](#)
- [37] H. Chen, M. Gouné, and S. van der Zwaag. Analysis of the stagnant stage in diffusional phase transformations starting from austenite–ferrite mixtures. *Comp. Mat. Sci.*, 55:34–43, 2012. [10](#), [92](#), [125](#)

REFERENCES

- [38] L.Q. Chen. Phase-field models for microstructure evolution. *Ann. Rev. Mat. Res.*, 32:113–140, 2002. [127](#)
- [39] S-L Chen, K-C Chou, and Y.A Chang. On a new strategy for phase diagram calculation 1. Basic principles. *CALPHAD*, 17(3):237–250, 1993. [5](#), [18](#)
- [40] S.-L. Chen, J.-Y. Zhang, X.-G. Lu, K.-C. Chou, and Y.A. Chang. Application of Graham scan algorithm in binary phase diagram calculation. *J. Phase Equil. Dif.*, 27(2):121–125, 2006. [5](#), [18](#)
- [41] S.L. Chen, S. Daniel, F. Zhang, Y.A. Chang, X.Y. Yan, F.Y. Xie, R. Schmid-Fetzer, and W.A. Oates. The PANDAT software package and its applications. *CALPHAD*, 26(2):175–188, 2002. [5](#), [18](#)
- [42] T.L. Chow. *Mathematical Methods for Physicists: A concise introduction*. Cambridge University Press, 2000. [66](#)
- [43] J.W. Christian. Crystallographic theories, interface structures, and transformation mechanisms. *Met. Mat. Trans. A*, 25:1821–1839, 1994. [7](#), [62](#)
- [44] J.W. Christian. *The Theory of Transformations in Metals and Alloys*. Pergamon, 2002. [7](#), [8](#), [62](#), [70](#)
- [45] C.B. Clemons, S.I. Hariharan, and G.W. Young. Asymptotic solutions of a phase-field model for alloy solidification. *SIAM J. Appl. Math.*, 62(6):1952–1979, 2002. [157](#)
- [46] D.E. Coates. Diffusion-controlled precipitate growth in ternary systems 1. *Met. Mat. Trans. B*, 3(5):1203–1212, 1972. [84](#), [85](#)
- [47] D.E. Coates. Diffusion-controlled precipitate growth in ternary systems 2. *Met. Mat. Trans. B*, 4(4):1077–1086, 1973. [84](#), [85](#)
- [48] D.E. Coates. Precipitate growth kinetics for Fe-C-X alloys. *Met. Trans. B*, 4(1):395–396, 1973. [84](#), [121](#)
- [49] J.A.D Connolly and D.M Kerrick. An algorithm and computer program for calculation composition phase diagrams. *CALPHAD* 11, 11(1-55), 1987. [5](#), [18](#)

REFERENCES

- [50] M. Cottura, Y. Le Bouar, A. Finel, B. Appolaire, K. Ammar, and S. Forest. A phase field model incorporating strain gradient viscoplasticity: Application to rafting in Ni-base superalloys. *J. Mech. Phys. Sol.*, 60:1243–1256, 2012. [127](#)
- [51] R. Courant and D. Hilbert. *Methods of Mathematical Physics*. John Wiley & Sons, Inc., 1989. [145](#)
- [52] R.T. DeHoff. Diffusion-controlled growth in polycomponent systems. *Solid to Solid Phase Transformation*, pages 503–520, 1982. [84](#)
- [53] B. Echebarria, R. Folch, A. Karma, and M. Plapp. Quantitative phase-field model of alloy solidification. *Phys. Rev. E*, 70:061604–1–22, 2004. [168](#)
- [54] J. Eiken, B. Bottger, and I. Steinbach. Multiphase-field approach for multicomponent alloys with extrapolation scheme for numerical application. *Phys. Rev. E*, 73(066122), 2006. [130](#), [133](#)
- [55] M.E. Emelianenko, Z.-K. Liu, and Q. Du. A new algorithm for the automation of phase diagram calculation. *Comp. Mat. Sci.*, 35(61-74), 2005. [5](#), [18](#)
- [56] M. Enomoto. Influence of solute drag on the growth of proeutectoid ferrite in Fe-C-Mn alloy. *Acta Mat.*, 47(3):3533–3540, 1999. [9](#), [63](#)
- [57] M. Enomoto. Influence of solute drag on the growth of proeutectoid ferrite in Fe-C-Mn alloy. *Acta Mat.*, 47(13):3533–3540, 1999. [8](#), [62](#)
- [58] M. Enomoto. Simulation of ferrite growth in continuously cooled low-carbon iron alloys. *Met. Mat. Trans. A*, 33(8):2309–2316, 2002. [119](#)
- [59] M. Enomoto. Local conditions at moving α/γ boundaries of proeutectoid ferrite transformation in iron alloys. *Met. Mat. Trans. A*, 37(1703-1710), 2006. [89](#), [90](#), [104](#), [119](#)
- [60] F.C. Frank. Radially symmetric phase growth controlled by diffusion. *Proc. Royal Soc. London A*, 201:586–599, 1950. [7](#), [62](#), [71](#), [85](#)

-
- [61] E. Gamsjäger, M. Militzer, F. Fazeli, J. Svoboda, and F.D. Fischer. Interface mobility in case of the austenite-to-ferrite phase transformation. *Comp. Mat. Sci.*, 37:94–100, 2006. [11](#), [126](#)
- [62] H. Garcke and B. Stinner. Second order phase field asymptotics for multi-component systems. *Interf. Free Bound.*, 8:131–157, 2006. [138](#), [157](#)
- [63] J.W. Gibbs. *The Collected Works of J. Willard Gibbs*, volume I. Thermodynamics. Longmans, Green & Co, 1928. [7](#), [61](#)
- [64] A. Gilbert and W.S. Owen. Diffusionless transformation in iron-nickel, iron-chromium and iron-silicon alloys. *Acta Mat.*, 10(1):45–54, 1962. [81](#)
- [65] K. Glasner. Solute trapping and the non-equilibrium phase diagram for solidification of binary alloys. *Physica D*, 151(2-4):253–270, 2001. [139](#), [182](#)
- [66] D. Godard. *Influences de la précipitation sur le comportement thermomécanique lors de la trempe d'un alliage Al-Zn-Mg-Cu*. PhD thesis, INPL, 1998. [8](#), [62](#)
- [67] J. Agren. Computer simulations of the austenite/ferrite diffusional transformations in low alloyed steels. *Acta Met.*, 30:841–851, 1982. [71](#)
- [68] S.R. De Groot and P. Mazur. *Non-equilibrium thermodynamics*. Dover Publications, 1962. [9](#), [63](#), [68](#), [129](#)
- [69] F.S. Ham. Shape-preserving solutions of the time-dependent diffusion equation. *Quart. Appl. Math.*, 17(2):137–145, 1959. [71](#)
- [70] S.I. Hariharan and G.W. Young. Comparison of asymptotic solutions of a phase-field model to a sharp-interface model. *SIAM J. Appl. Math.*, 62(1):244–263, 2001. [157](#)
- [71] M. Hillert. Diffusion and interface control of reactions in alloy. *Met. Trans. A*, 6(1):5–19, 1975. [9](#), [63](#), [76](#), [121](#), [134](#)
- [72] M. Hillert. *Phase Equilibria Phase Diagrams and Phase Transformations. Their Thermodynamic Basis*. University Press, Cambridge, 1998. [89](#)

REFERENCES

- [73] M. Hillert. Solute drag, solute trapping and diffusional dissipation of gibbs energy. *Acta Mat.*, 47(18):4481–4505, 1999. [9](#), [63](#), [68](#)
- [74] M. Hillert. The compound energy formalism. *J. Alloys. Comp.*, 320:161–176, 2001. [6](#), [19](#), [25](#), [32](#)
- [75] M. Hillert. Critical limit for massive transformation. *Met. Mat. Trans.*, 33 A:2299–2308, 2002. [77](#)
- [76] M. Hillert. Nature of local equilibrium at the interface in the growth of ferrite from alloyed austenite. *Scr. Mat.*, 46(6):447–453, 2002. [9](#), [63](#), [93](#)
- [77] M. Hillert. *Thermodynamics and Phase Transformations – The selected works of Mats Hillert*, chapter The growth of ferrite, bainite and martensite, pages 113–158. Éditions de Physique, 2006. [67](#)
- [78] M. Hillert and M. Jarl. A model for alloying effects in ferromagnetic metals. *CALPHAD*, 2(3):227–238, 1978. [22](#)
- [79] M. Hillert and M. Shalin. Modeling of solute drag in the massive phase transformation. *Acta Mat.*, 48:461–468, 2000. [9](#), [63](#), [121](#)
- [80] M. Hillert and L-I Staffansson. Introduction to "the regular solution model for stoichiometric phases and ionic melts. *Acta Chem. Scand.*, 24:3618–3626, 1970. [25](#)
- [81] M. Hillert and Bo. Sundman. A treatment of the solute drag on moving grain boundaries and phase interfaces in binary alloys. *Acta Met.*, 24(8):731–743, 1976. [8](#), [9](#), [63](#)
- [82] M. Hillert and Bo. Sundman. A solute-drag treatment of the transition from diffusion-controlled to diffusionless solidification. *Acta Mat.*, 25(1):11–18, 1977. [8](#), [63](#)
- [83] G. Horvay and J.W. Cahn. Dendritic and spheroidal growth. *Acta Met.*, 9:695–705, 1961. [7](#), [62](#), [71](#)

REFERENCES

- [84] C.-J. Huang, D.J. Browne, and S. McFadden. A phase-field simulation of austenite to ferrite transformation kinetics in low carbon steels. *Acta Mat.*, 54(1):11–21, 2006. [163](#)
- [85] W. Huang. Thermodynamics of the Co-Fe-Mn system. *CALPHAD*, 14(1): 11–22, 1989. [23](#)
- [86] A. Hultgren. Isothermal transformation of austenite. *Trans. ASM*, 36: 915–989, 1947. [8](#), [62](#), [84](#)
- [87] C.R. Hutchinson, A. Fuchsmann, and Y. Brechet. The diffusional formation of ferrite from austenite in Fe-C-Ni alloys. *Met. Mat. Trans. A*, 35:1211–1221, 2004. [90](#), [91](#), [92](#), [107](#), [117](#), [118](#)
- [88] C.R. Hutchinson, A. Fuchsmann, H.S. Zurob, and Y. Bréchet. A novel experimental approach to identifying kinetic transitions in solid state phase transformations. *Scr. Mat.*, 50:285–289, 2004. [92](#)
- [89] C.R. Hutchinson, H.S. Zurob, and Y.J.M. Brechet. The growth of ferrite in Fe-C-X alloys: the role of thermodynamics, diffusion, and interfacial conditions. *Met. Mat. Trans. A*, 37:1711–1720, 2006. [90](#), [91](#), [93](#), [123](#)
- [90] G. Inden. Computer calculation of the free energy contributions due to chemical and/or magnetic ordering. *In Proc. CALPHAD V*, pages 1–13, 1976. [21](#)
- [91] G.P. Ivantsov. *Dokl. Akad. Nauk. SSSR*, 58:567, 1947. [7](#), [62](#)
- [92] M. Izumiyama, M. Tsuchiya, and Y. Imai. Effect of cooling rate on A_3 temperatures of iron and iron-nickel binary alloys. *Sci. Rep. Res. Inst. Tohoku Univ.*, 22A(93-105), 1970. [81](#)
- [93] B. Jönsson and J. Agren. On the massive transformation. *Acta Met. Mat.*, 38(3):433–438, 1990. [83](#)
- [94] Kenneth R. Jolls and Daniel C. Coy. Visualizing the gibbs models. *Ind. Eng. Chem. Res.*, 47(15):4973–4987, 2008. [5](#), [18](#)

REFERENCES

- [95] S.J. Jones and H.K.D.H. Bhadeshia. Kinetics of the simultaneous decomposition of austenite into several transformation products. *Acta Mat.*, 45(7):2911–2920, 1997. [7](#), [61](#)
- [96] A. Karma. Phase-field formulation for quantitative modeling of alloy solidification. *Phys. Rev. Lett.*, 87(11):115701, 2001. [134](#), [168](#), [181](#), [182](#)
- [97] A. Karma and W.J. Rappel. Phase-field method for computationally efficient modeling of solidification with arbitrary interface kinetics. *Phys. Rev. E*, 53(4):R3017, 1996. [127](#), [134](#), [139](#), [148](#), [157](#), [181](#)
- [98] A. Karma and W.J. Rappel. Quantitative phase-field modeling of dendritic growth in two and three dimensions. *Phys. Rev. E*, 57(4):4323–4349, 1998. [127](#), [134](#), [139](#), [148](#), [157](#), [181](#)
- [99] S.G. Kim. A phase-field model with antitrapping current for multicomponent alloys with arbitrary thermodynamic properties. *Acta Mat.*, 55:4391–4399, 2007. [134](#), [168](#)
- [100] S.G. Kim. Large-scale three-dimensional simulation of ostwald ripening. *Acta Mat.*, 55:6513–6525, 2007. [134](#)
- [101] S.G. Kim, W.T. Kim, and T. Suzuki. Interfacial compositions of solid and liquid in a phase-field model with finite interface thickness for isothermal solidification in binary alloys. *Phys. Rev. E*, 58(3):3316–3323, 1998. [132](#)
- [102] SG Kim, WT Kim, and T. Suzuki. Phase-field model for binary alloys. *Phys. Rev. E*, 60(6):7186–7197, 1999. [127](#), [129](#), [130](#), [132](#), [133](#), [134](#), [157](#), [159](#), [161](#), [168](#), [170](#), [181](#)
- [103] P. Korzhavyi and all. Electronic structure and effective chemical and magnetic exchange interactions in bcc Fe-Cr alloys. *Phys. Rev. B*, 79(5), 2009. [23](#)
- [104] H.A. Kramers. Brownian motion in a field of force and the diffusion model of chemical reactions. *Physica*, 7(4):284–304, 1940. [70](#)

-
- [105] Lagerstrom. *Matched Asymptotic Expansions. Ideas and Techniques*, volume 76. American Mathematical Society, 1988. [142](#)
- [106] Y.C. Liu, F. Sommer, and E.J. Mittemeijer. The austenite–ferrite transformation of ultralow-carbon Fe–C alloy; transition from diffusion- to interface-controlled growth. *Acta Mat.*, 54:3383–3393, 2006. [83](#)
- [107] I. Loginova, J. Odqvist, G. Amberg, and J. Agren. The phase-field approach and solute drag modeling of the transition to massive $\gamma \rightarrow \alpha$ transformation in binary alloys. *Acta Mat.*, 51:1327–1339, 2003. [83](#), [135](#), [161](#)
- [108] I. Loginova, J. Agren, and G. Amberg. On the formation of widmanstätten ferrite in binary Fe–C – phase-field approach. *Acta Mat.*, 52:4055–4063, 2004. [134](#)
- [109] C.H.P. Lupis. *Chemical Thermodynamics of Materials*. Elsevier. New York, NY, 1983. [29](#), [32](#), [35](#)
- [110] T.B. Massalski. Massive transformation revisited. *Met. Mat. Trans. A*, 33:2277–2283, 2002. [69](#)
- [111] M.G. Meozzi, J. Sietsma, and S. van der Zwaag. Phase field modelling of the interfacial condition at the moving interphase during the $\gamma \rightarrow \alpha$ transformation in C–Mn steels. *Comp. Mat. Sci.*, 34:290–297, 2005. [134](#), [161](#)
- [112] M.G. Meozzi, J. Sietsma, S. van der Zwaag, M. Apel, P. Schaffnit, and I. Steinbach. Analysis of the $\gamma \rightarrow \alpha$ transformation in a C–Mn steel by phase-field modeling. *Met. Mat. Trans. A*, 36:2327–2340, 2005. [134](#), [161](#)
- [113] M.G. Meozzi, J. Sietsma, and S. van der Zwaag. Analysis of $\gamma \rightarrow \alpha$ transformation in a Nb micro-alloyed C–Mn steel by phase field modelling. *Acta Mat.*, 54:1431–1440, 2006. [134](#), [161](#)
- [114] M.G. Meozzi, J. Eiken, M. Apel, and J. Sietsma. Quantitative comparison of the phase-transformation kinetics in a sharp-interface and a phase-field model. *Comp. Mat. Sc.*, 50:1846–1853, 2011. [161](#), [170](#), [182](#)

-
- [115] M. Militzer. Computer simulation of microstructure evolution in low carbon sheet steels. *ISIJ Int.*, 47(1):1–15, 2007. [11](#), [126](#)
- [116] D.A. Mirzayev, O.P. Morozov, and M.M. Shteynberg. *Phys. Met. Metall.*, 36:96–105, 1973. [81](#)
- [117] N. Moelans, B. Blanpain, and P. Wollants. An introduction to phase-field modeling of microstructure evolution. *Comp. Coupl. Phase Diag. Thermochem.*, 32:268–294, 2008. [127](#)
- [118] S.A. Mujahid and H.K.D.H. Bhadeshia. Coupled diffusional/displacive transformations: addition of substitutional alloying elements. *J. Phys. D: Applied Physics*, 34:2573–2580, 2001. [68](#)
- [119] P. Di Napoli. *Modélisation des évolutions microstructurales par changement de phases dans les alliages de titane β -métastables*. PhD thesis, INPL, 2010. [74](#)
- [120] P. Di Napoli, B. Appolaire, E. Aeby-Gautier, and A. Bénéteau. Modeling of $\beta \rightarrow \alpha$ transformation in complex titanium alloys. *Solid State Phen.*, 172-174:1044–1049, 2011. [8](#), [9](#), [62](#), [63](#)
- [121] P. Di Napoli, B. Appolaire, E. Aeby-Gautier, and A. Bénéteau. Modeling of $\beta \rightarrow \alpha$ transformation in complex titanium alloys. In *Proc. Ti2011*, 2011. [9](#), [63](#)
- [122] M. Ode and T. Suzuki. Numerical simulation of initial microstructure evolution of Fe-C alloys using a phase-field model. *ISIJ Int.*, 42(4):368–374, 2002. [134](#)
- [123] M. Ode, S.G. Kim, and T. Suzuki. Phase-field model for solidification of ternary alloys. *ISIJ Int.*, 40(9):870–876, 2000. [134](#)
- [124] J. Odqvist. On the transition to massive growth during the $\gamma \rightarrow \alpha$ transformation in Fe-Ni alloys. *Scr. Mat.*, 52:193–197, 2005. [9](#), [63](#), [93](#), [110](#), [113](#), [122](#), [161](#)

REFERENCES

- [125] J. Odqvist, M. Hillert, and J. Agren. Effect of alloying elements on the γ to α transformation in steel. *Acta Mat.*, 50:3211–3225, 2002. [9](#), [63](#), [64](#), [93](#), [101](#), [102](#), [107](#), [108](#), [109](#), [112](#), [113](#), [117](#), [123](#), [161](#)
- [126] J. Odqvist, B. Sundman, and J. Agren. A general method for calculating deviation from local equilibrium at phase interfaces. *Acta Mat.*, 51:1035–1043, 2003. [66](#)
- [127] J. Odqvist, Bo. Sundman, and J Agren. A general method for calculating deviation from local equilibrium at phase interfaces. *Acta Mat.*, 51:1035–1043, 2003. [9](#), [63](#), [71](#), [77](#), [119](#), [122](#), [123](#)
- [128] M. Ohno and K. Matsuura. Quantitative phase-field modeling for dilute alloy solidification involving diffusion in the solid. *Phys. Rev. E*, 79:031603–1–15, 2009. [134](#), [157](#), [168](#)
- [129] K. Oi, C. Lux, and G.R. Purdy. A study of the influence of Mn and Ni on the kinetics of the proeutectoid ferrite reaction in steels. *Acta Mat.*, 48 (2147-2155), 2000. [92](#), [102](#), [105](#), [106](#), [123](#)
- [130] L. Onsager. Reciprocal relations in irreversible processes. I. *Phys. Rev.*, 37: 405–426, 1931. [65](#)
- [131] A. Phillon, H.S. Zurob, C.R. Hutchinson, H. Guo, V. Malakhov, J. Nakano, and G.R. Purdy. Studied of the influence of alloying elements on the growth of ferrite from austenite under decarburization conditions: Fe-C-Ni alloys. *Met. Mat. Trans. A*, 35:1237–1242, 2004. [92](#)
- [132] M. Plapp. Remarks on some open problems in phase-field modelling of solidification. *Phil. Mag.*, 91:25–44, 2010. [182](#)
- [133] M. Plapp. Unified derivation of phase-field models for alloy solidification from a grand-potential functional. *Phys. Rev. E*, 84:031601–1–15, 2011. [130](#), [132](#)
- [134] W.H. Press, S.A. Teukolsky, W.T. Vetterling, and B.P. Flannery. *Numerical Recipes in C - The Art of Scientific Computation*. Cambridge university, 1992. [32](#), [33](#), [40](#)

-
- [135] G.R. Purdy. The theory of diffusional phase transformations and microstructure. *Metallography*, 7:131–168, 1975. [84](#)
- [136] G.R. Purdy and Y.J.M. Bréchet. A solute drag treatment of the effects of alloying elements on the rate of the proeutectoid ferrite transformation in steels. *Acta Met. Mat.*, 43(10):3763–3774, 1995. [9](#), [63](#), [119](#)
- [137] G.R. Purdy and Y.J.M. Bréchet. A solute drag treatment of the effects of alloying elements on the rate of the proeutectoid ferrite transformation in steels. *Acta Met. Mat.*, 43(10):3763–3774, 1995. [101](#), [102](#)
- [138] G.R. Purdy, D.H. Weichert, and J.S. Kirkaldy. The growth of proeutectoid ferrite in ternary iron-carbon-manganese austenites. *Trans. Met. Soc. AIME*, 230:1025–1034, 1964. [84](#)
- [139] G.R. Purdy, J. Agren, A. Borgenstam, Y. Bréchet, M. Enomoto, T. Furuhara, E. Gamsjager, M. Goune, M. Hillert, C.R. Hutchinson, M. Militzer, and H.S. Zurob. ALEMI: A ten-year history of discussions of alloying-element interactions with migrating interfaces. *Met. Mat. Trans. A*, 42:3703–3718, 2011. [11](#), [119](#), [126](#)
- [140] D. Rodney, Y. Le Bouar, and A. Finel. Phase field methods and dislocations. *Acta Materialia*, 51:17–30, 2003. [127](#)
- [141] O.U. Salman, A. Finel, R. Delville, and D. Schryvers. The role of phase compatibility in martensite. *J. Appl. Phys.*, 111:103517–1–12, 2012. [127](#)
- [142] R.F. Sekerka, C.L. Jeanfils, and R.W. Heckel. *Lectures on the theory of phase transformations*, chapter The moving boundary problem. Metallurgical Society of AIME, 1975. [7](#), [61](#)
- [143] A. Settefrati. *Étude expérimentale et modélisation par champ de phase de la formation de α dans les alliages de titane β -métastable*. PhD thesis, INPL Nancy, 2012. [127](#)
- [144] J. Sietsma and S. van der Zwaag. A concise model for mixed-mode phase transformations in the solid state. *Acta Mat.*, 52(14):4143–4152, 2004. [11](#), [75](#), [76](#), [122](#), [126](#), [144](#), [169](#), [181](#)

REFERENCES

- [145] J. Stefan. Über die theorie der eisbildung, insbesondere über die eisbildung im polarmeere. *Annal. Phys. Chem.*, 42:269–286, 1891. [7](#), [62](#)
- [146] I. Steinbach. Phase-field models in materials science. *Mod. Sim. Mat. Sci. Eng.*, 17:0730031, 2009. [127](#)
- [147] Bo. Sundman, B. Jansson, and J-O Andersson. The Thermo-Calc databank system. *CALPHAD*, 9:153–190, 1985. [23](#)
- [148] J. Svoboda, F.D. Fischer, and E. Gamsjäger. Influence of solute segregation and drag on properties of migrating interfaces. *Acta Mat.*, 50:967–977, 2002. [66](#)
- [149] J. Svoboda, E. Gamsjäger, F.D. Fischer, and P. Fratzl. Application of the thermodynamic extremal principle to the diffusional phase transformations. *Acta Mat.*, 52:959–967, 2004. [66](#)
- [150] J.G. Swanson, W.D. ans Parr. *J. Iron Steel Inst*, 204(104-106), 1964. [81](#)
- [151] O. Thuillier. PhD thesis, Université de Rouen, 2007. [91](#)
- [152] O. Thuillier, F. Danoix, M. Coune, and D. Blavette. Atom probe tomography of the austenite-ferrite interphase boundary composition in a model alloy Fe-C-Mn. *Scr. Mat.*, 55(11):1071–1074, 2006. [92](#)
- [153] D. Turnbull. Theory of grain boundary migration rates. *Trans. AIME*, 191: 1–7, 1961. [70](#)
- [154] F.J. Vermolen, E. Javierre, C. Vuik, L. Zhao, and S. van der Zwaag. A three-dimensional model for particle dissolution in binary alloys. *Comp. Mat. Sci.*, 39:767–774, 2006. [8](#), [62](#)
- [155] A. Viardin. *Modélisation par champ de phases de la croissance de la ferrite allotriomorphe dans les aciers Fe-C-Mn*. PhD thesis, INPL Nancy, 2010. [3](#), [10](#), [11](#), [15](#), [76](#), [91](#), [113](#), [123](#), [125](#), [126](#), [127](#), [131](#), [133](#), [134](#), [163](#), [170](#), [172](#), [173](#), [174](#), [175](#), [181](#), [182](#)

REFERENCES

- [156] A. Viardin, B. Appolaire, M. Gouné, N. Perevoshchikova, and E. Aeby-Gautier. Phase field modeling of the austenite to ferrite transformation in Fe-C-Mn: from paraequilibrium to local equilibrium. *in Prep.* [10](#), [113](#), [125](#), [134](#), [172](#), [173](#), [175](#), [181](#)
- [157] Y. Wang, B. Appolaire, S. Denis, P. Archambault, and B. Dussoubs. Study and modelling of microstructural evolutions and thermomechanical behaviour during the tempering of steel. *Int. J. Micr. Mat. Prop.*, 1(2): 197–207, 2006. [8](#), [62](#)
- [158] A.A. Wheeler, W.J. Boettinger, and G.B. McFadden. Phase-field model for isothermal phase transitions in binary alloys. *Phys. Rev. A*, 45(10): 7424–7439, 1992. [132](#)
- [159] E.A. Wilson. *Met. Sci.*, 18:471–484, 1984. [81](#)
- [160] A. Yamanaka, T. Takaki, and Y. Tomita. Multi-phase-field modeling of diffusive solid phase transition in carbon steel during continuous cooling transformation. *J. Cryst. Growth*, 310(7-9):1337–1342, 2008. [134](#)
- [161] H. Yasuda, T. Nagira, M. Yoshiya, A. Sugiyama, N. Nakatsuka, M. Kiire, M. Uesugi, K. Umetani, and K. Kajiwara. Massive transformation from δ phase to γ phase in Fe-C alloys and strain induced in solidifying shell. *IOP Conf. Ser.: Mat. Sci. Eng.*, 33:012036–1–8, 2012. [83](#)
- [162] C. Zener. Kinetics of decomposition of austenite. *Trans. AIME*, 167:550–595, 1946. [72](#)
- [163] C. Zener. Theory of growth of spherical precipitates from solid solution. *J. Appl. Phys.*, 20:950–953, 1949. [7](#), [62](#), [71](#)
- [164] H.S. Zurob, C.R. Hutchinson, A. Béché, G.R. Purdy, and Y.J.M. Bréchet. A transition from local equilibrium to paraequilibrium kinetics for ferrite growth in fe-c-mn: A possible role of interfacial segregation. *Acta Mat.*, 56:2203–2211, 2008. [123](#)

REFERENCES

- [165] H.S. Zurob, C.R. Hutchinson, Y. Brechet, H. Seyedrezai, and G.R. Purdy. Kinetic transitions during non-partitioned ferrite growth in Fe-C-X alloys. *Acta Mat.*, 57:2781–2792, 2009. [92](#), [123](#)
- [166] D. Zwillinger. *Handbook of differential equations*. Academic Press, 1997. [145](#)

Modélisation de la transformation austénite/ferrite dans les aciers

Résumé

La thèse porte sur la modélisation de la transformation de l'austénite en ferrite dans les aciers en mettant l'accent sur les conditions thermodynamiques et cinétiques aux interfaces α/γ en cours de croissance de la ferrite. Dans une première partie, la thèse se concentre sur la description des équilibres thermodynamiques entre α et γ à l'aide de la méthode CalPhad. Nous avons développé un nouvel algorithme hybride combinant la construction d'une enveloppe convexe avec la méthode classique de Newton-Raphson. Nous montrons ses possibilités pour des aciers ternaire Fe-C-Cr et quaternaire Fe-C-Cr-Mo dans des cas particulièrement difficiles. Dans un second chapitre, un modèle à interface épaisse a été développé. Il permet de prédire l'ensemble du spectre des conditions à l'interface α/γ au cours de la croissance de la ferrite, de l'équilibre complet au paraéquilibre avec des cas intermédiaires des plus intéressants. Nous montrons que de nombreux régimes cinétiques particuliers dans les systèmes Fe-C-X peuvent être prévus avec un minimum de paramètres d'ajustement, principalement le rapport entre les diffusivités de l'élément substitutionnel dans l'interface épaisse et dans le volume d'austénite. Le troisième chapitre porte sur l'étude d'un modèle de champ de phase. Une analyse approfondie des conditions à l'interface données par le modèle est réalisée en utilisant la technique des développements asymptotiques. En utilisant les connaissances fournies par cette analyse, le rôle de la mobilité intrinsèque d'interface sur la cinétique et les régimes de croissance est étudié, à la fois dans le cas simple d'alliages binaires Fe-C et dans le cas plus complexe d'alliages Fe-C-Mn.

Mots-clefs : Transformation de phase, équilibre thermodynamique, conditions d'interface, ferrite, champ de phase

Modeling of austenite to ferrite transformation in steels

Abstract

The PhD thesis deals with the modeling of austenite to ferrite transformation in steels focusing on the thermodynamic and kinetics conditions at the α/γ interfaces during the ferrite growth. The first chapter deals with the determination of thermodynamic equilibria between α and γ with CalPhad thermodynamic description. We have developed a new hybrid algorithm combining the construction of a convex hull to the more classical Newton-Raphson method to compute two phase equilibria in multicomponent alloys with two sublattices. Its capabilities are demonstrated on ternary Fe-C-Cr and quaternary Fe-C-Cr-Mo steels. In the second chapter, we present a thick interface model aiming to predict the whole spectrum of conditions at an α/γ interface during ferrite growth, from full equilibrium to paraequilibrium with intermediate cases as the most interesting feature. The model, despite its numerous simplifying assumptions to facilitate its numerical implementation, allows to predict some peculiar kinetics in Fe-C-X systems with a minimum of fitting parameters, mainly the ratio between the diffusivities of the substitutional element inside the thick interface and in bulk austenite. The third chapter deals with the phase field model of austenite to ferrite transformation in steels. A thorough analysis on the conditions at the interface has been performed using the technique of matched asymptotic expansions. Special attention is given to clarify the role of the interface mobility on the growth regimes both in simple Fe-C alloys and in more complex Fe-C-Mn alloys.

Key words: Phase transformation, thermodynamic equilibrium, interface conditions, ferrite, phase field